

**Modelling neurological diseases using patient-
derived induced pluripotent stem cells**

Inaugural dissertation

for the attainment of the title of doctor
in the Faculty of Mathematics and Natural Sciences
at the Heinrich Heine University Düsseldorf

presented by

Soraia Alexandra Araújo Martins
from Chaves, Portugal

Düsseldorf, April 2021

from the institute for Stem Cell Research and Regenerative Medicine
at the Heinrich Heine University Düsseldorf

Published by permission of the
Faculty of Mathematics and Natural Sciences at
Heinrich Heine University Düsseldorf

Supervisor: Prof. Dr. James Adjaye
Co-supervisor: Prof. Dr. Gerhard Fritz

Date of the oral examination: 10/03/2021

Abstract

Neurological diseases, ranging from neurodevelopmental to neurodegenerative disorders, affect millions of individuals worldwide. These diseases present an enormous economic, emotional and physical burden to the affected individuals, their families and the society. One of the major obstacles of studying neurological diseases is the inaccessibility to primary brain samples, and in the cases where the tissue is available, primary neurons cannot be maintained and propagated *in vitro*. While transgenic animal models and immortalized cell lines have been widely used, they do not accurately replicate the human brain physiology, genetics and developmental patterns. Therefore, human models are needed to investigate the underlying molecular mechanisms of these diseases.

Recent advances in induced pluripotent stem cell (iPSC) technology have opened a new avenue to study neurological diseases in an unprecedented way, not only providing excellent tools to identify therapeutic targets, but also giving insights into the underlying molecular mechanism. The use of patient-derived iPSCs overcomes many challenges that are posed from studying complex disease pathways in the brain, which can now be unravelled in a cell-culture dish. The work described in this thesis aimed to employ patient-derived iPSCs to model a neurodegenerative disease, Alzheimer's disease (AD), and a rare neurodevelopmental disease, Nijmegen Breakage Syndrome (NBS).

The generation of iPSCs from late-onset Alzheimer's disease (LOAD) patients carrying the rare *triggering receptor expressed on myeloid cells 2 (TREM2)* R47H variant and the establishment of iPSC-derived neuronal cultures to model AD are described in chapter 2. We report for the first time the stimulation of the iPSC-derived neuronal cultures with an Amyloid- β (A β)-S8C dimer. Through this novel approach, and by employing global transcriptome analysis, we were able to identify metabolic dysregulation, impaired phagocytosis-related pathways, altered inflammatory response and endoplasmic reticulum (ER)-stress as the early events underlying LOAD in neurons carrying the *TREM2* R47H variant. In another study, we were able to show that amyloid-precursor-protein (APP) processing and A β production are controlled by the adaptor protein 2 (AP-2), a complex required for APP endocytosis. We found decreased AP-2 levels in the AD neuronal culture, suggesting cells

expressing *TREM2* R47H variant might transcriptionally down-regulate AP-2 levels in the brains of AD patients. The new insights from the mechanisms underlying the earlier pathology of AD identified here provide new opportunities for screening of potential therapeutic targets.

The use of iPSCs to model NBS, a rare autosomal recessive disorder caused by mutations within (*nibrin*) *NBN*, a DNA-damage repair protein, is described in chapter 3. We generated for the first time an NBS-iPSC line carrying the *NBN* 647del5 mutation employing a non-integrative method. NBS-iPSCs were used to implement 3D cerebral organoids to decipher the molecular mechanisms underlying microcephaly, one of the hallmarks of NBS. We showed that NBS-organoids carrying the homozygous 647del5 *NBN* mutation are significantly smaller in size than control-organoids and have a disrupted cyto-architecture. NBS patient-derived organoids exhibit premature differentiation together with neuronatin overexpression, and key pathways related to DNA damage response and cell cycle are differentially regulated compared to controls. Moreover, we show that after exposure to bleomycin, a genotoxic agent, NBS-organoids undergo delayed p53-mediated DNA damage response and aberrant trans-synaptic signalling, which ultimately leads to neuronal apoptosis. Our data provide insights into how mutations within *NBN* alter neurogenesis in NBS patients, thus providing a proof of concept that cerebral organoids are a valuable tool for studying DNA damage-related disorders.

Together the work presented in this thesis highlights the tremendous opportunities to address neuronal pathologies using patient-derived iPSCs. Specifically, we proved that iPSCs derived from AD and NBS patients are a powerful platform for evaluation of disease-related phenotypes, opening new avenues for the disease modelling and drug discovery fields.

Zusammenfassung

Mehrere Millionen Patienten weltweit leiden unter neurologischen Erkrankungen. Sowohl neuronale Entwicklungsstörungen als auch neurodegenerative Erkrankungen stellen enorme wirtschaftliche, emotionale und physische Belastungen für die betroffenen Patienten, ihre Familien und die Gesellschaft dar. Eines der größten Hindernisse für das Studium von neuronalen Erkrankungen ist die Tatsache, dass es unmöglich ist humane Gehirnbiospien für detaillierte Untersuchungen zu erhalten. Selbst wenn diese zur Verfügung stehen, sind die möglichen Analysen stark eingeschränkt, da primäre Neurone *in vitro* weder erhalten noch vermehrt werden können. Alternativ stehen Tiermodelle und immortalisierte Zelllinien zur Verfügung, die jedoch weder die humane Hirnphysiologie, noch die Genetik oder Entwicklungsmuster korrekt widerspiegeln. Daher werden dringend humane Modelle benötigt, die Untersuchungen der molekularen Grundlagen von neurologischen Erkrankungen ermöglichen.

Verbesserte Protokolle für die Arbeit mit induzierten pluripotenten Stammzellen (iPSCs) und ihre Differenzierung in die neuronale Richtung haben in den letzten Jahren neue Möglichkeiten eröffnet, die molekularen Grundlagen von neurologischen Erkrankungen zu untersuchen und therapeutische Ziele zu identifizieren. Die Verwendung von iPSCs, die aus Patientenzellen generiert wurden, hilft dabei die komplexen Signalwege, die diesen Erkrankungen zu Grunde liegen, in der Zellkultur zu analysieren.

In der vorliegenden Arbeit wurden aus Patientenzellen gewonnene iPSCs verwendet, um die neurodegenerative Alzheimer Demenz (AD) sowie die neuronale Entwicklungsstörung Nijmegen Breakage Syndrom (NBS) *in vitro* zu modellieren.

In Kapitel 2 wird die Generierung von iPSCs aus Zellen eines Patienten mit spät ausbrechender Alzheimer Demenz (LOAD) beschrieben. Diese Zellen, die die seltene *triggering receptor expressed on myeloid cells 2 (TREM2)* R47H Variante tragen, wurden anschließend als Modell für AD verwendet. Hier konnten wir erstmals die *in vitro* generierten neuronalen Kulturen mit einem Amyloid β (A β)-S8C Dimer stimulieren. Durch diesen neuartigen Ansatz, in Kombination mit Transkriptomanalysen, ist es uns gelungen frühe Ereignisse, wie metabolische Disregulation, reduzierte Phagozytose, veränderte

Entzündungsantworten und endoplasmischen Retikulum (ER)-Stress, zu identifizieren, die in Neuronen mit der TREM2 R47H Variante zu LOAD führen. In einer weiteren Studie konnten wir zeigen, dass die Prozessierung des Amyloid-Vorläuferproteins (APP) und die A β -Produktion durch den Adaptor Protein Komplex-2 (AP-2) kontrolliert werden, der für die APP Endozytose verantwortlich ist. Wir konnten reduzierte AP-2 Level in der neuronalen AD Kultur nachweisen. Dies legt nahe, dass Zellen mit der *TREM2* R47H Variante die Transkription von AP-2 auch im Gehirn der AD Patienten herabregulieren. Diese neuen Einblicke in die Mechanismen der frühen Pathologie von AD ermöglichen in der Zukunft die Suche nach neuen therapeutischen Ansätzen.

In Kapitel 3 ist beschrieben, wie iPSCs verwendet werden können, um die seltene autosomal rezessive Erkrankung NBS zu studieren. Diese wird durch Mutationen im *Nibrin* Gen (*NBN*), das für ein Protein der DNS-Schadensreparatur codiert, ausgelöst. Wir haben erstmals durch Verwendung einer nicht-integrativen Methode eine NBS-iPSC Linie mit der *NBN* 647del5 Mutation erzeugt. Diese Zellen wurden zu 3D zerebralen Organoiden differenziert, um die molekularen Mechanismen, die einem der prominentesten NBS-Phänotypen, der Mikrozephalie, zu Grunde liegen, zu analysieren. Wir konnten zeigen, dass NBS-Organoiden mit der homozygoten 647del5 *NBN* Mutation signifikant kleiner sind als wildtyp Organoiden und dass zusätzlich auch ihre Zellarchitektur gestört ist. NBS-Organoiden differenzieren vorzeitig in die neuronale Richtung. Gleichzeitig weisen sie eine erhöhte Neuronatin Expression auf und ihre DNS-Schadensantwort sowie ihr Zellzyklus weichen von dem der Kontrollzellen ab. Zusätzlich konnten wir zeigen, dass das genotoxische Agens Bleomycin in NBS-Organoiden zu einer verzögerten Aktivierung der p53-vermittelten DNS-Schadensantwort, sowie zu aberranten trans-synaptischen Signalen führt. Dies resultiert schlussendlich in vermehrter Apoptose der Neurone. Unsere Daten geben Einblick in die *NBN*-vermittelten Veränderungen in der Neurogenese bei NBS-Patienten und zeigen auf, wie zerebrale Organoiden das Studium von Erkrankungen ermöglichen, denen DNS-Schäden zu Grunde liegen.

Zusammenfassend zeigt diese Arbeit die neuartigen Möglichkeiten auf, die sich durch die Verwendung von aus Patienten generierten iPSCs für das Studium neurologischer Erkrankungen ergeben. Insbesondere haben wir gezeigt, dass iPSCs von AD und NBS Patienten als

eine Plattform dienen können, um die krankheitsassoziierten Phänotypen zu studieren. Dies öffnet neue Möglichkeiten im Bereich der Krankheitsmodellierung und für die Medikamentenentwicklung.

Contents

Abstract	iii
Zusammenfassung	v
List of Tables	xiii
List of Figures	xv
Abbreviations	xvii
1 Introduction	1
1.1 Human induced pluripotent stem cells	1
1.1.1 Induction of pluripotency: mechanisms of cell reprogramming	2
1.1.2 Pluripotency assessment of iPSCs	5
1.1.3 Applications of iPSC-derived cells	6
1.2 Human brain development	8
1.2.1 Neurogenesis	10
1.2.2 Molecular mechanisms regulating neocortex development	12
1.3 <i>In vitro</i> neuronal differentiation using iPSCs	14
1.3.1 Cerebral organoids	16
1.4 Patient-derived iPSCs to model neurological diseases	18
1.4.1 Alzheimer’s disease	20
1.4.2 Nijmegen breakage syndrome	23
1.5 Aims and scope of this thesis	26
2 Results I:	
Modelling AD using patient-derived iPSCs	29

2.1	Lymphoblast-derived integration-free iPSC line AD-TREM2-1 from a 67 year-old Alzheimer's disease patient expressing the TREM2 p.R47H variant	30
2.2	Lymphoblast-derived integration-free iPSC line AD-TREM2-3 from a 74 year-old Alzheimer's disease patient expressing the TREM2 p.R47H variant	35
2.3	Lymphoblast-derived integration-free ISRM-CON9 iPS cell line from a 75 year old female	40
2.4	IPSC-Derived Neuronal Cultures Carrying the Alzheimer's Disease Associated TREM2 R47H Variant Enables the Construction of an A β -Induced Gene Regulatory Network	45
2.5	AP-2 reduces amyloidogenesis by promoting BACE1 trafficking and degradation in neurons	74
3	Results II:	
	Modelling NBS using patient-derived 3D cerebral organoids	107
3.1	Fibroblast-derived integration-free iPSC line ISRM-NBS1 from an 18-year old Nijmegen Breakage Syndrome patient carrying the homozygous <i>NBN</i> c.657_661del5 mutation	108
3.2	Impaired p53-mediated DNA damage response contributes to microcephaly in Nijmegen Breakage Syndrome patient-derived cerebral organoids	113
4	General Discussion	143
4.1	Discussion	143
4.1.1	Modelling Alzheimers disease using patient-derived iPSCs	144
4.1.2	Modelling Nijmegen Breakage Syndrome using patient-derived cerebral organoids	148
4.2	Conclusion and future perspectives	151
5	References	153
6	Appendix	169
6.1	Acknowledgements	170
6.2	Scientific publications	172

6.3 Declaration of Authorship	176
---	-----

List of Tables

1	Summary of studies using genomically unaltered iPSC-derived neurons from patients with LOAD.	23
2	Malformations of the cortical development modelled using cerebral organoids.	26

List of Figures

1	Schematic representation of the reprogramming process of somatic to iPSCs	3
2	Applications of human iPSCs-derived cells	8
3	Schematic overview of the neural tube formation and neuronal patterning .	10
4	Schematic overview of the neurogenesis process in the neocortex	12
5	Differentiation of neuronal subtypes from iPSCs.	15
6	Schematic illustration of cerebral organoids	18
7	Schematic representation of the major aims and achievements of the thesis.	144

Abbreviations

Aβ	Amyloid β
AP-2	Adaptor protein-2
AD	Alzheimer's Disease
APP	Amyloid precursor protein
BMP	Bone morphogenic protein
CNC	Central nervous system
DDR	DNA-damage response
DNA	Deoxyribonucleic acid
EOAD	Early-onset Alzheimer's Disease
FGF	Fibroblast grow factor
hESCs	Human embryonic stem cells
IPs	Intermediate progenitors
ICM	Inner cell mass
iPSCs	Induced pluripotent stem cells
LOAD	Late-onset Alzheimer's Disease
mRNA	messenger ribonucleic acid
NBN	Nibrin
NNAT	Neuronatin
NBS	Nijmegen Breakage Syndrome
NECs	Neuroepithelial cells

NPCs	Neural progenitor cells
OCT4	Octamer-binding transcription factor 4
PSCs	Pluripotent stem cells
RGCs	Radial glia cells
SOX2	SRY-Box Transcription Factor 2
SHH	Sonic hedgehog
SVZ	Subventricular zone
TP53	Cellular tumor antigen p53
TREM2	Triggering receptor expressed on myeloid cells 2
VZ	Ventricular Zone

1 | Introduction

1.1 Human induced pluripotent stem cells

Stem cells are defined as undifferentiated cells present in the embryonic, fetal and adult stages of life. Due to their capacity to self-renew and to differentiate into different cell types, stem cells are known to be the building blocks of tissue and organs. According to their cell potency, which depends on their origin and derivation, stem cells can be classified as totipotent, pluripotent, multipotent or unipotent [1]. Totipotent stem cells are derived from the blastomere and are capable to give rise to extra-embryonic tissue, plus all tissues of the body and germline. After mitotic cell division, compaction and cavitation of the blastomeres, the blastocyst is generated. It is composed of a trophoblast layer and an inner cell mass (ICM), in which pluripotent stem cells (PSCs) reside [2]. These cells are capable of self-renewal and differentiation into all three germ layers- ectoderm, mesoderm and endoderm, however this property is restricted to a specific time period of pre-implantation development. As PSCs differentiate into cell lineages their self-renewal capacity decreases which leads to the loss of pluripotency. Multipotent stem cells are found in most tissues and are restricted to developing the mature cells of their tissue of origin. Unipotent stem cells can self-renew however exhibit a limited developmental potential, only being able to originate a single cell type. Given that the developmental potential of totipotency cannot be used *in vitro*, PSCs correspond to a stable state which allows the generation of any cell type of the human body, offering unique advantages for developmental studies, disease modelling and stem cell therapy [3,4].

A key milestone in the stem cell research field was achieved through the isolation of human embryonic stem cells (hESCs) by James Thomson in 1998 [5]. hESCs are derived from the

ICM of the blastocyst and can retain their self-renewal capacity, thus can be kept in an undifferentiated state for prolonged periods in culture and can be differentiated into the three germ layers. The contribution of the hESCs into the stem cell research field was astonishing, however evoked several ethical controversies since embryos are then needed regularly. In an effort to circumvent these ethical considerations, a ground-breaking win in the stem cell field was achieved in 2007 by Takahashi and Yamanaka. Through the ectopic expression of four transcription factors OCT4, SOX2, KLF4 and c-MYC, human dermal fibroblasts were genetically reprogrammed into an “ESCs-like state”, named induced pluripotent stem cells (iPSCs) [6]. These cells met the pluripotency criteria: could be expanded indefinitely *in vitro* and were capable of differentiating into the three germ layers. Nowadays, iPSCs can be generated by a variety of reprogramming methods from a wide range of adult somatic cells, representing a powerful system with an extensive range of applications, from basic research, disease modelling, drug discovery and regenerative and transplant medicine [7].

1.1.1 Induction of pluripotency: mechanisms of cell reprogramming

iPSC reprogramming is a dynamic process that involves multiple steps to repress the expression of somatic genes and re-express the pluripotency-associated transcription factors [8]. To achieve the pluripotent state, somatic cells undergo transitions in their gene expression profile, epigenetic remodelling, metabolism, and cellular morphology [3]. The reprogramming of somatic cells has been in constant development in order not to only increase the efficiency of reprogramming but also to maintain pluripotency and genomic stability. A plethora of studies reporting the generation of iPSCs employing different reprogramming factors combined with different strategies of delivery and reprogramming enhancers have been published [9].

The first human iPSCs generated by Takahashi and colleagues were established by retrovirus-mediated expression of four reprogramming factors octamer-binding transcription factor 4 (OCT4), SRY-Box Transcription Factor 2 (SOX2), Krueppel-like factor 4 (KLF4) and the proto-oncogene c-Myc, known as the OSKM Yamanaka factors, in dermal fibroblasts. In the same year, Yu *et al.*, (2007) described a modified version of the OSKM factors, by replacing KLF4 and c-MYC by the homeobox protein NANOG and protein lin-28 homolog

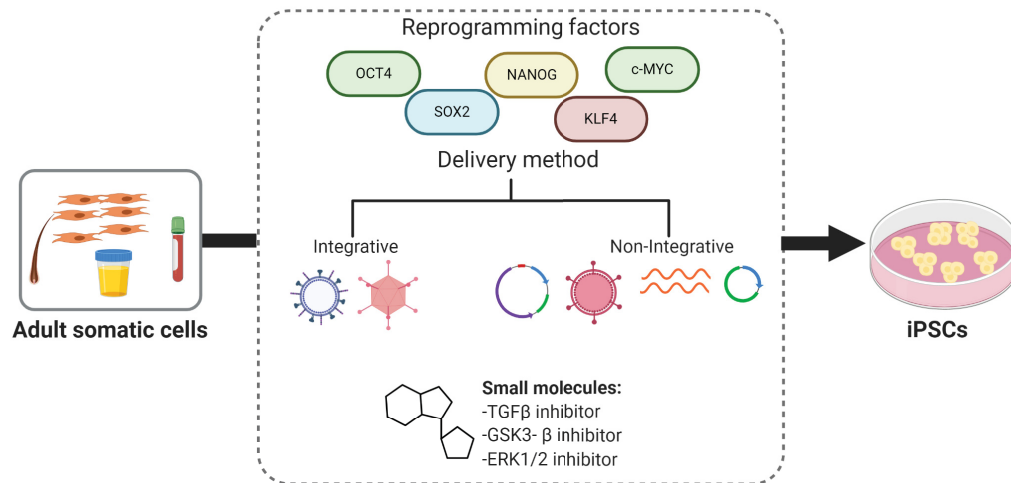


Figure 1 – Schematic representation of the reprogramming process of somatic to iPSCs. A variety of adult somatic cells can be used as starting material. To achieve an efficient reprogramming, different combinations of transcription factors (OCT4, SOX2, NANOG, KLF4 and c-MYC) can be delivered to the cells by an integrative or non-integrative method. To enhance the reprogramming efficiency and the quality of the generated iPSCs, small molecules that block TGF β , GSK3- β and ERK1/2 pathways are commonly used in combination with the transcription factors. Created with BioRender.com.

A (LIN28) [10]. OCT4, SOX2 and NANOG are considered the core transcriptional regulatory circuit that governs pluripotency and self-renewal, from which OCT4 is indispensable and remains as the preeminent transcription factor [3]. The combination of the two sets of transcription factors has a synergetic effect in the reprogramming efficiency [11]. To facilitate the reprogramming efficiency, many researchers have employed “reprogramming enhancers”, that not only allow achieving the pluripotency stage but also the acquisition of the capacity to proliferate indefinitely. The identification of p53 as a roadblock of reprogramming, which prevents the reprogramming of DNA-damaged cells, led to the insertion of a short hairpin RNA (shRNA) cassette of *cellular tumor antigen p53 TP53* or chemical inhibition of p53 during the reprogramming process [12]. Silencing *TP53* expression extremely increases the reprogramming efficiency and highlights the incredible stress that cells are subjected to during the reprogramming process. However, blocking such an important pathway might have detrimental consequences, in which cells can escape apoptosis and senescence and cause teratoma formation [13].

The first reprogramming methods were based on retroviral and lentiviral expressing vec-

tors, offering a high reprogramming efficiency. However, these vectors can cause insertional mutagenesis compromising the genomic stability, resulting in harmful effects and thus limiting their use in clinical applications [8]. To improve the quality of iPSCs, different alternative delivery systems to generate integration-free iPSCs have emerged, including viral/non-viral delivery and direct transfection of the reprogramming factors. Non-integrating viruses like adenovirus and Sendai virus can efficiently generate iPSCs without being integrated into the host genome. To completely circumvent the inherent problems of the viral delivery system, episomal vectors, transposon systems, minicircle vectors, synthetic RNA replicons, human artificial chromosomes and nanoparticles carriers have been described for iPSCs reprogramming. Alternative methods such as synthetic mRNA and recombinant proteins can reprogramme somatic cells into iPSCs [9]. Currently, Sendai viruses are a highly effective reprogramming method, however episomal reprogramming shows great advantages due to a high consistency in the generated iPSCs, a more rapid reprogramming agent elimination and are well suited for clinical translation [7].

To enhance the efficiency of reprogramming, transcription factors are combined with small molecules that promote dedifferentiation by acting in signalling pathways and epigenetic mechanisms, a promising strategy with unique advantages. Cellular reprogramming is associated with epigenetic erasure and resetting modulated by epigenetic modifiers in order to enhance the expression of pluripotency-associated genes and suppress the somatic-associated genes [3]. In that regard, reprogramming can be enhanced by small molecules that modulate the epigenetic enzymes such as the commonly used histone deacetylase inhibitors (valproic acid) and methyltransferase inhibitors (5'-azacytidine and RG108) [14]. During reprogramming cells also undergo a metabolic switch, i.e. the transition from oxidative phosphorylation to glycolysis [15]. Small molecules that promote glycolytic metabolism by targeting 3-phosphoinositide-dependent protein kinase 1 (PDK1) / phosphoinositide 3-kinases (PI3K) / serine/threonine-protein kinase AKT- signalling and hypoxic conditions (hypoxia-inducible factor 1-alpha (HIF-1 α) activation) enhance reprogramming [16]. Another crucial step is mesenchymal to epithelial transition (MET) leading to a remarkable morphological change with distinct cell-cell interactions characteristic of iPSCs [17]. Inhibition of transforming growth factor beta (TGF β) signalling, responsible for the

opposite process, by the small molecule A-83-01, has been shown to be critical for the efficient generation of iPSCs. Another important player in the MET transition is the activation of the WNT/ β -catenin pathway achieved by the glycogen synthase kinase 3 beta (GSK3- β) inhibitor CHIR99021. Using the chemical combination of A-83-01, CHIR99021 and PD035901, an extracellular signal-regulated kinase 1/2 (ERK1/2) inhibitor to eliminate differentiation-inducing signalling from mitogen-activated protein kinase 1 (MAPK), together with the OSKM factors has been proven to increase the efficiency of reprogramming and the quality of the iPSC generated [7].

Apart from the delivery method, the combination of transcription factors and the use of small molecules to enhance reprogramming, the choice of the starting material is another important factor in achieving an easy, efficient and fast generation of iPSCs. Different somatic cell types can be used, of which dermal fibroblasts are the most commonly used because they are easy to culture and expand. However, reprogramming fibroblasts has some disadvantages such a low reprogramming efficiency and the need to perform an invasive biopsy in order to obtain the starting material [18]. Blood cells derived from peripheral blood or umbilical cord blood can also be used as a primary cell source, as a less invasive method when compared to dermal fibroblasts [19]. A wide range of other cell types have also been described as starting material to generate iPSCs, such as keratinocytes isolated from hair follicles, mesenchymal stem cells, primary hepatocytes, neural stem cells, amniotic fluid cells and pancreatic B cells [20]. In view of finding a somatic cell source which is non-invasive to obtained, reproducible, simple and easily accessible, urine samples became a valuable and promising resource with high reprogramming efficiency [21,22].

1.1.2 Pluripotency assessment of iPSCs

As mentioned above, the reprogramming process is an extremely complex event with many roadblocks, which can result in partially reprogrammed cells [11]. Thus, it is essential to assess the pluripotency potential and the quality of the generated iPSCs. Accordingly, apart from all morphological attributes, which include unlimited self-renewal, on a molecular level iPSCs must express the core nuclear transcription factors OCT4, NANOG and SOX2, the keratan sulfate antigens TRA-1-60 and TRA-1-81, the stage-specific embryonic

antigen 4 (SSEA4) and functional telomerase. At a functional level, iPSCs must exhibit the ability to differentiate into the three germ layers, which can be assessed *in vivo* (teratoma formation) or *in vitro* (embryoid body formation). Also, the global transcriptome profile must have a high correlation with the ESCs, and the culture must be free of bacteria, mycoplasma, yeast and fungi [23,24]. In addition to the molecular and functional characterization of pluripotency, it is essential to ensure genomic stability. Recent studies have identified the presence of mutations in iPSCs, which can be due to the presence of pre-existing variations in the parental somatic cells, mutations induced during the reprogramming process or passage-induced mutations arising from the prolonged periods of culture. The presence of genomic instability in iPSCs can lead to unfavourable outcomes, including malignant outgrowth which can have severe implications for clinical transplantation [25].

1.1.3 Applications of iPSC-derived cells

Since its first report in 2007, human iPSC technology has offered unprecedented valuable contributions to the biomedical and medical sciences field. Great progress has been made to create new differentiation protocols of iPSCs into countless cell types representing nearly all tissues of the body [26]. With the extraordinary unlimited self-renewal and potential to functionally differentiate *in vitro*, iPSC-derived cells are promising for a variety of applications in cell therapy, disease modelling, drug discovery and toxicity testing. Additionally, *in vitro* differentiation of human iPSCs recapitulates aspects of human development, providing a new model system with unique advantages for developmental studies [14,27].

Among the medical applications, one of the most astonishing aspects of the iPSCs technology is the possibility to generate cells for clinical therapy. iPSC-derived cells can be transplanted into patients to replace the damaged cells or tissues. Cell therapy has been investigated in a wide range of disorders with promising results from preclinical studies. Currently, a wide number of stem cell-based clinical trials to treat central nervous system disorders, retinal degenerative diseases, heart diseases and diabetes are ongoing [28]. Although the clinical applications such as cell transplantation are considered the best application of iPSCs, patient-derived iPSCs hold a tremendous potential for disease modelling and drug discovery, as iPSC-derived cells recapitulate the disease molecular and cellular

phenotype from the donor.

Disease modelling involves the generation of iPSCs from patients and further differentiation into disease-relevant cells, offering a model system which overcomes the issues associated with animal models and post-mortem tissue [29]. Recent advances in genome editing techniques enable the introduction of disease-causing mutations into wild-type iPSCs and the elimination of such mutations in patient-derived iPSCs to create isogenic controls for iPSC-based disease modelling [30]. To date, many patient-derived iPSCs have been established and used for disease modelling of neurological diseases (see section 1.4.), hepatologic diseases, haematological and immunological diseases, endocrinology/metabolic diseases and cardiac diseases [26]. Apart from disease modelling, drug screening based on patient-derived iPSCs has been widely used to evaluate more than 1000 compounds for several diseases, from which several candidates are under clinical trials. iPSCs derived from healthy donors or patients can also be used to assess the efficacy of new drugs and the prediction of toxicology. [30].

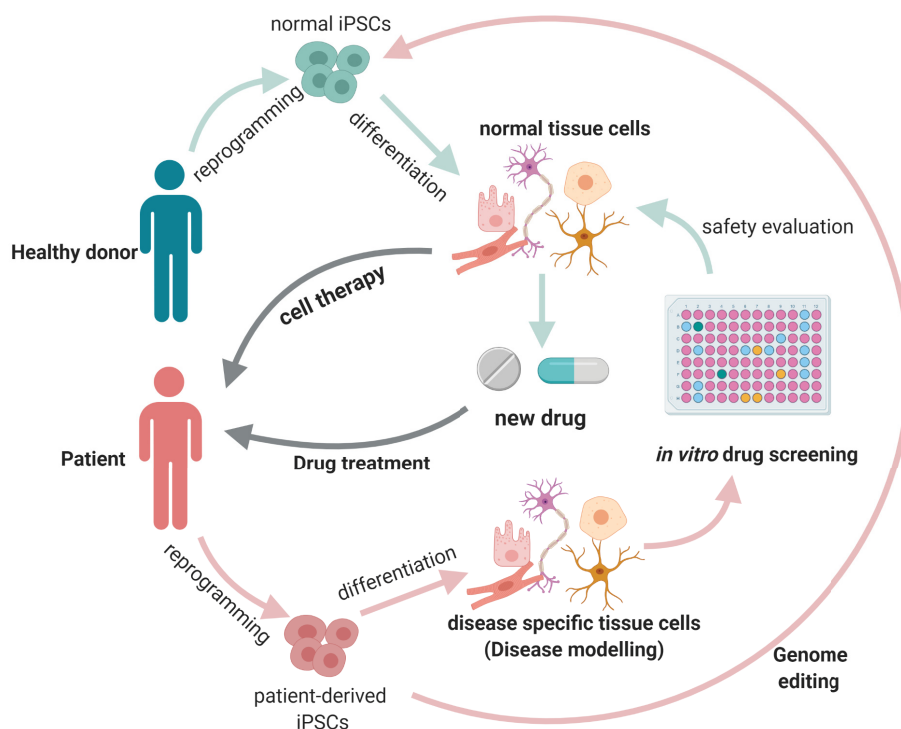


Figure 2 – Applications of human iPSCs-derived cells. iPSCs can be reprogrammed from healthy donors and differentiated into a variety of cell types, which can be used for cell therapy and to evaluate the toxicology and efficacy of new therapeutic compounds. Patient-derived iPSCs can be reprogrammed into cells harboring the disease phenotype. These cells can be used to study the etiology and the molecular mechanisms underlying the disease and for drug-screening. Genome editing techniques allow the correction of mutations that can be potentially used for autologous cell transplantation or create isogenic controls for disease modelling studies. Adapted from [14]. Created with BioRender.com

1.2 Human brain development

The human brain is the most complex, dynamic and enigmatic organ in the body. Building this highly organized system is an extended process that begins in the third gestational week and it takes on average 20 to 25 years to mature, some arguing it endures throughout the lifespan [31,32]. A mature brain is composed of about 100 billion neurons, the information processing cells, which form complex connections with other neurons and other cells [31]. Apart from the hundreds of different neuronal cell types, a diverse range of glia cells, such as astrocytes and oligodendrocytes, and microglia are part of the neocortex, the largest and most important brain information processing network [33]. Astrocytes are the most abun-

dant glia cells and play essential functions in neuronal survival, blood-brain barrier maintenance and in synaptic formation, strength and turnover. Oligodendrocytes are responsible for the myelination of the neuronal axons allowing a fast saltatory nerve conduction and axon integrity. Representing 10% of the total glia cells, microglia are the myeloid resident cells in the brain which are responsible for removing damaged neurons, pathogens and molecules in order to maintain the health of the central nervous system (CNS) [34]. To achieve such cognitive and behaviour repertoire, which defines our human nature, the generation of these specialized neuronal and glia cells is intricately orchestrated at appropriate locations and with the right timing, a multistep process controlled by intrinsic and extrinsic factors [33].

The development of the neocortex starts right after gastrulation, the process by which the three germ layers ecto-, endo- and mesoderm are formed. Cells located along the ectoderm became specialized toward the neuronal fate, known as neuroepithelial cells (NECs). This process is called neural induction and it is responsible for the formation of the neuronal plate, or the neuroepithelial layer (Figure 3A). This highly polarized neuroepithelium folds and fuses to form the neuronal tube, the first well-defined neuronal structure [31]. The NECs form a single layer of cells that lines around the neural tube immediately adjacent to its hollow cavity which will later develop into the ventricular system of the brain. For that reason, the layer of NECs constitutes the ventricular zone (VZ) of the neural tube and are the founders from which all neurons and glia cells will be generated. The neural tube undergoes regional patterning, a morphogenic process coordinated by temporally and spatially morphogen gradients. These signals are diffused from discrete regions and form the basis for specifying the NECs to region-specific neural progenitor subtypes. The anterior-posterior axis (or rostral-caudal axis) patterning is regulated by a gradient of members of the fibroblast growth factor (FGF) family, WNT signalling and retinoids, whereas the dorsal-ventral axes patterning is regulated by the opposite gradient between bone morphogenic proteins (BMPs) and WNT signalling, and sonic hedgehog (SHH). The gradient of morphogens along these axes allows the subdivision of the neural tube into four major regions, which later will establish the forebrain, midbrain, hindbrain and spinal cord [32,35] (Figure 3B, C).

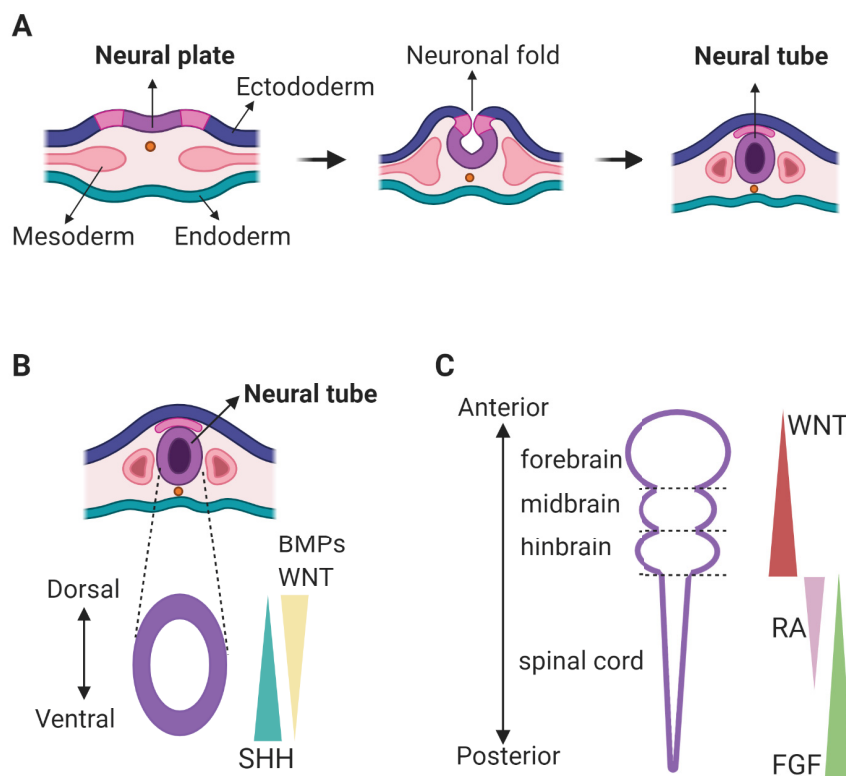


Figure 3 – Schematic overview of the neural tube formation and neuronal patterning. A) After gastrulation, ectodermal tissue differentiates and forms the neural plate. The neural plate fold closes to form the neural tube, which will originate the forebrain, midbrain, hindbrain and spinal cord. B) The dorsal-ventral axis in the forebrain are regulated dorsally by WNT and BMPs and ventrally by SHH. C) In the anterior-posterior axes, the WNT gradient dictates the regionalization of the forebrain, midbrain, hindbrain and anterior spinal cord, spinal cord segmentation is governed by RA and FGF gradients. BMP: bone morphogenic protein; FGF: fibroblast grow factor; RA: retinoid acid; SHH: sonic hedgehog. Created with BioRender.com.

1.2.1 Neurogenesis

Until this stage, the pool of NECs present is far too small to start the generation of neurons, a process called neurogenesis. Due to the intrinsic capacity of self-renewal, NECs undergo successive rounds of symmetric division, which can generate two cells with the same identity. At the onset of neurogenesis of the neocortex, NECs transform into radial glia cells (RGCs) characterized by a high expression of the master regulator of neurogenesis paired containing homeodomain transcription factor PAX6, which promotes RGCs proliferation and spindle orientation [36]. RGCs exhibit an apical-basal polarity and primarily switch from symmetric division to asymmetric neurogenic division, which gives rise

to a new RGC and a neuron [37]. This cell fate determination is influenced by apical-basal cues, mainly by apical components such as primary cilium, centromeres and adherent junctions [36]. During asymmetric division, RGCs can also give rise to two daughter cells with different identities, one neuron and one intermediate progenitor (IP). IPs are transiently amplifying the progenitor pool, delaminating from the VZ to settle in the subventricular zone (SVZ), where they divide symmetrically to self-renew before undergoing the terminal division originating two neurons [38,39]. In a later developmental stage, RGCs undergo another asymmetric division with oblique and horizontal cleavages generating IPs and basal radial-glia cells (bRGCs), which remain in the SVZ. These two populations increase the neuronal output and the related size expansion of the neocortex. In the last stage of neurogenesis, RGCs undergo a terminal symmetric division, giving birth to two neurons. The progenitors remain in the proliferative zone (VZ and SVZ) whereas the postmitotic neurons migrate basally. Neurons require the RGCs as a cellular scaffold to support their migration into the developing neocortex, resulting in the formation of a well-organized six-layered cortical plate. Earlier migrating neurons form the deepest layers and the later migrating neurons form the more superficial layers [31,40]. After the cortical layer formation gliogenesis occurs, in which RGCs detach from the apical surface, migrate in the direction of the basal surface and terminally differentiate into astrocytes and oligodendrocytes. A simplified overview of neurogenesis is depicted in Figure 4.

After neuronal migration, neurons that reached their target region need to develop neuronal processes to allowed them to become integrated into neuronal networks. This process starts with axonal and dendritic outgrowth, synapsis formation with pre- and postsynaptic specializations and synapse stabilization. The accuracy and efficiency in synapse connectivity and the neural circuit is the most remarkable future of the nervous system fundamental to life-long learning, memory, behaviour and cognition [41]. While most of the neocortex developmental events involve proliferation, there are two processes that involve substantial loss of neural elements: cell death by apoptosis and selective elimination of axons, dendrites and synapses. These nonpathological events play an essential role in adjusting connections between neurons and compensate errors which led to mislocations and misprojections [31]. The high levels of apoptosis across the neocortex may be important to

eliminate cell populations that have only a transient function in brain development [42].

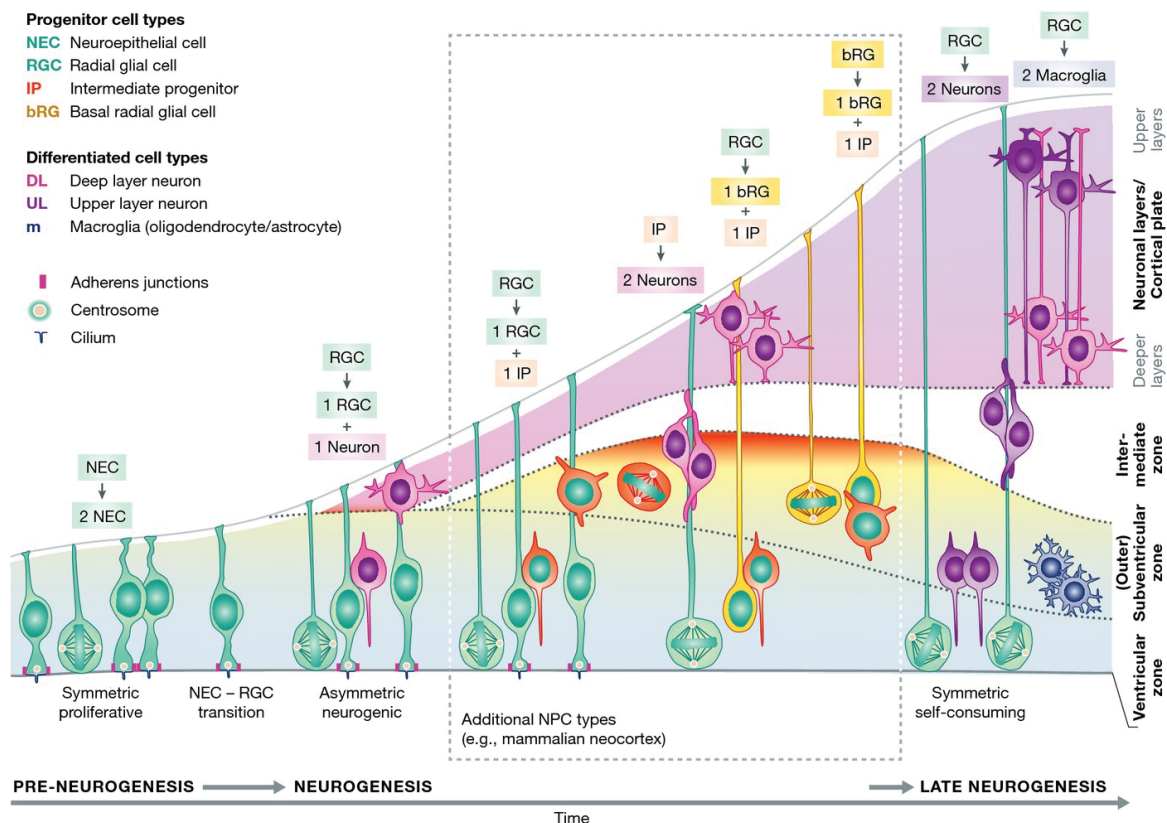


Figure 4 – Schematic overview of the neurogenesis process in the neocortex. Reproduced with kind permission from [36].

1.2.2 Molecular mechanisms regulating neocortex development

Multiple neural progenitor zones contribute to the complexity and variety of different neuronal cell types found in the different regions, generating the immense neuronal heterogeneity found in the mature neocortex [33]. As mentioned above, the initial neuronal fate is established during the early embryogenesis by the regionalization along the anterior-posterior and dorsal-ventral axes commanded by a cross-regulatory transcription factor network. The delimitation of the forebrain from the mid- and hindbrain occurs by reciprocal inhibition of OTX2 and GBX2. PAX6 is expressed in the neural progenitor cells (NPCs) in the dorsal telencephalon and antagonizes the transcription factors GSX1 and GSX2, expressed in the NPCs of the ventral telencephalon [43]. These signalling events not only pattern the distinct regions but also initiate transcriptional signalling cascades, which give rise to the different

neural subtypes found in the cortical layers. There are two broad classes of cortical neurons: interneurons and projection neurons. The astonishing types of projections neurons found in the different cortical layers are originated in the dorsal telencephalon. NPCs expressing PAX6 and EMX1/2 upregulate the expression of the transcription factors NEUROG1 and NEUROG2, which induce the glutamatergic projection neurons fate by the induction of the downstream targets NeuroD and T-box brain genes TBR2 and TBR1. In contrast, NPCs in the ventral telencephalon express GSH1/2, NKX2.1 and ASCL1 that instruct the generation of GABAergic interneurons, repressing the dorsal identity [33,44]. Progress has been made to identify the transcription factors involved in the sequential generation of specific types of neurons present in the cortical layers. A cross-repressive interaction by transcription factors is responsible for the identity of the projection neurons. CTIP2 plays a central role in the specification of neurons located in the layer V. However, repression of CTIP2 is necessary to promote the generation of layer VI and II/III by TBR1 and STAB2, respectively. However, the specific mechanism which mediates the different neuronal outputs still remains unclear [45].

The regulation of the expression of the transcription factors which are essential for the switch of the NPCs from proliferation to differentiation, as well as the induction of specific NPCs, is essentially triggered by the Notch, WNT, SHH and FGF pathways [36]. At early stages, the WNT/ β -catenin pathway promotes the expansion and folding of the neuroepithelium, while the FGF pathway promotes the transition of the NECs into RGCs, which is also promoted by the activation of the Notch signalling pathway. FGF is also important for the anterior-posterior patterning. Proliferation and self-renewal of the neural progenitors is controlled by the FGF pathway via regulating the cell cycle proteins. The cell cycle kinetics are also regulated by the SHH pathway. Notch pathway also promotes the proliferation of the RGCs, however activation in later stages inhibits the generation of IPs. Regarding the WNT pathway, the effects of the signalling are complex and time-regulated. Activation of this pathway at early developmental stages promotes proliferation and self-renewal of the RGCs, while in later stages it promotes the maturation of RGCs into IPs. Similar inputs are originated by the BMP pathway, which at early developmental stages induces neurogenesis, while at later stages blocks neurogenesis in order to promote astrogenesis. The

MAPK-ERK pathway also controls the proliferation of the NPCs and prevents premature differentiation [45,46]. Apart from these extracellular signals, the behaviour of the NPCs is affected by numerous other factors. Retinoid acid produced in the meninges is essential for the switch of RGCs from symmetric to asymmetric division. The Cajal-Retzius cells, the first neurons to be born, secrete reelin which amplifies Notch signalling promoting RGCs proliferation. Feed-back signals to RGCs are also derived from the later-born cortical neurons, which express signalling molecules such as Neurotrophin-3 and FGF9, regulating cell fate choices and the switch of dividing RGCs to astrogenesis [36].

Controlling the pool size of the NPCs plays a central role in cortical development. Alterations in the proliferation, migration, differentiation and survival of the NPCs can lead to variations in the final neuronal output and the size of the neocortex inducing brain malformations [47].

1.3 *In vitro* neuronal differentiation using iPSCs

Starting with the work of Ramón y Cajal more than 100 years ago, the field of neuroscience has striven to elucidate the complexity of the human brain. Over the past years stem cell research has blossomed and iPSC technology offers a practical way to study the structure, development and function of the brain. The ability to guide iPSCs to highly enriched or pure neuronal subtypes holds a great potential to dissect the underlying molecular mechanisms and treatment of neurological diseases[48]. iPSC-based neural induction models recapitulate key molecular and cellular features thought to occur *in vivo*, however an efficient differentiation of iPSCs into specialized neuronal subtypes remains challenging. Extensive progress in creating robust methods to control the regional identity of PSCs-derived neural progenitors and neurons has been made. As *in vivo* brain development, *in vitro* differentiation relies on strategies to modulate the exogenous levels of the signalling molecules part of the fundamental brain developmental program: BMP, WNT, SHH and FGF. By mimicking these cues, it is possible to generate regional specific neural progenitors which can be expanded and then matured into neurons and glia cells [49].

A widely used strategy to convert iPSCs into early neural lineages is the use of the “dual-

SMAD inhibition” method. It uses two small molecules to inhibit the SMAD-dependent TGF β and BMP signalling pathways, which channels differentiation toward anterior neuroectodermal lineage [50]. This method is particularly useful in monolayer systems and can replace the EBs formation. In the absence of morphogens or the presence of FGFs or WNT inhibitors, NECs became committed to the forebrain fate. However, NECs patterning into midbrain and hindbrain can be achieved by dose-dependent inhibition of the GSK3 β and thus activation of the WNT pathway [51]. At this stage, it is also possible to effectively specify NECs to progenitors with particular identities along the dorsal-ventral axis by a regulation of SHH concentrations and/or balance between SHH and WNTs [52]. Regional patterning of the NPCs allows the generation of neurons with a particular transmitter property based on their intrinsic properties [35]. Figure 5 summarizes the different neural subtypes that can be originated from iPSCs through neural induction, regional patterning and neural differentiation.

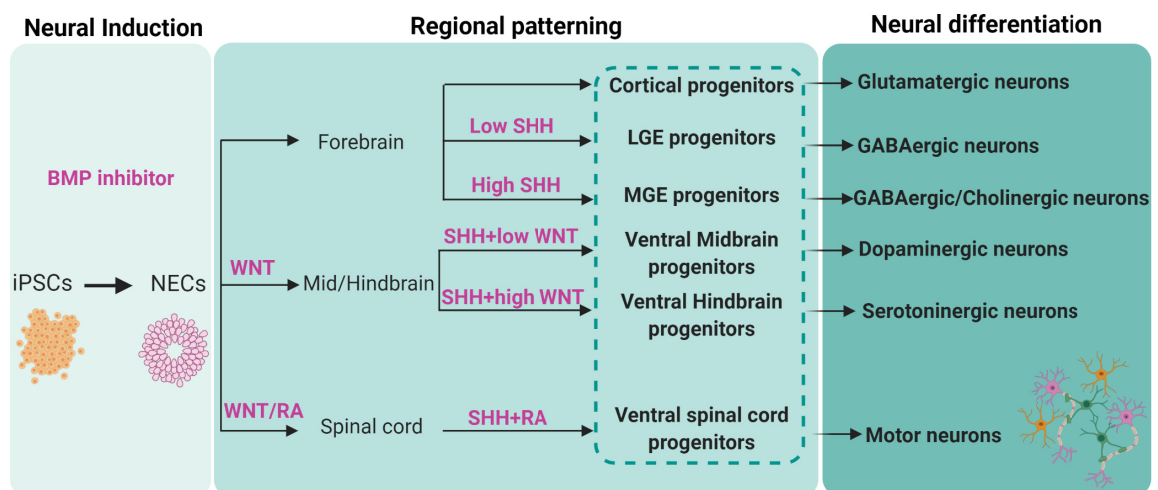


Figure 5 – Differentiation of neuronal subtypes from iPSCs. Different neuronal subtypes can be differentiated from iPSCs through neuronal induction, regional patterning and neuronal differentiation. Pink indicates the morphogens applied in each step. BMP, bone morphogenic protein; LGE, lateral ganglionic eminence; MGE, medial ganglionic eminence; NECs, neuroepithelial cells; RA, retinoic acid; SHH, sonic hedgehog. Adapted from [35].

In the conventional two-dimensional (2D) cell culture systems, these patterned NPCs are arranged in characteristic monolayer rosette structures, composed of the polarized RGCs at the center and the IPs located at the peripheral region [53]. The further expansion of these NPCs can be done in suspension, with the rosette-containing cells forming neuro-

spheres. The last step of neurogenesis is achieved by the terminal differentiation of the patterned NPCs into the different subtype functional neurons. Neurotrophic factors such as brain-derived growth factor (BDNF), glia-derived growth factor (GDNF) and insulin growth factor (IGF) promote the survival and differentiation of neurons and thus allowing the formation of functional neuronal networks [52]. The ability to generate defined neuronal populations carrying a disease phenotype was a significant step forward in disease modelling, allowing the focus to be placed on the neural subtype affected in the specific neurological disorders. 2D differentiation methods are easy to handle and can be very effective in single cell type differentiation. However, it is noteworthy to argue that 2D models mostly fail to recapitulate the human brain complexity, creating a need for more physiologically relevant models with human-specific features of brain development [54].

1.3.1 Cerebral organoids

Methodologies to attempt to creating of neuronal 3D models from PSCs have been pursued since the late 2000s with the pioneer work from Sasai Laboratory, demonstrating that NPCs in 3D aggregation culture could self-organise and form apico-basal polarized cortical tissue[55]. The breakthrough in the development of 3D brain organoids was achieved with the work from Knoblich Laboratory with the generation of 3D neuronal structures containing regions that resembled various independent brain regions, so-called cerebral organoids [56]. This work paved the way to a new field of research, and over the past few years, an array of different cerebral organoid protocols have been developed.

The generation of 3D cerebral organoids from iPSCs can follow two different methodologies, unguided methods and guided methods. Unguided methods rely on self-patterning and self-organization, thus iPSCs are cultured in serum-free medium in the absence of external patterning factors. As a result, the generated cerebral organoids from iPSCs exhibit a variety of cell lineage identities ranging from forebrain, midbrain and hindbrain, to retina, choroid plexus and mesoderm[57]. For that reason, these cerebral organoids are also referred to as whole-brain organoids, however the brain region composition varies across individual organoids and especially across iPSC lines [56,58–60]. On the other hand, guided methods use patterning factors to specify the neural progenitor fate, generating brain region-specific

organoids[61]. Guidance along the anterior-posterior and dorsal-ventral axes is achieved, as in the 2D methods of differentiation, by the time-dependent modulation of the WNT and SHH pathways. By this modulation, different protocols to generate dorsal and ventral telencephalon [62,63], forebrain [64], thalamus [65], hypothalamus [66], midbrain [67] and hindbrain [68] have been developed. A critical advancement in recent studies was the fusion of organoids from different regions, which has been particularly useful to study neuronal migration and the formation of neural connections [69,70]. While region-specific organoids are very useful to study the impact of genetic defects on a specific disease-associated brain region, the generation of these sub-specific regions is still a challenge. Currently, the cortical organoid protocols which generate cells with mixed identity are still the most commonly used [64,71,72]. These protocols combine the dual-SMAD inhibition method to pattern the iPSCs to a neuroectoderm identity with the intrinsic self-organization capacity of the NPCs [73]. The use of extracellular matrix components, like Matrigel, improves the organization of the neuroepithelium *in vitro*. Another crucial approach is the use of agitating conditions which provide enhanced nutrient and oxygen distribution, promoting the formation of much larger cerebral organoids resembling those *in vivo* ventricles[56,64].

Cerebral organoids derived from iPSCs are self-organizing structures which recapitulate with considerable accuracy the temporal neurodevelopmental trajectory similar to fetal development. iPSCs undergo neural induction to adopt the neuroectodermal fate with the neural progenitors self-organized into 3D structures featuring the apical lumen, designated ventricular-like zones. Immediately adjacent to these proliferative and polarized structures containing NPCs, a thin and dense layer of intermediate progenitors and immature neurons can be found, resembling the subventricular zone (Figure 6). As *in vivo*, the RGs in these regions resemble their mitotic behaviour and dynamics undergoing symmetric and asymmetric division. These cells will over time give rise to postmitotic neurons and glia cells, making up the six-layered cortical-like structure [56,60,66,74]. The generated neurons exhibit functional maturity, forming functional synapses. Notably, not only the cytoarchitecture of the cerebral organoids mimics aspects of the human brain, but also shares similar epigenomic and transcriptional programs, features of the fetal brain [75].

The exciting advances in the brain organoid field have opened up new boulevards and tools

for getting a better understanding of the human brain development. iPSC-derived organoids maintain the human genomic context and thus hold a great and unique potential in modelling neurodevelopment and other neurological diseases, allowing to address new questions that are limited in other model systems.

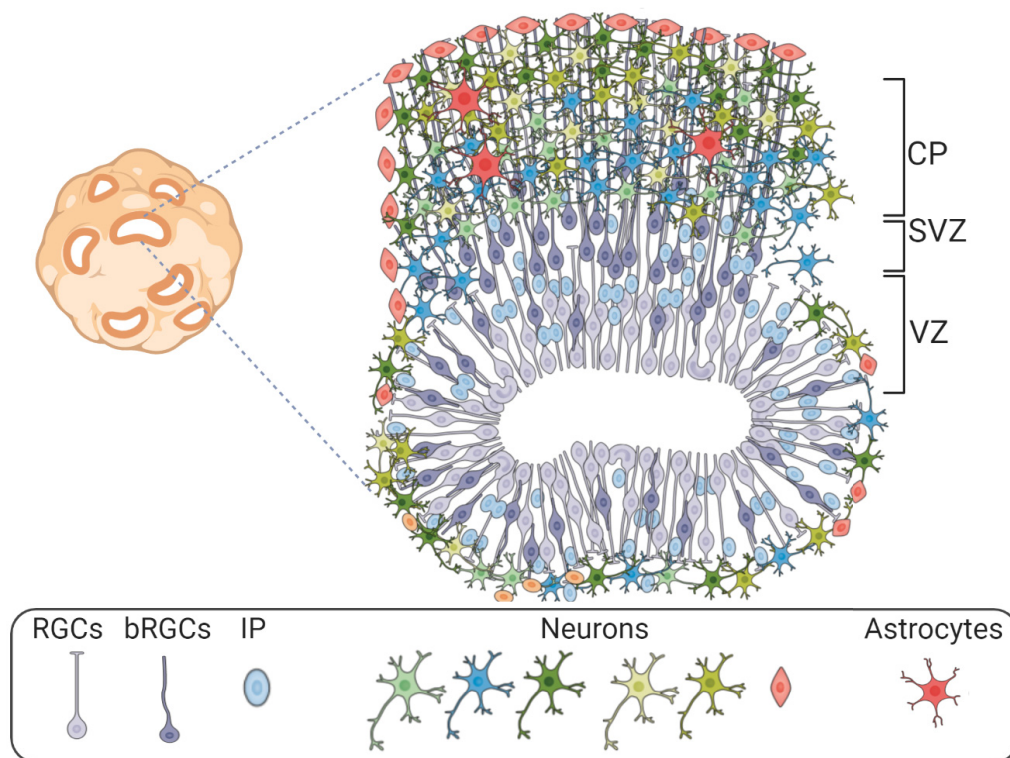


Figure 6 – Schematic illustration of cerebral organoids. Mature organoids display a ventricular-zone (VZ) like structure with radial glia cells (RGCs), a subventricular-like zone composed of basal radial glia cells (bRGCs) and intermediate progenitors (IP) and a cortical plate (CP) where the postmitotic neurons expressing the cortical layer makers and astrocytes. Adapted from [76].

1.4 Patient-derived iPSCs to model neurological diseases

Neurological diseases, ranging from neurodevelopmental, neuropsychiatric and neurodegenerative diseases, affect millions of individuals worldwide. These diseases present an enormous economic, emotional and physical burden to the affected individuals, their families and the society [77,78]. One of the major obstacles of studying neurological diseases is the inaccessibility to primary brain samples, and in the cases where the tissue is available, primary neurons cannot be maintained and propagated *in vitro*. While transgenic

animal models and immortalized cell lines have been developed and widely used, they do not accurately reproduce the human brain physiology, genetics and developmental patterns [79]. The potential of using iPSCs from patients with intractable diseases and their subsequent differentiation into the disease-relevant cell type has revolutionised the research of neurological diseases. Patient-derived iPSCs are a source of great hope, not only with the tremendous applications in regenerative medicine but also for disease modelling, overcoming the many challenges that are posed from studying complex disease pathways in the brain, which can now be unravelled in a cell-culture dish. Thus, *in vitro* disease models contain the patient-specific genetic information, which with the application of a multi-omic analysis allows investigating disease-relevant genetic and molecular pathways in a physiological cellular microenvironment, which have heretofore remained unknown. Recently, progress has been made to generate 3D *in vitro* systems to more closely recapitulate the complex multicellular composition and architectural elements of the brain. Comprehensive 2D and 3D disease-specific iPSCs have been established to study neurological diseases at a cellular level, whether they are defined genetic disorders or are caused by a combination of environmental and genetic factors, with key examples mentioned below [61,80,81].

Among neurological diseases, iPSC-derived models to study neurodegenerative diseases have been extensively employed, particularly to study Alzheimer's disease (for details, see 1.4.1), Frontotemporal dementia, Amyotrophic lateral sclerosis, Parkinson's disease and Huntington's disease. New mechanisms related to neurodegenerative diseases have been elucidated using iPSCs, especially when familiar mutations are involved [79,81,82]. However, neurodegenerative diseases are complex and heterogeneous since many different cell types and regions within the brain are affected. Accordingly, 3D culture systems with more complex cell types and technologies that accelerate aging in a dish have been developed [83]. iPSC technology has also created new possibilities for the study of psychiatric diseases. Schizophrenia has been the most successful example, being the first psychiatric disease to be modelled with patient-derived iPSCs, where reduced connectivity of the iPSC-derived neurons was shown [83]. The pathophysiology of psychiatric diseases, which are highly polygenic and influenced by environmental factors, is still poorly understood. Patient-derived iPSCs have paved new opportunities to capture the complex genetic archi-

tecture and signaling pathway dysregulation, allowing not only the understanding of the pathophysiology of psychiatric diseases, but also testing of antipsychotic drugs. Following schizophrenia, a plethora of psychiatric and neurodevelopmental diseases have been modelled using patient-derived iPSC: bipolar disorder, autism spectrum disorder, Fragile X Syndrome, Rett syndrome, Angelman syndrome and Down syndrome [81,85,86]. Initially, modelling neurodegenerative, psychiatric and neurodevelopmental diseases was based on iPSC-derived 2D monolayer models. Currently, with some exceptions, these models have been applied to the 3D organoid culture approach, providing unique data [54]. The study of malformations of the cortical development disorders, including microcephaly, macrocephaly (for details, see 1.4.2) and lissencephaly has made incredible progress. A more detailed insight into the underlying disease mechanism, progression and a potential therapy was achieved using 3D cerebral organoid cultures [87,88]. The use of patient-derived iPSCs and the constant improvement in developing sophisticated and physiologically relevant 3D brain models provide, for the first time, a powerful platform to study human neurological diseases.

1.4.1 Alzheimer's disease

Alzheimer's disease (AD) is the most common neurodegenerative disease, estimated to affect 50 million people worldwide, a number that is estimated to increase to more than 131 million in 2050 [89]. Clinically, it is characterized by a progressive decline of the cognitive functions and disruption of basic functions, representing a significant public health problem. Since its first description in 1907 by Alois Alzheimer, some progress has been made in understanding the numerous underlying pathophysiological mechanisms. Pathologically, AD is characterized by two hallmarks: the presence of extracellular amyloid plaques composed of amyloid-beta ($A\beta$) peptide and intracellular neurofibrillary tangles composed of the protein Tau [90]. The specific molecular mechanisms by which the crosstalk between $A\beta$ and Tau contribute to the disease etiology and neurodegeneration have been under extensive study. However, despite these intensive efforts, there are still no effective treatment or prevention strategies due to the difficulties in generating *in vitro* models that recapitulate the AD pathology [91,92].

AD is classified into early-onset AD (EOAD) or familial AD, and late-onset AD (LOAD) or sporadic AD. Studies of familial AD revealed important aspects of the genetic factors implicated in the disease, such as the causal mutations in *APP*, coding for amyloid precursor protein, and in *PSEN1* and *PSEN2*, coding presenilin 1 and presenilin 2, which form the catalytic core of the γ -secretase complex [93]. The development of transgenic animal models and cell models provided evidence that these mutations increase the $A\beta$ load, which laid the foundation for the “amyloid cascade hypothesis”. Accordingly, the $A\beta$ peptides derived from sequential proteolytic cleavage of APP by the β -secretase and the γ -secretase complex, drives the disease progression resulting in the formation of the intracellularly, hyper-phosphorylated Tau. Because of the imbalanced crosstalk between $A\beta$ and Tau, multiple neuropathological mechanisms ensue, such as synaptic toxicity, toxicity in the endoplasmic reticulum, endosomes and lysosomes, mitochondrial dysregulation and microglia-derived inflammatory responses, finally leading to neuronal death [92]. While cellular and animal models allowed linking *APP*, *PSEN1* and *PSEN2* mutations with neurodegeneration, more than 95% of all AD cases are sporadic. LOAD shares the major characteristics of familial AD, including the presence of amyloid plaques and deposits of Tau, however, there are no clear familiar patterns, making it a very complex and multifactorial disease [94,95]. The genetics of LOAD have been widely investigated and many genetic risk factors have been implicated in increasing its susceptibility. Individuals carrying one $\epsilon 4$ allele of the *apolipoprotein E (APOE)* have a 3-fold increased risk of AD, while individuals carrying the two $\epsilon 4$ alleles face an approximately 12-fold increased risk of AD [96]. In the last decade, genome-wide association studies (GWAS) and large-scale sequencing projects have led to the discovery of other genetic variants in more than 40 loci that influence the risk for LOAD. These genes are involved in biological pathways such as cholesterol metabolism, APP metabolism, MAPT metabolism, cytoskeleton and axon development, immune response and endocytosis/vesicle-mediated transport and epigenetics [97]. The expression of these genetic risk factors is not restricted to neurons, with many being expressed in astrocytes, oligodendrocytes, microglia and endothelial cells. One of the multiple generic risk variants is the rare p.Arg47His (R47H) variant within the *triggering receptor expressed on myeloid cells 2 (TREM2)*, which has been shown to increase the risk

of developing AD by 2–3-fold. *APOE* and *TREM2* variants are the high risk factors linked to LOAD. Several other low risk factors have been identified, such as *SORL1*, *PICALM*, *BINI* and *CD2AP* variants, which have been implicated in alterations in the localization of both APP and secretases [98–101]. Despite the identification of these risk factors, their overall contribution to LOAD pathology is still not fully understood. The development of new physiological relevant models that capture pathologies and allow disease mechanisms to be investigated would be a great asset.

AD patient-derived iPSCs have provided an important proof-of-principle regarding the utility of such cells for a better understanding of the molecular mechanisms associated with the etiology of AD [102–104]. However, most of the iPSC-based AD models have a focus on the characterization of the EOAD-linked mutations in *APP* or *PSEN1*. iPSCs-derived neurons from EOAD patients show an increase in the overall A β levels, increased or altered processing and localization of APP, an increase in Tau and phosphorylated Tau, and the activation of GSK3 β , commonly noted across multiple studies [103].

Strikingly few studies have so far modelled LOAD using patient-derived iPSCs. These studies have been largely limited due to the lack of genetic characterization of iPSCs. While increased A β levels and phosphorylated Tau have been the focus in EOAD studies, LOAD iPSC-based models failed to recapitulate the key pathological hallmarks, or a high variability across the iPSC lines was observed. Table 1 summarizes the key findings in iPSC-derived neurons from patients with LOAD. Future work in developing better iPSC-based disease models for LOAD is needed to identify the novel disease mechanisms so that an effective therapy can be developed.

Table 1 – Summary of studies using genomically unaltered iPSC-derived neurons from patients with LOAD.

Study	Culture method	Cells analysed	Genetic risk factor	AD phenotype	Additional observations
Israel et al. [104]	2D	Neurons	<i>APOE</i> $\epsilon 3/\epsilon 3$	\uparrow A β 40, \uparrow p-tau, \uparrow GSK3	\uparrow very large early endosomes
Hossini et al. [105]	2D	Neurons		\uparrow GSK3	
Ochalek et al. [106]	2D	Neurons		\uparrow A β 42:40, \uparrow APP, \uparrow GSK3 β , \uparrow p-Tau	
Young et al. [107]	2D	Neurons	<i>SOLR</i> variant		
Kondo et al. [108]	2D	Neurons and astrocytes		\uparrow ER stress, \uparrow OS, \uparrow A β intracellular oligomers	\uparrow ROS
Flamier et al. [109]	2D	Neurons			
Lee et al. [110]	3D	Neurons			
Balez et al. [111]	2D	Neurons	<i>APOE</i> $\epsilon 3/\epsilon 4$	\uparrow A β 42	Shorter neurites; hyperexcitable neuronal phenotype
Chen et al. [112]	3D	Neurons			Alterations in axon proteins and immune response pathways
Duan et al. [113]	2D	Neurons	<i>APOE</i> $\epsilon 3/\epsilon 4$	\uparrow A β 42:40	Increase susceptibility to glutamate induced excitotoxic death

1.4.2 Nijmegen breakage syndrome

Nijmegen Breakage Syndrome (NBS) is a rare autosomal recessive genetic disorder caused by mutations within nibrin (*NBN*) [115]. NBS was first described in 1979 at the University of Nijmegen and since then has been classified as a chromosomal instability syndrome [116]. It is considered a multisystemic disorder characterized by severe and progressive microcephaly, growth retardation, bird-like facial appearance, premature ovarian failure,

deterioration of the cognitive functions, immunodeficiency, chromosomal instability and elevated sensitivity to ionizing radiation. In a few cases other brain developmental abnormalities have been reported, including neuronal migration disorder, agenesis of the corpus callosum and arachnoid cysts [117–119]. More than 40% of the patients develop malignancy diseases by the age of 20 years, which together with the high recurrent infections are the major cause of death [118].

Despite being a rare disease with an estimated worldwide prevalence at 1:100000 live births, the carrier frequencies in Eastern Europe is as extremely high as 1:155 [121]. More than 90% of the NBS patients are homozygous for a founder mutation, a five base pair deletion in exon 6 (657del5) within *NBN*. Due to alternative translation from a cryptic start site upstream of the deletion, this mutation leads to the truncation of the wild-type protein into two different fragments: a 26 kDa amino-terminal protein (p26) and a 70 kDa carboxy-terminal (p70), which retain some residual functions [122]. *NBN*, *MRE11* and *RAD50* form the MNR complex which plays a central role in DNA damage signalling and repair, telomere maintenance, proper centromere duplication, cell cycle checkpoint activation and processing of stalled replication forks [123]. At a cellular level, lymphoblasts and fibroblasts from NBS patients exhibit chromosomal instability with impaired cell cycle and regulation of apoptosis [124–127].

During neurodevelopment the rapid proliferation of the NPCs generates high levels of oxidative stress, being essential to have a firmly functional DNA damage response (DDR) pathway. Thus, it is expected that deficiency in this pathway causes many syndromes with pronounced pathology [128,129]. In fact, mutations in genes that have been linked to microcephaly encode proteins involved in cell cycle regulation, centrosome formation, spindle orientation, microtubule organization and DNA repair. However, the functional consequences of *NBN* 657del5 during the neurodevelopment remain largely unexplored, inherent to the challenge in modelling this disease. Few studies in mouse models based on *Nbn* conditional knockdowns were performed. Nonetheless, the mouse models do not reproduce the brain-related phenotype seen in patients and in the ones that the microcephaly phenotype was present, divergent results were found. While inactivation of *Nbn* in the mouse neuronal tissue resulted in decreased proliferation of the NPCs and increased apoptosis of postmitotic

neurons in the cerebellum, by activation of p53 [130], other studies showed that deletion of *Nbn* in the mouse central nervous system affects proliferation and apoptosis mainly in the cortex proliferating area (VZ), affecting only NPCs [131].

To bridge the gap between animal models and the human phenotype of NBS, iPSC technology and the derivation of cerebral organoids provides the best platform to derive a reliable human disease model to study the neurodevelopment defects observed NBS patients. We previously reported that fibroblasts from NBS patients can be reprogrammed into iPSC and thus bypassing premature senescence [127]. Differentiation of the NBS-iPSCs into NPCs showed these cells have de-regulated expression of neural developmental genes due to the inability to maintain normal levels of p53 [132]. As the guardian of the genome, inappropriate p53 activation can act as a driver of a wide spectrum of developmental defects [133]. Recently, Navarro *et al.*, found that *TP53* knockdown resulted in brain organoids with disorganized stem cell layer and reduced cortical progenitor cells and neurons [134]. Indeed, cerebral organoids have been extremely valuable to study malformations of the cortical development resulting from the disruption of the neurodevelopmental processes. A number of disorders involving defects in cellular organization and tissue architecture such as microcephaly, macrocephaly, lissencephaly and periventricular heterotopia have been modelled using brain organoids, as summarized in Table 2. Although only a few studies with microcephaly patient-derived iPSCs were performed, a shared phenotype was observed in the cerebral organoids: premature differentiation of the NPCs pointed as a consequence of a premature shift from symmetric to asymmetric division of the RGCs [56,135–137]. So far, no DNA damage-related diseases have been modelled using cerebral organoids [138]. Cerebral organoids have provided new insights into the mechanisms underlying malformations of cortical development. This fascinating technology is a valuable tool to model NBS, not only to understand the molecular mechanism underlying it, but also to create possible treatments for this devastating disease.

Table 2 – Malformations of the cortical development modelled using cerebral organoids.

Study	Condition	Gene	Phenotype observed	Patient-derived iPSCs
Lancaster et al.[56]	Congenital microcephaly	<i>CDK5RAP2</i>	Decrease NPCs proliferation, premature differentiation	yes
Gabriel et al.[135]	Seckel syndrome/ microcephaly	<i>CENPJ</i>	Decrease NPCs proliferation, premature differentiation	yes
Li et al.[136]	Congenital microcephaly	<i>ASPM</i>	Severe defects in structural organization; Reduced NPCs	yes
Zhang et al.[137]	Congenital microcephaly	<i>WDR62</i>	Decrease NPCs proliferation, premature differentiation	Genetically engineered
Li et al.[139]	Macrocephaly	<i>PTEN</i>	Increased size, lack of folding, delayed terminal RGCs differentiation	Genetically engineered
Iefremova et al.[140]	Miller-Dieker syndrome/ lissencephaly	17p13.3 del	Overall size reduction, premature RGCs differentiation, increased in horizontal cleavages	yes
Bershteyn et al.[141]	Miller-Dieker syndrome/ lissencephaly	17p13.3 del	Increased apoptosis in the VZ; mitotic defects in the bRGCs; increased in horizontal cleavage plan	yes
Klaus et al.[142]	periventricular heterotopia	<i>FAT4</i>	Changes in the morphology of neural progenitor cells, defective neuronal migration dynamics	yes
	periventricular heterotopia	<i>DCHI</i>	Changes in the morphology of neural progenitor cells, defective neuronal migration dynamics	yes

1.5 Aims and scope of this thesis

Neurological diseases, ranging from neurodevelopmental to neurodegenerative diseases, affect millions of individuals worldwide and present an enormous economic, emotional and

physical burden to the affected individuals, their families and the society. The development of *in vitro* iPSC-based models, which recapitulate some aspects of disease-related phenotype can potentially contribute to the unravelling of mechanisms specific to neurological diseases and help identify potential therapeutic targets. In this thesis we focused on two different neurological diseases, AD and NBS. The main goal was (1) the generation of patient-derived iPSCs, (2) establishment of neuronal differentiation models that recapitulate the features of the disease, and (3) perform multi-omic analysis to unravel new molecular mechanism underlying the diseases pathogenesis. To achieve this, we utilized a combination of approaches ranging from 2D neuronal cultures to 3D cerebral organoids models.

In chapter 2, the focus was on iPSC-based AD modelling. The aims proposed for this chapter were: (1) generation and characterization of iPSC lines from AD patients carrying the *TREM2* R47H mutation; (2) establishment of functional 2D neuronal cultures that recapitulate the disease phenotype; (3) multi-omic analysis to unravel the early molecular mechanism underlying late-onset AD; and (4) proof-of-concept of AD 2D neuronal cultures applicability to identify new mechanisms of APP processing and A β production and therefore identifying new novel therapeutical targets of AD.

In chapter 3, the focus was on iPSC-based NBS modelling and the specific aims were (1) generation and characterization of iPSC line from NBS patient carrying the homozygous *NBN* 657del5 mutation; (2) establishment of functional 3D cerebral organoid culture systems that recapitulate the disease phenotype, and (3) multi-omic analysis to unravel the molecular mechanism underlying microcephaly in NBS patients. Finally, in chapter 4 we discuss our iPSC models and the findings in the context of the recent literature, their contribution to understanding AD and NBS diseases and the next steps in future research.

2 | Results I:

Modelling AD using patient-derived iPSCs

2.1 Lymphoblast-derived integration-free iPSC line AD-TREM2-1 from a 67 year-old Alzheimer's disease patient expressing the TREM2 p.R47H variant

Soraia Martins, Hatice Yigit, Martina Bohndorf, Nina Graffmann, Aurelian Robert Fiszl, Wasco Wruck Kristel Slegers, Christine Van Broeckhoven and James Adjaye

Stem Cell Research 29, (2018) 60-63

Abstract

Human lymphoblast cells from a male diagnosed with Alzheimer's disease (AD) expressing the *TREM2* p.R47H variant were used to generate integration-free induced pluripotent stem cells (iPSCs) by over-expressing episomal-based plasmids harbouring OCT4, SOX2, NANOG, LIN28, c-MYC and L-MYC. AD-TREM2-1 was defined as pluripotent based on (i) expression of pluripotency-associated markers (ii) embryoid body-based differentiation into cell types representative of the three germ layers and (iii) the similarity between the transcriptome of the iPSC line and the human embryonic stem cell line H1 with a Pearson correlation of 0.947.

Author's contribution: 60%

Conceptualization: **SM** and **JA**. Methodology: **SM**, **HY**, **MB**, **NG** and **ARF**; Data curation: **WW**, Resources: **KS** and **CVB**. Manuscript writing: **SM** and **JA**. All authors have read and agreed to the published version of the manuscript.

Status: Published in *Stem Cell Research* (doi.org/10.1016/j.scr.2018.03.011)

This is an open access article under the terms of the Creative Commons Attribution 4.0 License.



Contents lists available at ScienceDirect

Stem Cell Research

journal homepage: www.elsevier.com/locate/scr

Lab Resource: Stem Cell Line

Lymphoblast-derived integration-free iPSC line AD-TREM2-1 from a 67 year-old Alzheimer's disease patient expressing the TREM2 p.R47H variant



Soraia Martins^a, Hatice Yigit^a, Martina Bohndorf^a, Nina Graffmann^a, Aurelian Robert Fiszl^a, Wasco Wruck^a, Kristel Slegers^{b,c}, Christine Van Broeckhoven^{b,c}, James Adjaye^{a,*}

^a Institute for Stem Cell Research and Regenerative Medicine (ISRM), Medical Faculty, Heinrich-Heine-University Düsseldorf, Moorenstr. 5, 40225 Düsseldorf, Germany

^b Neurodegenerative Brain Disease Groups, Department of Molecular Genetics, VIB, Antwerp, Belgium

^c Laboratory of Neurogenetics, Institute Born-Bunge, University of Antwerp, Belgium

ARTICLE INFO

Article history:

Received 28 February 2018

Received in revised form 6 March 2018

Accepted 16 March 2018

Available online 20 March 2018

ABSTRACT

Human lymphoblast cells from a male diagnosed with Alzheimer's disease (AD) expressing the TREM2 p.R47H variant were used to generate integration-free induced pluripotent stem cells (iPSCs) by over-expressing episomal-based plasmids harbouring OCT4, SOX2, NANOG, LIN28, c-MYC and L-MYC. AD-TREM2-1 was defined as pluripotent based on (i) expression of pluripotency-associated markers (ii) embryoid body-based differentiation into cell types representative of the three germ layers and (iii) the similarity between the transcriptome of the iPSC line and the human embryonic stem cell line H1 with a Pearson correlation of 0.947.

© 2018 The Authors. Published by Elsevier B.V. This is an open access article under the CC BY-NC-ND license (<http://creativecommons.org/licenses/by-nc-nd/4.0/>).

Resource table.

Unique stem cell line identifier	HHUUKD1003-A
Alternative name(s) of stem cell line	AD-TREM2-1
Institution	Institute for Stem Cell Research and Regenerative Medicine, Medical Faculty, Heinrich-Heine-University VIB – Department of Molecular Genetics, Antwerp, Belgium
Contact information of distributor	James Adjaye, james.adjaye@med.uni-duesseldorf.de
Type of cell line	iPSCs
Origin	Human
Additional origin info	Age: 67 year-old Sex: male
Cell source	Human lymphoblast cells.
Clonality	Clonal
Method of reprogramming	Episomal vectors oriP/EBNA-1 backbone containing OCT4, SOX2, KLF4, LIN28 and L-MYC
Genetic modification	NO
Type of modification	n/a
Associated disease	Alzheimer's disease
Gene/locus	TREM2 (NM_018965) gene located on chromosome 6p21.1 Genotype: p.R47H substitution (rs75932628)
Method of modification	n/a
Name of transgene or resistance	none

Inducible/constitutive system	n/a
Date archived/stock date	4 June 2014
Cell line repository/bank	n/a
Ethical approval	Ethics Committee of the University Hospital Antwerp and the University of Antwerp, Belgium.

Resource utility

The TREM2 p.R47H variant was identified as a risk factor for AD. AD-TREM2-1 iPSC line was generated from an AD patient expressing the TREM2 R47H variant and can be used to provide insights into the role played by microglia and neuro-inflammation in the development and progression of AD.

Resource details

Alzheimer's disease (AD) is a neurodegenerative disease and the most common form of late-onset dementia. A link between microglia-related genes with AD risk was identified by a series of GWAS studies. One of these genetic risk variants is the rare R47H mutation within the microglia receptor TREM2, which results in a three-fold increase in the risk for developing AD (Guerreiro et al., 2013, Jonsson et al. 2013).

Here we report the generation of an iPSC line (AD-TREM2-1) from a sporadic AD patient expressing the TREM2 missense mutation p.R47H. To generate this iPSC line, the lymphoblast cell line - Lymph1

* Corresponding author.

E-mail address: james.adjaye@med.uni-duesseldorf.de (J. Adjaye).

(Cuyvers et al. 2014) derived from a 67-year-old male AD patient (age at onset 65) was used.

Briefly, the lymphoblast cell line Lymph1 was reprogrammed employing oriP/EBNA-1-based episomal plasmids expressing OCT4, SOX2, KLF4, C-MYC, L-MYC, LIN28 and a p53 shRNA. Confirmation of the vector dilution of AD-TREM2-1 was carried out by analyzing expression of exogenous *OCT4* (vector) (top panel). Endogenous *OCT4* analysis (lower panel) was performed as an internal PCR control (Fig. 1A). Pluripotency was confirmed by (i) expression of OCT4, SOX2, NANOG, SSEA4, TRA-1-60 and TRA-1-81 (Fig. 1B), (ii) embryoid body (EB)-based spontaneous differentiation into cell types representative of the

three germ layers, namely ectoderm (NESTIN, TUBB3 - Tubulin beta-3 chain), mesoderm (SMA – smooth muscle actin) and endoderm (AFP – Alpha fetoprotein) (Fig. 1C) and (iii) OCT4 flow cytometry analysis (Fig. 1D). The DNA fingerprinting of AD-TREM2-1 iPSC line was identical to the parental lymphoblast line Lymph1 (Supplementary file 1). Chromosomal content analysis revealed a normal 46, XY karyotype (Fig. 1E). As depicted in the Dendrogram (Fig. 1F), the transcriptome of the lymphoblast line is distinct from AD-TREM2-1 and the embryonic stem cell line H1, which cluster together with a Pearson correlation of 0.947. The reprogramming process did not alter the TREM2 missense mutation p.R47H - a heterozygous base substitution (G>A) as indicated by the

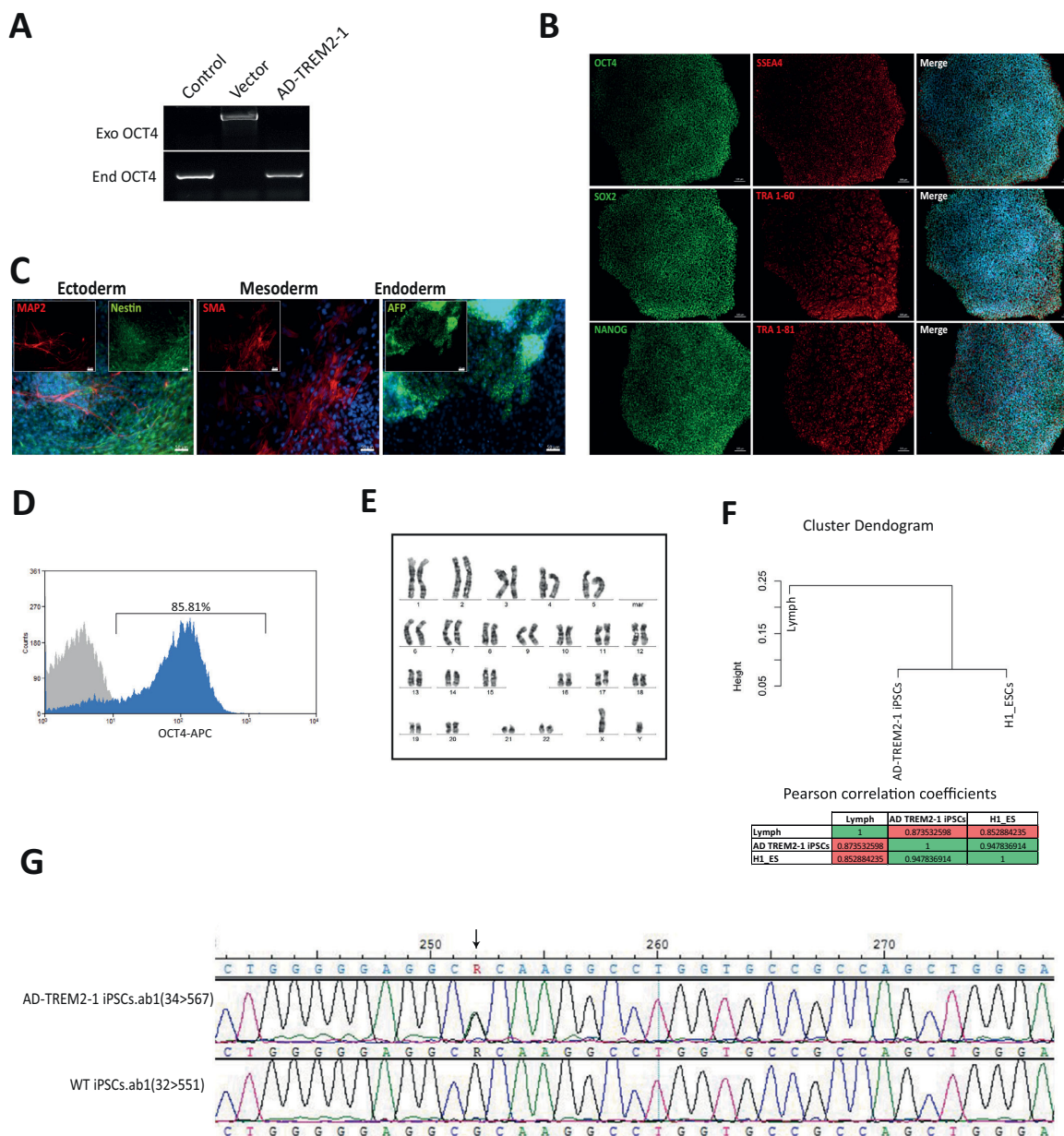


Fig. 1. Characterisation of AD-TREM2-1 iPSC line.

black arrow (Fig. 1G). A PCR-based Mycoplasma contamination test was negative (Supplementary file 2).

Materials and methods

Cell culture

The lymphoblast cell line Lymph1 (Cuyvers et al. 2014) was cultured in RPMI 1640 supplemented with 15% fetal bovine serum (Invitrogen™), 1% Glutamax (Invitrogen™), 1% Sodium pyruvate (Invitrogen™) and 1% Penicillin/Streptomycin (Invitrogen™) at 37 °C and 5% CO₂.

Derivation of ISRM AD TREM2-1

Lymphoblasts (Lymph1) were reprogrammed by nucleofection of oriP/EBNA-1- episomal-based plasmids (expressing OCT4, SOX2, KLF4, L-MYC, LIN28 and a p53 shRNA) at the Biomedicum Stem Cell Center, University of Helsinki, Finland, as a service. Well defined distinct iPSCs colonies were manually picked and passaged for expansion under feeder-free conditions on Matrigel®-coated plates in E8 medium (Invitrogen™). Further characterisations were carried out at ISRM-HHU, Düsseldorf, Germany.

PCR

Genomic DNA was isolated from Lymph1, AD-TREM2-1 and the human embryonic stem cell line (H1) using the DNeasy Blood and Tissue Kit (Qiagen). Vector dilution and STR analysis were confirmed by PCR amplification using the primers EndOCT4, ExoOCT4, D17S1296 and DS21S2055. Absence of mycoplasma contamination was confirmed using cell culture supernatant from a dense culture. PCR was performed using GoTaq® DNA Polymerase (Promega). Primer sequences are shown in Table 2.

EB formation

Pluripotency was confirmed by EB-based differentiation. First, the iPSCs were cultured on Matrigel®-coated plates until sub-confluent and then further cultured for a week in a T25 flask in high glucose DMEM, containing 1% NEAA. Afterwards, EBs were replated onto gelatin coated 12-well plate for 3–4 days.

Flow cytometry and immunofluorescence-based detection of pluripotency associated proteins

iPSCs and differentiated EBs were fixed with 4% paraformaldehyde for 15 min at room temperature. After blocking with 5% normal goat serum in 0.5% Triton-X100 PBS solution, cells were incubated with the primary antibody overnight at 4 °C. The following antibodies were used for the characterisation – anti-OCT4, anti-SOX2, anti-NANOG and anti-SSEA4, anti-TRA-1-60 and anti-TRA-1-81; for the germ layer differentiation – anti-Nestin, anti-β3 Tubulin, anti-SMA and anti-AFP. Alexa-488 or Alexa-555-conjugated secondary antibodies and Hoechst were used to visualize the signal. Fluorescent images were obtained by an inverse fluorescence microscope LSM 700 (Carl Zeiss). Flow-cytometric analysis using an anti-Oct3/4 antibody conjugated to APC (Miltenyl Biotec) was carried out using the CyAn ADP Flow Cytometer (Dako). Unstained cells were used as negative control (Table 1).

Karyotype analysis

The karyotype analysis was evaluated and performed at the Institute of Human Genetics and Anthropology, Heinrich-Heine-University, Düsseldorf.

Bidirectional Sanger sequencing

Genotyping of TREM2 p.R47H was performed on genomic DNA by PCR amplification and Sanger sequencing of exon 2 as described in Cuyvers et al. (2014).

RNA-based microarray analysis

Total RNA from cell lysate was isolated using Direct-zol RNA Mini Prep (Zymo Research) in combination with peqGold TriFast (PeqLab Biotechnology) according to the manufacturer's protocol. Microarray analysis was outsourced to the Genomics/Transcriptomic Laboratory of the BMFZ, HHU, Düsseldorf. Affymetrix raw data in form of CEL files was read into the R/Bioconductor environment (Gentleman et al. 2004) using the package affy (Gautier et al. 2004). Probesets were normalized with the rma method and probesets with a coefficient of variation greater than 0.1 were filtered for the cluster analysis. Cluster analysis was performed employing the function hclust parameterized with Pearson correlation as similarity measure and centroid linkage as agglomeration method.

Table 1
Characterisation and validation.

Classification	Test	Result	Data
Morphology Phenotype	Photography	Normal	Fig. 1 panel B
	Immunocytochemistry	Expression of pluripotency associated markers: OCT4, SOX2, NANOG, SSEA4, TRA-1-60, and TRA-1-81	Fig. 1 panel B
Genotype Identity	Flow cytometry	85.81% OCT4 positive cells	Fig. 1 panel C
	Karyotype (G-banding) and resolution	46XX, Resolution 150–300	Fig. 1 panel E
	Microsatellite PCR (mPCR) STR analysis	Not done DNA Fingerprinting PCR: two sites tested, matched	– Supplementary file 1
Mutation analysis (IF APPLICABLE) Microbiology and virology	Sequencing	TREM2 p.R47H heterozygous mutation	Fig. 1 panel H
	Southern Blot OR WGS Mycoplasma	Not applicable Mycoplasma testing by PCR Negative	– Supplementary file 2
Differentiation potential	Embryoid body formation OR Teratoma formation OR Scorecard	Expression of germ layer specific proteins Ectoderm: NESTIN, MAP2 Endoderm: AFP Mesoderm: SMA	Fig. 1 panel D
Donor screening (OPTIONAL)	HIV 1 + 2 Hepatitis B, Hepatitis C	Not tested	–
Genotype additional info (OPTIONAL)	Blood group genotyping	Not tested	–
	HLA tissue typing	Not tested	–

Table 2
Reagents details.

Antibodies used for immunocytochemistry/flow-cytometry			
	Antibody	Dilution	Company Cat # and RRID
Flow-cytometry	Anti-OCT3/4-APC	1:11	Miltenyi Biotec Cat# 130-109-764, RRID: AB_2653082
Pluripotency Markers	Rabbit anti-OCT4	1:400	Cell Signaling Technologies; #28405 RRID: AB_2167691
Pluripotency Markers	Rabbit anti-SOX2	1:400	Cell Signaling Technologies; #35795 RRID: AB_2195767
Pluripotency Markers	Rabbit anti-NANOG	1:800	Cell Signaling Technologies; #49035 RRID: AB_10559205
Pluripotency Markers	Mouse anti-Tra-1-60	1:1000	Cell Signaling Technologies; #47465 RRID: AB_2119059
Pluripotency Markers	Mouse anti-Tra-1-81	1:1000	Cell Signaling Technologies; #47455 RRID: AB_2119060
Pluripotency Markers	Mouse anti-SSEA4	1:1000	Cell Signaling Technology Cat# 47555, RRID: AB_1264259
Differentiation Markers	Rabbit anti-Nestin	1:250	Sigma Aldrich; N5413 RRID: AB_1841032
Differentiation Markers	Anti- α SMA	1:1000	Dako; # M0851, RRID:AB_2223500
Differentiation Markers	Rabbit anti-AFP	1:200	Cell Signaling Technology Cat# 21375, RRID:AB_2209744
Differentiation Markers	Mouse anti-MAP2	1:500	Synaptic Systems Cat# 188011, RRID:AB_2147096
Secondary antibodies	Anti-mouse-Alexa555	1:2000	Thermo Fisher Scientific Cat# A10521, RRID: AB_2534030
Secondary antibodies	Anti-rabbit-Alexa488	1:2000	Thermo Fisher Scientific Cat# A27034, RRID: AB_2536097
Nuclear Co-Staining	Hoechst	1:5000	Thermo Fisher Scientific Cat# H3569, RRID: AB_2651133
Primers			
	Target	Forward/reverse primer (5'–3')	
Fingerprinting	D21S2055	AACAGAACCAATAGGCTATCTATC/TACAGTAAATCACTTGGTAGGAGA	
Fingerprinting	D17S1296	TTTTGGTATTGGCCATCCTA/GAAAGGAACAGAGACAGAGG	
Episomal Plasmid (Exo)	OCT4	AGTGAGAGGCAACCTGGAGA/AGGAATCTTCTTCCACGA	
Endogenous OCT4	OCT4	GTGGAGGAAGCTGACAACAA/ATTCTCCAGGTTGCCTCTCA	
Mycoplasma	16S rRNA gene from Mycoplasma	GGGAGCAAACAGGATTAGATACCCT/TGCACCATCTGTCACTCTGTTAACCTC	

Acknowledgements

JA acknowledges support from the Medical Faculty, Heinrich-Heine-University, Düsseldorf. Research at the Antwerp site was funded in part by the Belgian Science Policy Office Interuniversity Attraction Poles program (BELSPO, www.belspo.be), the Flanders Impulse Program on Networks for Dementia Research (VIND) and the University of Antwerp Research Fund (<http://www.uantwerpen.be/>). JA, KS and CVB are members of the EU project- AgedBrainSYSBIO. The AgedBrainSYSBIO project received funding from the European Union's Seventh Framework Programme for research, technological development and demonstration under grant agreement no 305299.

Appendix A. Supplementary data

Supplementary data to this article can be found online at <https://doi.org/10.1016/j.scr.2018.03.011>.

References

- Cuyvers, E., Bettens, K., Philtjens, S., Van Langenhove, T., Gijssels, L., van Zee, J., Engelborghs, S., Vandenbulcke, M., Van Dongen, J., Geerts, N., et al., 2014. Investigating the role of rare heterozygous TREM2 variants in Alzheimer's disease and frontotemporal dementia. *Neurobiol. Aging* 35 (726 e711–726 e729).
- Gautier, L., Cope, L., Bolstad, B.M., Irizarry, R.A., 2004. Affy—analysis of Affymetrix GeneChip data at the probe level. *Bioinforma. (Oxf., Engl.)* 20 (3):307–315. <https://doi.org/10.1093/bioinformatics/btg405>.
- Gentleman, R.C., Carey, V.J., Bates, D.M., Bolstad, B., Dettling, M., Dudoit, S., Ellis, B., Gautier, L., Ge, Y., Gentry, J., Hornik, K., Hothorn, T., Huber, W., Iacus, S., Irizarry, R., Leisch, F., Li, C., Maechler, M., Rossini, A.J., Sawitzki, G., Smith, C., Smyth, G., Tierney, L., Yang, J.Y.H., Zhang, J., 2004. Bioconductor: open software development for computational biology and bioinformatics. *Genome Biol.* 5 (10):R80. <https://doi.org/10.1186/gb-2004-5-10-r80>.
- Guerreiro, R., Wojtas, A., Bras, J., Carrasquillo, M., Rogava, E., Majounie, E., Cruchaga, C., Sassi, C., Kauwe, J.S., Younkin, S., et al., 2013. TREM2 variants in Alzheimer's disease. *N. Engl. J. Med.* 368, 117–127.
- Jonsson, T., Stefansson, H., Steinberg, S., Jonsdottir, I., Jonsson, P.V., Snaedal, J., Bjornsson, S., Huttenlocher, J., Levey, A.I., Lah, J.J., et al., 2013. Variant of TREM2 associated with the risk of Alzheimer's disease. *N. Engl. J. Med.* 368, 107–116.

2.2 Lymphoblast-derived integration-free iPSC line AD-TREM2-3 from a 74 year-old Alzheimer's disease patient expressing the TREM2 p.R47H variant

Soraia Martins, Hatice Yigit, Martina Bohndorf, Nina Graffmann, Aurelian Robert Fiszl, Wasco Wruck Kristel Slegers, Christine Van Broeckhoven and James Adjaye

Stem Cell Research 30, (2018) 141-144

Abstract

Human lymphoblast cells from a male diagnosed with Alzheimer's disease (AD) expressing the TREM2 p.R47H variant were used to generate integration-free induced pluripotent stem cells (iPSCs) by over-expressing episomal-based plasmids harbouring OCT4, SOX2, KLF4, LIN28, L-MYC and p53 shRNA. The derived iPSC line – AD-TREM2-3 was defined as pluripotent based on (i) expression of pluripotency-associated markers (ii) embryoid body-based differentiation into cell types representative of the three germ layers and (iii) the similarity between the transcriptome of the iPSC line and the human embryonic stem cell line H1 with a Pearson correlation of 0.940.

Author's contribution: 60%

Conceptualization: **SM** and JA. Methodology: **SM**, HY, MB, NG and ARF; Data curation: WW, Resources: KS and CVB. Manuscript writing: **SM** and JA. All authors have read and agreed to the published version of the manuscript.

Status: Published in *Stem Cell Research* (doi.org/10.1016/j.scr.2018.05.018)

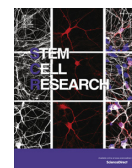
This is an open access article under the terms of the Creative Commons Attribution 4.0 License.



Contents lists available at ScienceDirect

Stem Cell Research

journal homepage: www.elsevier.com/locate/scr



Lab Resource: Stem Cell Line

Lymphoblast-derived integration-free iPSC line AD-TREM2-3 from a 74 year-old Alzheimer's disease patient expressing the TREM2 p.R47H variant



Soraia Martins^a, Hatice Yigit^a, Martina Bohndorf^a, Nina Graffmann^a, Aurelian Robert Fiszl^a, Wasco Wruck^a, Kristel Slegers^{b,c}, Christine Van Broeckhoven^{b,c}, James Adjaye^{a,*}

^a Institute for Stem Cell Research and Regenerative Medicine, Medical Faculty, Heinrich-Heine-University Düsseldorf, Moorenstr. 5, 40225 Düsseldorf, Germany

^b Neurodegenerative Brain Disease Groups, Department of Molecular Genetics, VIB, Antwerp, Belgium

^c Laboratory of Neurogenetics, Institute Born-Bunge, University of Antwerp, Belgium

ABSTRACT

Human lymphoblast cells from a male diagnosed with Alzheimer's disease (AD) expressing the TREM2 p.R47H variant were used to generate integration-free induced pluripotent stem cells (iPSCs) by over-expressing episomal-based plasmids harbouring OCT4, SOX2, KLF4, LIN28, L-MYC and p53 shRNA. The derived iPSC line – AD-TREM2-3 was defined as pluripotent based on (i) expression of pluripotency-associated markers (ii) embryoid body-based differentiation into cell types representative of the three germ layers and (iii) the similarity between the transcriptome of the iPSC line and the human embryonic stem cell line H1 with a Pearson correlation of 0.940.

Resource table.		Method of reprogramming	Episomal vectors oriP/EBNA-1 backbone containing OCT4, SOX2, KLF4, LIN28, L-MYC and a p53 shRNA
Unique stem cell line identifier	HHUUKDi004-A	Genetic Modification	NO
Alternative name(s) of stem cell line	ISRM AD TREM2-3	Type of Modification	n/a
Institution	Institute for Stem Cell Research and Regenerative Medicine, Medical Faculty, Heinrich-Heine-University, Düsseldorf, Germany Vlaams Instituut voor Biotechnologie (VIB) – Department of Molecular Genetics, Antwerp, Belgium	Associated disease	Alzheimer's disease
Contact information of distributor	James Adjaye, james.adjaye@med.uni-duesseldorf.de	Gene/locus	TREM2 p.R47H heterozygous
Type of cell line	iPSCs	Method of modification	n/a
Origin	Human	Name of transgene or resistance	None
Additional origin info	Age:74 year-old Sex: male	Inducible/constitutive system	n/a
Cell Source	Human lymphoblast cells	Date archived/stock date	4 June 2014
Clonality	Clonal	Cell line repository/bank	n/a
		Ethical approval	Ethics Committee of the University Hospital Antwerp and the University of Antwerp, Belgium (Approval number: 13/15/161)

* Corresponding author.

E-mail address: james.adjaye@med.uni-duesseldorf.de (J. Adjaye).

<https://doi.org/10.1016/j.scr.2018.05.018>

Received 9 May 2018; Received in revised form 23 May 2018; Accepted 25 May 2018
Available online 01 June 2018

1873-5061/ © 2018 The Authors. Published by Elsevier B.V. This is an open access article under the CC BY-NC-ND license (<http://creativecommons.org/licenses/by-nc-nd/4.0/>).

1. Resource utility

The *TREM2* p.R47H variant was identified as a risk factor for AD. AD-TREM2-3 iPSC line was generated from an AD patient expressing the *TREM2* R47H variant and can be used to provide insights into the role played by microglia and neuro-inflammation in the development and progression of AD.

2. Resource details

Late onset Alzheimer's disease (LOAD) is the most common form of dementia and the number of individuals is expected to triple by 2050. A link between microglia-related genes with LOAD risk was identified by a recent series of GWAS studies. One of these genetic risk variants is the rare R47H mutation within the microglia receptor *TREM2*, which results in a three-fold increase in the risk for developing AD (Guerreiro et al., 2013; Jonsson et al., 2013).

Here we report the generation of an iPSC line (AD-TREM2-3) from a sporadic AD patient expressing the *TREM2* missense mutation p.R47H. To generate this iPSC line, the Epstein-Barr Virus (EBV)-immortalized lymphoblast cell line – Lymph3 (Cuyvers et al., 2014) derived from a 74-year-old male AD patient (age at onset 74) was used.

Briefly, the lymphoblast cell line Lymph3 was reprogrammed employing oriP/EBNA-1-based episomal plasmids expressing OCT4, SOX2, KLF4, LIN28, L-MYC and a p53 shRNA. Confirmation of the vector dilution of AD-TREM2-3 was carried out by analyzing expression of exogenous *OCT4* (vector) (top panel). Endogenous *OCT4* analysis (lower panel) was performed as an internal PCR control (Fig. 1A). Pluripotency was confirmed by (i) expression of OCT4, SOX2, NANOG, TRA-1-60 and TRA-1-81 (Fig. 1B), (ii) embryoid body (EB)-based spontaneous differentiation into cell types representative of the three germ layers, namely ectoderm (β III-Tubulin), mesoderm (SMA – smooth muscle actin) and endoderm (AFP – Alpha fetoprotein) (Fig. 1D) and (iii) OCT4 flow cytometry analysis (Fig. 1C). The DNA fingerprinting of AD-TREM2-3 iPSC line was identical to the parental lymphoblast line Lymph3 (Supplementary file 1). Chromosomal content analysis revealed a normal 46, XY karyotype (Fig. 1E). As depicted in the Dendrogram (Fig. 1F), the transcriptome of the lymphoblast line is distinct from ISRM AD TREM2-1 and the embryonic stem cell line H1, which cluster together with a Pearson correlation of 0.940. The reprogramming process did not alter the *TREM2* missense mutation p.R47H – a heterozygous base substitution (G > A) as indicated by the black arrow (Fig. 1G). A PCR-based Mycoplasma contamination test was negative (Supplementary file 1).

3. Materials and methods

3.1. Cell culture

The lymphoblast cell line Lymph3 (Cuyvers et al., 2014) was cultured in RPMI1640 supplemented with 15% fetal bovine serum (FBS) (Invitrogen), 1% Glutamax (Invitrogen), 1% Sodium pyruvate (Invitrogen) and 1% Penicillin/Streptomycin (P/S) (Invitrogen) at 37 °C and 5% CO₂.

3.2. Derivation of AD-TREM2-3

Lymphoblast (Lymph3) were reprogrammed by nucleofection of oriP/EBNA-1- episomal-based plasmids (expressing OCT4, SOX2, KLF4, L-MYC, LIN28 and a p53 shRNA) at the Biomedicum Stem Cell Center, University of Helsinki, Finland, as a service. Well defined distinct iPSC colonies were manually picked and passaged for expansion under feeder-free conditions on Matrigel®-coated plates in E8 medium (Invitrogen). The iPSCs were passaged based on colony growth (every 6–7 days) in a ratio of 1:6 using PBS lacking calcium and magnesium (Gibco) and cultured at 37 °C and 5% CO₂. Further characterisations

were carried out at ISRM-HHU, Düsseldorf, Germany (Table 1).

3.3. PCR

Genomic DNA was isolated from Lymph3, AD-TREM2-3 and the human embryonic stem cell line (H1) using the DNeasy Blood and Tissue Kit (Qiagen). Vector dilution and STR analysis were confirmed by PCR amplification using the primers EndOCT4 (product size 113 bp), ExoOCT4 (product size 657 bp), D17S1296 and DS21S2055. Absence of mycoplasma contamination was confirmed using cell culture supernatant from a dense culture (product size 265–278 bp). PCR was performed using GoTaq® DNA Polymerase (Promega). Reaction was performed as following protocol: 95 °C for 2 min; 35 cycles of reaction: 95 °C for 30 s, 63 °C for 30 s and 72 °C for 30 s; and 72 °C for 5 min on a 96 Universal Gradient peqSTAR (peqLab PCR machine). Primer sequences are shown in Table 2.

3.4. EB formation

Pluripotency was confirmed by EB-based differentiation. First, the iPSCs were cultured on Matrigel®-coated plates until sub-confluent, thereafter the iPSCs colonies were removed with a cell scraper and transferred to a low attachment T25 flask in EBs Medium (high glucose DMEM supplemented with 10% FBS, 1% NEAA and 1% P/S) during 1 week. Afterwards, EBs were replated onto a gelatin coated 12-well plate for 3–4 days in EBs Medium.

3.5. Immunocytochemistry

iPSCs and differentiated EB cells were fixed with 4% paraformaldehyde for 15 min at room temperature (RT), washed with PBS, blocked during 1 h at RT with 5% normal goat serum in 0.5% Triton- \times 100 PBS solution. Cells were incubated with the primary antibody overnight at 4 °C. The following antibodies were used for the characterisation – anti-OCT4, anti-SOX2, anti-NANOG, anti-TRA-1-60 and anti-TRA-1-81; for the germ layer differentiation – anti- β III Tub, anti-SMA and anti-AFP. To detect the signal, cell were washed with PBS and Alexa488 or Alexa555-conjugated secondary antibodies were incubated during 1 h at RT together. Cell nuclei were visualized using Hoechst 33,258. Fluorescent images were obtained by an inverse fluorescence microscope LSM700 (Carl Zeiss).

3.6. Flow cytometry

iPSCs were dissociated into single cells with TrypLE Express (Gibco) and fixed with Fixation Buffer (BioLegend) for 20 min at RT. Cells were permeabilized with Intracellular Staining Permeabilization Wash Buffer (BioLegend) 10 min at RT followed by the incubation with anti-Oct3/4 antibody APC-conjugated (Miltenyl Biotec) 30 min at 4 °C, according to the manufacturer's instructions. Flow-cytometric analysis was carried out using the CyAn ADP Flow Cytometer (Dako) and the data analysis was performed using the Summit software. Unstained cells were used as negative control.

3.7. Karyotype analysis

The karyotype analysis was performed at the Institute of Human Genetics and Anthropology, HHU, Düsseldorf. Nineteen metaphases were counted with a G-band resolution between 150 and 300. The iPSC line was karyotyped 9 passages after the line was generated.

3.8. Bidirectional sanger sequencing

Genotyping of *TREM2* p.R47H was performed on genomic DNA by PCR amplification and Sanger sequencing of exon 2 as described in Cuyvers et al. (2014).

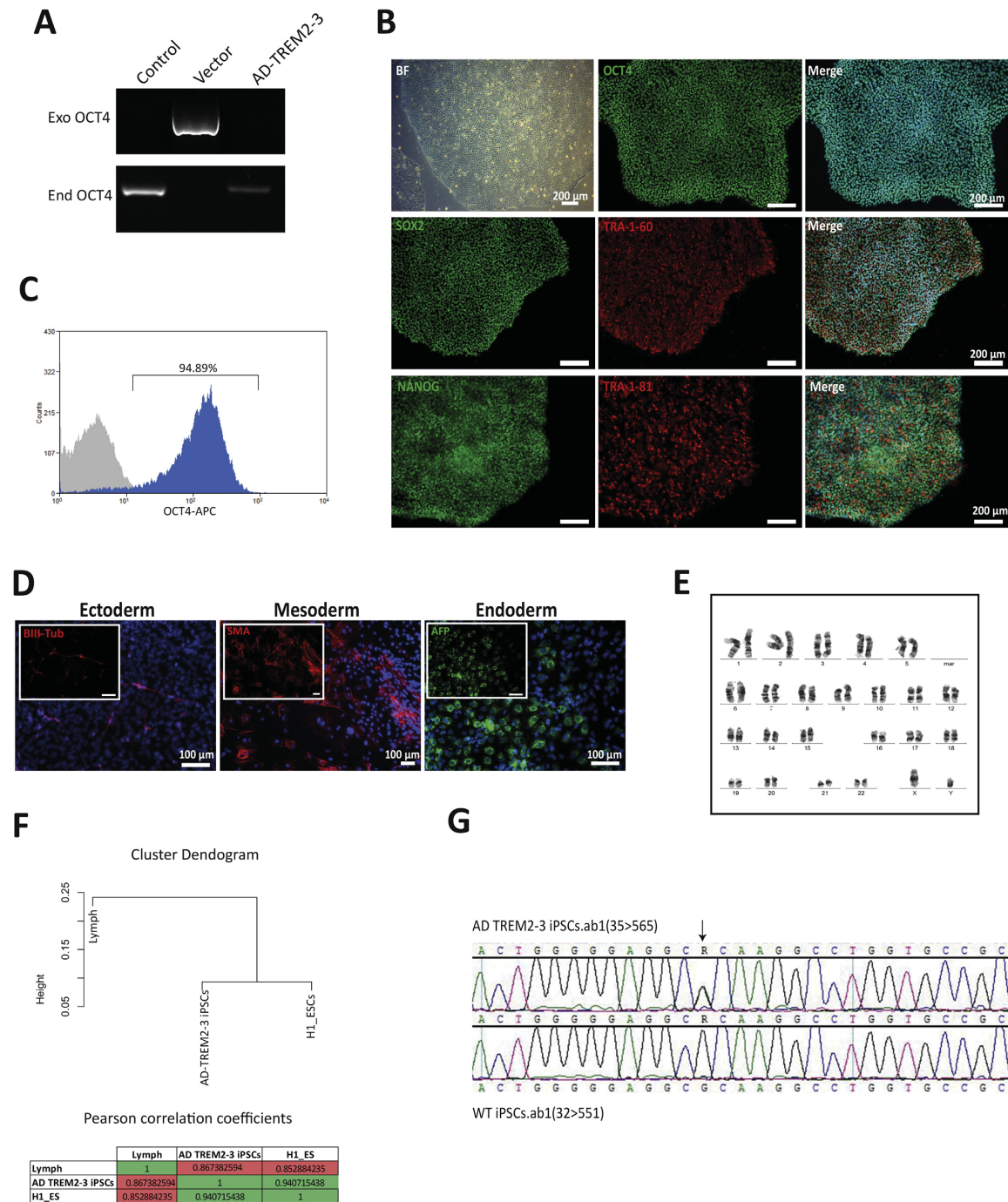


Fig. 1. Characterisation of AD-TREM2-3 iPSC line.

3.9. RNA-based microarray analysis

Total RNA was isolated using Direct-zol RNA MiniPrep (Zymo Research) in combination with peqGold TriFast (PeqLab Biotechnology) according to the manufacturer's protocol. Microarray analysis was

outsourced to the Genomics/Transcriptomic Laboratory of the BMFZ, HHU, Düsseldorf. Affymetrix raw data in form of CEL files was read into the R/Bioconductor environment (Gentleman et al., 2004) using the package affy (Gautier et al., 2004). Probesets were normalized with the *rma* method and probesets with a coefficient of variation greater than

Table 1
Characterisation and validation.

Classification	Test	Result	Data
Morphology	Photography	Normal	Fig. 1 panel B
Phenotype	Immunocytochemistry	Expression of pluripotency associated markers: OCT4, SOX2, NANOG, TRA-1-60, and TRA-1-81	Fig. 1 panel B
	Flow cytometry	94.89% OCT4 positive cells	Fig. 1 panel C
Genotype	Karyotype (G-banding) and resolution	46 XX, Resolution 150-300	Fig. 1 panel E
Identity	Microsatellite PCR (mPCR)	Not done	N/A
	STR analysis	DNA Fingerprinting PCR: two sites tested, matched	Supplementary file 1
Mutation analysis (IF APPLICABLE)	Sequencing	TREM2 p.R47H heterozygous mutation	Fig. 1 panel G
	Southern Blot OR WGS	Not applicable	N/A
Microbiology and virology	Mycoplasma	Mycoplasma testing by PCR: negative	Supplementary file 1
Differentiation potential	Embryoid body formation OR Teratoma formation OR Scorecard	Expression of germ layer specific proteins Ectoderm: βIII-Tub Endoderm: AFP Mesoderm: SMA	Fig. 1 panel D
Donor screening (OPTIONAL)	HIV 1 + 2 Hepatitis B, Hepatitis C	Not tested	N/A
Genotype additional info (OPTIONAL)	Blood group genotyping	Not tested	N/A
	HLA tissue typing	Not tested	N/A

Table 2
Reagents details.

Antibodies used for immunocytochemistry/flow-cytometry			
	Antibody	Dilution	Company Cat # and RRID
Flow-cytometry	Anti-OCT3/4-APC	1:11	Miltenyi Biotec Cat# 130-109-764, RRID: AB_2653082
Pluripotency Markers	Rabbit anti-OCT4	1:400	Cell Signaling Technologies; #2840S RRID: AB_2167691
Pluripotency Markers	Rabbit anti-SOX2	1:400	Cell Signaling Technologies; #3579S RRID: AB_2195767
Pluripotency Markers	Rabbit anti-NANOG	1:800	Cell Signaling Technologies; #4903S RRID: AB_10559205
Pluripotency Markers	Mouse anti-Tra-1-60	1:1000	Cell Signaling Technologies; #4746S RRID: AB_2119059
Pluripotency Markers	Mouse anti-Tra-1-81	1:1000	Cell Signaling Technologies; #4745S RRID: AB_2119060
Differentiation Markers	Mouse anti-βIII Tub	1:200	Cell Signaling Technologies; #4466 RRID: AB_1904176
Differentiation Markers	anti-aSMA	1:1000	Dako; # M0851, RRID: AB_2223500
Differentiation Markers	Rabbit anti-AFP	1:200	Cell Signaling Technology Cat# 2137S, RRID: AB_2209744
Secondary antibodies	anti-mouse-Alexa555	1:2000	Thermo Fisher Scientific Cat# A10521, RRID: AB_2534030
Secondary antibodies	anti-rabbit-Alexa488	1:2000	Thermo Fisher Scientific Cat# A27034, RRID: AB_2536097
Nuclear Co-Staining	Hoechst	1:5000	Thermo Fisher Scientific Cat# H3569, RRID: AB_2651133

Primers		
	Target	Forward/Reverse primer (5'-3')
Fingerprinting	D21S2055	AACAGAACCAATAGGCTATCTATC/TACAGTAAATCACTGGTAGGAGA
Fingerprinting	D17S1296	TTTTGGTATTGGCCATCCTA/ GAAAGAACACAGAGACAGGG
Episomal Plasmid (Exo)	OCT4	AGTGAGAGGCAACCTGGAGA/AGGAACTGCTTCCTCACGA
Endogenous OCT4	OCT4	GTGGAGGAAGCTGACAAACA/ATTCTCCAGTTGCCTCTCA
Mycoplasma	16S rRNA gene from Mycoplasma	GGGAGCAAACAGGATTAGATACCCT/TGCACCATCTGCACTCTGTTAACCTC

0.1 were filtered for the cluster analysis. Cluster analysis was performed employing the function *hclust* parameterized with Pearson correlation as similarity measure and centroid linkage as agglomeration method.

Appendix A. Supplementary data

Supplementary data to this article can be found online at <https://doi.org/10.1016/j.scr.2018.05.018>.

References

Cuyvers, E., Bettens, K., Philijns, S., Van Langenhove, T., Gijssels, I., van Zee, J., Engelborghs, S., Vandenbulcke, M., Van Dongen, J., Geerts, N., et al., 2014. Investigating the role of rare heterozygous TREM2 variants in Alzheimer's disease

and frontotemporal dementia. *Neurobiol. Aging* 35 (726 e711–726 e729).
 Gautier, L., Cope, L., Bolstad, B.M., Irizarry, R.A., 2004. Affy—analysis of Affymetrix GeneChip data at the probe level. *Bioinformatics* (Oxford, England) 20 (3), 307–315. <http://dx.doi.org/10.1093/bioinformatics/btg405>.
 Gentleman, R.C., Carey, V.J., Bates, D.M., Bolstad, B., Dettling, M., Dudoit, S., Ellis, B., Gautier, L., Ge, Y., Gentry, J., Hornik, K., Hothorn, T., Huber, W., Iacus, S., Irizarry, R., Leisch, F., Li, C., Maechler, M., Rossini, A.J., Sawitzki, G., Smyth, C., Smyth, G., Tierney, L., Yang, J.Y.H., Zhang, J., 2004. Bioconductor: open software development for computational biology and bioinformatics. *Genome Biol.* 5 (10), R80. <http://dx.doi.org/10.1186/gb-2004-5-10-r80>.
 Guerreiro, R., Wojtas, A., Bras, J., Carrasquillo, M., Rogaeva, E., Majounie, E., Cruchaga, C., Sassi, C., Kauwe, J.S., Younkin, S., et al., 2013. TREM2 variants in Alzheimer's disease. *N. Engl. J. Med.* 368, 117–127.
 Jonsson, T., Stefansson, H., Steinberg, S., Jonsdottir, I., Jonsson, P.V., Snaedal, J., Bjornsson, S., Huttenlocher, J., Levey, A.I., Lah, J.J., et al., 2013. Variant of TREM2 associated with the risk of Alzheimer's disease. *N. Engl. J. Med.* 368, 107–116.

2.3 Lymphoblast-derived integration-free ISRM-CON9 iPSC cell line from a 75 year old female

Soraia Martins, Martina Bohndorf, Friederike Schröter, Fatima Assar, Wasco Wruck, Kristel Slegers, Christine Van Broeckhoven and James Adjaye

Stem Cell Research 26, (2018) 76-79

Abstract

Human lymphoblast cells were used to generate integration-free induced pluripotent stem cells (iPSCs) employing episomal-based plasmids expressing OCT4, SOX2, NANOG, LIN28, c-MYC and L-MYC. The derived iPSCs were defined as pluripotent based on (i) expression of pluripotency-associated markers, (ii) embryoid body-based differentiation into cell types representative of the three germ layers and (iii) the similarity between the transcriptomes of the iPSC line and the human embryonic stem cell line H1 with a Pearson correlation of 0.95.

Author's contribution: 50%

Conceptualization: **SM**, FS and JA. Methodology: **SM**, MB, FS and FA; Data curation: WW, Resources: KS and CVB. Manuscript writing: SM and JA. All authors have read and agreed to the published version of the manuscript.

Status: Published in Stem Cell Research (doi.org/10.1016/j.scr.2017.12.007)

This is an open access article under the terms of the Creative Commons Attribution 4.0 License.



Contents lists available at ScienceDirect

Stem Cell Research

journal homepage: www.elsevier.com/locate/scr

Lab resource: Stem Cell Line

Lymphoblast-derived integration-free ISRM-CON9 iPSC cell line from a 75 year old female

Soraia Martins^a, Martina Bohndorf^a, Friederike Schröter^a, Fatima Assar^a, Wasco Wruck^a, Kristel Slegers^{b,c}, Christine Van Broeckhoven^{b,c}, James Adjaye^{a,*}^a Institute for Stem Cell Research and Regenerative Medicine, Medical Faculty, Heinrich-Heine-University Düsseldorf, Moorenstrasse 5, Düsseldorf 40225, Germany^b Neurodegenerative Brain Disease Groups, Department of Molecular Genetics, VIB, Antwerp, Belgium^c Laboratory of Neurogenetics, Institute Born-Bunge, University of Antwerp, Belgium

ARTICLE INFO

Article history:

Received 29 November 2017

Received in revised form 12 December 2017

Accepted 12 December 2017

Available online 13 December 2017

ABSTRACT

Human lymphoblast cells were used to generate integration-free induced pluripotent stem cells (iPSCs) employing episomal-based plasmids expressing OCT4, SOX2, NANOG, LIN28, c-MYC and L-MYC. The derived iPSCs were defined as pluripotent based on (i) expression of pluripotency-associated markers, (ii) embryoid body-based differentiation into cell types representative of the three germ layers and (iii) the similarity between the transcriptomes of the iPSC line and the human embryonic stem cell line H1 with a Pearson correlation of 0.95.

© 2017 The Authors. Published by Elsevier B.V. This is an open access article under the CC BY-NC-ND license (<http://creativecommons.org/licenses/by-nc-nd/4.0/>).

Resource table

Unique stem cell line identifier	HHUUKDi002-A
Alternative name of stem cell line	ISRM-CON9
Institution	Institute for Stem Cell Research and Regenerative Medicine, Medical Faculty, Heinrich-Heine-University VIB – Department of Molecular Genetics, Antwerp, Belgium
Contact information of distributor	James Adjaye, james.adjaye@med.uni-duesseldorf.de
Type of cell line	iPSC
Origin	Human
Additional origin info	Age: 75 Sex: Female
Cell Source	Human lymphoblast cells
Clonality	Clonal
Method of reprogramming	Episomal vectors with the oriP/EBNA-1 backbone containing OCT4, SOX2, KLF4, LIN28 and L-MYC
Associated disease	None
Method of modification	n/a
Gene correction	No
Name of transgene or resistance	None
Inducible/constitutive system	n/a
Date archived/stock date	4 June 2014
Cell line repository/bank	n/a
Ethical approval	Ethics Committee of the University Hospital Antwerp and the University of Antwerp, Belgium.

* Corresponding author.

E-mail address: james.adjaye@med.uni-duesseldorf.de (J. Adjaye).

Resource utility

The age of the donor make these iPSCs a valuable resource as a control line for studying age-associated risk of pathogenic variants and age-related disease modelling. Given the lymphoid origin, this line may also be useful for studying the concept of epigenetic memory after reprogramming.

Resource details

Lymphoblast cells were derived from a 75 year old individual with an APOE $\epsilon 3/\epsilon 3$ genotype and expressing the CR1 isoform F/F (low risk of Alzheimer's disease-AD). The association with AD is higher in individuals expressing the risk factors apolipoprotein E (APOE) $\epsilon 4$ alleles and CR1 isoform S (Brouwers et al., 2012). The cells were reprogrammed employing oriP/EBNA-1-based episomal plasmids expressing OCT4, SOX2, KLF4, C-MYC, L-MYC, LIN28 and a p53 shRNA. Both clones of CON9-iPSC lines were negative for EBNA-1 and oriP (Fig. 1A). Pluripotency was confirmed by (i) expression of OCT4, SOX2, NANOG, c-MYC, TRA-1-60 and TRA-1-81 (Fig. 1B), (ii) embryoid body (EB)-based spontaneous differentiation into cell types representative of the three germ layers, namely ectoderm (NESTIN, PAX6), mesoderm (SMA – smooth muscle actin, Brachyury) and endoderm (SOX17) (Fig. 1C) and (iii) OCT4 flow cytometry analysis (Fig. 1D). The DNA fingerprinting of ISRM-CON9-iPSC line was identical to the parental lymphoblast line (CON9) (Supplementary file 1). Chromosomal content analysis revealed a 46, XX karyotype (Fig. 1E). As depicted in the Denrogram (Fig. 1F), the transcriptome of the lymphoblast line (CON9) is distinct from both pluripotent cell lines- ISRM-CON9 ESC- H1, which

<https://doi.org/10.1016/j.scr.2017.12.007>1873-5061/© 2017 The Authors. Published by Elsevier B.V. This is an open access article under the CC BY-NC-ND license (<http://creativecommons.org/licenses/by-nc-nd/4.0/>).

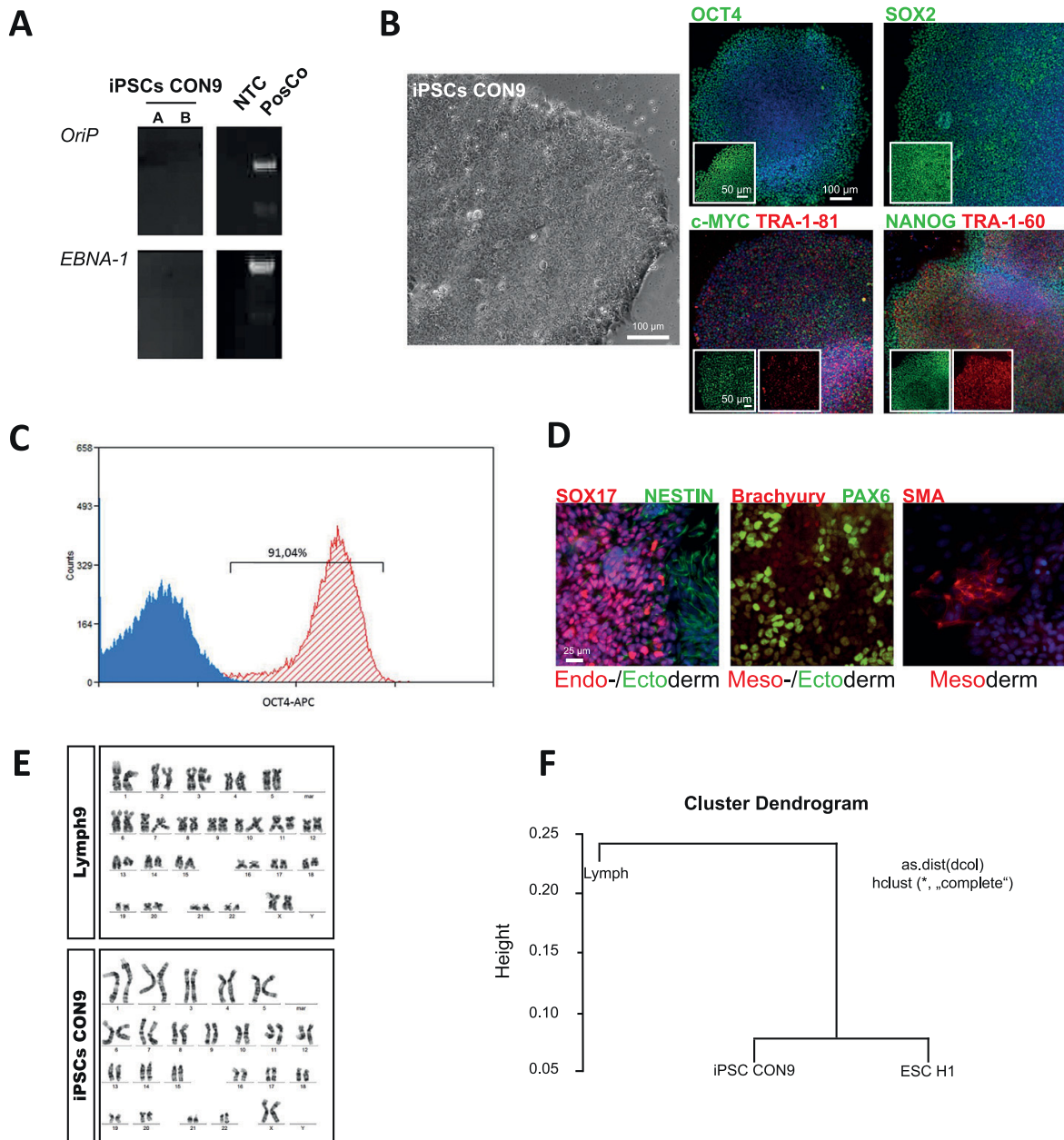


Fig. 1. Characterization of ISRM-CON9 iPSC line.

cluster together with a Pearson correlation of 0.95. A PCR-based Mycoplasma contamination test was negative (Supplementary file 2).

1. Materials and methods

1.1. Cell culture

The lymphoblast cell line CON9 (Brouwers et al., 2012) was cultured in RPMI 1640 supplemented with 15% fetal bovine serum (Invitrogen™), 1% Glutamax (Invitrogen™), 1% Sodium pyruvate

(Invitrogen™) and 1% Penicillin/Streptomycin (Invitrogen™) at 37 °C and 5% CO₂.

1.2. Derivation of the iPSC cell line

Lymphoblast cells CON9 were reprogrammed by nucleofection of oriP/EBNA-1-episomal-based plasmids (expressing OCT4, SOX2, KLF4, L-MYC, LIN28 and a p53 shRNA) at the Biomedicum Stem Cell Center, University of Helsinki, Finland, as a service. Colonies emerged two to four weeks post nucleofection. Well defined distinct iPSCs colonies

Table 1
Characterization and validation details of ISRM-CON9 iPSC line.

Classification	Test	Result	Data
Morphology Phenotype	Photography	Normal	Fig. 1 panel B
	Immunocytochemistry	Expression of pluripotency associated markers: OCT4, SOX2, NANOG, TRA-1-60, and TRA-1-81	Fig. 1 panel B
Genotype Identity	Flow cytometry	91.04% OCT4 positive cells	Fig. 1 panel C
	Karyotype (G-banding) and resolution	46XX, Resolution 150–300	Fig. 1 panel E
	Microsatellite PCR (mPCR)	Not done	–
Mutation analysis (if applicable)	STR analysis	DNA Fingerprinting PCR: two sites tested, matched	Supplementary file 1
	Sequencing	Not applicable	–
Microbiology and virology	Southern Blot OR WGS	Not applicable	–
	Mycoplasma	Mycoplasma testing by PCR Negative	Supplementary file 1
Differentiation potential	Embryoid body	Expression of germ layer specific proteins Ectoderm: NESTIN, PAX6 Endoderm: SOX17 Mesoderm: SMA and Brachyury	Fig. 1 panel D
Donor screening (optional)	HIV 1 + 2 Hepatitis B, Hepatitis C	Not tested	–
Genotype additional info (optional)	Blood group genotyping	Not tested	–
	HLA tissue typing	Not tested	–

were manually picked and passaged for expansion under feeder-free conditions on Matrigel®-coated plates in E8 medium (Invitrogen™).

1.3. Polymerase chain reaction

RT-PCR to assess the expression levels of the transgenes was carried out by the Biomedicum Stem Cell Center, University of Helsinki, Finland.

1.4. Embryoid body formation

To confirm pluripotency in ISRM-CON9, Embryoid body (EB)-based differentiation was performed. First, the iPSCs were cultured on matrigel coated plates until sub-confluent and further cultured in ultra-low attachment flask (Corning) in FTDA medium (Frank et al., 2012). Afterwards, the EBs were replated onto gelatine-coated plates, again in FTDA medium lacking bFGF and Dorsomorphin.

1.5. Flow cytometry and immunofluorescence-based detection of pluripotency associated proteins

iPSCs and differentiated EB cells were fixed with 4% paraformaldehyde for 15 min at room temperature. After blocking with 5% normal goat serum in 0.5% Triton-X100 PBS solution, cells were incubated with the primary antibody overnight at 4 °C. The following antibodies were used: for the iPSC characterization – anti-OCT4, anti-SOX2, anti-NANOG and anti-TRA-1-60 or anti-TRA-1-81; for the germ layer differentiation – anti-Nestin, anti-SMA, anti-SOX17, anti-Brachyury and anti-PAX6. Alexa 488 or Cy3-conjugated secondary antibodies were used to visualize the signal. Co-staining was accomplished using nuclear Hoechst. The wells were covered with PBS solution and the fluorescent images obtained by an inverse fluorescence microscope LSM 700 (Carl Zeiss) and analyzed employing Adobe Photoshop software (Adobe, USA). Flow-cytometric analysis using an anti-Oct3/4 antibody conjugated to APC (Miltenyl Biotec) was carried out using the CyAn ADP Flow Cytometer (Dako). Unstained cells were used as negative control (Table 1).

Table 2
Antibodies used for immunocytochemistry/flow-cytometry.

	Antibody	Dilution	Company Cat # and RRID
Flow-cytometry	Anti-OCT3/4-APC	1:11	Miltenyl Biotec Cat# 130-109-764, RRID: AB_2653082
Pluripotency markers	Rabbit anti-OCT4	1:400	Cell Signaling Technologies; #2840S RRID: AB_2167691
Pluripotency markers	Rabbit anti-SOX2	1:400	Cell Signaling Technologies; #3579S RRID: AB_2195767
Pluripotency markers	Rabbit anti-NANOG	1:800	Cell Signaling Technologies; #4903S RRID: AB_10559205
Pluripotency markers	Mouse anti-Tra-1-60	1:1000	Cell Signaling Technologies; #4746S RRID: AB_2119059
Pluripotency markers	Mouse anti-Tra-1-81	1:1000	Cell Signaling Technologies; #4745S RRID: AB_2119060
Differentiation markers	Rabbit anti-Nestin	1:250	Sigma Aldrich; N5413 RRID: AB_1841032
Differentiation markers	anti- α SMA	1:1000	Dako; # M0851, RRID:AB_2223500
Differentiation markers	Mouse anti-Sox17	1:50	R and D Systems Cat# AF1924, RRID:AB_355060
Differentiation markers	Goat anti-Brachyury	1:500	R&D Systems; # AF2085 RRID: AB_2200235
Differentiation markers	Mouse anti-Pax6	1:1000	Synaptic System; #153011 RRID: AB_887758
Secondary antibodies	anti-mouse-Cy3	1:2000	Thermo Fisher Scientific Cat# A10521, RRID: AB_2534030
Secondary antibodies	anti-rabbit-Alexa488	1:2000	Thermo Fisher Scientific Cat# A27034, RRID: AB_2536097
Nuclear co-staining	Hoechst	1:5000	Thermo Fisher Scientific Cat# H3569, RRID: AB_2651133
Primers			
	Target	Forward/Reverse primer (5'–3')	
Fingerprinting	D10S1214	ATTGCCCAAACTTTTGTG/TGAGACAGCTCTGGGAAG	
Fingerprinting	D21S2055	AACAGAACCAATAGGCTATCTATC/TACAGTAACTACTGTGGAGAGA	
Mycoplasma	16S rRNA gene from mycoplasma	GGGAGCAACAGGATTAGATACCCT/TGCACCATCTGTCACTGTGTAACCTC	

1.6. Karyotype analysis

The karyotype analysis was evaluated and performed at the Institute of Human Genetics and Anthropology, Heinrich-Heine-University, Düsseldorf.

1.7. DNA fingerprinting analysis

Genomic DNA was isolated from the lymphoblast cell line Lymph9, the derived ISRM-CON9-iPSC line, and the human embryonic stem cell line (H1) using the DNeasy Blood and Tissue Kit (Qiagen). STR analysis was performed by PCR amplification using primers DS10S1214 and DS21S2055. Primer sequences are shown in Table 2.

1.8. RNA-based microarray analysis

Total RNA from cell lysate was isolated using Direct-zol RNA Mini Prep (Zymo Research) in combination with peqGold TriFast (PeqLab Biotechnology) according to the manufacturer's protocol. Microarray analysis was outsourced to the Genomics/Transcriptomic Laboratory of the BMFZ, Heinrich-Heine-University, Düsseldorf. Affymetrix raw data in form of CEL files was read into the R/Bioconductor environment (Gentleman et al., 2004) using the package *affy* (Gautier et al., 2004). Probesets were normalized with the *rma* method and probesets with a coefficient of variation greater than 0.1 were filtered for the cluster analysis. Cluster analysis was performed employing the function *hclust* parameterized with Pearson correlation as similarity measure and centroid linkage as agglomeration method.

Acknowledgements

JA acknowledges support from the Medical Faculty, Heinrich-Heine-University, Düsseldorf. Research at the Antwerp site was funded in part

by the Belgian Science Policy Office Interuniversity Attraction Poles Program (BELSPO, www.belspo.be), the Flanders Impulse Program on Networks for Dementia Research (VIND) and the University of Antwerp Research Fund (<http://www.uantwerpen.be/>). JA, KS and CVB are members of the EU project- AgedBrainSYSBIO. The AgedBrainSYSBIO project received funding from the European Union's Seventh Framework Programme for research, technological development and demonstration under grant agreement no 305299.

Supplementary data

Supplementary data to this article can be found online at <https://doi.org/10.1016/j.scr.2017.12.007>.

References

- Brouwers, N., van Cauwenberghe, C., Engelborghs, S., Lambert, J.-C., Bettens, K., Le Bastard, N., Pasquier, F., Montoya, A.G., Peeters, K., Mattheijssens, M., Vandenberghe, R., Deyn de, P.P., Cruts, M., Amouyel, P., Sleegers, K., van Broeckhoven, C., 2012. Alzheimer risk associated with a copy number variation in the complement receptor 1 increasing C3b/C4b binding sites. *Mol. Psychiatry* 17 (2):223–233. <https://doi.org/10.1038/mp.2011.24>.
- Frank, S., Zhang, M., Schöler, H.R., Greber, B., 2012. Small molecule-assisted, line-independent maintenance of human pluripotent stem cells in defined conditions. *PLoS One* 7 (7):e41958. <https://doi.org/10.1371/journal.pone.0041958>.
- Gautier, L., Cope, L., Bolstad, B.M., Irizarry, R.A., 2004. *affy*—analysis of Affymetrix GeneChip data at the probe level. *Bioinformatics* (Oxford, England) 20 (3): 307–315. <https://doi.org/10.1093/bioinformatics/btg405>.
- Gentleman, R.C., Carey, V.J., Bates, D.M., Bolstad, B., Dettling, M., Dudoit, S., Ellis, B., Gautier, L., Ge, Y., Gentry, J., Hornik, K., Hothorn, T., Huber, W., Iacus, S., Irizarry, R., Leisch, F., Li, C., Maechler, M., Rossini, A.J., Sawitzki, G., Smith, C., Smyth, G., Tierney, L., Yang, J.Y.H., Zhang, J., 2004. Bioconductor: open software development for computational biology and bioinformatics. *Genome Biol.* 5 (10):R80. <https://doi.org/10.1186/gb-2004-5-10-r80>.

2.4 IPSC-Derived Neuronal Cultures Carrying the Alzheimer's Disease Associated TREM2 R47H Variant Enables the Construction of an A β -Induced Gene Regulatory Network

Soraia Martins, Andreas Müller-Schiffmann, Lars Erichsen, Martina Bohndorf, Wasco Wruck, Kristel Slegers, Christine Van Broeckhoven, Carsten Korth and James Adjaye

International Journal of Molecular Sciences, (2020) 21,4516

Abstract

Genes associated with immune response and inflammation have been identified as genetic risk factors for late-onset Alzheimer's disease (LOAD). The rare R47H variant within triggering receptor expressed on myeloid cells 2 (TREM2) has been shown to increase the risk for developing Alzheimer's disease (AD) 2–3-fold. Here, we report the generation and characterization of a model of late-onset Alzheimer's disease (LOAD) using lymphoblast-derived induced pluripotent stem cells (iPSCs) from patients carrying the TREM2 R47H mutation as well as from control individuals without dementia. All iPSCs efficiently differentiated into mature neuronal cultures, however AD neuronal cultures showed a distinct gene expression profile. Furthermore, manipulation of the iPSC-derived neuronal cultures with an A β -S8C dimer highlighted metabolic pathways, phagosome and immune response as the most perturbed pathways in AD neuronal cultures. Through the construction of an A β -induced gene regulatory network, we were able to identify an AB signature linked to protein processing in the endoplasmic reticulum (ER), which emphasized ER-stress, as a potential causal role in LOAD. Overall, this study has shown that our AD-iPSC based model can be used for in-depth studies to better understand the molecular mechanisms underlying the etiology of LOAD and provides new opportunities for screening of potential therapeutic targets.

Author's contribution: 70%;

Conceptualization: **SM** and **JA**; Methodology: **SM**, **AMS**, **LE** and **MB**; Formal analysis: **SM**, **AMS**, **WW** and **JA**; Data curation: **WW**; Investigation: **SM**, **AMS**, **MB**; Resources:

KS, CVB and CK; Writing—original draft preparation: **SM**; Writing—review and editing: JA, WW, AMS, KS, CVB and CK; Supervision: JA. All authors have read and agreed to the published version of the manuscript.

Status: Published in International Journal of Molecular Sciences

(doi:10.3390/ijms21124516)

This is an open access article under the terms of the Creative Commons Attribution 4.0 License.



Article

IPSC-Derived Neuronal Cultures Carrying the Alzheimer's Disease Associated *TREM2* R47H Variant Enables the Construction of an A β -Induced Gene Regulatory Network

Soraia Martins ¹, Andreas Müller-Schiffmann ², Lars Erichsen ¹, Martina Bohndorf ¹, Wasco Wruck ¹, Kristel Slegers ^{3,4}, Christine Van Broeckhoven ^{3,4}, Carsten Korth ² and James Adjaye ^{1,*}

¹ Institute for Stem Cell Research and Regenerative Medicine, Medical Faculty, Heinrich-Heine University, 40225 Düsseldorf, Germany; Soraia.Martins@med.uni-duesseldorf.de (S.M.); Lars.Erichsen@med.uni-duesseldorf.de (L.E.); Martina.Bohndorf@med.uni-duesseldorf.de (M.B.); Wasco.Wruck@med.uni-duesseldorf.de (W.W.)

² Department of Neuropathology, Heinrich-Heine University, 40225 Düsseldorf, Germany; Andreas.Mueller@med.uni-duesseldorf.de (A.M.-S.); ckorth@uni-duesseldorf.de (C.K.)

³ Neurodegenerative Brain Diseases Group, VIB-Center for Molecular Neurology, University of Antwerp, 20610 Antwerp, Belgium; kristel.slegers@uantwerpen.vib.be (K.S.); christine.vanbroeckhoven@uantwerpen.vib.be (C.V.B.)

⁴ Department of Biomedical Sciences, University of Antwerp, 20610 Antwerp, Belgium

* Correspondence: james.adjaye@med.uni-duesseldorf.de

Received: 27 May 2020; Accepted: 23 June 2020; Published: 25 June 2020



Abstract: Genes associated with immune response and inflammation have been identified as genetic risk factors for late-onset Alzheimer's disease (LOAD). The rare R47H variant within triggering receptor expressed on myeloid cells 2 (*TREM2*) has been shown to increase the risk for developing Alzheimer's disease (AD) 2–3-fold. Here, we report the generation and characterization of a model of late-onset Alzheimer's disease (LOAD) using lymphoblast-derived induced pluripotent stem cells (iPSCs) from patients carrying the *TREM2* R47H mutation, as well as from control individuals without dementia. All iPSCs efficiently differentiated into mature neuronal cultures, however AD neuronal cultures showed a distinct gene expression profile. Furthermore, manipulation of the iPSC-derived neuronal cultures with an A β -S8C dimer highlighted metabolic pathways, phagosome and immune response as the most perturbed pathways in AD neuronal cultures. Through the construction of an A β -induced gene regulatory network, we were able to identify an A β signature linked to protein processing in the endoplasmic reticulum (ER), which emphasized ER-stress, as a potential causal role in LOAD. Overall, this study has shown that our AD-iPSC based model can be used for in-depth studies to better understand the molecular mechanisms underlying the etiology of LOAD and provides new opportunities for screening of potential therapeutic targets.

Keywords: late onset Alzheimer's disease; iPSC-derived neuronal cultures; *TREM2* R47H; A β S8C dimer

1. Introduction

Currently, there are 47 million people worldwide living with dementia, a number that is estimated to increase to more than 131 million in 2050 [1]. Alzheimer's disease (AD) is a neurodegenerative disease and the most common and devastating cause of dementia, contributing to 60–70% of all cases [2]. AD is clinically characterized by a progressive decline of cognitive functions and, according to the classical

amyloid hypothesis two key molecules have been implicated in AD neuropathology: amyloid-beta (A β) and the protein TAU [3]. A β peptides are derived from sequential proteolytic cleavages of the amyloid precursor protein (APP). They form extracellular aggregated deposits known as amyloid plaques. Intracellularly, hyper-phosphorylated TAU forms aggregates composed of twisted filaments known as neurofibrillary tangles (NFTs). As a consequence of the imbalanced crosstalk between A β and TAU, multiple neuropathological mechanism ensue, such as, synaptic toxicity, mitochondrial dysregulation and microglia-derived inflammatory responses, finally leading to neuronal death [4,5]. Age is the greatest risk factor for AD and it can be divided into early-onset AD (EOAD) when the patients are younger than 65, and late-onset AD (LOAD) when the patients manifest symptoms after the age of 65 [6]. Despite EOAD being responsible for a small minority of all cases, the studies of familial AD patients (fAD) have revealed important aspects of the genetic factors implicated in the disease, such as the causal mutations in *APP*, *PSEN1* and *PSEN2*. On the other hand, LOAD is a very complex and multifactorial disease where most cases are sporadic with no clear familial pattern of disease [7,8]. Many genetic risk factors have been implicated in increasing the susceptibility for LOAD, among which is the well established apolipoprotein E (*APOE*). Individuals carrying one ϵ 4 allele have a 3-fold increased risk of AD while individuals carrying the two ϵ 4 alleles face an approximately 12-fold increased risk of AD [9,10]. More recently genome-wide association studies (GWAS) and large scale sequencing projects have led to the discovery of other genetic variants in more than 40 loci that influence the risk for LOAD [11–16]. These genes are known to be involved in biological pathways such as cholesterol metabolism, APP metabolism, MAPT metabolism, cytoskeleton and axon development, immune response and endocytosis/vesicle-mediated transport and epigenetics [17,18]. As a more direct link between immune responses and AD, especially microglia-related genes with an increased risk for developing LOAD were identified by high-throughput sequencing technologies [19,20]. One of the multiple genetic risk variants identified in these studies is the rare p.Arg47His (R47H) variant within the triggering receptor expressed on myeloid cells 2 (*TREM2*), which has been shown to increase the risk of developing AD by 2–3-fold in several European and North American populations [19–24].

TREM2 is a cell surface receptor of the immunoglobulin superfamily expressed on various cells of the myeloid lineage including CNS microglia, bone osteoclasts, alveolar and peritoneal macrophages [25]. According to neuropathology studies in AD patients, animal models and in vitro studies, the *TREM2* R47H variant induces a partial loss of function of *TREM2*, compromising microglia function and thus contributing to the development of AD. *TREM2* deficiency in AD mouse models and patients carrying the R47H variant showed decreased clustering of microglia around the plaques, thereby facilitating the build-up of A β plaques and injury to adjacent neurons [26–29]. Recent data have shown that cells expressing the R47H variant displayed impaired *TREM2*-A β binding and altered *TREM2* intracellular distribution and degradation, thus providing a potential mechanism by which *TREM2* R47H mutation increases the risk for LOAD [30,31]. The adoption of induced pluripotent stem cells (iPSCs) technology provides a platform to derive a reliable human disease model for better understanding the effect of risk factors in neurons derived from primary cells of affected patients. iPSC modeling of AD has provided an important proof-of-principle regarding the utility of such cells for a better understanding of the molecular mechanisms associated with the etiology of AD. So far, a number of the human iPSC-based AD models have concentrated on using iPSCs derived from EOAD or LOAD patients with unidentified mutations [32–38].

Here, we report for the first time the generation and characterization of a model of LOAD using lymphoblast-derived iPSCs from patients harboring the R47H mutation in *TREM2*, as well as from control individuals without dementia. To date gene regulatory networks governing LOAD have been generated using human AD brain biopsies. In our current study, we have shown the feasibility of using an iPSC-based approach to derive biologically meaningful pathways and an A β -induced regulatory network from neuronal cultures that mirrors some of the pathways that have been identified by the LOAD brain biopsies, namely immune response, phagocytosis and unfolded protein response pathways [39]. Our study thus demonstrates that AD iPSC-derived neuronal cultures can be used for

in depth studies to understand the molecular mechanisms underlying the onset of Alzheimer's disease and for screening of potential therapeutic targets.

2. Results

2.1. Ipscs Efficiently Differentiate into a Functional Neuronal Culture

iPSCs derived from lymphoblasts from two LOAD patients carrying the *TREM2* R47H risk variant (AD2-2 and AD2-4), as well as aged-matched control individuals without dementia (CON8 and CON9) were used for this study [40–43]. The summary of the characteristics of the iPSC lines used in this study as well as their APOE status are shown in Table 1.

Table 1. Summary of the healthy controls and Alzheimer's disease (AD) induced pluripotent stem cell (iPSC) lines used in this study.

iPSCs Name	Status	AD Risk Variant	Age	Age at Onset	Gender	APOE Genotype	Reference
CON8	Control individual	Control	69	-	M	3/4	[43]
CON9	Control individual	Control	75	-	F	3/3	[40]
AD-2-2	AD patient	<i>TREM2</i> p.R47H heterozygous	65	60	M	4/4	[42]
AD-2-4	AD patient	<i>TREM2</i> p.R47H heterozygous	67	64	F	2/4	[41]

It has been suggested that GABAergic neurotransmission plays a very important role in AD pathogenesis such as A β toxicity, hyperphosphorylation of TAU and the APOE effect [44–46]. In light of this information, we modified a previously established embryoid body-based protocol [47] to generate iPSC-derived neuronal cultures enriched in GABAergic interneurons. Figure 1A shows the timeline schematic for the protocol in which all iPSC lines were successfully differentiated into neuronal networks enriched in GABAergic interneurons within a course of 80 days (Figure S1). To qualitatively characterize the progression of differentiation, we performed immunostaining for various markers during the differentiation process. Neural rosettes expressed the progenitor markers PAX6 and Nestin (Figure 1B) and after being selected and grown as neurospheres for 7 days, the progenitor cells (SOX1⁺) acquired predominantly a forebrain identity due to the expression of the medial ganglionic eminence (MGE) transcription factor NKX2.1 (Figure 1C), in addition to the telencephalic transcription factor FOXG1 (Figure 1D). After maturation, the neural cultures were composed of GFAP⁺ glia cells and neurons expressing the pan-neuronal markers Tubulin Beta-III and MAP2 (Figure 1E). Neurons differentiated for 80 days expressed the maturation markers Synapsin I (SYN1) and neurofilaments (SMI-32; Figure 1F), as well as the neurotransmitter, GABA (Figure 1G). In order to assess the maturation status of the neuronal cultures, we performed RNA sequencing to analyze the transcriptome profile at day 80. Figure 1H shows a heat map of Pearson correlation analysis for key maturation neuronal markers together with the glia markers OLIG2 and GFAP in the iPSC-derived neuronal cultures compared to commercially bought RNA from fetal, adult and AD brain. All iPSC-derived neuronal cultures expressed similar levels of dopaminergic and serotonergic markers and higher levels of GABAergic interneuron markers. To complement and independently confirm these expression data, quantitative real-time PCR (qRT-PCR) analysis was carried out to evaluate the expression levels of GABAergic interneuron markers *PV*, *SOM*, *CALB2*, *GAD67* and *GAD65* (Figure S1). Despite the variability of expression levels of the different markers, we observed that the iPSC-derived neuronal cultures might be composed mostly of somatostatin (SST) and calretinin (CALB2) subtypes of GABA

interneurons. Moreover, due to the low expression level observed for *TREM2* when compared with the commercially bought fetal, adult and AD brain RNA, qRT-PCR was performed for all iPSC-derived neuronal cultures. *TREM2* is expressed in all lines but however significantly upregulated in AD2-2 (Figure 1I). Taken together, we proposed (i) that the presence of the *TREM2* R47H variant in the AD2-2 and AD2-4 lines has no significant effect on the neuronal differentiation capacity when compared to the control lines CON8 and CON9, (ii) though we did not analyze our neuronal cultures for the presence of microglia, the mixed neuronal culture might probably harbor these.

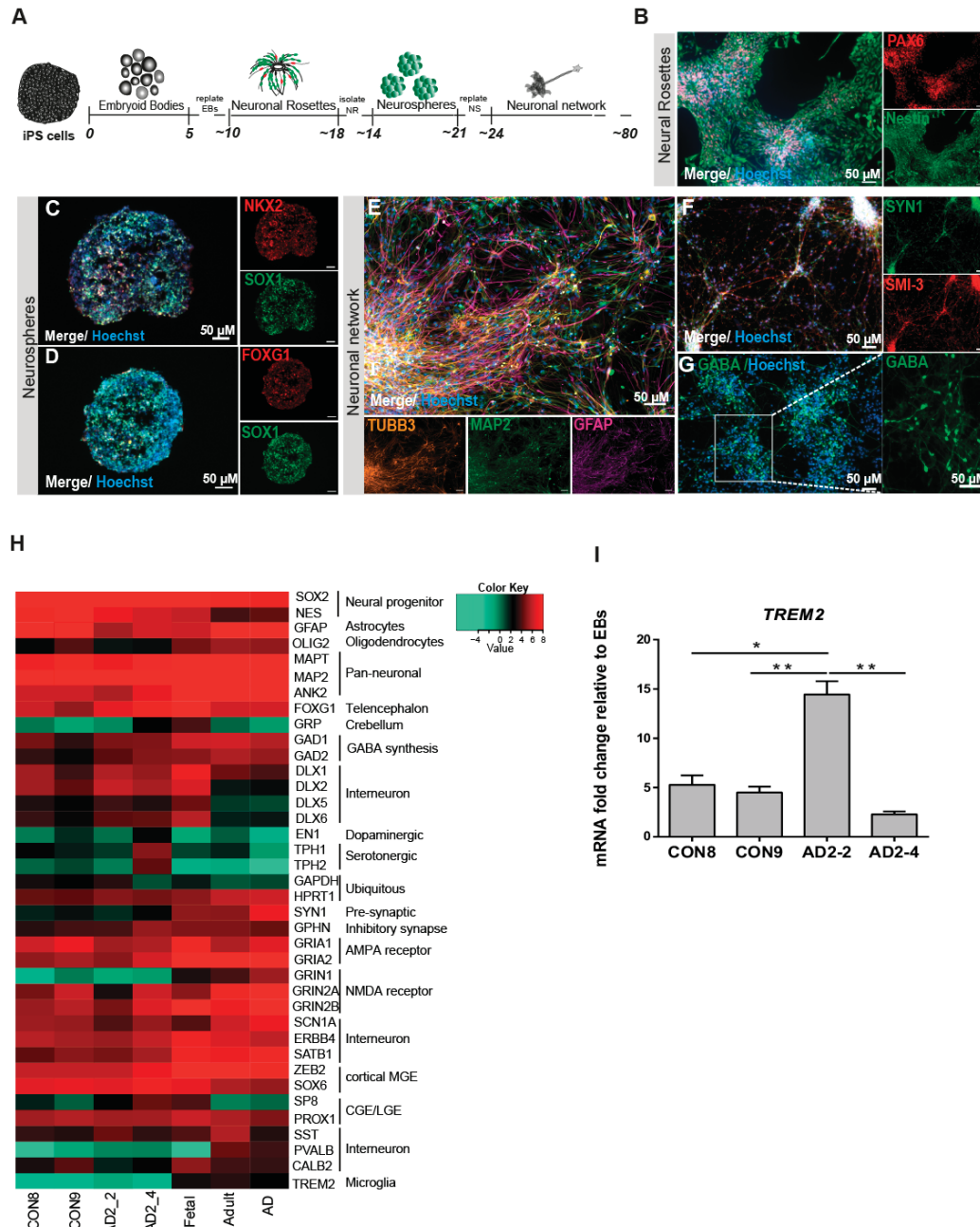


Figure 1. Differentiation and characterization of iPSC-derived neuronal cultures. (A) Scheme illustrating the main stages of the differentiation protocol for generating iPSC-derived neuronal network enriched in GABAergic interneurons. (B-G) Representative immunocytochemistry images of (B) neural rosettes

expressing the progenitor markers PAX6 (red) and Nestin (green), (C) neurosphere expressing the progenitor marker SOX1 (green) and the MGE marker NKX2.1 (red), (D) neurosphere expressing the progenitor marker SOX1 (green) and the forebrain marker FOXG1 (red), (E) neuronal network expressing the pan-neuronal markers TUBB3 (orange) and MAP2 (green) as well as GFAP (magenta), (F) neural maturation markers SYN1 (green) and SMI-3 (red) and (G) interneurons expressing the neurotransmitter GABA (green). Nuclei are stained with Hoechst. Scale bar, 50 μ M. (H) Heatmap of Pearson correlation analysis of RNA-seq data from neural differentiation of control (CON8 and CON9) and AD lines (AD2_2 and AD2_4) and commercially bought RNA from fetal, adult and AD brain for neural progenitor, early neuronal and mature dopaminergic, serotonergic, GABAergic interneuronal markers and glia markers. (I) Relative gene expression of TREM2 in iPSC-derived GABAergic interneurons network from control and AD lines shown as fold change relative to embryoid bodies (EBs). * $p < 0.05$, ** $p < 0.01$, one-way ANOVA, followed by Tukey's multiple comparisons test. Data are presented as mean \pm SEM from three independent experiments.

2.2. The AD Neuronal Network Shows a Distinct Gene Expression Associated with Metabolism and Immune-Related Pathways

To obtain an overview of the transcriptome changes between the AD (AD2-2 and AD2-4) and the control (CON8 and CON9) neuronal cultures, we screened for differentially expressed genes (DEGs). Employing RNA-seq, we identified 4990 genes exclusively expressed in the AD neuronal cultures (Figure 2A). BiNGO was used to perform gene ontology (GO) term enrichment analysis of the 4990 genes, the results are illustrated as a tree-like structure (Figure 2B, Table S1). In depth analyses of the cellular component identified significant enrichment associated with membrane and extracellular space. Regarding biological processes, these genes were significantly enriched in processes related to the response to the stimulus and transport. Moreover, molecular functions such as signal transducer activity, receptor activity and transporter activity, including ion membrane transporter activity and channel activity were significantly enriched. Kyoto Encyclopedia of Genes and Genomes (KEGG) pathway analysis revealed metabolic pathways, which include drug metabolism—cytochrome P450, retinol metabolism and steroid hormone biosynthesis together with a neuroactive ligand–receptor interactor (Figure 1C). As it has been shown that TREM2 regulates innate immunity in AD [48], we additionally analyzed GO terms for biological processes of immune-related genes within the 4990 gene set. Remarkably, 14 significantly enriched terms associated with the regulation of innate and adaptive immune response were identified (Figure 2D). Overall, these data may suggest that AD neuronal cultures exhibit alterations in key signaling pathways related to metabolism and the immune system.

2.3. Characterization of AD Hallmarks in CON and AD Neuronal Cultures

Numerous evidence support the notion that the small oligomers of $A\beta_{42}$ are intricately associated with the amyloid cascade [49,50]. However, recent studies have shown that $A\beta$ dimers, abundantly detected in brains of AD patients, are sufficient to account for neurotoxicity and initiating the amyloid cascade [51–54]. Here, we aimed at investigating the effects of the TREM2 R47H mutation in $A\beta$ production as well as the response of CON and AD iPSC-derived neuronal cultures to stimulations with the well described $A\beta$ -S8C dimer [55–57]. After 4 months of differentiation, neurospheres were dissociated into single cells and differentiated for a further 6 weeks. $A\beta$ levels were measured and the neuronal cultures were stimulated with 500 nM of the $A\beta$ -S8C dimer for 72 h (Figure 3A). Conditioned media from the non-stimulated CON and AD lines were analyzed for comparative $A\beta_{40}$ and $A\beta_{42}$ levels employing ELISA. Interestingly, neurons derived from the AD iPSCs lines (AD2-2 and AD2-4) and the CON iPSCs lines (CON8 and CON9) secreted $A\beta$ with similar $A\beta_{42}$ ratio (Figure 3B–D). We further performed Western blot analysis to evaluate the levels of TAU phosphorylation at Ser202/Thr205 (AT8 epitope), total TAU and total APP after stimulation with the $A\beta$ -S8C dimer (Figure 3E). Although phosphorylation of TAU was found in all neuronal cultures, no significant differences in the expression levels of total TAU (Figure 3F) and phosphorylated TAU (Figure 3G) were observed between AD and

CON neuronal cultures after treatment with the A β -S8C dimer. Surprisingly, the results revealed that stimulation with the A β -S8C dimer induced a modest and uniform increase in the expression levels of APP in all CON and AD neuronal cultures (Figure 3H). To focus on the effect of the A β -S8C dimer, we quantified APP levels in pooled samples, and this revealed significantly increased APP expression (Figure 3I). Taken together, these results confirm that the neuronal cultures (CON8 and AD) secrete A β and although no significant differences in the expression of total and phosphorylated TAU were observed, APP expression was significantly elevated after A β -S8C dimer stimulation. We therefore conclude that the CON and the AD iPSC-derived neuronal cultures were capable of recapitulating in vitro the hallmarks of AD-like cellular pathology.

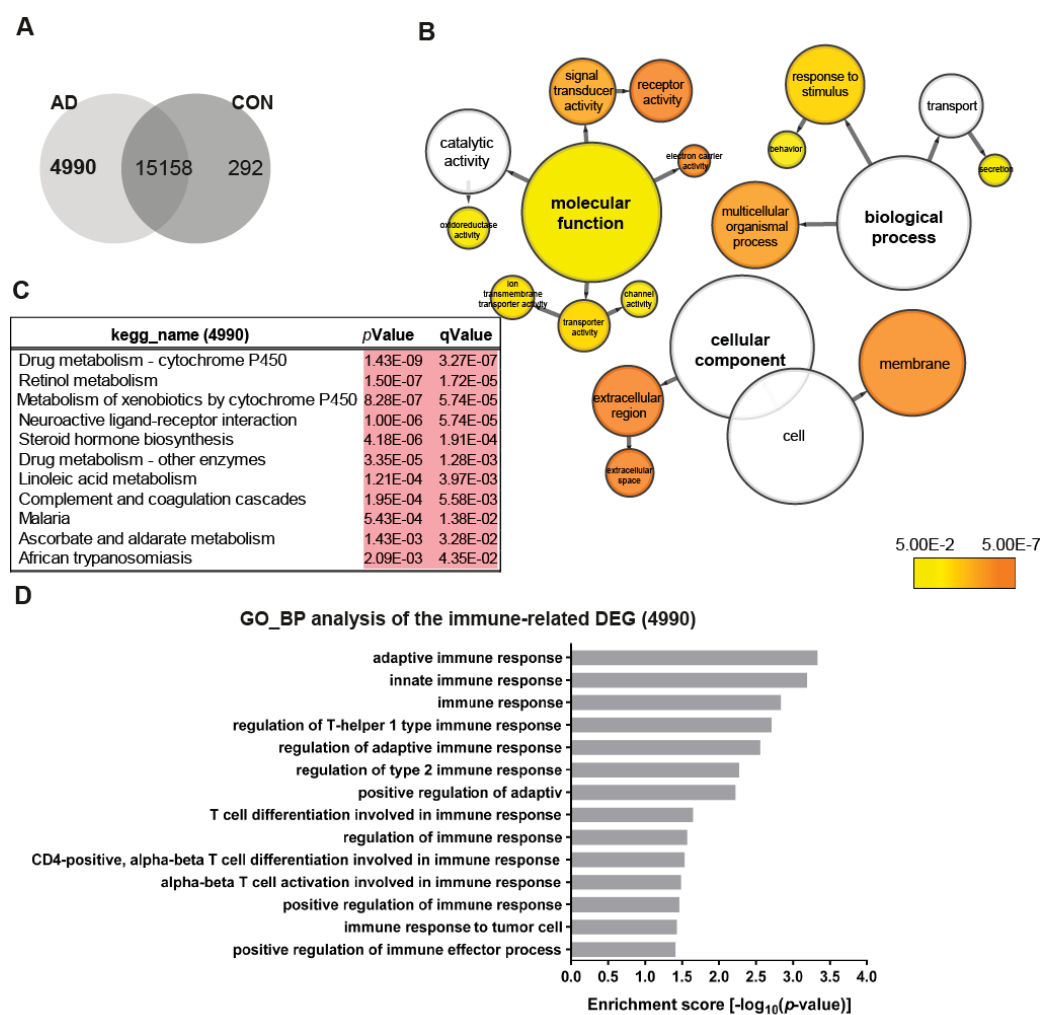


Figure 2. Distinct gene expression profiles associated with AD neuronal networks. **(A)** Venn diagram illustrating genes exclusively expressed in the AD neural network (4990), the control (CON) network (292) or common between both (intersection -15158) (detection p -value < 0.05). **(B)** BiNGO analysis of the differentially expressed genes (DEGs; 4990) exclusively expressed in the TREM2 neuronal network (4990). The orange color of the circles correspond to the level of significance of the over-represented gene ontology (GO) category and the size of the circles is proportional to the number of genes in the category (p -value < 0.05). **(C)** Kyoto Encyclopedia of Genes and Genomes (KEGG) pathway analysis of the genes exclusively expressed in the AD neuronal network (4990). **(D)** Significantly enriched gene ontology (GO) terms (biological processes) of the genes exclusively expressed in the AD neuronal network (4990) associated with immune system processes (p -value < 0.05).

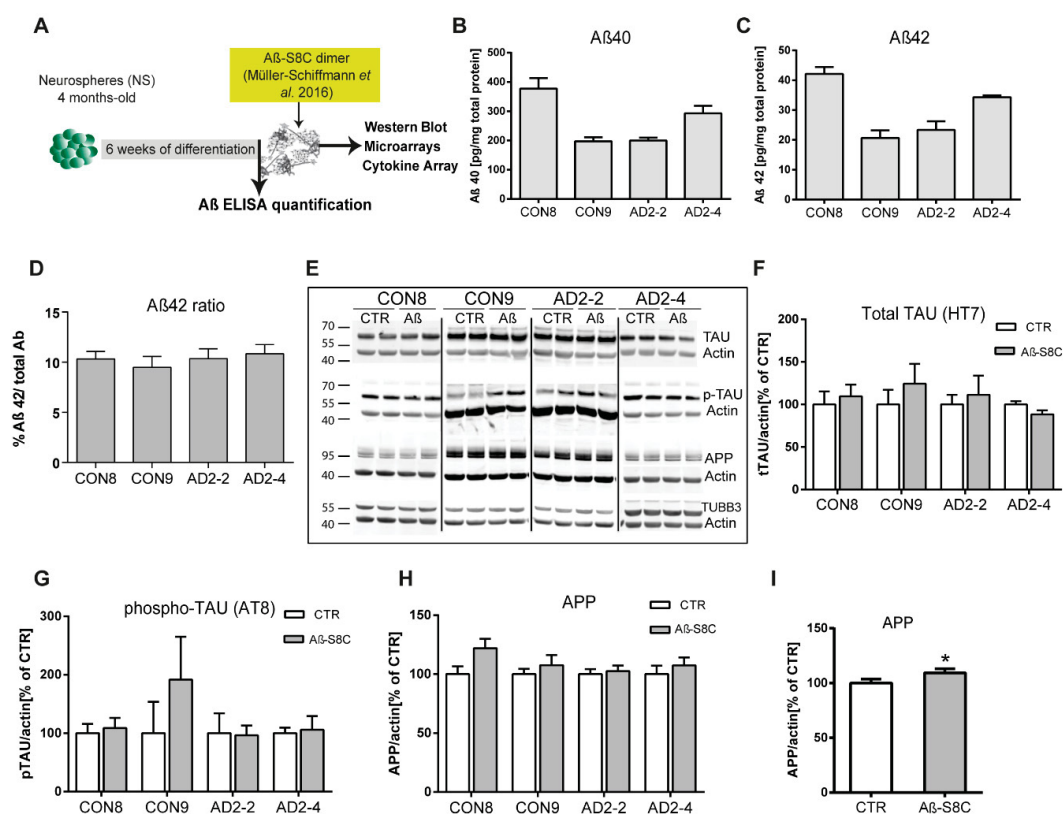


Figure 3. Stimulation of iPSC-derived neuronal cultures with the A β -S8C dimer. (A) Scheme illustrating the approach. Neurospheres were maintained for 4 months in culture, dissociated into single cells, differentiated for 6 weeks then stimulated with 500 nM of A β -S8C dimer for 72 h. Western blotting, microarrays and cytokine arrays were performed. (B–D) ELISA quantification of (B) total A β 40, (C) total A β 42 levels and (D) A β 42/A β 40+42 ratio from media collected from the interneuronal network and normalized to the total protein content. All data are presented as mean \pm SEM from six independent experiments. (E) Representative Western blot images of endogenous TAU, phosphorylated TAU (Ser 202 and Thr 205), APP and the neural differentiation marker β III-Tubulin after stimulation with 500 nM of the A β -S8C dimer. β -ACTIN was used as a loading control. (F–H) Quantification of (F) total TAU, (G) phosphorylated TAU and (H) APP levels. Results are normalized against β -ACTIN and shown as a percentage of control (CTR). All data are presented as mean \pm SEM from 3 independent experiments. (I). Effect of the A β -S8C dimer on APP levels in iPSCs derived neuronal network (CON8, CON9, AD2-2 and AD2-4) compared to control. Data are presented as mean \pm SEM from 3 independent experiments from 4 biological replicates. * $p < 0.05$, one-tail t-test versus control.

2.4. The A β -S8C Dimer Induces Metabolic Dysregulation in AD Neuronal Cultures

To assess the impact of the A β -S8C dimer on the gene expression profiles of CON and AD iPSC-derived neuronal cultures, we performed transcriptome analysis of CON8 and AD2-4 iPSC-derived neuronal cultures before and post stimulation with the A β -S8C dimer. This analysis identified differential expressed genes (DEGs) between the control and A β -S8C dimer treatment. Hierarchical cluster analysis revealed a clear separation of CON8 and AD-TREM2-4 iPSC-derived neuronal cultures (Figure 4A). Remarkably, CON8_A β clustered separately from AD2-4_A β , therefore implying that genetic background effects were more pronounced than the response elicited by the A β -S8C dimer.

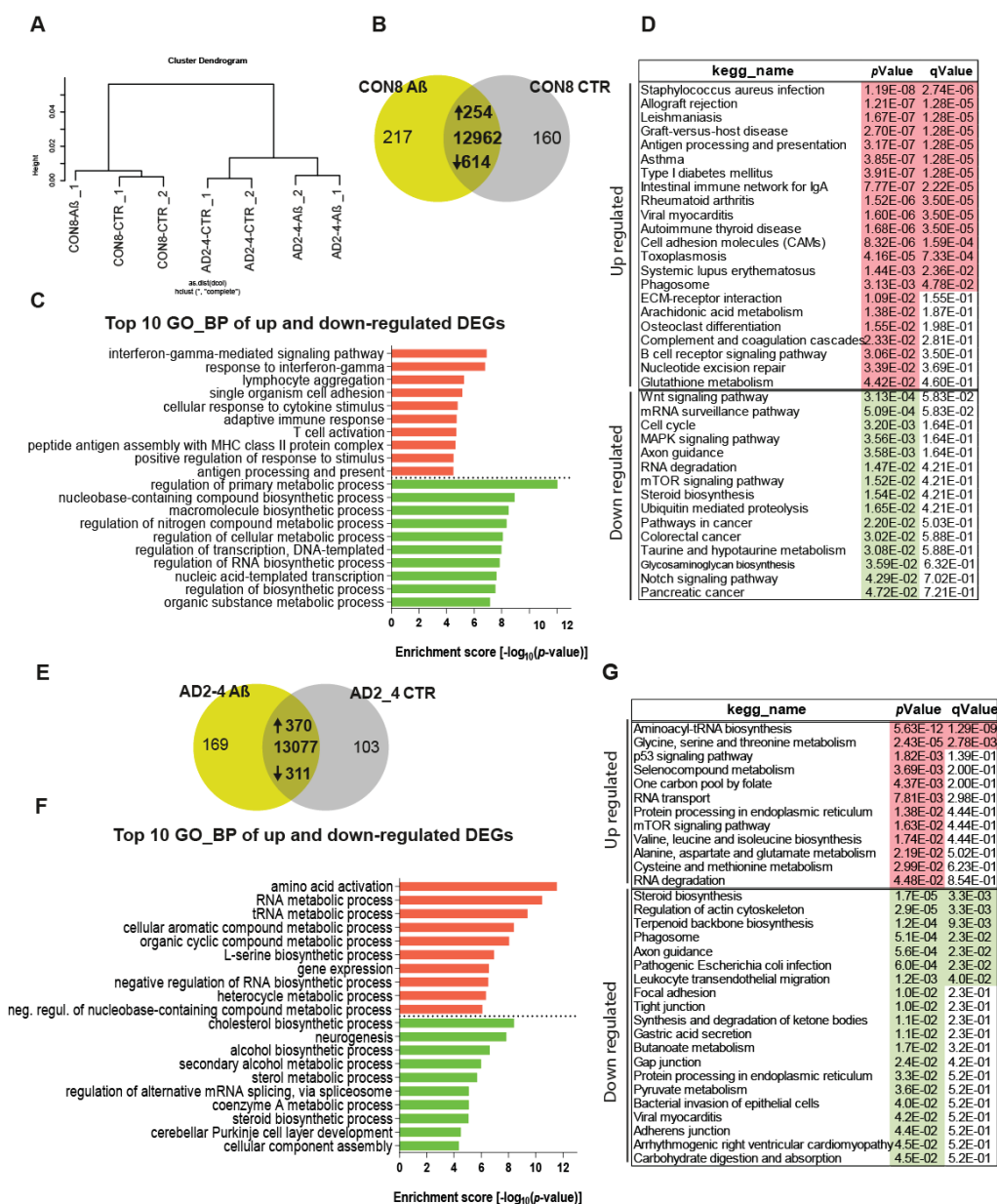


Figure 4. Gene expression profiles of the CON8 and AD2-4 neuronal cultures stimulated with the A β -58C dimer. (A) Dendrogram obtained by hierarchical cluster analysis of microarray-based (Affymetrix) gene expression data for CON8 and AD2-4 stimulated with the A β -58C peptide. Transcriptomes of CON8-CTR cluster with CON8-AB while those of the AD2-4-CTR cluster separately with TREM2-4-AB. (B) Venn diagram showing genes expressed only in the CON8 neuronal network subjected to A β -58C peptide stimulation (green), the control condition (grey) and common to both conditions (intersection; detection p value < 0.05). (C) Top 10 significantly enriched gene ontology (GO) terms for biological processes of DEGs upregulated (254-red) and downregulated (614-green) subjected to A β -58C peptide stimulation in CON8 neuronal cultures (p -value < 0.05). (D) KEGG enrichment analysis of up- and downregulated DEGs (p -value < 0.05). (E) Venn diagram showing genes expressed only in the AD2_4 neuronal culture when stimulated with the A β -58C peptide (green), the control condition (grey) and common to both conditions (intersection; detection p value < 0.05). (F) Top 10 significantly enriched gene ontology (GO) terms for biological processes of DEGs upregulated (370-red) and downregulated (311-green) subjected to A β -58C peptide stimulation in the AD2_4 neuronal cultures (p -value < 0.05). (G) KEGG enrichment analysis of up- and downregulated DEGs (p -value < 0.05).

Evaluation of DEGs in CON8 neuronal cultures before and after stimulation with the A β -S8C dimer identified 868 genes (Figure 4B), 254 were upregulated and 614 downregulated (Table S1). Figure 4C shows the related Top10 GO BP (biological processes) terms. Upregulated genes in CON8_A β were significantly enriched for GO terms such as interferon-gamma-mediated signaling pathway and cellular response to cytokine stimulus. In contrast, the downregulated genes in CON8_A β in comparison to control were associated with the GO terms, regulation of primary metabolic processes and regulation of RNA biosynthetic process. In agreement with the GO analysis, KEGG pathway analysis for the same set of genes revealed the upregulated genes in CON8_A β to be associated in pathways related to inflammatory responses, for example, *Staphylococcus aureus* infection and antigen processing and presentation. In addition, CON8_A β also showed upregulation of the phagosome pathway, while Wnt signaling pathway and axon guidance were among the downregulated KEGG pathways (Figure 4D, Table S1).

Focusing on AD neuronal cultures, 681 DEGs were identified when comparing A β -S8C dimer stimulated and non-stimulated AD2-4 neuronal cultures (Figure 4F), of these 370 were upregulated and 311 downregulated (Table S2). Figure 4F lists the Top 10 GO BP terms. The upregulated genes in AD2-4_A β were significantly enriched for amino acid activation and RNA metabolic process. In contrast, the downregulated genes were associated amongst others with cholesterol biosynthetic process and neurogenesis. KEGG pathway analysis revealed upregulation of pathways such as glycine, serine and threonine metabolism, p53 signaling pathway and mTOR signaling pathway. Surprisingly, in contrast to CON8_A β , AD2-4 neuronal cultures stimulated with A β -S8C dimers showed down-regulation of the phagosome pathway (Figure 4G, Table S2). Taken together, these results imply that the AD2-4 neuronal cultures respond in a unique way to A β -S8C dimer stimulation, namely a metabolic dysregulation in contrast to an inflammatory response, which could be observed in the CON8 neuronal cultures.

2.5. A β -S8C Dimer Stimulation of the AD Neuronal Culture Revealed Indications of Impaired Phagocytosis-Related Pathway

TREM2 is crucial for regulating phagocytosis in microglia and the effect in phagocytosis by the AD-associated *TREM2* mutations have recently been a focus of studies [58–63]. As described above, phagocytosis appeared as a significantly upregulated pathway in CON8 but was downregulated in AD2-4 neuronal cultures after A β stimulation. We then analyzed differential expression of genes associated with this pathway. Figure 5A depicts the KEGG annotated phagosome pathway with upregulated genes in CON8_A β (red) and those downregulated in AD2-4_A β (green). After stimulation with the A β -S8C dimer, CON8 induced upregulation of *HLA-DMA*, *HLA-DMB*, *HLA-DOA*, *HLA-DPB1*, *HLA-DQA1*, *HLA-DQB1*, *HLA-DRB1* and *HLA-F*, all genes associated with the Major Histocompatibility complex II (MHCII). In contrast to the AD2-4 non-stimulated cultures, stimulation with the A β -S8C dimer induced down-regulation of *TUBB4A*, *TUBB4B*, *DYNC1H1*, *LAMP2*, *ATP6V1A*, *ACTB*, *THBS1*, *CALR* and *TUBBA1C*. Table S3 shows the relative mRNA expression, from which the expression of *CALR*, *DYNC1H1*, *LAMP2*, *HLA-DOA* and *HLA-DQB1* was confirmed by RT-PCR (Figure 5B). Taken together, these results suggest that neuronal cultures harboring the *TREM2* R47H variant but not controls likely undergo an impaired phagocytosis response in the presence of the A β -S8C dimer.

2.6. AD Neuronal Cultures Show a Compromised Inflammatory Response-Related Gene Expression Pattern upon Stimulation with the A β -S8C Dimer

Based on the fact that dysregulated cytokine production from microglia, astrocytes and neurons are associated with the development of AD [64], we analyzed the cytokine expression profile as well as the secretion profile from the AD neuronal cultures after stimulation with the A β -S8C dimer. Employing microarray-based global gene expression data, a heatmap-based analysis of 100 key cytokines (extracted from the Proteome Profiler Human XL Cytokine Array, R&D systems) revealed that stimulation with the A β -S8C dimer induced transcriptional changes in a subset of these genes in AD-TREM2-4 (Figure 6A). Interestingly, the AD2-2 neuronal culture showed down-regulation of

cytokines, chemokines and acute phase genes such as *IL1RL1*, *IL13*, *IL15*, *IL16*, *IL27*, *IL32*, *CXCL10*, *CXCL11*, *TFRC*, *SERPINE1*, *C5*, *THBS1*, *RLN2*, *SPP1*, *EGF*, *LIF*, *GC*, *BSG*, *MPO*, *CST3*, *FLT3LG* and *CCL20*. Surprisingly, only *IGFBP2*, *RBP4*, *VEGFA*, *CXCL5*, *IL19* and *TDGF1* had higher expression levels after A β -S8C dimer stimulation when compared to the control samples. We next aimed at determining if stimulation with the A β -S8C dimer could also alter the secretion of cytokines and chemokines in the AD neuronal cultures. To this end, we collected the cell culture supernatants from the AD2-2 and AD2-4 neuronal cultures 72 h post stimulation with the A β -S8C dimer and from non-stimulated controls. Thereafter, we carried out secretome analysis employing the proteome profiler cytokine array (Figure 6B). In agreement with the previous results, the level of secretion of all cytokines and chemokines decreased after A β -S8C dimer stimulation when compared to control (Figure 6C), with the exception of ICAM-1, MIF and SerpinE1. Taken together, these results might imply that AD neuronal cultures compromise the efficient activation of the inflammasome pathway in response to A β -S8C dimer stimulation.

2.7. A Protein–Protein Interaction (PPI) Network Identifies an AD-Depended A β -S8C Signature

To gain insights into a probable gene expression signature triggered by the A β -S8C dimer in LOAD, we focused on genes exclusively expressed in the AD neuronal culture after stimulation with the A β -S8C dimer. A Venn diagram analysis revealed that most (12687) genes were expressed in common between CON and AD with and without A β -S8C dimer stimulation (Figure 7A, Table S4). However, 95 genes were exclusively expressed in AD neuronal cultures stimulated with A β -S8C dimer. GO analysis (Figure 7B) unveiled several terms related to neuron and immune-system related processes including stimulatory C-type lectin receptor signaling pathway as most significant. Pathway analysis of the 95 AD A β -S8C genes (Figure 7C) revealed neuroactive ligand-receptor interaction as the most significant pathway and metabolic pathways with the higher number of genes. The 95 genes were further analyzed in a protein–protein interaction network (PPI) based on interactions from the BioGrid database resulting in a network containing APP and a big hub centered around *HSPA5*, which encodes the endoplasmic reticulum chaperone BiP (Figure 7D). *HSPA5* has been reported to control the activation of the unfolding protein response (UPR), a pro-survival pathway in response to ER stress caused by misfolded proteins. Since there is evidence that the ER stress response, namely the UPR plays a role in the pathogenesis of AD [65], we took a deeper look into the GO terms related to ER after A β -S8C dimer stimulation (Table S2, highlighted in yellow). We observed that the A β -S8C dimer triggered an ER stress response, which elevated the expression of *ATF3* and *DDIT* in both CON and AD. Interestingly, the ER stress response was more prominent in the AD neuronal cultures, where several genes from the UPR were upregulated (*XBP1*, *AT4*, *PUMA* and *HERPUD1*) in contrast to *HSPA5* and *CALR*, which were downregulated (Figure 8, Table S5). These results highlighted the unique response triggered by the A β -S8C dimer in the AD neuronal cultures. By generating a PPI network we were able to link the A β -S8C signature genes to ER-stress, namely the activation of UPR.

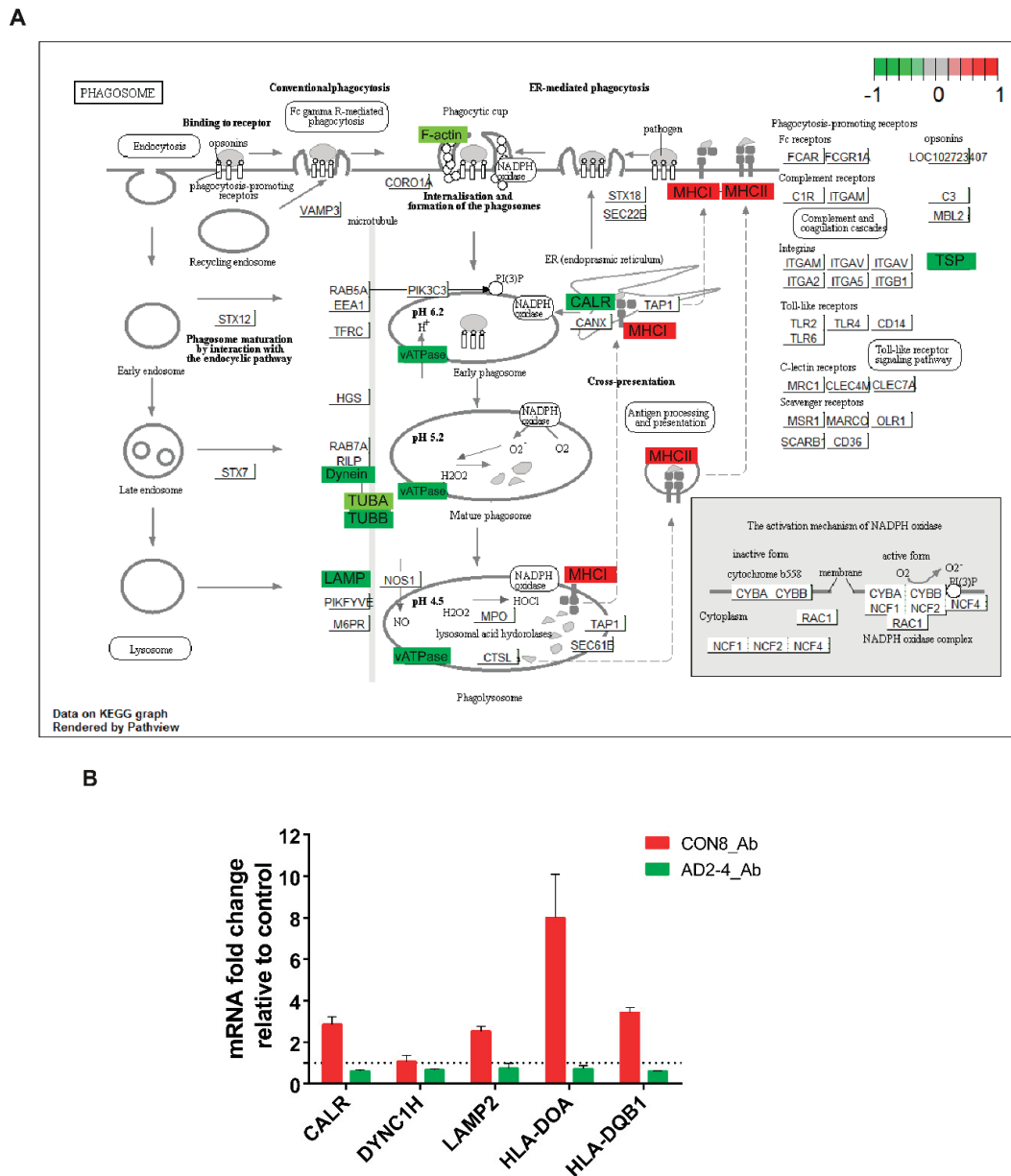


Figure 5. Representation of the KEGG phagosome pathway. (A) Upregulated DEGs genes in response to A β -S8C peptide stimulation in CON8 neuronal cultures are shown as red boxes and downregulated DEGs in AD2-4 neuronal cultures are shown as green boxes. (B) Relative gene expression of *CALR*, *DYNC1H1*, *LAMP2*, *HLA-DOA* and *HLA-DQB1* analyzed by RT-PCR. Data are presented as mean \pm SEM from two independent experiments.

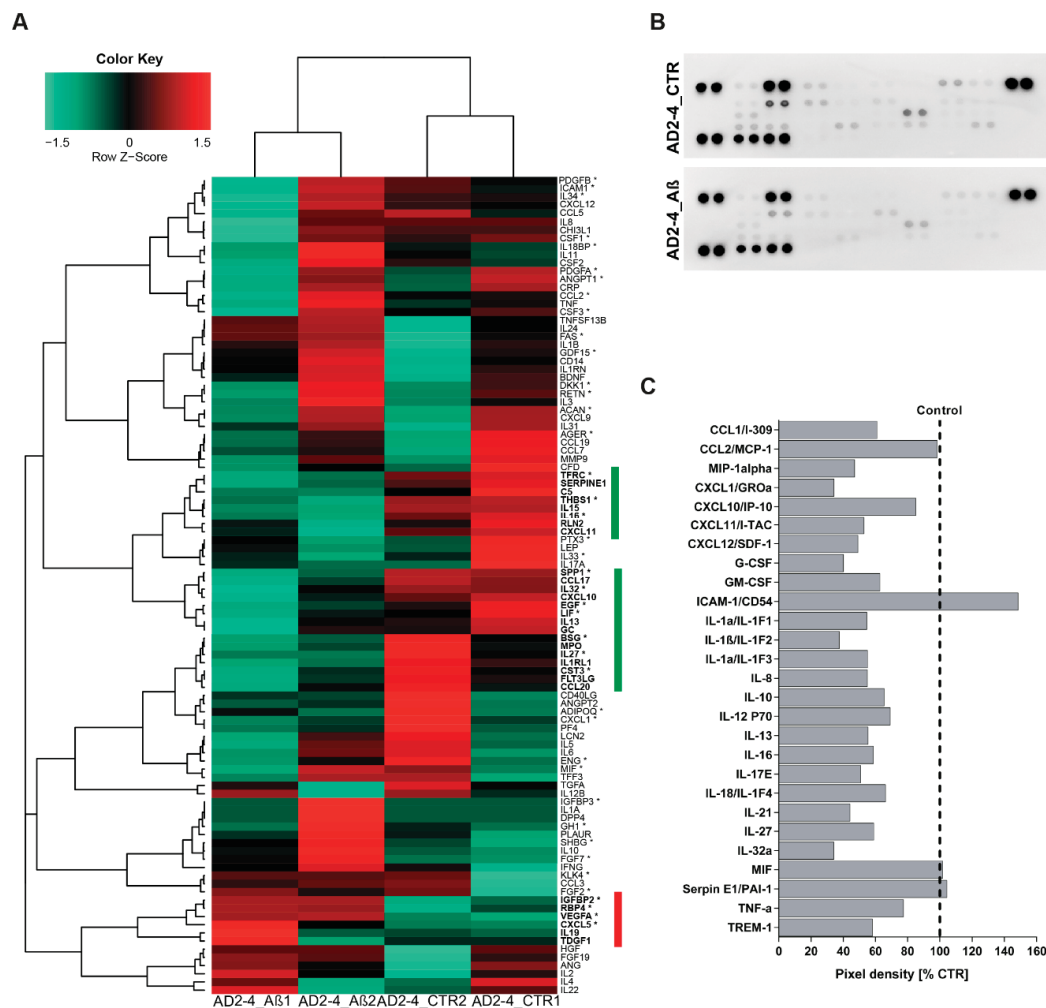


Figure 6. Analysis of cytokine expression and secreted factors in AD neuronal cultures upon A β -S8C stimulation. **(A)** Heatmap of Pearson correlation analysis of microarrays data from AD neural differentiation under A β -S8C stimulation (AD2-4_A β 1 and AD2-4_A β 2) or control (AD2-4_CTR1 and AD2-4_CTR2) showing the differential expression of cytokines. The highlighted genes in green represent a cluster of cytokines downregulated upon A β -S8C stimulation whereas the highlighted genes in red represent an upregulated cluster of cytokines. **(B)** Human cytokine array showing the effect of the A β -S8C peptide on the secreted factors of neuronal cultures from pooled AD2-2 and AD2-4 culture supernatants of control condition and 72 h of A β -S8C stimulation. **(C)** Quantitative analysis of the secreted factors shows that A β -S8C treatment decreases the amount of secreted cytokines in AD neuronal cultures.

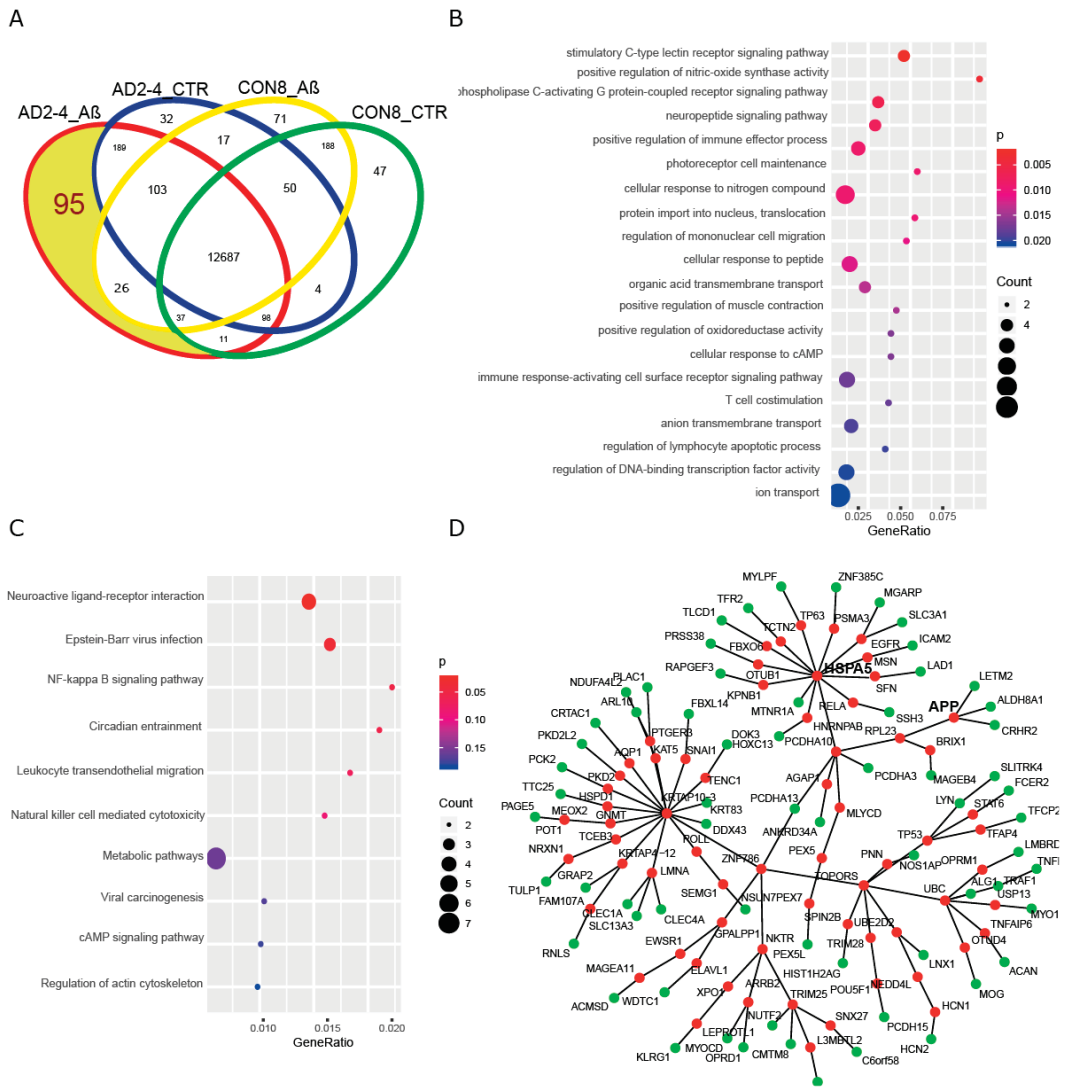


Figure 7. Aβ-S8C stimulated AD neuronal cultures activate a protein-protein interaction network, which includes APP and HSPA5. **(A)** Venn diagram dissecting 95 genes expressed in Aβ-S8C stimulated AD neuronal cultures from genes expressed in AD control and healthy neuronal cultures with and without Aβ-S8C stimulation. **(B)** Dot plot of gene ontologies (biological process) overrepresented in the 95 AD_Aβ genes. **(C)** Dot plot of KEGG pathways overrepresented in the 95 AD_Aβ genes. **(D)** Protein–protein interaction network derived from the 95 AD_Aβ genes with APP and HSPA5. Nodes from the 95 genes are colored green and the nodes added using the Biogrid database to connect the network are colored red.

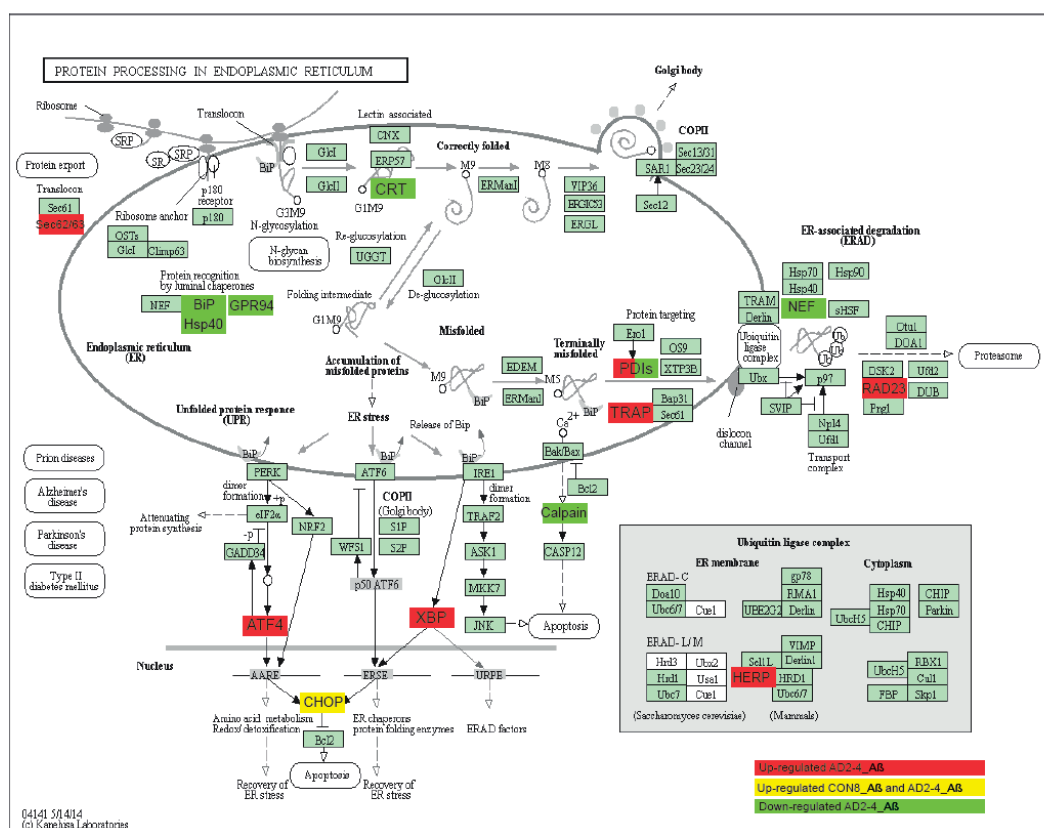


Figure 8. Representation of the KEGG protein process in endoplasmic reticulum pathway. Upregulated DEGs genes in response to $A\beta$ -S8C stimulation in AD2-4 neuronal cultures are shown as red boxes, upregulated DEGs genes in response to $A\beta$ -S8C stimulation in CON 8 and AD2-4 neuronal cultures are shown in yellow boxes and downregulated DEGs in AD2-4 neuronal cultures are shown as green boxes.

3. Discussion

While the mechanisms underlying the etiology of AD have been a focus of study over several decades, the current knowledge about the etiology and pathogenesis of AD are still incomplete. The use of primary neurons from animal models and immortalized cell lines based on modifications in *APP*, *PSEN1* and *PSEN2* has provided some insights into EOAD. While these models are helpful for studying a specific causal mutation (EOAD), there are several hurdles and limitations associated with studying LOAD, which requires the endogenous expression of genetic mutations and their genetic interactions. Understanding the biological implications of the recently identified genetic risk variants, namely the R47H substitution in *TREM2*, is essential to enable the establishment of genotype–phenotype correlations, which can lead to potential novel therapeutic approaches. The breakthrough development of iPSCs technology provides the most applicable tool to create an in vitro sporadic patient-derived model. Although modeling AD using patient-derived iPSCs has been prominent, a handful of studies to date have generated and characterized iPSC-derived neuronal cultures from LOAD patients [32,33,35,37,38]. This is the first study describing the generation and characterization of a model of LOAD based on $A\beta$ dimer stimulated neuronal cultures originating from lymphoblast-derived iPSCs derived from LOAD patients carrying the missense mutation R47H in *TREM2*.

First, we differentiated the iPSCs to neurons using a modified protocol described by Liu et al., 2013 and analyzed the distinct progression steps during the differentiation process. Transcriptome analysis and immunocytochemistry confirmed the ability of our modified protocol to derive neurons and glia cells within our neuronal cultures. Based on gene expression comparison between the iPSC-neuronal

cultures with commercially bought fetal, adult and AD brain RNA we could show that our cells expressed the expected maturation markers. Thus, our results imply that lymphoblast-derived iPSCs from LOAD patients and healthy donors can be robustly differentiated into neuronal cultures. Moreover, we did not observe profound differences in the differentiation and maturation propensity between iPSCs derived from LOAD patients and healthy donors, in agreement with previous reports [33,35,37,38]. Cheng-Hathaway et al. and Sudom et al. reported that *Trem2* R47H knock-in mice showed reduced *Trem2* mRNA and protein expression in the brain as well as reduced soluble fragments of Trem2 (sTrem2) in plasma [66,67]. More recently, Xiang et al. reported that a mouse-specific splicing caused this reduction and *TREM2* mRNA levels were normal in both iPSC-derived microglia and in patient brains with the *TREM2* R47H variant [68]. We therefore evaluated if *TREM2* expression was different in LOAD patients carrying the *TREM2* R47H variant compared to the control. Our results indicate that *TREM2* mRNA was significantly upregulated in AD2-2 but not in the AD2-4 neuronal cultures compared to the control. This ambiguity is probably due to the limitations imposed by our small sample size. In addition, our neuronal culture is composed mainly of neurons so the *TREM2* positive cells are in low abundance.

Although the neuronal cultures derived from LOAD patients and healthy donors did not exhibit differences in morphology or expression of differentiation markers, transcriptome analysis showed a distinct profile. Interestingly, GO analysis revealed that the proteins encoded by the 4990 genes exclusively expressed in AD neuronal cultures were predominantly mapped in the cell membrane and in the extracellular space. These genes were involved in (i) biological processes (BP) terms such as response to stimulus and secretion and (ii) molecular functions (MF) terms such as signal transducer activity, receptor activity, transporter activity, channel activity and ion transmembrane transporter activity. As part of these exclusively expressed genes we also identified genes of the matrix metalloproteinases (MMPs) family, for example *MMP2* and *MMP9*. Metalloproteinases play an important role in the pathogenesis of AD. While *MMP2* might have a protective role, *MMP9* expression, which is increased in AD patients, is induced by A β and it can influence TAU aggregation [69]. Furthermore, members of the ATP-binding cassette (ABC) and the solute carrier (SLC) families were over-represented in the GO_MF. ABC transporters have been implicated in AD pathophysiology, associated with processes leading to the accumulation of A β in the CNS. Importantly, we observed the exclusive expression of GLUT4 (*SLC2A4*), a crucial insulin sensitive glucose transporter upregulated in AD patients, which is responsible for regulating glucose metabolism in neurons [70,71]. As anticipated, we also identified GO terms related to the regulation of the innate and adaptive immune response as significantly enriched. Implications of these results are that our AD neuronal cultures show a distinct signal transducer and transporter activity that may contribute to metabolic alterations, to an inadequate immune response and ultimately to neurotoxicity. According to the amyloid cascade theory, accumulation of A β plays a key role in triggering the cascade of events underlying the pathogenesis of EOAD. However some studies have shown that A β secretion is not altered in LOAD-derived neurons [37,72]. In accordance, our results show that AD cultures secreted A β with a similar A β_{1-42} to A β_{1-40} ratio as the control. Nonetheless, the levels of A β_{1-40} and A β_{1-42} were highly reproducible across multiple differentiations (six) and lines (four), thus establishing our cell culture model as robust for manipulating the production of A β . We subsequently aimed at evaluating the potential effect of A β in our neuronal cultures in order to close the gap in our understanding of the mechanisms that are underlying the early stages of AD. A β -S8C dimer can induce neurotoxicity and abnormal synaptic signaling, together with impaired cognitive functions in the absence of plaque pathology, thus mimicking the early stages of AD [55]. A β -induced TAU hyper-phosphorylation has been described to initiate the signaling cascade alterations that culminate in NFT formation and neuronal degeneration [73]. Phosphorylation of the AT8 epitope (Ser202/Thr205) has been found to be elevated in sAD-derived neurons [37]. We were not able to detect an increase in phosphorylation of TAU at Ser202/Thr205 upon A β -S8C dimer treatment. In addition, there were no differences in the levels of phosphorylation detected between control and AD neuronal cultures in the non-stimulated conditions. TAU can be phosphorylated on more than 80 residues,

and it is known that Ser422 is phosphorylated earlier than Ser202/Thr205 during NFTs formation [74]. Based on these facts and the results obtained, we can assume that the duration of incubation of the A β -S8C dimer was presumably not long enough to detect increased phosphorylation at Ser202/Thr205. Our results show that independent of the genetic background, incubation with the A β -S8C dimer increased the levels of total APP. A more in-depth analysis of APP processing will provide more insights into the pathogenic role of the *TREM2* R47H variant in EOAD.

In addition to interfering with total APP levels, A β -S8C dimer stimulation induced a remarkable and significant transcriptome change in the control as well as in the AD neuronal cultures. Annotation and enrichment analysis revealed that the upregulated DEGs induced by A β -S8C stimulation in the control neuronal cultures are related to immune system activation (interferon-gamma-mediated signaling pathway, cellular response to cytokine stimulus and adaptive immune response). A β soluble species have also been linked to an attenuation of the Wnt signaling pathway, in addition to putative effects on cell cycle, contributing to synaptic dysfunction and neurodegeneration. In accord, our data revealed that Wnt signaling and cell cycle were downregulated after A β -S8C stimulation in the control neuronal cultures. On the contrary, the AD neuronal cultures responded in a completely different manner to stimulation with the A β -S8C dimer.

The effect of the AD-associated *TREM2* mutations on phagocytosis is an active area of study but so far variable results have been obtained. While R47H transduced HEK cells displayed a reduced up-take of latex beads and A β_{1-42} , no changes were observed in the fluorescent pH-sensitive rhodamine *Escherichia coli* (pHrodo-linked *E. coli*) uptake assay [61]. Additionally, *TREM2*^{+R47H} transdifferentiated microglia-like cells [58] and microglia-like cells derived from *TREM2* T66M^{+/-}, T66M^{-/-} and W50C^{-/-} hPSCs, also showed no defects in the *E. coli* uptake [59,63]. However, Piers et al. showed that iPSC-derived microglia harboring the *TREM2* R47H mutation exhibit a substantial deficit in the ability to phagocytose β -Amyloid [75]. We found that the control neuronal cultures upregulated the phagosome pathway after A β -S8C stimulation, namely the genes associated with MHCII. These observations are in line with previous reports where incubation with A β led to an accumulation of MHC-II and AD patients also showed upregulation of MHC-II [76]. On the contrary, these genes were not differentially regulated in our AD neuronal cultures, but interestingly other genes associated with the phagosome pathway were downregulated. Calreticulin is encoded by the *CALR* gene. It is an endoplasmic reticulum protein that interacts with A β , and is considered as a scavenger for A β_{1-42} [77]. Low levels of calreticulin have been observed in AD brains, and it has been suggested that this down-regulation can lead to the pathological processes of AD [78]. Notably, the levels of tubulins *TUBB4A* and *TUBB4B* were downregulated, supported by Hondius et al., where the levels of these tubulins identified by mass spectrometry analysis in human post-mortem brain tissue were significantly decreased over the progressive stages of AD [79]. On the other hand, lysosome-associated membrane protein 2 (LAMP-2) together with other lysosome-related proteins was found to be increased in CSF from AD patients [80]. Interestingly, *LAMP2* was downregulated in our AD neuronal cultures leading us to speculate that R47H AD carriers have a unique response to phagocytosis, probably due to the partial loss of function of *TREM2* activity.

The analysis of pro-inflammatory cytokines at the levels of mRNA and the secretome of the AD neuronal cultures in response to A β -S8C stimulation are of particular interest. Although the mRNA expression of the *IL-1 β* , *IL-6*, *TNF- α* and *MIP-1 α* proinflammatory cytokines was upregulated in some of the samples, the secretion of these cytokines was downregulated. A recent study using iPSC-derived microglia-like cells from patients carrying the T66M and W50C missense mutation within *TREM2* showed that these cells have a deficit in the cytokine release [63]. Indeed, *SPP1* and *GPNMB*, encoding osteopontin and osteoactivin, were also downregulated in AD neuronal cultures and not in the control after A β -S8C stimulation. *SPP1* and *GPNMB* are microglia activation-related transcripts that are upregulated in AD models and associated with A β accumulation. In support of our data, it was recently reported that *SPP1* and *GPNMB* reflect *TREM2* signaling and the expression is highly sensitive to the R47H variant [26]. Interestingly, there was a cluster of genes associated with insulin

resistance, which was upregulated after A β -S8C stimulation. Increased levels of RBP4 were found in APP/PSEN1 mice and in insulin resistant humans [81]. Along the same track, it has been suggested that IGF2BP2 plays a role in AD progression [82]. Both of these genes were indeed upregulated in response to A β -S8C in our AD neuronal cultures, thus further lending credence to the fact that metabolic dysfunction plays an important role in the pathogenesis of AD. It is noticeable that A β -S8C triggers a unique response in AD neuronal cultures, when compared to the control. The creation of a PPI network between the exclusively expressed genes in the AD after A β -S8C stimulation revealed *HSPA5* as the core of the A β -S8C signature. *HSPA5*, a chaperone protein that upon accumulation of unfolded proteins controls the activation of the UPR sensors [65], was found down-regulated after A β -S8C in our AD TREM2 neuronal cultures. Katayama et al. found that *HSPA5* levels are reduced in the brains of AD patients [83]. Although A β -S8C stimulation upregulates *ATF3* and *DDIT3* (CHOP) in both CON and AD neuronal cultures, the prominent alteration in the UPR was observed in the AD TREM2 cultures with the upregulation of *XPB1*, *ATF4*, *BBC3*, *HERPUD1* and *CALR*. In support of our data, several studies have shown upregulation of the UPR in brain samples of AD patients [84,85]. According to Han et al. insufficient protein-folding homeostasis by UPR increases expression of *ATF4* and CHOP and initiates the ER-stress-mediated cell death, activating target genes involved in protein synthesis like aminoacyl-tRNA synthetases and RNA metabolic processes leading to oxidative stress and cell death [86]. Interestingly, biological processes related with increased protein synthesis such as amino acid activation and RNA metabolic process together with the KEGG pathway protein processing in the endoplasmic reticulum were upregulated in AD neuronal cultures. It seems that A β -S8C stimulation leads to the activation of the UPR that initially might be protective, however if the balance in proteostasis is not re-established, ER-stress-mediated cell death might mediate neurodegeneration in AD.

4. Materials and Methods

4.1. iPSC Lines

The iPSC lines derived from AD patients as well as control individuals without dementia used in this study have been characterized and published [40–43], as detailed in Table 1. All participants and/or their legal guardian provided written informed consent for participation in the study. Ethical approval was obtained by the Ethics Committee of the University Hospital Antwerp and the University of Antwerp (Approval number 13/15/161 obtained on 22 April 2013). AD patients were ascertained at the memory clinic of the ZNA Middelheim, Antwerpen, Belgium in the frame of a prospective study of neurodegenerative and vascular dementia in Flanders, Belgium. Ethnicity-matched healthy individuals were screened for neurological or psychiatric antecedents, neurological complaints and organic disease involving the central nervous system. Ascertainment and *TREM2* p.R47H genotyping are described in detail in [24]. iPSCs were maintained on Matrigel-coated (Corning, Bedford, MA, USA) plates in StemMACs culture medium (Miltenyi Biotec, Bergisch Gladbach, Germany). The medium was changed every day and the cells were passaged every 5–6 days using PBS without calcium and magnesium (Gibco, Life Technologies, Karlsruhe, Germany).

4.2. Neural Differentiation of the iPSC Lines

For the induction of GABAergic interneurons, iPSCs were differentiated using an embryoid body-based protocol [47] with modifications. On day 1, the iPS cells were harvested and recultivated in suspension in neural induction medium (NIM; DMEM/F-12 (Gibco, Life Technologies, Karlsruhe, Germany), 1% NEAA (Lonza, Basel, Switzerland), 1% N2 supplement (Gibco, Life Technologies, Karlsruhe, Germany), 2 μ g/mL of Heparin (Sigma-Aldrich, Steinheim, Germany) and 1% P/S) supplemented with 1 μ M purmorphamine (Tocris, Bristol, UK), a SHH agonist. At day 5 the formed aggregates, called embryoid bodies (EBs), were harvested and replated as adherent cells in the same medium and the same concentration of purmorphamine. From day 10 to 18, primitive

neuroepithelia structures were formed and neural rosettes were selected with STEMDiff Neural Rosette Selection reagent (Stem Cell Technologies, Vancouver, Canada) and recultured in suspension in NIM plus a B27 supplement (Gibco, Life Technologies, Karlsruhe, Germany; without retinoic acid) and 20 ng/mL of EGF and FGF2 (both PreproTech, Hamburg, Germany). After 10 days the cells maintained as aggregates (neurospheres) were dissociated into single cells with accutase (Gibco, Life Technologies, Karlsruhe, Germany) and replated on Matrigel (Corning, Bedford, MA, USA) for the final differentiation in neural differentiating medium (NDM; Neurobasal 1% NEAA, 1% N2 supplement and 1% P/S) supplemented with 1 μ M of cAMP (Thermo Fisher Scientific, Rockford, IL, USA) and 10 ng/mL of BDNF, GDNF and IGF-1 (all Immuno Tools, Friesoythe, Germany). The iPSC-derived neurons were cultivated for approximately 80 days.

4.3. Cryosection of Neurospheres

Neurospheres were fixed in 4% paraformaldehyde (PFA) for 30 min at room temperature, washed with PBS and cryoprotected in 30% sucrose in PBS overnight at 4 °C. Subsequently, these neurospheres were transferred into embedding medium (Tissue-Tek OCT Compound 4583, Sakura Finetek), snap-frozen on dry ice and stored at -80 °C. Neurospheres were cut into 10 μ m thin slides using a Leica CM3050 S cryostat (Leica Biosystems, Wetzlar, Germany).

4.4. Immunofluorescence Stainings

Cells were fixed with 4% paraformaldehyde for 15 min at room temperature (RT). Neurosphere slides were thawed, dried and rehydrated in PBS. Fixed cells and neurosphere slides were permeabilized with 0.2% Triton X-100 for 10 min and blocked with 3% BSA in PBS for 1 h. Samples were then incubated with the following primary antibodies overnight at 4 °C: mouse anti-PAX6 (1:1000, SySy, Goettingen, Germany # 153011), rabbit anti-Nestin (1:400, Sigma Aldrich, Steinheim, Germany #N5413), mouse anti-NKX2.1 (1:1000, Merck Millipore, Burlington, MA, USA #MAB5460), goat anti-SOX1 (1:200, R&D, Bristol, UK # MAB3369), mouse anti-FOXG1 (1:1000, Biozol, Eching, Germany # LS-C197226), mouse anti- β III-tubulin (1:200, Cell Signaling, Danvers, MA, USA #TU-20), rabbit anti-MAP2 (1:1000, SySy, Goettingen, Germany #188002), guinea pig anti-GFAP (1:500, SySy, Goettingen, Germany #173004), guinea pig anti-Synapsin 1 (1:500, SySy, Goettingen, Germany #106004), mouse anti-SMI-3 (1:2000, Biologend, San Diego, CA, USA #SMI-312R) and rabbit anti-GABA (1:1000, Sigma Aldrich, Steinheim, Germany #A2052). After washing with PBS, cells were then incubated with the appropriate secondary antibody conjugated with Alexa-488, Alexa-555 or Alexa-647 (1:500, Invitrogen, Thermo Fisher Scientific, Rockford, IL, USA) for 1 h at RT. The nuclear stain Hoechst 33258 (2 μ g/mL, Sigma-Aldrich, Steinheim, Germany) was added at the time of the secondary antibody incubation. Slices were mounted in ImmuMount (Thermo Fisher Scientific, Rockford, IL, USA) and fluorescent images were obtained by a LSM 700 microscope (Carl Zeiss AG, Jena, Germany), and analyzed in Adobe Photoshop software CS6 (Adobe, USA).

4.5. Immunoblotting of Lysates from A β -S8C Dimer Stimulated Cells

iPSC-derived neurons were differentiated for six weeks and then stimulated with 500 nM of oxidized S8C dimers [55] for 72 h. Cells were then washed three times with PBS and then lysed in PBS/1% NP40 + complete protease inhibitor cocktail (Sigma-Aldrich, Steinheim, Germany) and phosphatase inhibitor cocktail 2 (Sigma-Aldrich, Steinheim, Germany). Lysates were cleared by centrifugation at 20.000g for 10 min and quantified with the DC Protein assay Kit (Bio-Rad, Hercules, CA, USA). Of the lysates 25 μ g were then separated on NuPAGE 4-12% Bis-Tris gels (Invitrogen, Thermo Fisher Scientific, Rockford, IL, USA) and blotted to a 0.2 μ m nitrocellulose membrane for 2 h at 400 mA. The blots were blocked in PBS containing 5% skim milk and then probed with the following primary antibodies over night at 4 °C: mouse anti-total TAU (HT7, 1:1000, Thermo Fisher Scientific, Rockford, IL, USA#MN1000), mouse anti-phospho TAU Ser202/Thr205 (AT8, 1:1000, Thermo Fisher Scientific, Rockford, IL, USA#MN1020), rabbit anti-APP (CT15, 1:3500), rabbit anti- β actin (1:5000,

Sigma-Aldrich, Steinheim, Germany #A2066) and mouse anti β III-tubulin (1:1000, Cell Signaling, Danvers, MA, USA #TU-20). After washing the blots three times with PBS/0.05% Tween20 they were incubated with the appropriate secondary antibody: goat anti-mouse IRDye 680RD and 800CW as well as goat anti-rabbit IRDye 680RD and 800CW (all from LI-COR Biosciences, Lincoln, NE, USA). Following three times washing with PBS/0.05% Tween20 the fluorescent signals were quantified by applying the Odyssey infrared imaging system (LI-COR Biosciences, Lincoln, NE, USA).

4.6. Measurement of A β 1-40 and A β 1-42 by ELISA

A β 1-40 and A β 1-42 concentrations from cleared supernatants of differentiated iPSCs were quantified by using the Amyloid beta 40/42 Human ELISA Kits (#KHB3441 and KHB3481; Thermo Fisher Scientific, Rockford, IL, USA) according to the manufacturer's recommendations. Results were normalized to the protein concentration of the cells. The cells were washed three times with PBS and lysed in PBS/ 1% NP40. The protein content was then measured with the DC Protein assay Kit (Bio-Rad, Hercules, CA, USA).

4.7. RNA Isolation and Quantitative RT-PCR

Total RNA was extracted from cell lysates using Direct-zol RNA Mini Prep kit (Zymo Research, Freiburg, Germany) in combination with peqGOLD TriFast (PeqLab Biotechnologie, Darmstadt, Germany) according to the manufacturer's protocol. Of purified RNA 0.5 μ g was used for first-strand cDNA synthesis using TaqMan reverse transcription reagent (Applied Biosystems, Rockford, IL, USA). cDNA was used for subsequent PCR. Real-time quantification of genes was conducted for three independent cultures from each iPSC-derived interneuron line using the SYBR@Green RT-PCR assay (Applied Biosystems, Waltham, Massachusetts, USA). Primer sequences are provided in Table S6 (Primers were purchased from Eurofins Genomics). Amplification, detection of specific gene products and quantitative analysis were performed using a 'ViiA7' sequence detection system (Applied Biosystem, Waltham, Massachusetts, USA). The expression levels were normalized relative to the expression of the housekeeping gene RPS16 using the comparative Ct-method $2^{-\Delta\Delta C_t}$.

4.8. Generation of Deep Sequencing Data

Deep sequencing data of cDNA from iPSC-derived neuronal cultures were generated at the Neuromics Support Facility at the VIB- University Antwerpen Center for Molecular Neurology. Sequence libraries were constructed using QuantSeq 3' mRNA-Seq Library Prep Kit (Lexogen, Greenland, NH, USA). Sequencing was performed by Illumina NextSeq sequencing. Reads were single-end with a read length of 151. Samples from two independent experiments ($n = 4$ cell lines) were multiplexed onto the sequencing flow cell and the measured reads were demultiplexed for follow-up processing. Total RNA from human adult brain, human brain clinically diagnosed with AD and human fetal brain were purchased from BioChain[®], Newark, CA USA

4.9. Analysis of Deep Sequencing Data

The demultiplexed fastq files were aligned against the GRCh38 genome with the HISAT2 (version 2.1.0) alignment software [87] using options for clipping the 50 bases at the 3' end of each read. The exact HISAT2 command, which was mainly derived from the parameter optimizations of Barruzzo et al. [88], was:

```
hisat2 -p 7 -trim3 50 -N 1 -L 20 -i S,1,0.5 -D 25 -R 5 -mp 1,0 -sp 3,0 -x hisatindex/grch38 -U input.fastq.gz -S output.sam
```

The resulting BAM files were sorted by coordinates applying SAMtools software [89]. Reads were summarized per gene with the subread (1.6.1) featurecounts software [90] against the gencode.v22.annotation.gtf using parameter `-t exon -g gene_id`. Summarized reads were normalized in R using the voom normalization [91] algorithm from the limma package [92] filtering genes, which were expressed with CPM (counts per million) > 2 in at least two samples.

4.10. Analysis of Microarray Data

cDNA from iPSC-derived GABAergic interneurons from CON8 and AD-TREM2-4 untreated (CTR) and treated with A β -S8C dimer was subjected to hybridization in duplicates on the GeneChip PrimeView Human Gene Expression Array (Affymetrix, Thermo Fisher Scientific, Rockford, IL, USA) at the BMFZ (Biomedizinisches Forschungszentrum) core facility of the Heinrich-Heine University, Düsseldorf. Data analysis of the Affymetrix raw data was performed in the R/Bioconductor [93] environment using the package affy [94]. The obtained data were background-corrected and normalized by employing the robust multi-array average (RMA) method from the package affy. Hierarchical clustering dendrograms and heatmaps were generated using the heatmap.2 function from the gplots package with Pearson correlation as similarity measure and color scaling per genes [95]. Expressed genes were compared in Venn diagrams employing package VennDiagram [96]. Gene expression was assessed with a threshold of 0.05 for the detection-*p*-value, which was calculated as described in the supplementary methods in Graffmann et al. [97]. The datasets generated and analyzed during the current study are available in the GEO repository (<https://www.ncbi.nlm.nih.gov/geo/>) under the accession number GSE143951.

4.11. Protein Interaction Network

A protein interaction network was constructed from the set of 95 genes expressed exclusively in A β -S8C stimulated TREM2 neurons in the Venn diagram analysis. Interactions associated with *Homo sapiens* (taxonomy id 9606) were filtered from the Biogrid database version 3.4.161 [98]. From this dataset interactors and additionally interactors of these interactors starting at the proteins coded by the above-mentioned set of 95 genes were extracted. The resulting complex network was reduced by searching the shortest paths between the original set via the method get.shortest.paths () from the R package igraph [99]. The protein network consisting of these shortest paths was plotted employing the R package network [100] marking proteins from the original set in green and inferred proteins in red.

4.12. Gene Ontology and Pathway Analysis

Based on the set of 95 genes expressed exclusively in A β -S8C stimulated TREM2 neurons in the Venn diagram analysis over-represented gene ontology terms and KEGG (Kyoto Encyclopedia of Genes and Genomes) pathways [101] were determined. The hypergeometric test was used for over-representation analysis—in the version from the GOstats package [102] for GO terms and the version from the R base package for KEGG pathways, which had been downloaded from the KEGG database in March 2018. Dot plots of the most significant GO terms and KEGG pathways were done via the function ggplot() from the R package ggplot2 indicating *p*-values from the hypergeometric test on a red-blue color scale, number of significant genes in the dedicated pathway (G) by the size of the dots and ratios of the number of significant genes in the dedicated pathway/GO to the total number of genes in that pathway/GO on the x-axis.

4.13. Human Cytokine Array

The secretion of cytokines in AD neuronal cultures before and after stimulation with the A β -S8C dimer was measured employing the Proteome Profiler Human Cytokine Array kit (R&D System, USA). The assay was performed following the manufacturer's instructions. Briefly, AD2-2 and AD2-4 cell culture supernatants from control and 72 h of A β -S8C dimer stimulation were collected, pooled and mixed with a cocktail of biotinylated detection antibodies for further incubation in a nitrocellulose cytokine array membrane with the immobilized capture antibodies spotted in duplicates. Chemiluminescent detection of the streptavidin-HRP secondary antibody was performed and the average signal (pixel density) was determined for the pair of duplicate spots using Image J (U.S. National Institutes of Health, Bethesda, Maryland, MD, USA). The relative change in cytokine levels

was performed comparing the intensity of the spots in the A β -S8C dimer stimulated membrane with the control membrane, which was set to 100%.

4.14. Statistical Analysis

Statistical analysis was performed with GraphPad Prism Software version 6.01 (GraphPad software, San Diego, CA, USA). For comparisons of the mean between two groups, one-tail Student's *t*-test was performed. One-way ANOVA was used for statistical significance analysis for comparisons of the mean among 4 groups, followed by a post hoc test with the use of Tukey's multiple comparison test. Statistical significance was assumed at $p < 0.05$. All data are expressed as mean \pm standard error of the mean (SEM).

5. Conclusions

Our established neuronal cultures using lymphoblast-derived iPSCs from patients harboring the R47H mutation in TREM2 is a relevant model for investigating the effect of this variant in the etiology of LOAD. Comparative global transcriptome analysis identified a distinct gene expression profile in AD neuronal cultures, further suggesting that these lines exhibit alteration in key signaling pathways related to metabolism and immune system in comparison to control, thus implying the partial loss of function of TREM2 due to the R47H substitution. In addition, stimulation with the A β -S8C dimer revealed metabolic dysregulation, impaired phagocytosis-related pathway and altered inflammatory responses. Furthermore, our data strongly suggests that the A β -S8C dimer signature seems to be centered in the ER-stress response. In conclusion, our AD in vitro model is capable of efficiently responding to signaling cascades associated with the AD pathogenesis and thus is a promising cellular tool for investigating the molecular mechanisms underlying LOAD. Additionally, this cellular model can facilitate the discovery of new AD biomarkers, enable toxicology studies as well as the identification of potential drug targets for future therapy of this devastating disease.

Supplementary Materials: Supplementary materials can be found at <http://www.mdpi.com/1422-0067/21/12/4516/s1>.

Author Contributions: Conceptualization: S.M. and J.A.; Methodology: S.M., A.M.-S., L.E., M.B.; Formal analysis: S.M., A.M.-S., W.W., J.A.; Data curation: W.W.; Investigation: S.M., A.M.-S., M.B.; Resources: K.S., C.V.B. and C.K.; Writing—original draft preparation: S.M.; Writing—review and editing: J.A., W.W., A.M.-S., K.S., C.V.B., C.K.; Supervision: J.A. All authors have read and agreed to the published version of the manuscript.

Funding: JA acknowledges support from the Medical Faculty, Heinrich-Heine-University, Düsseldorf. JA, KS and CVB are members of the EU project—AgedBrainSYSBIO. The AgedBrainSYSBIO project received funding from the European Union's Seventh Framework Program for research, technological development and demonstration under grant agreement no 305299. Research at the Antwerp site is supported in part by the University of Antwerp Research Fund.

Acknowledgments: We thank Friederike Schröter for helping with the neuronal differentiations. We also thank the Zentrum für Informations- und Medientechnologie (ZIM) at the Heinrich-Heine University for the computational support.

Conflicts of Interest: The authors declare no conflict of interest.

References

1. Patterson, C. World Alzheimer Report 2018 The state of the art of dementia research: New frontiers. *Alzheimer's Dis. Int.* **2018**. [[CrossRef](#)]
2. Prince, M.; Comas-Herrera, A. Dementia Fact Sheet. WHO. 2017. Available online: <https://www.who.int/news-room/fact-sheets/detail/dementia> (accessed on 27 May 2020).
3. Hardy, J.A.; Higgins, G.A. Alzheimer's disease: The amyloid cascade hypothesis. *Science* **1992**, *256*, 184–185. [[CrossRef](#)] [[PubMed](#)]
4. Polanco, J.C.; Li, C.; Bodea, L.G.; Martinez-Marmol, R.; Meunier, F.A.; Götz, J. Amyloid- β and tau complexity - Towards improved biomarkers and targeted therapies. *Nat. Rev. Neurol.* **2018**, *14*, 22–40. [[CrossRef](#)] [[PubMed](#)]

5. Hardy, J.; Selkoe, D.J. The amyloid hypothesis of Alzheimer's disease: Progress and problems on the road to therapeutics. *Science* **2002**, *297*, 353–356. [[CrossRef](#)]
6. Cacace, R.; Sleegers, K.; van Broeckhoven, C. Molecular genetics of early-onset Alzheimer's disease revisited. *Alzheimer's Dement.* **2016**, *12*, 733–748. [[CrossRef](#)]
7. Carmona, S.; Hardy, J.; Guerreiro, R. The genetic landscape of Alzheimer disease. *Handb. Clin. Neurol.* **2018**, *148*, 395–408.
8. Bettens, K.; Sleegers, K.; Van Broeckhoven, C. Genetic insights in Alzheimer's disease. *Lancet Neurol.* **2013**, *12*, 92–104. [[CrossRef](#)]
9. Farrer, L.A.; Cupples, L.A.; Haines, J.L.; Hyman, B.; Kukull, W.A.; Mayeux, R.; Myers, R.H.; Pericak-Vance, M.A.; Risch, N.; Duijn, C.M. van Effects of Age, Sex, and Ethnicity on the Association Between Apolipoprotein E Genotype and Alzheimer Disease. *JAMA* **1997**, *278*, 1349. [[CrossRef](#)]
10. Bickeböller, H.; Champion, D.; Brice, A.; Amouyel, P.; Hannequin, D.; Didierjean, O.; Penet, C.; Martin, C.; Pérez-Tur, J.; Michon, A.; et al. Apolipoprotein E and Alzheimer disease: Genotype-specific risks by age and sex. *Am. J. Hum. Genet.* **1997**, *60*, 439–446.
11. Harold, D.; Abraham, R.; Hollingworth, P.; Sims, R. Genome-wide association study identifies variants at CLU and PICALM associated with Alzheimer's disease. *Nat. Genet.* **2009**, *41*, 1008–1093.
12. Hollingworth, P.; Harold, D.; Sims, R.; Gerrish, A.; Lambert, J.C.; Carrasquillo, M.M.; Abraham, R.; Hamshere, M.L.; Pahwa, J.S.; Moskvina, V.; et al. Common variants at ABCA7, MS4A6A/MS4A4E, EPHA1, CD33 and CD2AP are associated with Alzheimer's disease. *Nat. Genet.* **2011**, *43*, 429–435. [[CrossRef](#)] [[PubMed](#)]
13. Lambert, J.C.; Heath, S.; Even, G.; Champion, D.; Sleegers, K.; Hiltunen, M.; Combarros, O.; Zelenika, D.; Bullido, M.J.; Tavernier, B.; et al. Genome-wide association study identifies variants at CLU and CR1 associated with Alzheimer's disease. *Nat. Genet.* **2009**, *41*, 1094–1099. [[CrossRef](#)] [[PubMed](#)]
14. Naj, A.C.; Jun, G.; Beecham, G.W.; Wang, L.-S.; Vardarajan, B.N.; Buross, J.; Gallins, P.J.; Buxbaum, J.D.; Jarvik, G.P.; Crane, P.K.; et al. Common variants at MS4A4/MS4A6E, CD2AP, CD33 and EPHA1 are associated with late-onset Alzheimer's disease. *Nat. Genet.* **2011**, *43*, 436–441. [[CrossRef](#)]
15. Seshadri, S.; AL, F.; MA, I.; AL, D.; Gudnason, V.; Boada, M.; JC, B.; AV, S.; MM, C.; JC, L.; et al. Genome-wide analysis of genetic loci associated with Alzheimer disease. *JAMA J. Am. Med. Assoc.* **2010**, *303*, 1832–1840. [[CrossRef](#)] [[PubMed](#)]
16. Bellenguez, C.; Grenier-Boley, B.; Lambert, J.-C. Genetics of Alzheimer's disease: Where we are, and where we are going. *Curr. Opin. Neurobiol.* **2020**, *61*, 40–48. [[CrossRef](#)] [[PubMed](#)]
17. Verheijen, J.; Sleegers, K. Understanding Alzheimer Disease at the Interface between Genetics and Transcriptomics. *Trends Genet.* **2018**, *34*, 434–447. [[CrossRef](#)]
18. Van Cauwenberghe, C.; van Broeckhoven, C.; Sleegers, K. The genetic landscape of Alzheimer disease: Clinical implications and perspectives. *Genet. Med.* **2016**, *18*, 421–430. [[CrossRef](#)]
19. Guerreiro, R.; Wojtas, A.; Bras, J.; Carrasquillo, M.; Rogaeva, E.; Majounie, E.; Cruchaga, C.; Sassi, C.; Kauwe, J.S.K.; Younkin, S.; et al. TREM2 variants in Alzheimer's disease. *N. Engl. J. Med.* **2013**, *368*, 117–127. [[CrossRef](#)]
20. Jonsson, T.; Stefansson, H.; Steinberg, S.; Jonsdottir, I.; Jonsson, P.V.; Snaedal, J.; Bjornsson, S.; Huttenlocher, J.; Levey, A.I.; Lah, J.J.; et al. Variant of TREM2 associated with the risk of Alzheimer's disease. *N. Engl. J. Med.* **2013**, *368*, 107–116. [[CrossRef](#)]
21. Song, W.; Hooli, B.; Mullin, K.; Jin, S.C.; Cella, M.; Ulland, T.K.; Wang, Y.; Tanzi, R.E.; Colonna, M. Alzheimer's disease-associated TREM2 variants exhibit either decreased or increased ligand-dependent activation. *Alzheimer's Dement.* **2017**, *13*, 381–387. [[CrossRef](#)]
22. Sims, R.; van der Lee, S.J.; Naj, A.C.; Bellenguez, C.; Badarinarayan, N.; Jakobsdottir, J.; Kunkle, B.W.; Boland, A.; Raybould, R.; Bis, J.C.; et al. Rare coding variants in PLAG2, ABI3, and TREM2 implicate microglial-mediated innate immunity in Alzheimer's disease. *Nat. Genet.* **2017**, *49*, 1373–1384. [[CrossRef](#)] [[PubMed](#)]
23. Ruiz, A.; Dols-Icardo, O.; Bullido, M.J.; Pastor, P.; Rodríguez-Rodríguez, E.; López de Munain, A.; de Pancorbo, M.M.; Pérez-Tur, J.; Álvarez, V.; Antonell, A.; et al. Assessing the role of the TREM2 p.R47H variant as a risk factor for Alzheimer's disease and frontotemporal dementia. *Neurobiol. Aging* **2014**, *35*, 444.e1–444.e4. [[CrossRef](#)] [[PubMed](#)]

24. Cuyvers, E.; Bettens, K.; Philtjens, S.; Van Langenhove, T.; Gijssels, I.; van der Zee, J.; Engelborghs, S.; Vandenbulcke, M.; Van Dongen, J.; Geerts, N.; et al. Investigating the role of rare heterozygous TREM2 variants in Alzheimer's disease and frontotemporal dementia. *Neurobiol. Aging* **2014**, *35*. [[CrossRef](#)] [[PubMed](#)]
25. Colonna, M.; Wang, Y. TREM2 variants: New keys to decipher Alzheimer disease pathogenesis. *Nat. Rev. Neurosci.* **2016**, *17*, 201–207. [[CrossRef](#)] [[PubMed](#)]
26. Song, W.M.; Joshita, S.; Zhou, Y.; Ulland, T.K.; Gilfillan, S.; Colonna, M. Humanized TREM2 mice reveal microglia-intrinsic and -extrinsic effects of R47H polymorphism. *J. Exp. Med.* **2018**, *215*, 745–760. [[CrossRef](#)]
27. Wang, Y.; Cella, M.; Mallinson, K.; Ulrich, J.D.; Young, K.L.; Robinette, M.L.; Gilfillan, S.; Krishnan, G.M.; Sudhakar, S.; Zinselmeyer, B.H.; et al. TREM2 lipid sensing sustains the microglial response in an Alzheimer's disease model. *Cell* **2015**, *160*, 1061–1072. [[CrossRef](#)]
28. Jay, T.R.; Miller, C.M.; Cheng, P.J.; Graham, L.C.; Bemiller, S.; Broihier, M.L.; Xu, G.; Margevicius, D.; Karlo, J.C.; Sousa, G.L.; et al. TREM2 deficiency eliminates TREM2+ inflammatory macrophages and ameliorates pathology in Alzheimer's disease mouse models. *J. Exp. Med.* **2015**, *212*, 287–295. [[CrossRef](#)]
29. Yuan, P.; Condello, C.; Keene, C.D.; Wang, Y.; Bird, T.D.; Paul, S.M.; Luo, W.; Colonna, M.; Baddeley, D.; Grutzendler, J. TREM2 Haplodeficiency in Mice and Humans Impairs the Microglia Barrier Function Leading to Decreased Amyloid Compaction and Severe Axonal Dystrophy. *Neuron* **2016**, *90*, 724–739. [[CrossRef](#)]
30. Lee, C.Y.D.; Daggett, A.; Gu, X.; Jiang, L.L.; Langfelder, P.; Li, X.; Wang, N.; Zhao, Y.; Park, C.S.; Cooper, Y.; et al. Elevated TREM2 Gene Dosage Reprograms Microglia Responsivity and Ameliorates Pathological Phenotypes in Alzheimer's Disease Models. *Neuron* **2018**, *97*, 1032–1048.e5. [[CrossRef](#)]
31. Zhao, Y.; Wu, X.; Li, X.; Jiang, L.-L.; Gui, X.; Liu, Y.; Sun, Y.; Zhu, B.; Piña-Crespo, J.C.; Zhang, M.; et al. TREM2 Is a Receptor for β -Amyloid that Mediates Microglial Function. *Neuron* **2018**, *97*, 1023–1031.e7. [[CrossRef](#)]
32. Muratore, C.R.; Rice, H.C.; Srikanth, P.; Callahan, D.G.; Shin, T.; Benjamin, L.N.P.; Walsh, D.M.; Selkoe, D.J.; Young-Pearse, T.L. The familial Alzheimer's disease APPV717I mutation alters APP processing and Tau expression in iPSC-derived neurons. *Hum. Mol. Genet.* **2014**, *23*, 3523–3536. [[CrossRef](#)] [[PubMed](#)]
33. Hossini, A.M.; Megges, M.; Prigione, A.; Lichtner, B.; Toliat, M.R.; Wruck, W.; Schröter, F.; Nuernberg, P.; Kroll, H.; Makrantonaki, E.; et al. Induced pluripotent stem cell-derived neuronal cells from a sporadic Alzheimer's disease donor as a model for investigating AD-associated gene regulatory networks. *BMC Genomics* **2015**, *16*, 84. [[CrossRef](#)]
34. Yagi, T.; Ito, D.; Okada, Y.; Akamatsu, W.; Nihei, Y.; Yoshizaki, T.; Yamanaka, S.; Okano, H.; Suzuki, N. Modeling familial Alzheimer's disease with induced pluripotent stem cells. *Hum. Mol. Genet.* **2011**, *20*, 4530–4539. [[CrossRef](#)] [[PubMed](#)]
35. Israel, M.A.; Yuan, S.H.; Bardy, C.; Reyna, S.M.; Mu, Y.; Herrera, C.; Hefferan, M.P.; Van Gorp, S.; Nazor, K.L.; Boscolo, F.S.; et al. Probing sporadic and familial Alzheimer's disease using induced pluripotent stem cells. *Nature* **2012**, *482*, 216–220. [[CrossRef](#)]
36. Duan, L.; Bhattacharyya, B.J.; Belmadani, A.; Pan, L.; Miller, R.J.; Kessler, J.A. Stem cell derived basal forebrain cholinergic neurons from Alzheimer's disease patients are more susceptible to cell death. *Mol. Neurodegener.* **2014**, *9*, 3. [[CrossRef](#)]
37. Ochalek, A.; Mihalik, B.; Avci, H.X.; Chandrasekaran, A.; Téglási, A.; Bock, I.; Lo Giudice, M.; Tancos, Z.; Molnár, K.; László, L.; et al. Neurons derived from sporadic Alzheimer's disease iPSCs reveal elevated TAU hyperphosphorylation, increased amyloid levels, and GSK3B activation. *Alzheimers. Res. Ther.* **2017**, *9*, 90. [[CrossRef](#)]
38. Flamier, A.; El Hajjar, J.; Adjaye, J.; Fernandes, K.J.; Abdouh, M.; Bernier, G. Modeling Late-Onset Sporadic Alzheimer's Disease through BMI1 Deficiency. *Cell Rep.* **2018**, *23*, 2653–2666. [[CrossRef](#)]
39. Zhang, B.; Gaiteri, C.; Bodea, L.-G.; Wang, Z.; McElwee, J.; Podtelezchnikov, A.A.; Zhang, C.; Xie, T.; Tran, L.; Dobrin, R.; et al. Integrated Systems Approach Identifies Genetic Nodes and Networks in Late-Onset Alzheimer's Disease. *Cell* **2013**, *153*, 707–720. [[CrossRef](#)]
40. Martins, S.; Bohndorf, M.; Schröter, F.; Assar, F.; Wruck, W.; Slegers, K.; Van Broeckhoven, C.; Adjaye, J. Lymphoblast-derived integration-free ISRM-CON9 iPSC cell line from a 75 year old female. *Stem Cell Res.* **2018**, *26*. [[CrossRef](#)]

41. Schröter, F.; Slegers, K.; Cuyvers, E.; Bohndorf, M.; Wruck, W.; Van Broeckhoven, C.; Adjaye, J. Lymphoblast-derived integration-free iPSC cell line from a female 67-year-old Alzheimer's disease patient with TREM2 (R47H) missense mutation. *Stem Cell Res.* **2016**, *17*, 553–555. [[CrossRef](#)]
42. Schröter, F.; Slegers, K.; Cuyvers, E.; Bohndorf, M.; Wruck, W.; Van Broeckhoven, C.; Adjaye, J. Lymphoblast-derived integration-free iPSC cell line from a 65-year-old Alzheimer's disease patient expressing the TREM2 p.R47H variant. *Stem Cell Res.* **2016**, *16*, 113–115. [[CrossRef](#)] [[PubMed](#)]
43. Schröter, F.; Slegers, K.; Bohndorf, M.; Wruck, W.; Van Broeckhoven, C.; Adjaye, J. Lymphoblast-derived integration-free iPSC cell line from a 69-year-old male. *Stem Cell Res.* **2016**, *16*, 29–31. [[CrossRef](#)] [[PubMed](#)]
44. Levenga, J.; Krishnamurthy, P.; Rajamohamedsait, H.; Wong, H.; Franke, T.F.; Cain, P.; Sigurdsson, E.M.; Hoefler, C.A. Tau pathology induces loss of GABAergic interneurons leading to altered synaptic plasticity and behavioral impairments. *Acta Neuropathol. Commun.* **2013**, *1*, 34. [[CrossRef](#)] [[PubMed](#)]
45. Burgos-Ramos, E.; Hervás-Aguilar, A.; Aguado-Llera, D.; Puebla-Jiménez, L.; Hernández-Pinto, A.M.; Barrios, V.; Arilla-Ferreiro, E. Somatostatin and Alzheimer's disease. *Mol. Cell. Endocrinol.* **2008**, *286*, 104–111. [[CrossRef](#)] [[PubMed](#)]
46. Jo, S.; Yarishkin, O.; Hwang, Y.J.; Chun, Y.E.; Park, M.; Woo, D.H.; Bae, J.Y.; Kim, T.; Lee, J.; Chun, H.; et al. GABA from reactive astrocytes impairs memory in mouse models of Alzheimer's disease. *Nat. Med.* **2014**, *20*, 886–896. [[CrossRef](#)] [[PubMed](#)]
47. Liu, Y.; Liu, H.; Sauvey, C.; Yao, L.; Zarnowska, E.D.; Zhang, S.-C. Directed differentiation of forebrain GABA interneurons from human pluripotent stem cells. *Nat. Protoc.* **2013**, *8*, 1670–1679. [[CrossRef](#)]
48. Li, J.T.; Zhang, Y. TREM2 regulates innate immunity in Alzheimer's disease. *J. Neuroinflammation* **2018**, *15*, 107. [[CrossRef](#)]
49. Sengupta, U.; Nilson, A.N.; Kaye, R. The Role of Amyloid- β Oligomers in Toxicity, Propagation, and Immunotherapy. *EBioMedicine* **2016**, *6*, 42. [[CrossRef](#)]
50. Viola, K.L.; Klein, W.L. Amyloid β oligomers in Alzheimer's disease pathogenesis, treatment, and diagnosis. *Acta Neuropathol.* **2015**, *129*, 183–206. [[CrossRef](#)]
51. Klyubin, I.; Betts, V.; Welzel, A.T.; Blennow, K.; Zetterberg, H.; Wallin, A.; Lemere, C.A.; Cullen, W.K.; Peng, Y.; Wisniewski, T.; et al. Amyloid Protein Dimer-Containing Human CSF Disrupts Synaptic Plasticity: Prevention by Systemic Passive Immunization. *J. Neurosci.* **2008**, *28*, 4231–4237. [[CrossRef](#)]
52. Shankar, G.M.; Li, S.; Mehta, T.H.; Garcia-Munoz, A.; Shepardson, N.E.; Smith, I.; Brett, F.M.; Farrell, M.A.; Rowan, M.J.; Lemere, C.A.; et al. Amyloid- β protein dimers isolated directly from Alzheimer's brains impair synaptic plasticity and memory. *Nat. Med.* **2008**, *14*, 837–842. [[CrossRef](#)] [[PubMed](#)]
53. McDonald, J.M.; Savva, G.M.; Brayne, C.; Welzel, A.T.; Forster, G.; Shankar, G.M.; Selkoe, D.J.; Ince, P.G.; Walsh, D.M.; Medical Research Council. Cognitive Function and Ageing Study The presence of sodium dodecyl sulphate-stable A β dimers is strongly associated with Alzheimer-type dementia. *Brain* **2010**, *133*, 1328–1341. [[CrossRef](#)] [[PubMed](#)]
54. Brinkmalm, G.; Hong, W.; Wang, Z.; Liu, W.; O'Malley, T.T.; Sun, X.; Frosch, M.P.; Selkoe, D.J.; Portelius, E.; Zetterberg, H.; et al. Identification of neurotoxic cross-linked amyloid- β dimers in the Alzheimer's brain. *Brain* **2019**, *142*, 1441–1457. [[CrossRef](#)] [[PubMed](#)]
55. Müller-Schiffmann, A.; Herring, A.; Abdel-Hafiz, L.; Chepkova, A.N.; Schäble, S.; Wedel, D.; Horn, A.H.C.; Sticht, H.; de Souza Silva, M.A.; Gottmann, K.; et al. Amyloid- β dimers in the absence of plaque pathology impair learning and synaptic plasticity. *Brain* **2016**, *139*, 509–525. [[CrossRef](#)]
56. Abdel-Hafiz, L.; Müller-Schiffmann, A.; Korth, C.; Fazari, B.; Chao, O.Y.; Nikolaus, S.; Schäble, S.; Herring, A.; Keyvani, K.; Lamounier-Zepter, V.; et al. A β dimers induce behavioral and neurochemical deficits of relevance to early Alzheimer's disease. *Neurobiol. Aging* **2018**, *69*, 1–9. [[CrossRef](#)]
57. Müller-Schiffmann, A.; Andreyeva, A.; Horn, A.H.C.; Gottmann, K.; Korth, C.; Sticht, H. Molecular Engineering of a Secreted, Highly Homogeneous, and Neurotoxic A β Dimer. *ACS Chem. Neurosci.* **2011**, *2*, 242–248. [[CrossRef](#)]
58. Claes, C.; Van Den Daele, J.; Boon, R.; Schouteden, S.; Colombo, A.; Monasor, L.S.; Fiers, M.; Ordovás, L.; Nami, F.; Bohrmann, B.; et al. Human stem cell-derived monocytes and microglia-like cells reveal impaired amyloid plaque clearance upon heterozygous or homozygous loss of TREM2. *Alzheimer's Dement.* **2018**, *15*, 453–464. [[CrossRef](#)]

59. Brownjohn, P.W.; Smith, J.; Solanki, R.; Lohmann, E.; Houlden, H.; Hardy, J.; Dietmann, S.; Livesey, F.J. Functional Studies of Missense TREM2 Mutations in Human Stem Cell-Derived Microglia. *Stem Cell Rep.* **2018**, *10*, 1294–1307. [[CrossRef](#)]
60. Hsieh, C.L.; Koike, M.; Spusta, S.C.; Niemi, E.C.; Yenari, M.; Nakamura, M.C.; Seaman, W.E. A role for TREM2 ligands in the phagocytosis of apoptotic neuronal cells by microglia. *J. Neurochem.* **2009**, *109*, 1144–1156. [[CrossRef](#)]
61. Kleinberger, G.; Yamanishi, Y.; Suarez-Calvet, M.; Czirr, E.; Lohmann, E.; Cuyvers, E.; Struyfs, H.; Pettkus, N.; Wenninger-Weinzierl, A.; Mazaheri, F.; et al. TREM2 mutations implicated in neurodegeneration impair cell surface transport and phagocytosis. *Sci. Transl. Med.* **2014**, *6*, 243ra86. [[CrossRef](#)]
62. Takahashi, K.; Rochford, C.D.P.; Neumann, H. Clearance of apoptotic neurons without inflammation by microglial triggering receptor expressed on myeloid cells-2. *J. Exp. Med.* **2005**, *201*, 647–657. [[CrossRef](#)] [[PubMed](#)]
63. Garcia-Reitboeck, P.; Phillips, A.; Piers, T.M.; Villegas-Llerena, C.; Butler, M.; Mallach, A.; Rodrigues, C.; Arber, C.E.; Heslegrave, A.; Zetterberg, H.; et al. Human Induced Pluripotent Stem Cell-Derived Microglia-Like Cells Harboring TREM2 Missense Mutations Show Specific Deficits in Phagocytosis. *Cell Rep.* **2018**, *24*, 2300–2311. [[CrossRef](#)] [[PubMed](#)]
64. Domingues, C.; da Cruz e Silva, O.A.B.; Henriques, A.G. Impact of Cytokines and Chemokines on Alzheimer's Disease Neuropathological Hallmarks. *Curr. Alzheimer Res.* **2017**, *14*, 870–882. [[CrossRef](#)] [[PubMed](#)]
65. Doyle, K.M.; Kennedy, D.; Gorman, A.M.; Gupta, S.; Healy, S.J.M.; Samali, A. Unfolded proteins and endoplasmic reticulum stress in neurodegenerative disorders. *J. Cell. Mol. Med.* **2011**, *15*, 2025–2039. [[CrossRef](#)]
66. Cheng-Hathaway, P.J.; Reed-Geaghan, E.G.; Jay, T.R.; Casali, B.T.; Bemiller, S.M.; Puntambekar, S.S.; von Saucken, V.E.; Williams, R.Y.; Karlo, J.C.; Moutinho, M.; et al. The Trem2 R47H variant confers loss-of-function-like phenotypes in Alzheimer's disease. *Mol. Neurodegener.* **2018**, *13*, 29. [[CrossRef](#)]
67. Sudom, A.; Talreja, S.; Danao, J.; Bragg, E.; Kegel, R.; Min, X.; Richardson, J.; Zhang, Z.; Sharkov, N.; Marcora, E.; et al. Molecular basis for the loss-of-function effects of the Alzheimer's disease-associated R47H variant of the immune receptor TREM2. *J. Biol. Chem.* **2018**, *293*, 12634–12646. [[CrossRef](#)]
68. Xiang, X.; Piers, T.M.; Wefers, B.; Zhu, K.; Mallach, A.; Brunner, B.; Kleinberger, G.; Song, W.; Colonna, M.; Herms, J.; et al. The Trem2 R47H Alzheimer's risk variant impairs splicing and reduces Trem2 mRNA and protein in mice but not in humans. *Mol. Neurodegener.* **2018**, *13*, 49. [[CrossRef](#)]
69. Stomrud, E.; Björkqvist, M.; Janciauskiene, S.; Minthon, L.; Hansson, O. Alterations of matrix metalloproteinases in the healthy elderly with increased risk of prodromal Alzheimer's disease. *Alzheimers. Res. Ther.* **2010**, *2*, 20. [[CrossRef](#)]
70. Shah, K.; Desilva, S.; Abbruscato, T. The role of glucose transporters in brain disease: Diabetes and Alzheimer's Disease. *Int. J. Mol. Sci.* **2012**, *13*, 12629–12655. [[CrossRef](#)]
71. Katsel, P.; Roussos, P.; Beeri, M.S.; Gama-Sosa, M.A.; Gandy, S.; Khan, S.; Haroutunian, V. Parahippocampal gyrus expression of endothelial and insulin receptor signaling pathway genes is modulated by Alzheimer's disease and normalized by treatment with anti-diabetic agents. *PLoS ONE* **2018**, *13*, e0206547. [[CrossRef](#)]
72. Kondo, T.; Asai, M.; Tsukita, K.; Kutoku, Y.; Ohsawa, Y.; Sunada, Y.; Imamura, K.; Egawa, N.; Yahata, N.; Okita, K.; et al. Cell Stem Cell Modeling Alzheimer's Disease with iPSCs Reveals Stress Phenotypes Associated with Intracellular Ab and Differential Drug Responsiveness. *Cell Stem Cell* **2013**, *12*, 487–496. [[CrossRef](#)] [[PubMed](#)]
73. Wada, Y.; Ishiguro, K.; Itoh, T.J.; Uchida, T.; Hotani, H.; Saito, T.; Kishimoto, T.; Hisanaga, S. Microtubule-stimulated phosphorylation of tau at Ser202 and Thr205 by cdk5 decreases its microtubule nucleation activity. *J. Biochem.* **1998**, *124*, 738–746. [[CrossRef](#)] [[PubMed](#)]
74. Cruchaga, C.; Kauwe, J.S.K.; Harari, O.; Jin, S.C.; Cai, Y.; Karch, C.M.; Benitez, B.A.; Jeng, A.T.; Skorupa, T.; Carrell, D.; et al. GWAS of Cerebrospinal Fluid Tau Levels Identifies Risk Variants for Alzheimer's Disease. *Neuron* **2013**, *78*, 256–268. [[CrossRef](#)] [[PubMed](#)]
75. Piers, T.M.; Cosker, K.; Mallach, A.; Johnson, G.T.; Guerreiro, R.; Hardy, J.; Pocock, J.M. A locked immunometabolic switch underlies TREM2 R47H loss of function in human iPSC-derived microglia. *FASEB J.* **2020**, *34*, 2436–2450. [[CrossRef](#)] [[PubMed](#)]
76. Schettters, S.T.T.; Gomez-Nicola, D.; Garcia-Vallejo, J.J.; Van Kooyk, Y. Neuroinflammation: Microglia and T Cells Get Ready to Tango. *Front. Immunol.* **2017**, *8*, 1905. [[CrossRef](#)] [[PubMed](#)]

77. Duus, K.; Hansen, P.R.; Houen, G. Interaction of calreticulin with amyloid beta peptide 1-42. *Protein Pept. Lett.* **2008**, *15*, 103–107.
78. Lin, Q.; Cao, Y.; Gao, J. Serum Calreticulin Is a Negative Biomarker in Patients with Alzheimer's Disease. *Int. J. Mol. Sci.* **2014**, *15*, 21740–21753. [[CrossRef](#)]
79. Hondius, D.C.; van Nierop, P.; Li, K.W.; Hoozemans, J.J.M.; van der Schors, R.C.; van Haastert, E.S.; van der Vies, S.M.; Rozemuller, A.J.M.; Smit, A.B. Profiling the human hippocampal proteome at all pathologic stages of Alzheimer's disease. *Alzheimer's Dement.* **2016**, *12*, 654–668. [[CrossRef](#)]
80. Armstrong, A.; Mattsson, N.; Appelqvist, H.; Janefjord, C.; Sandin, L.; Agholme, L.; Olsson, B.; Svensson, S.; Blennow, K.; Zetterberg, H.; et al. Lysosomal network proteins as potential novel CSF biomarkers for Alzheimer's disease. *Neuromolecular Med.* **2014**, *16*, 150–160. [[CrossRef](#)]
81. Mody, N.; Agouni, A.; Mcilroy, G.D.; Platt, B.; Delibegovic, M. Susceptibility to diet-induced obesity and glucose intolerance in the APP SWE/PSEN1 A246E mouse model of Alzheimer's disease is associated with increased brain levels of protein tyrosine phosphatase 1B (PTP1B) and retinol-binding protein 4 (RBP4), and basal phosphorylation of S6 ribosomal protein. *Diabetologia* **2011**, *54*, 2143–2151. [[CrossRef](#)]
82. Bonham, L.W.; Geier, E.G.; Steele, N.Z.R.; Holland, D.; Miller, B.L.; Dale, A.M.; Desikan, R.S.; Yokoyama, J.S.; Initiative, A.D.N. Insulin-Like Growth Factor Binding Protein 2 Is Associated With Biomarkers of Alzheimer's Disease Pathology and Shows Differential Expression in Transgenic Mice. *Front. Neurosci.* **2018**, *12*, 476. [[CrossRef](#)] [[PubMed](#)]
83. Katayama, T.; Imaizumi, K.; Sato, N.; Miyoshi, K.; Kudo, T.; Hitomi, J.; Morihara, T.; Yoneda, T.; Gomi, F.; Mori, Y.; et al. Presenilin-1 mutations downregulate the signalling pathway of the unfolded-protein response. *Nat. Cell Biol.* **1999**, *1*, 479–485. [[CrossRef](#)] [[PubMed](#)]
84. Hamos, J.E.; Oblas, B.; Pulaski-Salo, D.; Welch, W.J.; Bole, D.G.; Drachman, D.A. Expression of heat shock proteins in Alzheimer's disease. *Neurology* **1991**, *41*, 345–350. [[CrossRef](#)] [[PubMed](#)]
85. Hoozemans, J.J.M.; Veerhuis, R.; Van Haastert, E.S.; Rozemuller, J.M.; Baas, F.; Eikelenboom, P.; Scheper, W. The unfolded protein response is activated in Alzheimer's disease. *Acta Neuropathol.* **2005**, *110*, 165–172. [[CrossRef](#)]
86. Han, J.; Back, S.H.; Hur, J.; Lin, Y.-H.; Gildersleeve, R.; Shan, J.; Yuan, C.L.; Krokowski, D.; Wang, S.; Hatzoglou, M.; et al. ER-stress-induced transcriptional regulation increases protein synthesis leading to cell death. *Nat. Cell Biol.* **2013**, *15*, 481–490. [[CrossRef](#)]
87. Kim, D.; Langmead, B.; Salzberg, S.L. HISAT: A fast spliced aligner with low memory requirements. *Nat. Methods* **2015**, *12*, 357–360. [[CrossRef](#)]
88. Baruzzo, G.; Hayer, K.E.; Kim, E.J.; Di Camillo, B.; FitzGerald, G.A.; Grant, G.R. Simulation-based comprehensive benchmarking of RNA-seq aligners. *Nat. Methods* **2017**, *14*, 135–139. [[CrossRef](#)]
89. Li, H.; Handsaker, B.; Wysoker, A.; Fennell, T.; Ruan, J.; Homer, N.; Marth, G.; Abecasis, G.; Durbin, R. The Sequence Alignment/Map format and SAMtools. *Bioinformatics* **2009**, *25*, 2078–2079. [[CrossRef](#)]
90. Liao, Y.; Smyth, G.K.; Shi, W. featureCounts: An efficient general purpose program for assigning sequence reads to genomic features. *Bioinformatics* **2014**, *30*, 923–930. [[CrossRef](#)]
91. Law, C.W.; Chen, Y.; Shi, W.; Smyth, G.K. Voom: Precision weights unlock linear model analysis tools for RNA-seq read counts. *Genome Biol.* **2014**, *15*, R29. [[CrossRef](#)]
92. Smyth, G.K. Linear Models and Empirical Bayes Methods for Assessing Differential Expression in Microarray Experiments. *Stat. Appl. Genet. Mol. Biol.* **2004**, *3*. [[CrossRef](#)] [[PubMed](#)]
93. Gentleman, R.C.; Carey, V.J.; Bates, D.M.; Bolstad, B.; Dettling, M.; Dudoit, S.; Ellis, B.; Gautier, L.; Ge, Y.; Gentry, J.; et al. Bioconductor: Open software development for computational biology and bioinformatics. *Genome Biol.* **2004**, *5*, R80. [[CrossRef](#)] [[PubMed](#)]
94. Gautier, L.; Cope, L.; Bolstad, B.M.; Irizarry, R.A. affy-analysis of Affymetrix GeneChip data at the probe level. *Bioinformatics* **2004**, *20*, 307–315. [[CrossRef](#)] [[PubMed](#)]
95. Warnes, G.R.; Bolker, B.; Bonebakker, L.; Gentleman, R.; Liaw, W.H.A.; Lumley, T.; Maechler, M.; Magnusson, A.; Moeller, S.; Schwartz, M.; et al. gplots: Various R Programming Tools for Plotting Data. *R Package Version* **2015**.
96. Chen, H.; Boutros, P.C. VennDiagram: A package for the generation of highly-customizable Venn and Euler diagrams in R. *BMC Bioinf.* **2011**, *12*, 35. [[CrossRef](#)] [[PubMed](#)]

97. Graffmann, N.; Ring, S.; Kawala, M.-A.; Wruck, W.; Ncube, A.; Trompeter, H.-I.; Adjaye, J. Modeling Nonalcoholic Fatty Liver Disease with Human Pluripotent Stem Cell-Derived Immature Hepatocyte-Like Cells Reveals Activation of PLIN2 and Confirms Regulatory Functions of Peroxisome Proliferator-Activated Receptor Alpha. *Stem Cells Dev.* **2016**, *25*, 1119–1133. [[CrossRef](#)]
98. Chatr-aryamontri, A.; Oughtred, R.; Boucher, L.; Rust, J.; Chang, C.; Kolas, N.K.; O'Donnell, L.; Oster, S.; Theesfeld, C.; Sellam, A.; et al. The BioGRID interaction database: 2017 update. *Nucleic Acids Res.* **2017**, *45*, D369–D379. [[CrossRef](#)]
99. Csardi, G.; Nepusz, T. The igraph software package for complex network research. *InterJournal* **2006**, *1695*, 1–9.
100. Butts, C. network: A Package for Managing Relational Data in R. *J. Stat. Softw.* **2008**, *24*, 2. [[CrossRef](#)]
101. Kanehisa, M.; Furumichi, M.; Tanabe, M.; Sato, Y.; Morishima, K. KEGG: New perspectives on genomes, pathways, diseases and drugs. *Nucleic Acids Res.* **2017**, *45*, D353–D361. [[CrossRef](#)]
102. Falcon, S.; Gentleman, R. Using GOstats to test gene lists for GO term association. *Bioinformatics* **2007**, *23*, 257–258. [[CrossRef](#)] [[PubMed](#)]



© 2020 by the authors. Licensee MDPI, Basel, Switzerland. This article is an open access article distributed under the terms and conditions of the Creative Commons Attribution (CC BY) license (<http://creativecommons.org/licenses/by/4.0/>).

2.5 AP-2 reduces amyloidogenesis by promoting BACE1 trafficking and degradation in neurons

Sujoy Bera, Santiago Cambor-Perujo, Elena Calleja Barca, Albert Negrete-Hurtado, Julia Racho, Elodie De Bruyckere, Christoph Wittich, Nina Ellrich, **Soraia Martins**, James Adjaye and Natalia L. Kononenko

EMBO Rep (2020)21:e47954

Abstract

Cleavage of amyloid precursor protein (APP) by BACE-1 (β -site APP cleaving enzyme 1) is the rate-limiting step in amyloid- β ($A\beta$) production and a neuropathological hallmark of Alzheimer's disease (AD). Despite decades of research, mechanisms of amyloidogenic APP processing remain highly controversial. Here, we show that in neurons, APP processing and $A\beta$ production are controlled by the protein complex-2 (AP-2), an endocytic adaptor known to be required for APP endocytosis. Now, we find that AP-2 prevents amyloidogenesis by additionally functioning downstream of BACE1 endocytosis, regulating BACE1 endosomal trafficking and its delivery to lysosomes. AP-2 is decreased in iPSC-derived neurons from patients with late-onset AD, while conditional AP-2 knockout (KO) mice exhibit increased $A\beta$ production, resulting from accumulation of BACE1 within late endosomes and autophagosomes. Deletion of BACE1 decreases amyloidogenesis and mitigates synapse loss in neurons lacking AP-2. Taken together, these data suggest a mechanism for BACE1 intracellular trafficking and degradation via an endocytosis-independent function of AP-2 and reveal a novel role for endocytic proteins in AD.

Author's contribution: 15%

SB and NLK contributed to the conception of the study and experimental design. SB, SC-P, ECB, AN-H, JR, EB, CW, NE, **SM**, and NLK performed the experiments, data analysis, and participated in the acquisition of data. JA provided reagents. SB and NLK prepared the manuscript. All the authors critically revised the manuscript and provided help with the interpretation of data. The final manuscript was read and approved by all authors.

Status: Published in EMBO Reports (doi.org/10.15252/embr.201947954)

This is an open access article under the terms of the Creative Commons Attribution 4.0 License.



AP-2 reduces amyloidogenesis by promoting BACE1 trafficking and degradation in neurons

Sujoy Bera^{1,†}, Santiago Cambor-Perujo¹, Elena Calleja Barca¹, Albert Negrete-Hurtado¹, Julia Racho¹, Elodie De Bruyckere¹, Christoph Wittich¹, Nina Ellrich¹, Soraia Martins² , James Adjaye² & Natalia L. Kononenko^{1,*} 

Abstract

Cleavage of amyloid precursor protein (APP) by BACE-1 (β-site APP cleaving enzyme 1) is the rate-limiting step in amyloid-β (Aβ) production and a neuropathological hallmark of Alzheimer's disease (AD). Despite decades of research, mechanisms of amyloidogenic APP processing remain highly controversial. Here, we show that in neurons, APP processing and Aβ production are controlled by the protein complex-2 (AP-2), an endocytic adaptor known to be required for APP endocytosis. Now, we find that AP-2 prevents amyloidogenesis by additionally functioning downstream of BACE1 endocytosis, regulating BACE1 endosomal trafficking and its delivery to lysosomes. AP-2 is decreased in iPSC-derived neurons from patients with late-onset AD, while conditional AP-2 knockout (KO) mice exhibit increased Aβ production, resulting from accumulation of BACE1 within late endosomes and autophagosomes. Deletion of BACE1 decreases amyloidogenesis and mitigates synapse loss in neurons lacking AP-2. Taken together, these data suggest a mechanism for BACE1 intracellular trafficking and degradation via an endocytosis-independent function of AP-2 and reveal a novel role for endocytic proteins in AD.

Keywords amyloidogenesis; axonal transport; BACE1; endocytosis; neurodegeneration

Subject Categories Membranes & Trafficking; Molecular Biology of Disease; Neuroscience

DOI 10.15252/embr.201947954 | Received 22 August 2019 | Revised 11 March 2020 | Accepted 13 March 2020 | Published online 23 April 2020

EMBO Reports (2020) 21: e47954

Introduction

Alzheimer's disease (AD) is the most prominent neurodegenerative disorder and a leading cause of dementia in the aging population [1]. It is well established that the increased amyloidogenic processing of amyloid precursor protein (APP), resulting in augmented production of either total amyloid-β (Aβ) or a shift in the Aβ₁₋₄₀:Aβ₁₋₄₂ ratio

toward formation of the more toxic Aβ₁₋₄₂, are key features underlying the pathogenesis of AD [2,3]. Based on the amyloid cascade hypothesis, an imbalance between Aβ production and clearance [1] results in increased amounts of Aβ in the form of monomers, oligomers, insoluble fibrils, and plaques. High levels of Aβ induce tau hyperphosphorylation and formation of neurofibrillary tangles in specific brain regions in AD patients, triggering synaptic dysfunction, inflammation, and oxidative stress in affected cells [4–6]. Thus, identifying cellular processes involved in the generation of Aβ peptide in neurons is of great importance for the development of novel drug targets or predictive biomarkers in AD.

Aβ peptide is liberated from the membrane-spanning APP by sequential proteolytic cleavage, employing β- and γ-secretases [7]. APP is first cleaved by the β-site APP cleaving enzyme 1 (BACE1) to generate the N-terminal soluble APPβ (sAPPβ) and the membrane-bound APP C-terminal fragment C99, which is subsequently cleaved by the γ-secretase to produce the Aβ. Conversely, APP can also be cleaved by α-secretases, which releases the soluble ectodomain portion of APPα (sAPPα) and prevents Aβ formation [8], or by the η-secretase, the alternative proteolytic processing pathway occurring under physiological conditions [9]. The cleavage of APP by BACE1 represents the rate-limiting step for Aβ generation [10]. The absence of Aβ plaques is reported in BACE1 null mice engineered to overexpress human APP (Tg2576+) [11], while double-transgenic mice obtained by crossing the mice that overexpress BACE1 and APP show enhanced Aβ generation and exacerbated Aβ pathology [12]. These data, along with the fact that both the activity and the expression pattern of BACE1 are elevated in human sporadic AD patients [13,14], provide a conceptual basis for a BACE1-dependent mechanism of Aβ accumulation and suggest BACE1 as a primary drug target for AD therapy [10]. However, BACE1 cleavage of several other substrates besides APP [15] is important for normal physiology [16,17], putting the safety of BACE1 inhibitors in question. These data taken together with the recent finding that oral BACE1 inhibitor Verubecestat does not slow disease progression in AD patients as compared with placebo [18] raise the demand for novel therapeutic targets in AD. An alternative approach to BACE1 inhibitors is an

¹ CECAD Research Center, University of Cologne, Cologne, Germany

² Institute for Stem Cell Research and Regenerative Medicine, Medical Faculty, Heinrich Heine University, Düsseldorf, Germany

*Corresponding author. Tel: +49 221 478 84302; E-mail: n.kononenko@uni-koeln.de

[†] Present address: Centre for Neuroscience and Regenerative Medicine, Faculty of Science, University of Technology Sydney, Sydney, NSW, Australia

indirect intervention with BACE1 protein levels in the brain through the regulation of BACE1 delivery to degradation organelles. However, despite two decades passing since the discovery of BACE1 [19,20], the precise regulation of BACE1 intracellular trafficking in neurons remains incompletely understood.

In neurons, BACE1 and APP are segregated during resting conditions, while neuronal activity induces their convergence into acidic microdomains (early and late endosomes) [21], providing an optimal environment for BACE1 enzymatic activity and APP cleavage [22]. While APP trafficking from the plasma membrane to endosomes is well established, intracellular sorting of BACE1 remains highly controversial. On the one hand, it has been postulated that BACE1 via the di-leucine motif in the cytoplasmic tail binds clathrin adaptor protein complex-2 (AP-2), which facilitates its endocytosis from the plasma membrane [23,24]. Conversely, the trafficking of BACE1 along a clathrin-independent pathway, regulated by the small GTPase ADP ribosylation factor 6 (ARF6), has also been proposed [25]. How these two pathways mechanistically contribute to the amyloidogenic processing of APP in neurons is currently unknown.

AP-2 is a heterotetrameric complex comprised of α , β , μ , and σ subunits that links clathrin and other endocytic proteins to sites of clathrin-mediated endocytosis (CME) [26]. Knockout of AP-2(μ) in mice causes early embryonic lethality [27], and depletion of AP-2(μ) in mammalian non-neuronal cells results in potent inhibition of CME due to loss of the entire AP-2 complex [28]. While the β , μ , and σ subunits of AP-2 complex are made from a single gene in mammals, the α subunit is encoded by two isogenes termed αA and αC that undergo alternative splicing in the brain [29]. Interestingly, AP-2 is not absolutely required for cargo internalization via CME in neurons, but has a prominent role in the reformation of synaptic vesicles from endosome-like vacuoles [30,31] and in transport of autophagosomes via the association of the appendage domain of the AP-2 αA with autophagy modifier LC3 [32]. Loss of neuronal AP-2 in mice impairs BDNF/TrkB signaling pathway and causes neurodegeneration [32]. Here, we demonstrate that AP-2 affects APP processing and A β production in neurons via the regulation of BACE1 intracellular trafficking. While not essential for BACE1 endocytosis, AP-2 controls BACE1 protein levels by mediating its trafficking *en route* to lysosomes. Strikingly, AP-2 is decreased in human iPSC-derived neurons from patients with late-onset AD. Taken together, our data identify a previously undescribed function of AP-2 in regulation of BACE1 levels in the brain and suggest a novel role for endocytic adaptors in AD.

Results

Endosomal trafficking, but not BACE1 endocytosis, requires AP-2

Previous results identified that a substantial pool of BACE1 is delivered to endosomes by the AP-2-dependent internalization from the plasma membrane [23]. Taken into account the fact that AP-2 and BACE1 are found in a complex in the mouse brain (Fig EV1A and B), we asked whether AP-2 regulates BACE1 endocytosis in neurons. To test this, we measured the kinetics of BACE1 endocytosis in primary neurons isolated from the cortex of AP-2 knockout (KO) mice, where the loss of the entire AP-2 heterotetramer without

a compensatory increase in AP-1 and AP-3 protein levels is achieved by a tamoxifen-inducible CAG-Cre-dependent recombination of floxed AP-2 μ allele (AP-2 $\mu^{lox/lox}$; CAG-Cre) [32]. To investigate the BACE1 trafficking, we took advantage of the previously characterized BACE1-eGFP construct additionally carrying a single HA tag after the propeptide cleavage site at the N-terminus [23]. WT and KO neurons, transiently expressing the HA-BACE1-eGFP that has a localization similar to endogenous BACE1 (Fig EV1C and D), were pulsed with the HA antibody for 30 min at 4°C to label the fraction of BACE1 on the plasma membrane, and endocytosed BACE1 was detected after 5, 20, or 40 min of chase at 37°C using standard immunocytochemistry procedures combined with acid-stripping of non-internalized HA antibody (Figs 1A and EV1E and F). In agreement with previous results [23], we observed that the amount of endocytosed BACE1 was decreased in AP-2 μ KO neurons at 20 and 40 min after the HA antibody pulse (Fig 1A). Surprisingly, AP-2 μ was not required for BACE1 endocytosis 5 min after the beginning of the assay (Fig 1A and B), suggesting that BACE1 endosomal recycling, but not endocytosis, might be AP-2-dependent. To test this, we next investigated BACE1 postendocytic trafficking in HA-BACE1-eGFP-expressing WT and AP-2 μ KO neurons by adopting a previously described protocol [33]. The amount of internalized BACE1 in neurons pulsed with the HA antibody for 20 min was analyzed after acid-stripping of non-endocytosed HA antibody under permeabilizing conditions (schematic in Fig 1C). To analyze BACE1 recycling back to the plasma membrane, the neurons that had undergone the 20-min pulse with the HA antibody were first acid-stripped, and internalized BACE1 was further chased for 20 min at 37°C. Subsequently, recycled BACE1 was detected at the plasma membrane under non-permeabilizing conditions (schematic in Fig 1E). The decrease in BACE1 internalization (Figs 1C and D, and EV1G) was accompanied by a substantial increase in BACE1 recycling back to the plasma membrane (Figs 1E and F, and EV1H), indicating that in the absence of AP-2, BACE1 is mistrafficked between endosomes and the plasma membrane such that the protein is more rapidly recycled.

To directly test whether blocking endosomal recycling in neurons lacking AP-2 restores BACE1 trafficking, we overexpressed in WT and AP-2 μ KO neurons a GTP binding-deficient mutant of RAB4-S22N, which is known to interfere with fast recycling of cargo proteins from the RAB4-positive recycling endosomes to the plasma membrane [34]. In agreement with the hypothesis above, we found that the overexpression of RAB4-S22N significantly reduced the recycling of BACE1 in neurons lacking AP-2 μ (Figs 1G and H, and EV1I-K). We also prevented the slow RAB11-dependent endosomal recycling of BACE1 by overexpression in control and AP-2 μ KO neurons of a dominant-negative S25N form of RAB11A [35]. The amount of BACE1 found under recycling conditions at the surface of AP-2 μ KO neurons overexpressing mutant eGFP-RAB11A-S25N was significantly reduced compared to either RAB11-eGFP (Fig 1I)- or eGFP-expressing KO cells (Fig EV1L), albeit with a slightly lower efficiency when compared to RAB4. Blocking either RAB4- or RAB11-dependent endosomal recycling was sufficient to upregulate the internalized fraction of BACE1 in AP-2 μ KO neurons (Figs 1J and K, and EV1M-O). Taken together, these data strongly indicate that AP-2 is not required for BACE1 endocytosis and regulates BACE1 endosomal trafficking. Without AP-2, BACE1 is mistrafficked to a recycling compartment, a phenotype that results in more BACE1

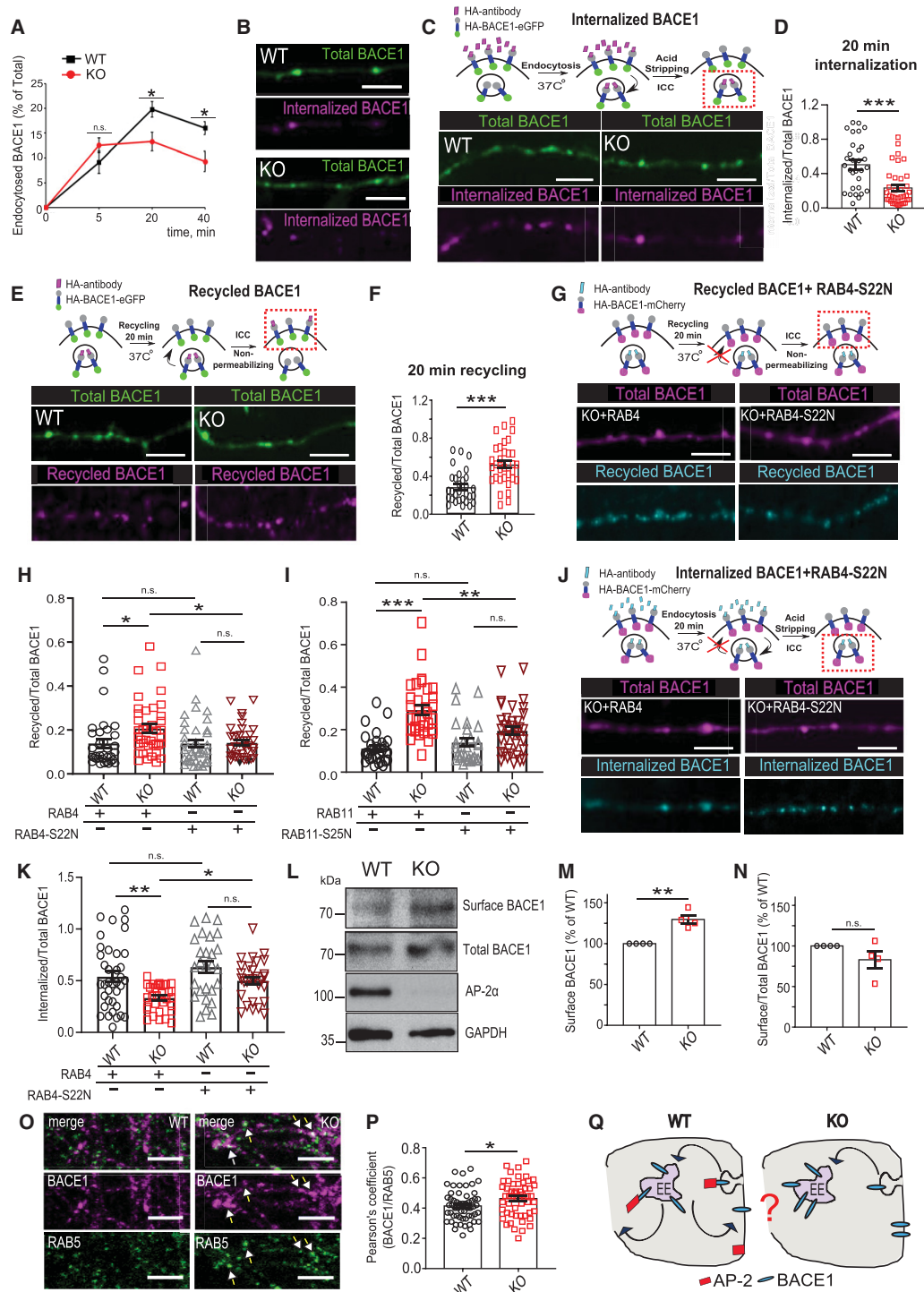


Figure 1.

Figure 1. AP-2 regulates BACE1 recycling and is mostly dispensable for BACE1 endocytosis.

- A BACE1 internalization kinetics after 20 min (WT: $19.79 \pm 1.89\%$, KO: $13.28 \pm 1.57\%$, $p^{\text{WT versus KO}} = 0.017$) and 40 min of HA antibody chase (WT: 15.99 ± 2.04 , KO: 9.29 ± 1.33 , $p^{\text{WT versus KO}} = 0.010$) is significantly decreased in AP-2 μ KO neurons (27 WT and 29 KO neurons).
- B Representative examples of internalized BACE1 after 5 min of HA antibody pulse in HA-BACE1-eGFP-overexpressing WT and KO neurons. Scale bar: 5 μm .
- C, D Internalized BACE1 levels after 20 min of HA antibody pulse in HA-BACE1-eGFP-overexpressing WT and KO neurons, calculated as the HA (internalized)/eGFP (total) signal intensity ratio (WT: 0.50 ± 0.052 , KO: 0.23 ± 0.036 , $P = 0.000$, 30 WT and 36 KO neurons, $N = 4$ biological replicates). Scale bar: 5 μm .
- E, F Recycled BACE1 levels after 20 min of HA antibody pulse in HA-BACE1-eGFP-overexpressing WT and KO neurons, calculated as the HA(recycled)/eGFP(total) signal intensity ratio (WT: 0.29 ± 0.031 , KO: 0.53 ± 0.040 , $P < 0.000$, 30 WT and 32 KO neurons, $N = 4$ biological replicates). Scale bar: 5 μm .
- G, H Recycled levels of BACE1 after 20 min of HA antibody pulse in HA-BACE1-mCherry-transfected WT and KO neurons, co-expressing either eGFP-RAB4 or eGFP-RAB4-S22N, calculated as the HA(recycled)/mCherry(total) signal intensity ratio (WT^{RAB4}: 0.14 ± 0.02 , KO^{RAB4}: 0.20 ± 0.02 , WT^{RAB4-S22N}: 0.14 ± 0.02 , KO^{RAB4-S22N}: 0.14 ± 0.01 , $p^{\text{WT}^{\text{RAB4}} \text{ versus } p^{\text{KO}^{\text{RAB4}}}} = 0.033$, $p^{\text{KO}^{\text{RAB4}} \text{ versus } p^{\text{KO}^{\text{RAB4-S22N}}}} = 0.035$, $p^{\text{WT}^{\text{RAB4-S22N}} \text{ versus } p^{\text{KO}^{\text{RAB4-S22N}}}} = 0.999$, $p^{\text{WT}^{\text{RAB4}} \text{ versus } p^{\text{WT}^{\text{RAB4-S22N}}}} > 0.999$, 34–38 neurons, $N = 4$ biological replicates). Scale bar: 5 μm .
- I Recycled levels of BACE1 after 20 min of HA antibody chase in HA-BACE1-mCherry-transfected WT and KO neurons, co-expressing either eGFP-RAB11 or eGFP-RAB11-S25N, calculated as the HA(recycled)/mCherry(total) signal intensity ratio (WT^{RAB11}: 0.11 ± 0.01 , KO^{RAB11}: 0.29 ± 0.02 , WT^{RAB11-S25N}: 0.14 ± 0.02 , KO^{RAB11-S25N}: 0.19 ± 0.02 , $p^{\text{WT}^{\text{RAB11}} \text{ versus } p^{\text{KO}^{\text{RAB11}}}} < 0.0001$, $p^{\text{WT}^{\text{RAB11}} \text{ versus } p^{\text{WT}^{\text{RAB11-S25N}}}} = 0.761$, $p^{\text{KO}^{\text{RAB11}} \text{ versus } p^{\text{KO}^{\text{RAB11-S25N}}}} = 0.001$, $p^{\text{WT}^{\text{RAB11-S25N}} \text{ versus } p^{\text{KO}^{\text{RAB11-S25N}}}} = 0.175$, 28–37 neurons per condition, $N = 3$ biological replicates).
- J, K Internalized levels of BACE1 after 20 min of HA antibody uptake in HA-BACE1-mCherry-transfected WT and KO neurons, co-expressing either eGFP-RAB4 or eGFP-RAB4-S22N, calculated as the HA(internalized)/mCherry(total) signal intensity ratio (WT^{RAB4}: 0.54 ± 0.05 , KO^{RAB4}: 0.33 ± 0.02 , WT^{RAB4-S22N}: 0.63 ± 0.06 , KO^{RAB4-S22N}: 0.50 ± 0.04 , $p^{\text{WT}^{\text{RAB4}} \text{ versus } p^{\text{KO}^{\text{RAB4}}}} = 0.004$, $p^{\text{KO}^{\text{RAB4}} \text{ versus } p^{\text{KO}^{\text{RAB4-S22N}}}} = 0.046$, $p^{\text{WT}^{\text{RAB4-S22N}} \text{ versus } p^{\text{KO}^{\text{RAB4-S22N}}}} = 0.182$, $p^{\text{WT}^{\text{RAB4}} \text{ versus } p^{\text{WT}^{\text{RAB4-S22N}}}} = 0.450$, 27–37 neurons per condition, $N = 3$ biological replicates). Scale bar: 5 μm .
- L, M BACE1 surface levels are increased in AP-2 μ KO neurons, when compared to the WT set to 100% (KO: $129.65 \pm 5.30\%$, $P = 0.005$, $N = 4$ biological replicates).
- N Surface versus total BACE1 ratio is not altered in AP-2 μ KO neurons when normalized to the WT set to 100% (KO: $83.02 \pm 10.93\%$, $P = 0.109$, $N = 4$ biological replicates).
- O, P Accumulation of endogenous BACE1 in RAB5-positive early endosomes, quantified using Pearson's co-localization coefficient (WT: 0.41 ± 0.01 , KO: 0.46 ± 0.02 , $p^{\text{WT versus KO}} = 0.021$, 58 WT and 54 KO neurons, $N = 4$ biological replicates). Scale bar: 10 μm . Arrows indicate BACE1 accumulation within RAB5-positive endosomes.
- Q Schematic illustration depicting the role of AP-2 in BACE1 endosomal trafficking.

Data information: Experimental designs are depicted in the top panels in (C, E, G, J), where analyzed BACE1 fraction is marked with the red square. All graphs show mean \pm SEM; statistical analysis was performed by unpaired two-tailed Student's *t*-test in (A, D, F, P), two-way ANOVA in (H, I, K), and one-sample Student's *t*-test in (M, N). n.s.—non-significant. * indicates $P \leq 0.05$; ** indicates $P \leq 0.01$; *** indicates $P \leq 0.001$.

being re-routed to the plasma membrane in AP-2 KO neurons. Since faster protein recycling should result in its accumulation on the plasma membrane surface, we performed biotinylation experiments to analyze the surface fraction of endogenous BACE1 in primary neurons lacking AP-2 μ . WT- and KO-cultured neurons were incubated with non-permeable biotin moieties at 4°C to tag protein domains at the extracellular level. After probing the extracted biotinylated proteins with the BACE1 antibody, we found that although a small fraction of BACE1 was localized at the plasma membrane of AP-2 μ KO neurons, this was not significant when normalized to total BACE1 protein levels (Figs 1L–N and EV1P), suggesting that faster recycling of BACE1 is accompanied by its intracellular retention in the KO condition. These data, together with the fact that more BACE1 was detected in AP-2 μ KO RAB5-positive early endosomes (Figs 1O and P, and EV1Q–S), indicate that AP-2 μ regulates BACE1 endosomal trafficking via a previously undescribed mechanism (Fig 1Q). Interestingly, although the data described above reveal that AP-2 is not absolutely required for BACE1 endocytosis, we found that it was indispensable for internalization of GABA_A receptor $\beta 3$ subunit (GABAR $\beta 3$) (Fig EV1T and U), another known cargo of AP-2 [36], suggesting a cargo-specific role for AP-2 in endocytosis in neurons.

BACE1 delivery to lysosomes is defective in AP-2 KO neurons

To further analyze the role of AP-2 in BACE1 intracellular trafficking, we examined BACE1 protein levels in cell lysates derived from the cortex of neuron-confined AP-2 μ KO mice (*Ap2m1*^{lox/lox}; *Tubulin 1 α* Cre) [32] (Fig EV2A–C). Using this model, we have previously shown that the levels of major endocytic proteins are

unaltered in the absence of AP-2 [32]. Since mice lacking AP-2 μ in neurons have been previously reported to die after postnatal day (p) 22, all subsequent *in vivo* experiments were performed with mice between p18 and p21 (Kononenko *et al*, 2017). In agreement with our data in cultured neurons (Figs EV1P and EV2D–G), we found that BACE1 protein levels were almost fivefold upregulated in cortical brain lysates lacking AP-2 μ (Fig 2A and B). BACE1 immunofluorescence levels were also significantly higher in the entorhinal cortex from AP-2 μ KO mice (Fig 2C and D). Moreover, our data revealed that while in control neurons, BACE1 was distributed longitudinally along the neurites, deletion of AP-2 μ resulted in large 3–5 μm spheroid-like accumulations of BACE1 distally from the cell body (Fig 2E and F). These changes in the protein level were not accompanied by upregulation of BACE1 gene expression (Fig EV2H), indicating that AP-2 regulates BACE1 proteins levels via a post-translational mechanism. Since BACE1 is known to be degraded via the lysosomal pathway [37], we postulated that the intracellular accumulation of BACE1 in neurons lacking AP-2 μ might result from its inefficient targeting to lysosomes and, thus, impaired BACE1 degradation. To test this hypothesis, we first analyzed the amount of BACE1 stalled within autophagosomes and late endosomes in control and AP-2 μ KO neurons. In agreement with our previous data (Kononenko *et al*, 2017), we observed significantly more autophagosomes in neurons lacking AP-2 μ that contained significantly more BACE1 when compared to control neurons (Figs 2G and H, and EV2I). Furthermore, increased amount of BACE1 was associated with organelles expressing late-endosomal marker RAB7A (Figs 2I and J, and EV2J). These data were also corroborated by significantly higher co-localization of BACE1 with RAB7A in the entorhinal cortex of AP-2 μ KO mice when compared

to their control littermates, while levels of lysosomal marker LAMP2a and neuronal marker MAP2 were not altered (Figs 2K and L, and EV2K and L). Since an increase in BACE1 protein levels in AP-2 μ KO neurons persisted upon inhibition of protein synthesis (Fig EV2M) and significantly less BACE1 was localized to AP-2 KO lysosomes (Fig 2M–O), we directly tested the hypothesis of delayed delivery of BACE1 to lysosomes under the AP-2 μ KO condition. We engineered a construct expressing BACE1 C-terminally tagged with monomeric Keima-Red (mKeima). mKeima is a coral-derived acid-stable fluorescent protein emitting different colored signals at acidic and neutral pH [38] (Fig 2P), which can be used as a reporter of cargo delivery to lysosomes (Fig EV2N and O). We expressed BACE1-mKeima-Red in cultured WT and AP-2 μ KO neurons and analyzed the 550 nm (acid pH)/438 nm (neutral pH) signal intensity ratio using live-cell confocal microscopy. The amount of BACE1 found in lysosomes of AP-2 μ KO neurons was significantly reduced when compared to control condition (Fig 2Q–S). Interestingly, in the absence of AP-2 the majority of BACE1-mKeima organelles with neutral pH was confined to distal processes (Fig EV2P). Taken together, our data indicate that AP-2 regulates BACE1 delivery to lysosomes in neurons.

AP-2 regulates intracellular transport of BACE1 in axons

What is the mechanism by which AP-2 controls lysosomal targeting of BACE1? We previously identified a novel non-canonical function of AP-2 in retrograde trafficking of TRKB receptors in the axon [32]. To test whether AP-2 also regulates the transport of cargo containing BACE1 vesicles, we first monitored the dynamics of co-traffic of AP-2 μ -mCherry and HA-BACE1-eGFP in cultured neurons by live imaging. Tagged AP-2 μ and BACE1 [23,39] were shown functional, since (i) AP-2 μ -mCherry was able to rescue clathrin-mediated endocytosis of transferrin in cells depleted for endogenous AP-2 μ (Fig EV3A and B), (ii) AP-2 μ -mCherry was substantially colocalized with endogenous AP-2 α upon its overexpression in neurons (Fig EV3C and D), (iii) HA-BACE1-eGFP increased β -site cleavage of APP, monitored by the levels of A β in HA-BACE1-eGFP-overexpressing cultured neurons (Fig EV3E and F), and iv) kinetics of retrograde BACE1 transport obtained in neurons overexpressing the HA-BACE1-eGFP were similar to velocities in neurons overexpressing the BACE1-eGFP (Fig EV3G). Using these constructs, we observed a close co-localization and co-traffic of AP-2 μ with BACE1 in axons (Figs 3A and B, and EV3H and I). Strong co-localization was also observed for endogenous proteins, labeled with specific antibodies (Fig EV3J and K). Next, we probed whether AP-2 is functionally required for BACE1 transport in neurons by analyzing the transport of BACE1-positive carriers in axons of WT and AP-2 μ KO neurons expressing the HA-BACE1-eGFP or BACE1-eGFP. In WT, axons around 40% of BACE1 puncta displayed bi-directional movement with an average velocity of about 0.4 μ m/s, consistent with previously described kinetics of BACE1 trafficking *in vivo* [40] (Fig 3C). In contrast, both the axonal motility and the velocity of BACE1 vesicles were greatly reduced in AP-2 μ KO axons (Figs 3D and E, and EV3M and N). This phenotype was specific since the re-expression of AP-2 μ restored the defective transport of BACE1 carriers (Fig 3F and G). Our previously published data indicate that AP-2 mediates the retrograde transport of axonal cargo via the association of its large brain-specific isoform

AP-2 α with the autophagy modifier protein LC3B (microtubule-associated protein 1A/1B light chain 3) and that its absence impairs retrograde transport of LC3-containing cargo and autophagosome processing in neurons [32]. Since a fraction of axonal BACE1 is known to be retrogradely transported in autophagosomes [41], we hypothesized that defective degradation of BACE1 in AP-2 μ KO neurons might result from its impaired axonal transport in autophagosomes. Live-cell imaging experiments revealed that axonal mobility and specifically the retrograde movement of BACE1-containing carriers positive for LC3B were greatly reduced in AP-2 μ KO neurons (Figs 3H and I, and EV3O). A similar result was obtained by the overexpression of LC3 binding-deficient mutant of AP-2 α in control neurons (Fig 3J and K). In agreement with recently published data [41], autophagosomes were required for efficient transport of BACE1, since significantly reduced axonal mobility of BACE1 was also observed in neurons lacking ATG5, an E3-like ligase mediating autophagosome expansion and maturation [42] (Fig EV3P and Q). Finally, to directly test whether BACE1 requires AP-2 for its trafficking in neurons, we overexpressed AP-2 binding-deficient mutant of BACE1 ([23], LL/AA mutant) in control neurons and measured BACE1 velocity using live-cell imaging. Interestingly, both the axonal mobility and the velocity of BACE1 vesicles were significantly reduced in neurons overexpressing BACE1 di-leucine mutant, when compared to neurons expressing the wild-type BACE1 (Fig 3L–N). Furthermore, this defect was accompanied by increased recycling of endocytosed BACE1 to the plasma membrane, in agreement with [22,25], and impaired BACE1 delivery to lysosomes, similar to the phenotype described in neuroglioma cells [43] (Fig EV3R–U). Together, these data suggest that AP-2 regulates BACE1 protein levels in primary neurons via functioning downstream of BACE1 endocytosis, regulating BACE1 endosomal trafficking and its delivery to lysosomes (Fig 3O).

AP-2 prevents amyloidogenic processing of APP

Given the significant defect in transport and lysosomal targeting of BACE1 in AP-2 μ KO neurons, we next explored the functional importance of AP-2 for amyloidogenic processing of APP. First, we tested whether BACE1 retains its β -secretase activity in AP-2 μ KO neurons by taking advantage of Lys612Val mutant of APP (mCherry-APP-P1-eGFP), which can be cleaved almost exclusively by BACE1 due to its inefficient cleavage by α -secretase [44]. This construct has been previously shown to be correctly expressed and targeted to the plasma membrane and intracellular organelles in neurons [45]. Once BACE1 cleaves the mCherry-containing N-terminal domain of the APP, the fluorescence intensity ratio between the green and the red signals increases (Fig EV4A). By analyzing the eGFP/mCherry signal intensity ratio in WT and AP-2 μ KO neurons, we found that BACE1-dependent APP cleavage was significantly higher in neurons lacking AP-2 μ (Figs 4A and B, and EV4B), indicating that stalled BACE1 retains its β -secretase activity. These data, taken together with the fact that significantly more APP puncta contained BACE1 in AP-2 μ KO neurons (Fig EV4C–E), suggest that increased amount of intracellular BACE1 might facilitate APP processing in AP-2-deficient brains. In agreement with this hypothesis, increased levels of C-terminal APP fragments (CTFs) were detected in brain sections from the entorhinal cortex of AP-2 KO mice, while the levels of Reelin (used as a marker of entorhinal

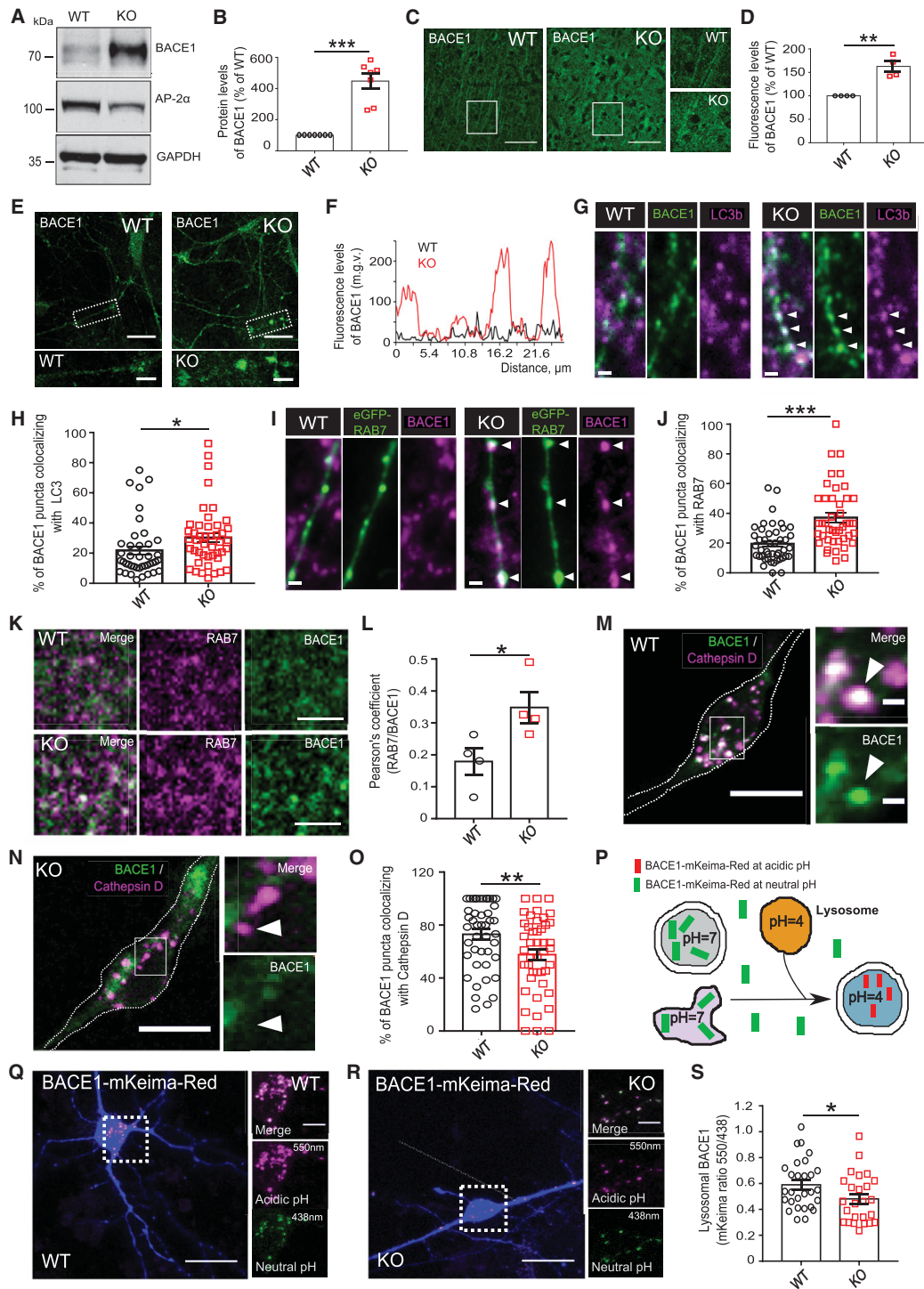


Figure 2.

Figure 2. AP-2 is required for lysosomal targeting of BACE1.

A, B BACE1 protein levels in cortical lysates of WT and AP-2 μ KO mice. Protein levels in the KO were normalized to the WT set to 100% (KO: 447.64 \pm 48.78%, $P < 0.000$, $N = 7$ biological replicates).

C, D Immunofluorescence levels of BACE1 are significantly increased in the cortex of AP-2 μ KO mice when normalized to the WT set to 100% (KO: 162.714 \pm 11.082%, $P = 0.005$, $N = 4$, biological replicates). Scale bar: 100 μ m.

E Localization of BACE1 in cultured WT and AP-2 μ KO neurons. Scale bars: 20 μ m, 5 μ m (inserts).

F Line plot of BACE1 immunofluorescence along the neurites indicated in (E).

G, H Percentage of BACE1 puncta colocalizing with the LC3b (WT: 21.75 \pm 2.88, KO: 30.28 \pm 2.97, $P = 0.043$, WT = 41, KO = 45 neurons, $N = 4$ biological replicates). Scale bar: 2 μ m. Arrowheads indicate BACE1 accumulation within LC3b-positive organelles.

I, J Percentage of BACE1 puncta colocalizing with the eGFP-RAB7 (WT: 19.54 \pm 1.91, KO: 37.09 \pm 3.13%, $P < 0.000$, WT = 44 and KO = 43 neurons, $N = 4$ biological replicates). Scale bar: 2 μ m. Arrowheads indicate BACE1 accumulation within RAB7-positive organelles.

K, L Co-localization of BACE1 and RAB7A in cortical sections of WT and AP-2 μ KO brains, quantified using Pearson's co-localization coefficient (WT: 0.18 \pm 0.04, KO: 0.35 \pm 0.05, $P = 0.038$, $N = 4$ biological replicates). Scale bar: 10 μ m.

M, N Representative fluorescence images of WT and AP-2 μ KO neurons transfected with HA-BACE1-mCherry and immunostained for Cathepsin D. Channels were false color-coded to better illustrate the co-localization. Scale bars: 10 μ m. Arrowheads indicate BACE1 accumulation in lysosomes in the WT, and its absence in the KO. Dotted line outlines the neuron.

O Lysosomal localization of BACE1 is decreased in KO neurons (WT: 73.05 \pm 3.80, KO: 57.68 \pm 4.28, $P = 0.008$, 45 WT and 44 KO neurons, $N = 4$ biological replicates).

P Schematic illustration of BACE1 delivery to lysosomes monitored via BACE1-mKeima-Red.

Q, R Representative fluorescence images of WT and AP-2 μ KO neurons transfected with BACE1-mKeima-Red and co-transfected with eBFP to reveal the neuronal morphology. Scale bars: 10 μ m, 2 μ m in zoomed images.

S The 550 nm/438 nm signal intensity ratio of BACE1-mKeima-Red quantified over the entire cell is significantly reduced in the KO condition compared to the WT (WT: 0.59 \pm 0.04, KO: 0.48 \pm 0.04, $P = 0.041$, 28 WT and 25 KO neurons, $N = 3$ biological replicates).

Data information: All graphs show mean \pm SEM; statistical analysis was performed by unpaired two-tailed Student's t -test in (H, J, L, O, S) and one-sample Student's t -test in (B, D). n.s.—non-significant. * indicates $P \leq 0.05$; ** indicates $P \leq 0.01$; *** indicates $P \leq 0.001$.

cortex layer II and a negative control) were unaltered (Figs 4C and D, and EV4F). Increased activity of BACE1 in brains lacking AP-2 μ was also confirmed by analyzing the cleavage of another BACE1 substrate L1 [46], whose processing was significantly elevated in AP-2 KO mice (Fig EV4G and H).

To precisely characterize the pathway responsible for increased CTF generation in AP-2 KO brains, we quantified the processing of APP in brain lysates from neuronal-confined AP-2 μ KO mice by Western blotting. In agreement with published data [44], we found that under physiological conditions, the majority of APP was cleaved by the α -secretase pathway, with CTF 83 being the predominant form of APP C-terminal fragments in WT cortical lysates (Fig 4E). Interestingly, in the cortex of AP-2 μ KO mice more APP was undergoing β -secretase-dependent cleavage, monitored by the levels of CTF 99 fragment (Fig 4F). These changes were, however, accompanied by an upregulation in CTF 83 (Fig 4G), likely as a consequence of increased α -secretase cleavage due to slightly higher amounts of APP present on the surface of AP-2 μ KO neurons (Fig EV4I and J). This accumulation of APP-CTFs was not a result of an increase in total APP levels (Fig 4H) and was unlikely mediated by the γ -secretase, because no change in the level of γ -secretase component Nicastrin was detected in AP-2 μ KO brains (Figs 4I and EV4K).

The inhibition of clathrin-mediated APP endocytosis by mutation of its C-terminally located internalization motif "YENPTY" increases soluble sAPP α secretion and reduces A β production [47]. To investigate whether defective endocytosis of APP in AP-2 μ -deficient neurons might result in a decrease in A β ₁₋₄₀ and A β ₁₋₄₂ peptide production, we monitored the levels of intracellular A β ₁₋₄₀ and A β ₁₋₄₂ in AP-2 μ KO axons using mouse monoclonal 12F4 and AB40.1 antibodies recognizing A β ₁₋₄₂ and A β ₁₋₄₀, respectively [48,49]. In contrary to the prediction above, we observed a significant rise of intracellular A β ₁₋₄₀ and A β ₁₋₄₂ peptides in neurons depleted for AP-2 μ (Fig 4J–M), a phenotype accompanied by a specific accumulation of A β ₁₋₄₂ within AP-2 KO autophagosomes (Fig EV4L and M). These changes were paralleled by an increase in the ratio of extracellular

A β ₁₋₄₂/A β ₁₋₄₀, likely due to a significant decrease in A β ₁₋₄₀ secretion (Figs 4N and EV4N and O), strongly suggesting that AP-2 functions not only upstream at the APP endocytosis level, but also downstream of the production of C99. With its ability to bind and traffic BACE1 toward lysosomal organelles (Figs 2 and 3), we next asked whether AP-2 mediates A β generation via BACE1-dependent pathway. Overexpression of fully endocytosis-competent LC3 binding-deficient mutant of AP-2 α _A [32] in control neurons produced an increase in BACE1 protein levels and a concomitant upregulation of A β ₁₋₄₂ peptide (Figs EV4P–R and 4O–Q). On the other hand, shRNA-mediated *Bace1* knockdown (KD) (Fig EV4S and T) significantly reduced A β ₁₋₄₂ peptide levels in AP-2 μ KO neurons, indicating that elevated levels of BACE1 in KO condition were directly responsible for increased amyloidogenic processing of APP (Fig 4R–T). Of note, A β ₁₋₄₂ peptide levels were not significantly altered by BACE1 KD in WT neurons. This is in agreement with a small effect of BACE1 KO on CTF99 levels [50], likely due to insensitivity of conventional protein detection techniques in analyzing the A β ₁₋₄₂ picogram range changes in the control condition [51]. The A β ₁₋₄₂ peptide accumulation in AP-2 KO neurons was due to the lost interaction of BACE1 with the AP-2, since elevated A β ₁₋₄₂ levels were detected in control neurons overexpressing AP-2 binding-deficient mutant of BACE1 (LL/AA) (Fig 4U and V) and were rescued upon re-expression of AP-2 μ in AP-2 KO neurons (Fig EV4U and V). Collectively, these data indicate that AP-2 regulates BACE1 trafficking in neurons to prevent amyloidogenic processing of APP.

Downregulation of BACE1 rescues amyloidogenesis and mitigates synapse loss in AP-2 KO neurons

Accumulations of A β are a hallmark of AD, and a recent transcriptome-wide association study identifies AP-2 α subunits as late-onset AD-associated genes [52]. Since decreased levels of AP-2 α , but not the AP-1 γ 1, were detected in iPSC-derived neurons from patients with late-onset AD (Figs 5A and B, and EV5A), we next asked

whether increased amyloidogenic processing of APP in neurons lacking AP-2 is relevant for AD-associated synaptic pathology. Previously, we have shown that AP-2 is not required for brain

development and functions to maintain the neuronal complexity [32]. To directly address the role of AP-2 in spine morphology *in vivo*, we adopted the AAV-mediated gene KD approach. To this

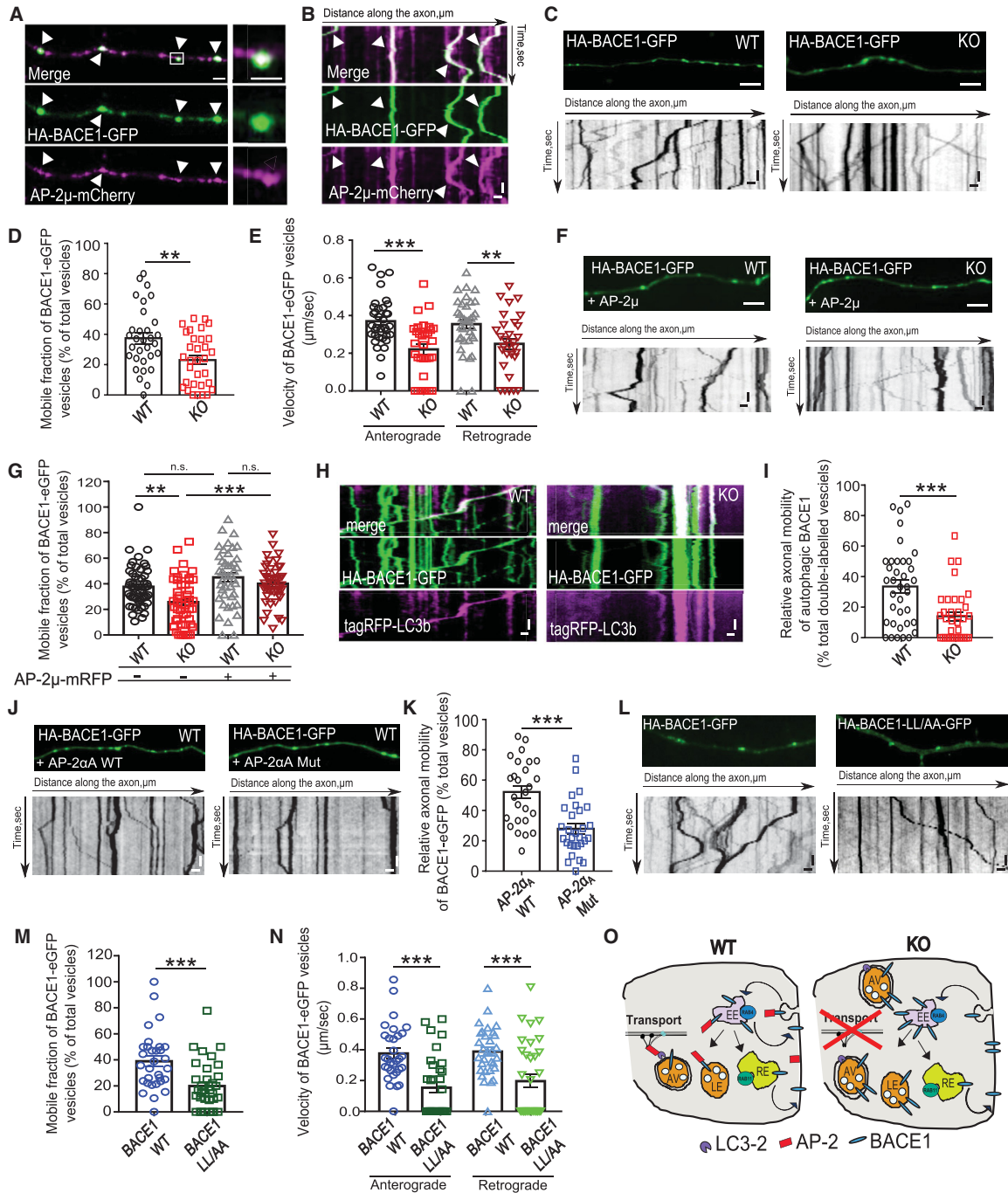


Figure 3.

Figure 3. AP-2 regulates axonal transport of BACE1.

A, B Representative fluorescence images (A) and corresponding kymographs (B) from time-lapse videos of control neurons transfected with HA-BACE1-eGFP and co-transfected with AP-2 μ -mCherry. Scale bars: (A) 2 μ m, 1.6 μ m inserts, (B) x = 2 μ m, y = 5s. Arrowheads in (A) correspond to BACE1 carriers indicated by the same arrowheads in (B).

C Representative fluorescence images and corresponding kymographs from time-lapse videos of WT and AP-2 μ KO neurons transfected with HA-BACE1-eGFP. Scale bar: 5 μ m top panels, x = 2 μ m, y = 5s bottom panels.

D Loss of AP-2 μ significantly decreases the BACE1 motility (WT: $37.42 \pm 3.79\%$, KO: $23.07 \pm 3.07\%$, $P = 0.003$, WT = 31, KO = 32 neurons, $N = 4$ biological replicates).

E Loss of AP-2 μ significantly decreases the anterograde and retrograde BACE1 velocity (WT^{Antero}: 0.37 ± 0.02 μ m/s, KO^{Antero}: 0.22 ± 0.03 μ m/s, $p_{WT^{Antero} \text{ versus } p_{KO^{Antero}}} < 0.000$; WT^{Retro}: 0.35 ± 0.02 μ m/s, KO^{Retro}: $0.25 \pm .03$ μ m/s, $p_{WT^{Retro} \text{ versus } p_{KO^{Retro}}} = 0.006$, WT = 35 and KO = 32 neurons, $N = 4$ biological replicates).

F Representative fluorescence images and corresponding kymographs from time-lapse videos of WT and AP-2 μ KO neurons co-transfected with HA-BACE1-GFP and AP-2 μ -mRFP. Scale bar: 5 μ m top panels, x = 2 μ m, y = 5s bottom panels.

G Bi-directional mobility of BACE1 carriers in WT and AP-2 μ KO neurons, co-expressing the AP-2 μ -mRFP (WT: $37.60 \pm 2.20\%$, KO: $25.61 \pm 2.67\%$, WT^{AP-2 μ -mRFP}: $45.04 \pm 3.27\%$, KO^{AP-2 μ -mRFP}: $40.07 \pm 2.37\%$, $p_{WT \text{ versus } KO} = 0.005$, $p_{KO \text{ versus } KO+AP-2\mu-mRFP} < 0.000$, $p_{WT \text{ versus } WT+AP-2\mu-mRFP} = 0.186$, $p_{WT+AP-2\mu-mRFP \text{ versus } KO+AP-2\mu-mRFP} = 0.570$, 43–53 neurons per condition, $N = 4$ biological replicates).

H Representative kymographs of WT and AP-2 μ KO neurons co-expressing the HA-BACE1-GFP and tagRFP-LC3B. Scale bars: x = 2 μ m, y = 5 s.

I Reduced bi-directional mobility of BACE1-containing autophagosomes in AP-2 μ KO neurons (WT: $33.53 \pm 4.19\%$, KO: $19.45 \pm 5.14\%$, $P = 0.000$, WT = 37 and KO = 35 neurons, $N = 4$ biological replicates).

J Representative kymographs of WT neurons co-expressing HA-BACE1-GFP and AP-2 α_A WT or AP-2 α_A Mut. Scale bar: 5 μ m top panels, x = 2 μ m, y = 5 s bottom panels.

K Mobility of BACE1 carriers is significantly decreased in neurons overexpressing the AP-2 α_A Mut compared to neurons expressing the AP-2 α_A WT (WT: $52.23 \pm 4.16\%$, Mut: 27.95 ± 3.31 , $P = < 0.000$, WT = 26 and Mut = 29 neurons, $N = 4$ biological replicates).

L Representative fluorescence images and corresponding kymographs from time-lapse videos of WT neurons transfected with either HA-BACE1-GFP or HA-BACE1-LL/AA-GFP. Scale bar: 5 μ m top panels, x = 2 μ m, y = 5 s bottom panels.

M Reduced mobility of BACE1-LL/AA-positive vesicles, when compared to WT BACE1 (WT: $38.97 \pm 1.40\%$, LL/AA: $19.89 \pm 1.77\%$, $P < 0.000$, WT = 31 and LL/AA = 33 neurons, $N = 4$ biological replicates).

N Reduced velocity of BACE1-LL/AA-positive vesicles, when compared to WT BACE1 (WT^{Antero}: 0.38 ± 0.03 μ m/s, LL/AA^{Antero}: 0.15 ± 0.03 μ m/s, $p_{WT^{Antero} \text{ versus } p_{LL/AA^{Antero}}} < 0.000$; WT^{Retro}: 0.39 ± 0.03 μ m/s, LL/AA^{Retro}: $0.25 \pm .03$ μ m/s, $p_{WT^{Retro} \text{ versus } p_{LL/AA^{Retro}}} = 0.000$, WT = 31 and LL/AA = 33 neurons, $N = 4$ biological replicates).

O Schematic illustration of how AP-2 regulates BACE1 intracellular trafficking and transport in neurons.

Data information: All graphs show mean \pm SEM; statistical analysis was performed by unpaired two-tailed Student's t-test in (D, E, I, K, M, N) and two-way ANOVA in (G). n.s.—non-significant. * indicates $P \leq 0.05$; ** indicates $P \leq 0.01$; *** indicates $P \leq 0.001$.

aim, we stereotactically delivered either control AAV-GFP^{CamKII α} vector or vector expressing Cre-GFP^{CamKII α} into the dentate gyrus of 9-week-old AP-2 μ lox/lox mice. We observed that 4 weeks postinjection, AAV-Cre-GFP^{CamKII α} -expressing granule neurons possessed significantly less dendritic spines, suggesting that AP-2 regulates synaptic density in mature brain (Fig 5C and D). In fact, dendritic spine density was also reduced in granule cells of neuronal-confined AP-2 KO (*Ap2m1*^{lox/lox}; *Tubulin 1 α* Cre) mice described earlier (Fig EV5B) and in primary hippocampal-cortical KO neurons (Fig EV5C and D). This phenotype was accompanied by a significant reduction in the co-localization of pre- and postsynaptic markers (Figs 5E and F, and EV5E) and was specific to AP-2 loss, since the re-expression of AP-2 μ restored synaptic density in AP-2 μ KO neurons (Fig EV5F and G). Next, we asked whether the loss of AP-2 μ in neurons causes cognitive dysfunction akin to changes reported for transgenic AD mouse models [53] and human patients [54]. We performed the novel object recognition task, which is widely used to assess the recognition memory decline in mice [55]. During the training session, both control and KO mice did not show a preference for either of two identical objects (Fig EV5H and I). Twenty-four hours later, control animals clearly favored the novel object compared to the familiar object, while AP-2 μ KO mice showed a significantly decreased preference toward the novel object, an indicator of impaired memory on novelty preference (Figs 5G and H, and EV5J). Remarkably, AP-2 μ KO mice were also significantly more active in the open field (Fig 5I and J), in agreement with the reported hyperactivity of AD mouse models [56,57].

Is increased amyloidogenic processing of APP due to the elevated levels of BACE1 directly responsible for synaptic dysfunctions observed in AP-2 μ KO mice? To answer this question, we used the

shRNA-mediated *Bace1* knockdown (KD) approach. We found that reduced synaptic density (Fig 5K and L) was rescued in AP-2 μ KO neurons deficient for BACE1. Lastly, to study the role of BACE1-mediated APP processing in AP-2 μ KO brains *in vivo*, we quantified the cell number and levels of APP-CTFs in the entorhinal cortex of AP-2 μ KO mice haploinsufficient for BACE1. Strikingly, BACE1 haploinsufficiency was enough to prevent the neurodegeneration, cell death, and APP-CTF accumulation in AP-2 μ KO brains (Figs 5M–Q and EV5K–M). These results confirm our observations from cultured AP-2 μ KO neurons and suggest that neuronal AP-2 prevents amyloidogenesis via regulating the intracellular levels of BACE1 in the brain.

Taken together, our results reveal a novel function for AP-2 in the regulation of APP processing and A β generation in neurons via promoting the intracellular trafficking and degradation of BACE1 (Fig 6). This function of AP-2 is independent of its role in BACE1 endocytosis and requires its association with LC3-containing autophagosomes, suggesting a combined pharmacological targeting of endocytic adaptors and autophagy as a new therapy for reducing the levels of A β in the AD brain.

Discussion

Our data reported here reveal an unexpected function for endocytic adaptor protein AP-2 in neurons, where it functions as a critical regulator of amyloidogenesis. We show that AP-2 controls neuronal APP processing by regulating the intracellular trafficking of BACE1. Loss of AP-2 μ causes stalling of BACE1-containing autophagosomes in axons, a phenotype that facilitates the intracellular generation of A β _{1–40} and A β _{1–42}.

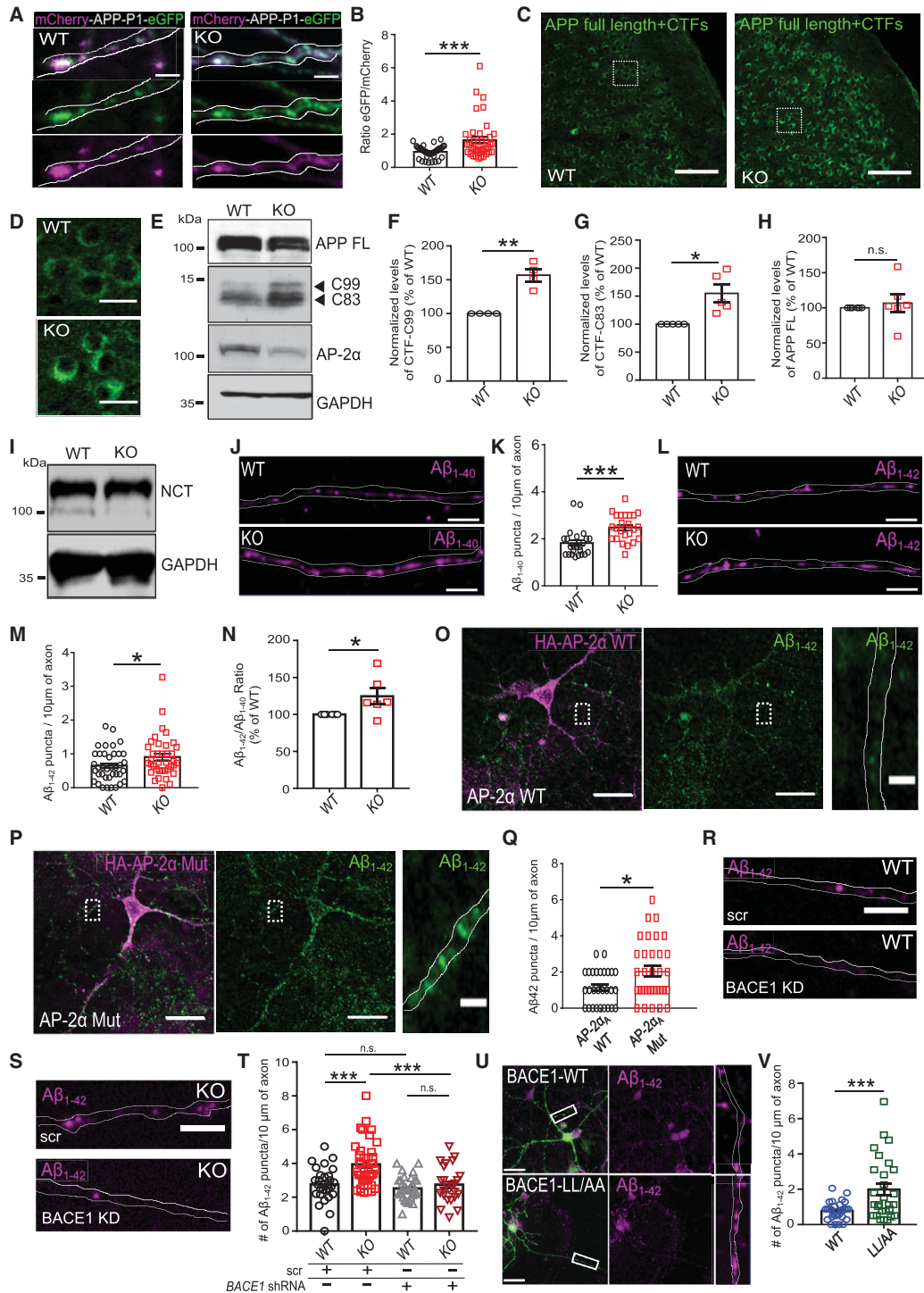


Figure 4.

Figure 4. AP-2 prevents amyloidogenic processing of APP in neurons.

A, B The eGFP/mCherry signal intensity ratio is significantly increased in mCherry-APP-P1-eGFP-expressing KO neurons comparing to the WT (WT: $0.94 \pm 0.06\%$, KO: 1.65 ± 0.18 , $P = 0.000$, WT = 39 and KO = 41 neurons, $N = 5$ biological replicates). Scale bars: 2 μm .

C, D Confocal images of WT and AP-2 μ KO entorhinal cortex immunostained with antibody recognizing total APP and APP-CTFs. Scale bars: 100 μm (C), 20 μm (D).

E–G Levels of APP-CTFs are significantly increased in AP-2 μ KO cortex compared to the WT set to 100% (KO^{C99}: $156.65 \pm 8.37\%$, $P = 0.004$, $N = 4$ biological replicates; KO^{C83}: $154.79 \pm 15.6\%$, $P = 0.012$; $N = 5$ biological replicates).

H Levels of full-length (FL) APP are unaltered in AP-2 μ KO cortex (KO^{APP FL}: $106.64 \pm 12.96\%$, $P = 0.315$, $N = 6$ biological replicates).

I Levels of Nicastrin (NCT) are unaltered in the AP-2 μ KO cortex (see also Fig EV4K).

J, K Intracellular levels of A β_{1-40} are significantly increased in AP-2 μ KO axons compared to the WT (WT^{A β_{1-40}} : 1.82 ± 0.12 , KO^{A β_{1-40}} : 2.45 ± 0.12 , $P = 0.000$, WT = 24 and KO = 24 neurons, $N = 3$ biological replicates). Scale bars, 5 μm .

L, M Intracellular levels of A β_{1-42} are significantly increased in AP-2 μ KO axons (WT^{A β_{1-42}} : 0.65 ± 0.08 , KO^{A β_{1-42}} : 0.91 ± 0.10 , $P = 0.046$, WT = 38 and KO = 38 neurons, $N = 3$ biological replicates). Scale bar: 5 μm .

N Significantly increased ratio of A β_{1-42} /A β_{1-40} measured by ELISA in the media of cultured AP-2 μ KO neurons compared to the WT set to 100% (KO: $124.57 \pm 10.97\%$, $P = 0.037$, $N = 6$ biological replicates).

O–Q Accumulation of intracellular A β_{1-42} in neurons overexpressing the AP-2- α -Mut comparing to neurons expressing the AP-2- α -WT (WT: 1.14 ± 0.18 , Mut: 2.06 ± 0.29 , $P = 0.011$, WT = 28 and Mut = 33 neurons, $N = 4$ biological replicates). Scale bars: 20 μm , 2 μm (inserts).

R–T Accumulation of intracellular A β_{1-42} is rescued upon BACE1 knockdown in AP-2 μ KO neurons (WT^{scr}: 2.76 ± 0.20 , KO^{scr}: 3.94 ± 0.21 ; WT^{shBACE1}: 2.52 ± 0.12 ; KO^{shBACE1}: 2.74 ± 0.21 ; pWT^{scr} versus pKO^{scr} = 0.000, pKO^{scr} versus pKO^{shBACE1} = 0.826; pWT^{shBACE1} versus pKO^{shBACE1} = 0.863; 27–39 neurons per condition, $N = 3$ biological replicates). Scale bar: 10 μm .

U, V Levels of intracellular A β_{1-42} are significantly upregulated in neurons overexpressing the HA-BACE1-LL/AA-GFP comparing to neurons expressing the HA-BACE1-GFP (BACE1: 0.78 ± 0.90 , BACE1-LL/AA: 1.99 ± 0.33 , $P = 0.000$, 28–29 neurons per condition, $N = 3$ biological replicates). Scale bar, 50 μm .

Data information: All graphs show mean \pm SEM; statistical analysis was performed by unpaired two-tailed Student's *t*-test in (B, K, M, N, Q, V), two-way ANOVA in (T), and one-sample Student's *t*-test in (F–H). n.s.—non-significant. * indicates $P \leq 0.05$; ** indicates $P \leq 0.01$; *** indicates $P \leq 0.001$.

Neuronal loss in AD is accompanied by the progressive accumulation of A β [1] and the presence of autophagosomes [58]. In neurons, unlike non-neuronal cells, the formation of autophagosomes and their turnover are spatially segregated, since autophagosomes are generated in distal axons and retrogradely transported along microtubules to the cell soma, which contains the majority of lysosomes [59]. Neuronal autophagy is regulated by a variety of cues, including endocytic adaptor proteins [60], which supply the plasma membrane for autophagosome formation [61] and regulate autophagosomal transport [32]. However, whether autophagosome trafficking mediated by endocytic adaptors regulates A β levels in the brain was previously unknown. Here, we report that endocytic adaptor AP-2 prevents amyloidogenic processing of APP via regulating *en route* trafficking of BACE1 toward lysosomes. Our data are in agreement with several studies indicating autophagosomes as an alternative site of A β generation in neurons [58,62,63] and suggest that autophagosome stalling observed in AD mouse models and human patients might be responsible for A β deposition in the brain.

Our results support the hypothesis according to which dysfunctional endosomal trafficking might underlie the earliest pathology of AD. Indeed, the presence of enlarged early endosomes precedes the A β peptide inclusions in patients with sporadic late-onset AD [64,65], while substantial number of the newly identified AD risk loci encodes proteins that function predominantly in endocytic trafficking, including PICALM, BIN1, and SORL1 [66]. To date, only a few studies examined the precise role of endocytic proteins in AD [33,67,68], and whether abnormal endosomal recycling in late-onset AD patients is a consequence of endocytic protein loss-of-function is currently unknown. We find that the endocytic complex AP-2, a clathrin adaptor, previously shown to be not essential for CME in neurons [30,31], but to function in synaptic vesicle reformation [30] and autophagosome transport [32], regulates intracellular trafficking of BACE1. We show that endocytic adaptor AP-2 is downregulated in iPSC-derived neurons from AD patients with carrying the *TREM2*^{R47H} risk variant, which is one of the strongest single allele genetic risk factor for sporadic late-onset AD [69]. These results taken together with a recent finding, revealing endocytosis among seven most

downregulated gene sets in the hippocampus of late-onset AD *TREM2*^{R47H} patients [preprint: 70], suggest an existing hypothesis that *TREM2*^{R47H}-induced immune response in microglial cells might transcriptionally regulate AP-2 levels in brains of AD patients. Our data demonstrate that AP-2 prevents A β generation by controlling the degradation of endosomal BACE1 and this function of AP-2 is of particular relevance for recognition memory in mice which is akin to the phenotype described for sporadic AD patients [54]. Our results are in line with a recent transcriptome-wide association study, which identifies both α subunits of the AP-2 complex as late-onset AD-associated genes [52]. Together with an earlier report indicating decreased expression levels of AP-2 α in the AD brain [71], our findings suggest that AP-2 changes observed in *TREM2*^{R47H}-carrying AD patients could partially be responsible for increased amyloidogenic processing of APP in the AD brain. However, further studies are needed to better delineate whether there is a relationship between *TREM2*^{R47H}-induced inflammatory response, AP-2 levels, and neuritic plaque deposition in human AD patients.

Several lines of evidence suggest that the role of AP-2 in trafficking of BACE1 is independent of its established role in endocytosis and requires the recently described interaction of AP-2 with autophagosomes [32]. First, we find that AP-2 is not essential for BACE1 endocytosis, but is required for its endosomal delivery to lysosomes (Figs 1 and 2). Second, AP-2 is associated and co-trafficked with BACE1-positive carriers in axons (Fig 3). Third, we show that defective BACE1 trafficking is phenocopied by overexpression of LC3 binding-deficient AP-2 α_A mutant (Fig 3), which is fully functional with respect to endocytosis [32]. Finally, in contrary to previously published data indicating the benefit of clathrin-mediated endocytosis inhibition in AD [72,73], we find that AP-2 deletion in neurons facilitates amyloidogenic APP processing and causes synaptic dysfunction (Figs 4 and 5). Our findings further strengthen the endocytosis-independent role for endocytic adaptors in neurons [32,33,74,75] and suggest that extremely polarized morphology of neuronal cells, where endocytic cargo has to be transported over long distances, might largely be responsible for the brain-confined phenotype of AD patients at the initial stages of the disease [76]. In

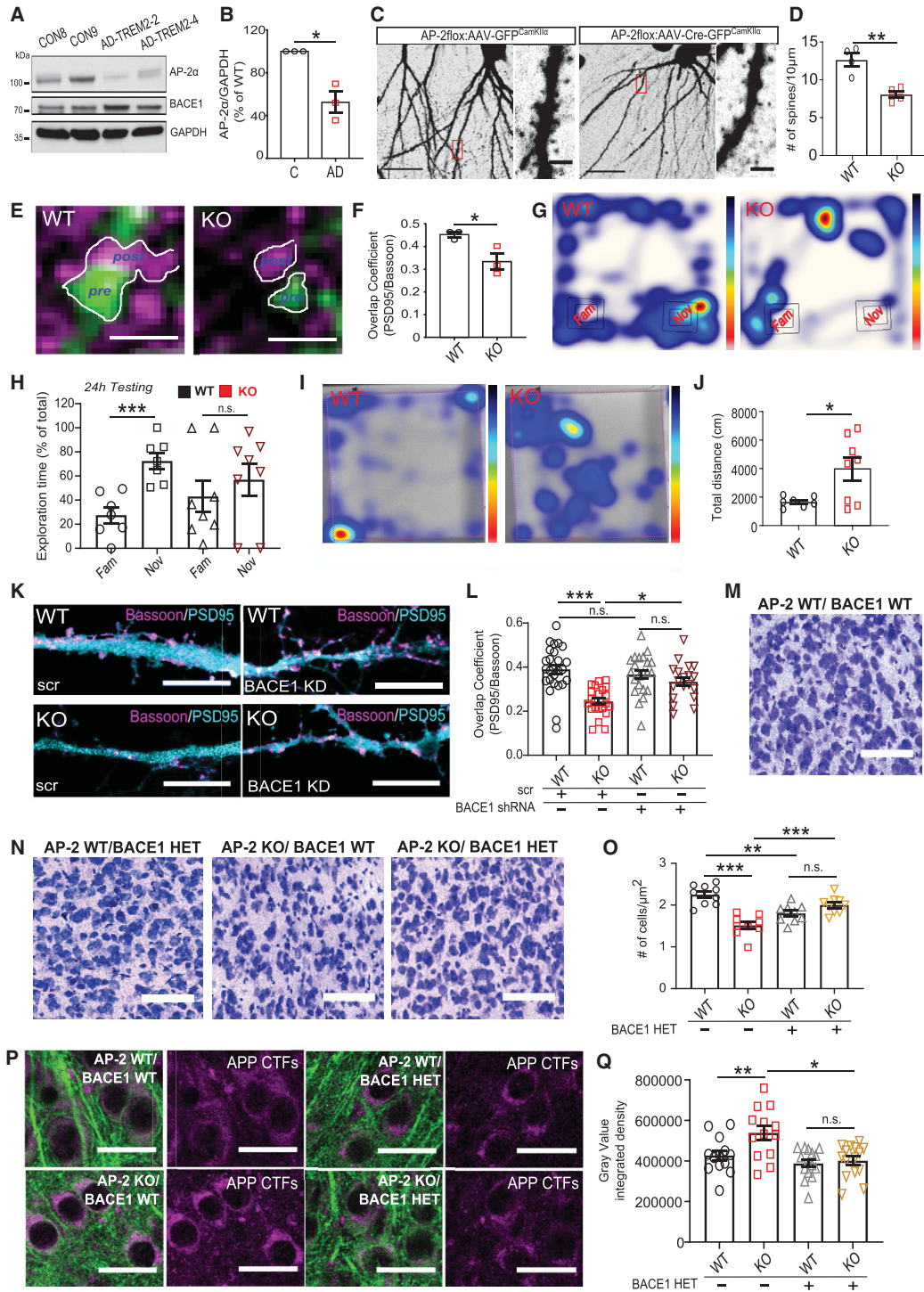


Figure 5.

Figure 5. Synaptic dysfunctions in AP-2 μ KO mice are mitigated by BACE1 haploinsufficiency.

A, B AP-2 μ levels normalized to GAPDH are significantly decreased in lysates of iPSC-derived neurons from late-onset AD patients carrying the *TREM2 p.R47H* (AD-TREM2-2 and AD-TREM2-4) variant compared to healthy controls (CON8 and CON9) set to 100% (AD^{TREM2}: 52.42 \pm 8.04%, P = 0.020, N = 3 biological replicates).

C Confocal images of either AP-2 WT (AAV-GFP^{CamkII α} -labeled) or AP-2 KO (AAV-Cre-GFP^{CamkII α} -labeled) granule neurons in the dentate gyrus of 13-week-old mice. Scale bars: 20 μ m, 2 μ m (inserts).

D Loss of AP-2 μ significantly decreases the number of spines on granule neurons (WT: 12.63 \pm 0.88, KO: 8.07 \pm 0.45, P = 0.004, N = 4 biological replicates).

E, F Overlap coefficient between the presynaptic marker Bassoon and the postsynaptic marker PSD95 is significantly decreased in the entorhinal cortex of AP-2 μ KO mice compared to the WT (WT: 0.45 \pm 0.02, KO: 0.33 \pm 0.06, P = 0.034, N = 3 biological replicates). Scale bar, 750 nm.

G, H Lost preference for the novel object (nov) comparing to the familiar object (fam) in AP-2 μ KO mice tested 24 h after training in NOR (WT^{fam}: 27.51 \pm 6.77, WT^{nov}: 72.49 \pm 6.77, pWT^{fam} versus WT^{nov} = 0.000; KO^{fam}: 43.9 \pm 13.12, KO^{nov}: 59.91 \pm 13.12, pKO^{fam} versus KO^{nov} = 0.469, N = 7 WT and 8 KO mice). Representative heatmaps are shown in (G).

I, J AP-2 μ KO mice are significantly more active in the open field compared to the WT (WT: 1663 \pm 139.08%, KO: 3976 \pm 802.30%, P = 0.020, N = 7 WT and 8 KO mice). Representative heatmaps are shown in (I).

K, L Overlap coefficient between Bassoon and PSD95 is rescued upon BACE1 KD in AP-2 μ KO neurons (WT^{scr}: 0.39 \pm 0.02; KO^{scr}: 0.24 \pm 0.01; WT^{shBACE1}: 0.37 \pm 0.02; KO^{shBACE1}: 0.33 \pm 0.02; pWT^{scr} versus pKO^{scr} < 0.000; pKO^{scr} versus pKO^{shBACE1} = 0.010; pWT^{scr} versus pWT^{shBACE1} = 0.813; pWT^{shBACE1} versus pKO^{shBACE1} = 0.623, 22–24 neurons for each condition, N = 3). Scale bars: 10 μ m.

M–O Neuronal loss is rescued in the entorhinal cortex of AP-2 μ KO mice haploinsufficient for BACE1 (AP-2^{WT}/BACE1^{WT}: 2.25 \pm 0.08, AP-2^{KO}/BACE1^{WT}: 1.51 \pm 0.08, AP-2^{WT}/BACE1^{HET}: 1.80 \pm 0.07, AP-2^{KO}/BACE1^{HET}: 2.00 \pm 0.07; p^{AP-2WT/BACE1WT} versus p^{AP-2KO/BACE1WT} < 0.000, p^{AP-2WT/BACE1WT} versus p^{AP-2WT/BACE1HET} = 0.001; p^{AP-2KO/BACE1WT} versus p^{AP-2KO/BACE1HET} = 0.000; p^{AP-2WT/BACE1HET} versus p^{AP-2KO/BACE1HET} = 0.268, N = 9 sections from N = 3 for each genotype). Scale bar: 100 μ m.

P, Q APP-CTF levels are rescued in the entorhinal cortex of AP-2 μ KO mice haploinsufficient for BACE1 (AP-2^{WT}/BACE1^{WT}: 427574 \pm 24021, AP-2^{KO}/BACE1^{WT}: 538895 \pm 34662, AP-2^{WT}/BACE1^{HET}: 389870 \pm 19842, AP-2^{KO}/BACE1^{HET}: 395389 \pm 21853; p^{AP-2WT/BACE1WT} versus p^{AP-2KO/BACE1WT} = 0.017, p^{AP-2WT/BACE1WT} versus p^{AP-2KO/BACE1HET} = 0.001; p^{AP-2WT/BACE1HET} versus p^{AP-2KO/BACE1HET} = 0.979; 13–15 sections, N = 3 mice for each genotype). Scale bars: 40 μ m.

Data information: All graphs show mean \pm SEM; statistical analysis was performed by one-sample Student's t -test in (B), unpaired two-tailed Student's t -test in (D, F, H, J) and two-way ANOVA in (L, O, Q). n.s.—non-significant. * indicates P \leq 0.05; ** indicates P \leq 0.01; *** indicates P \leq 0.001.

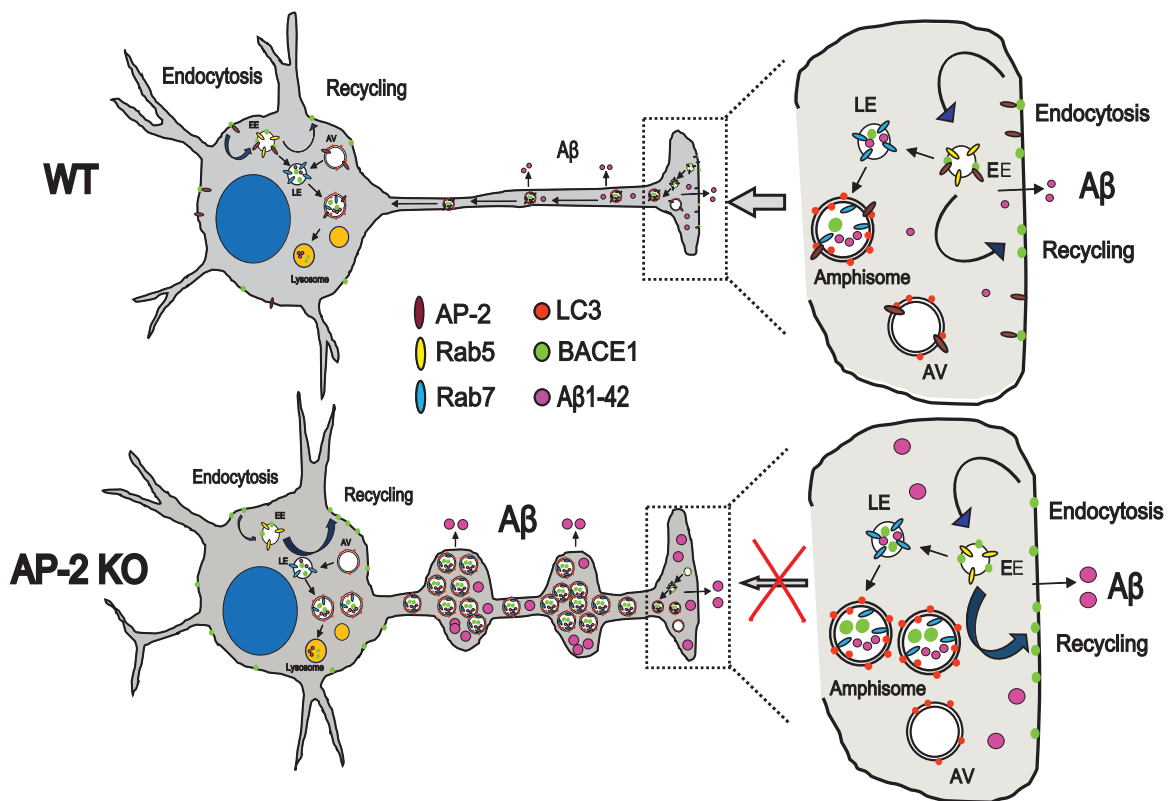


Figure 6. Hypothetical model explaining the role of AP-2 in intracellular trafficking of BACE1.

In WT neurons, AP-2 μ is required for transport of BACE1-containing autophagosomes and late endosomes en route to lysosomes. Absence of AP-2 μ causes defective axonal trafficking of BACE1 leading, which results in increased amyloidogenic processing of APP.

fact, since in *C. elegans* AP-2 has been reported to control the anterograde delivery of glutamate receptor GLR1 to the plasma membrane [77], our data suggest that the generalized defect of AP-2 loss on BACE1 trafficking might be due to additional, yet undescribed AP-2 functions in the secretory pathway in mammalian neurons.

Based on our data, the function of AP-2 in APP processing requires BACE1 endocytosis from the plasma membrane. The endocytosis of BACE1 is known to depend on the DISLL sequence located in its cytosolic tail [22], a sorting signal recognized by a variety of the adaptor proteins [78], including AP-2 [23]. In the absence of the di-leucine motif, BACE1 is recycled from the endosomal system to the cell surface at twice its normal rate [22], a phenotype also observed in AP-2 KO neurons in the current study. Thus, our results agree with the hypothesis that AP-2 is not required for BACE1 endocytosis (in agreement with Ref. [25]), but instead regulates the trafficking of BACE1 toward degradation compartments and its absence facilitates its recycling back to the plasma membrane. The AP-2-dependent sorting of BACE1 toward lysosomes is consistent with previously described role for AP-2 in clathrin coat assembly on these organelles [79]. We suggest that the function of AP-2 in BACE1 degradation and APP processing is of a special importance in neurons, where the synaptic activity triggers the convergence of usually distinctly located APP and BACE1 into amyloidogenic acidic microdomains [21]. This phenomenon can explain why AP-2-dependent amyloidogenesis might have been overlooked in the past [23]. In fact, recent data highlight BACE1 enrichment in synaptic vesicles [80], a presynaptic organelle, which is regenerated upon neuronal activity in AP-2-dependent manner [30]. Thus, our data propose a model where AP-2 functions at presynaptic membrane compartments to sort BACE1 to late endosomes and autophagosomes, thus regulating its degradation during neuronal activity. Lack of AP-2 could trigger a positive feedback loop between BACE1 internalization and A β production in highly active neurons, which in turn might lead to hyperexcitability due to intrinsic A β effect on expression of voltage-gated sodium channels [81]. Whether the degradation route of the APP is also directly mediated by the AP-2 remains to be determined, although autophagy-mediated degradation of APP-CTFs dependent on the neuronal-enriched AP-2 α has previously been reported [82]. Furthermore, a recent study revealed that neurotoxic A β levels in microglia are non-canonically regulated by autophagy, which mediates the LC3 recruitment to A β -containing clathrin-positive endosomes [83]. Irrespective of the precise mechanisms involved, results presented here identify a previously undescribed role for AP-2 in regulation of amyloidogenic processing of APP in neurons and lay the groundwork for the identification of novel therapeutic targets in AD.

Materials and Methods

Animals

C57/BL/6 mice were housed in polycarbonate cages at standard 12/12 day–night cycles, and water and food were provided *ad libitum*. All animal experiments were approved by the ethics committee of LANUV Cologne and were conducted according to the committee's guidelines. Conditional tamoxifen-inducible (*Ap2m1^{lox/lox} × inducible CAG-Cre*) and neuron-confined (*Ap2m1^{lox/lox} × Tubulin1 α -Cre*) AP-2 μ KO mice, as well as conditional tamoxifen-inducible ATG5 KO

(*Atg5^{fllox/fllox}; B6.Cg-Tg(CAG-Cre/Esr1*)5Amc/J*), were described previously [32]. Neuron-confined AP-2 μ KO mice were crossbred with BACE1 KO mice (*Bace1^{tm1Pcw}*, Jackson Laboratory, Stock #: 004714) to obtain the AP-2 μ KO: BACE1 HET mice.

Stereotaxic injection of AAV9-eGFP

Stereotaxic injections were performed either on 14-day-old WT and *Ap2m1^{lox/lox} × Tubulin1 α -Cre* mice or on 9-week-old *Ap2m1^{lox/lox}* mice. Mice were anesthetized with a mixture of ketamin (100 mg/kg)/xylazine (20 mg/kg)/acepromazine (3 mg/kg) and mounted in the Kopf stereotaxic frame. Local anesthetic was applied before opening of the scalp. A small craniotomy was performed above the point of injections. For 9-week-old animals, 200 nl of AAV9-eGFP^{CamKII α} or AAV9-Cre-eGFP^{CamKII α} was injected with a Hamilton syringe into the dentate gyrus (AP—3.5; ML—2.5; DV—2.5) with a 5-min delay after the penetration, and waiting another 15 min before withdrawing of the syringe. For the injections in 14-day-old animals, a 1 μ l Hamilton syringe filled with 300 nl of AAV9-eGFP^{CamKII α} was lowered into the thalamus, using following coordinates: AP—1.05; DL—1.32; depth—3.00. A volume of 150 nl AAV was delivered during 5 min, with a 5-min delay after the penetration, and waiting another 15 min before withdrawing of the syringe. The animal was given a dose of carprofen to reduce postsurgical pain before the end of the surgery. Suturing the skin over the wound completed the surgery, and the animal was allowed to recover. Mice were sacrificed by transcardial perfusion either 5–7 days after the surgery for 14-day-old animals or 4 weeks after the surgery for 9-week-old animals, and eGFP expression was analyzed by confocal microscopy (see Immunohistochemical analysis of brain sections).

Preparation of primary neurons and transfections

Primary neurons were isolated from cortex and hippocampus of p1–5 mice, according to the previously described protocol [84]. Homologous recombination of conditional AP-2 μ KO allele was induced by the addition of 0.4 μ M (Z)-4-hydroxytamoxifen (Sigma) immediately after plating. During medium renewal after 1 and 24 h, cells were treated with 0.2 and 0.4 μ M of tamoxifen, respectively. Ethanol was added to control neurons (WT) in an equal amount as tamoxifen. For most of the experiments, neurons were transfected at DIV 7–8 using optimized calcium phosphate protocol described previously [84] and always analyzed at DIV 10–12.

Immunocytochemistry on cultured neurons

Neurons were fixed on DIV 11–12 in 4% paraformaldehyde (PFA) in phosphate-buffered saline (PBS containing 137 mM NaCl, 2.7 mM KCl, 10 mM Na₂HPO₄, 1.8 mM K₂HPO₄, pH 7.4) for 15 min at room temperature (RT), washed three times with PBS, and blocked for 1 h at RT with blocking buffer containing 0.3% saponin (SERVA Electrophoresis GmbH) and 5% normal goat serum (NGS) in PBS. Neurons were then incubated with primary antibodies (Table EV1) in the blocking buffer for 1 h at RT. Coverslips were rinsed three times with PBS (5 min each) and incubated with corresponding secondary antibodies (Table EV1) for 30–60 min at RT in blocking solution. Subsequently, coverslips were washed three times in PBS and mounted in Immu-Mount (Thermo Scientific).

Kinetics of BACE1 endocytosis

To analyze the kinetics of BACE1 endocytosis, WT and AP-2 μ KO neurons were transfected with either HA-BACE1-eGFP or BACE1-eGFP plasmids at DIV 7–8. At DIV 11, neurons were incubated with the HA antibody for 30 min (pulse) at 4°C in osmolarity-adjusted NBA medium to label the surface BACE1. After that, the cells were transferred to CO₂ incubator at 37°C and kept for 5, 20, or 40 min to allow the endocytosis of HA antibody-bound BACE1 (chase). Afterward, the neurons were acid-stripped (0.5 M NaCl, 0.2 M acetic acid) for 4 s [33] to remove the surface-bound non-endocytosed HA antibody, washed two times with PBS, and fixed and immunostained under permeabilizing condition as described above. The levels of internalized BACE1 were quantified by determining the fluorescence ratio of the HA signal (endocytosed BACE1) to the eGFP expression (total BACE1) in WT and KO conditions.

BACE1 pulse-chase assay

To label the internalized fraction of BACE1, WT and AP-2 μ KO neurons, transfected either with HA-BACE1-eGFP or with HA-BACE1-mCherry plasmids and co-transfected either with eGFP, eGFP-RAB4, eGFP-RAB4S22N, eGFP-RAB11 or eGFP-RAB11S25N (see Table EV2), were first incubated with the HA antibody (pulse) in osmolarity-adjusted NBA medium in CO₂ incubator at 37°C for 20 min. Afterward, the neurons were acid-stripped (0.5 M NaCl, 0.2 M acetic acid) for 4 s [33] to remove the surface-bound non-endocytosed HA antibody and washed two times with PBS. Following the stripping, neurons were either fixed with 4% PFA (= internalized BACE1 fraction) or kept for 20 min (chase) at 37°C in the CO₂ incubator to allow the recycling of BACE1 back to the plasma membrane (= recycled BACE1 fraction) and subsequently fixed in 4% PFA. To visualize the internalized BACE1 fraction, fixed neurons were incubated in blocking buffer containing 0.3% saponin and 5% NGS in PBS and immunostained as described above. To reveal the recycled BACE1 fraction, fixed neurons were first blocked with 10% NGS in PBS (non-permeabilizing buffer) for 1 h at RT, rinsed three times with PBS, incubated with secondary antibody in PBS for 30 min, washed three times with PBS, and mounted using Immuno-mount. The levels of internalized or recycled BACE1 were quantified by determining the fluorescent ratio of the HA signal (internalized or recycled BACE1) to the eGFP or mCherry expression (total BACE1) in WT and KO conditions (see details under Analysis of immunofluorescence). For surface analysis of APP, WT and AP-2 μ KO neurons overexpressing mCherry-APP-eGFP were fixed and immunostained under non-permeabilizing condition (10% NGS in PBS) using mCherry antibody. The surface levels of APP were quantified by determining the mCherry (surface)/eGFP (total) fluorescence ratio for individual neurons.

Surface fraction analysis of GABAR β 3 receptors

WT and AP-2 μ KO neurons were fixed with 4% PFA and blocked with 10% NGS in PBS followed by immunostaining with surface GABAR β 3 antibody (recognizing the N-terminus, see Table EV1) under non-permeabilizing condition. Following the surface staining, neurons were postfixed with 2% PFA on ice and permeabilized with 0.1% Triton-X in PBS. Neurons were incubated in blocking buffer containing 0.3% Triton-X and 10% NGS in PBS. Following blocking,

neurons were immunostained for antibody to detect the total GABAR β 3 (recognizing the C-terminus, see Table EV1).

Analysis of immunofluorescence

Neurons were analyzed using Zeiss Axiovert 200M microscope equipped with 63 \times /1.4 oil DIC objective and the Micro-Manager software (Micro-Manager1.4, USA). For quantitative analysis, the area of the neuron, including the cell body and the axon, was manually selected using the ImageJ selection tools (ROI Manager) and the mean gray value was quantified within the ROI after the background subtraction. To quantify the levels of endocytosed and recycled BACE1, the HA signal (endocytosed or recycled fractions) and the GFP or mCherry signals (total levels of BACE1 expression) were individually quantified for each neuron. Next, the ratio of HA immunofluorescence to either eGFP or mCherry was generated for WT and KO conditions. To quantify the surface levels of GABAR β 3, the surface and total GABAR β 3 levels were individually quantified for each neuron and a ratio of surface to total was generated for WT and KO conditions. Axons were identified based on the distinct morphology, and the percentage of co-localization between BACE1 and LC3, APP, or RAB7 in cultured neurons was manually quantified for different axonal fragments. The percentage of co-localization between BACE1 and Cathepsin D was quantified in the soma. Co-localization between endogenous BACE1/RAB5 and BACE1/AP-2 α was determined by Pearson's correlation coefficient using ImageJ Coloc 2 plugin. A β puncta were manually quantified for each axonal fragment and represented as a number of puncta per 10 μ m of axonal length. To determine the levels of A β in the autophagosomes, first the axonal autophagosomes were selected as region of interest (ROI) and the amount of A β was quantified within the selected ROI. For the mCherry-APP-P1-eGFP cleavage assay, mean gray values of mCherry and GFP signals were quantified separately and the ratio of eGFP/mCherry was determined.

Analysis of the spine density

Cultured WT and AP-2 μ KO neurons were transfected with eGFP at DIV 7–8 to visualize the neuronal morphology and fixed between DIV 11–12 (the latest possible time point before occurrence of cell death in AP-2 KO neurons, Kononenko *et al*, 2017). To quantify the spine number, 2–3 small ROIs were selected along the primary dendrites for each neuron. The number of spines was quantified manually per 10 μ m of dendritic length. Similar analysis was also performed with *in vivo* samples.

A β rescue experiments using BACE1 knockdown in cultured neurons

WT and AP-2 μ KO neurons were transfected with eGFP and co-transfected either with BACE1 shRNA-NLS-RFP (Tables EV2 and EV3, [85]) or with scrambled (scr) shRNA-NLS-RFP at DIV 7. At DIV 11–12, the neurons were fixed in 4% PFA in PBS for 15 min at RT, washed three times, and then permeabilized and blocked for 1 h with the solution containing 5% NGS and 0.1% saponin (blocking buffer). Next, the neurons were incubated with the primary antibody (A β 42, Table EV1), diluted in the blocking buffer for 1 h at RT. Following the incubation, the coverslips were rinsed four times

with PBS (2–5 min each) and incubated with Alexa 647-conjugated secondary antibody (1:500) in the blocking buffer for 30 min. Subsequently, the coverslips were washed three times in PBS and mounted using Immu-mount. Fluorescence images were acquired using Zeiss Axiovert 200M microscope equipped with 63×/1.4 oil DIC objective and the Micro-Manager software (Micro-Manager1.4, USA). Transfected neurons were identified by co-expression of eGFP and NLS-RFP. To quantify the number of A β puncta, 30- to 40- μ m-long axonal fragment was derived from individual neuron using ImageJ ROI manager plugin. A β puncta were manually quantified from each fragment per 10 μ m of axonal length.

A β rescue experiments upon AP-2 overexpression in cultured neurons

WT and AP-2 μ KO neurons were first transfected with mCherry or AP-2 μ -mRFP at DIV 6. At DIV 11–12, the neurons were fixed in 4% PFA in PBS for 15 min at RT and immunostained with primary antibody against A β 42 as described above. Fluorescence images were acquired using Zeiss Axiovert 200M microscope equipped with 63×/1.4 oil DIC objective and the Micro-Manager software (Micro-Manager1.4, USA). Transfected neurons were identified by the expression of mCherry or mRFP. To quantify the number of A β puncta, 30- to 40- μ m-long axonal fragment were randomly selected from individual neuron using ImageJ ROI manager plugin. A β puncta were manually quantified from each axonal fragment and represented as a number of puncta per 10 μ m of axonal length.

Live imaging

Cultured WT and AP-2 μ KO neurons were either transfected with HA-BACE1-eGFP and BACE1-eGFP alone or co-transfected with AP-2 μ -mCherry, AP-2 μ -mRFP, RFP-LC3B-G120, HA-AP-2 α WT, or HA-AP-2 α Mut at DIV 7–8. In case of HA-BACE1-eGFP, a single HA tag was introduced after the propeptide cleavage site [23]. In control experiments, it was confirmed that BACE1 chimeric protein is able to process APP with efficiencies similar to WT BACE1 [23]. Transfected neurons were imaged at 37°C at DIV 9–11 in basic buffer (170 mM NaCl, 3.5 mM KCl, 0.4 mM KH₂PO₄, 20 mM N-Tris[hydroxyl-methyl]-methyl-2-aminoethane-sulphonic acid (TES), 5 mM NaHCO₃, 5 mM glucose, 1.2 mM Na₂SO₄, 1.2 mM MgCl₂, 1.3 mM CaCl₂, pH 7.4) using Zeiss Axiovert 200M microscope (Observer. Z1, Zeiss, USA) equipped with 63×/1.40 oil DIC objective, a pE-4000 LED light source (CoolLED), and Hamamatsu Orca-Flash4.0 V2 CMOS digital camera. Time-lapse images of neurons were acquired every second for 60 s using Micro-Manager software (Micro-Manager1.4, USA). To quantify the motility of axonal carriers, small axonal fragments were generated using ImageJ ROI manager and kymographs were derived by Kymomaker software [86]. The number of moving and stationary carriers was manually quantified from kymographs.

Rescue experiments using the HA-BACE1-LL/AA-eGFP construct

Cultured control neurons were transfected either with HA-BACE1-eGFP or HA-BACE1-LL/AA-eGFP plasmids at DIV 5–6, and experiments were performed at DIV 10–12. To determine the motility of BACE1 vesicles, live-cell imaging was performed using the protocol for AP-2 μ KO neurons, described above. For the quantification of A β

puncta, the neurons were fixed with 4% PFA, followed by immunostaining with A β antibody (see Table EV1), and the quantification of A β puncta per 10 μ m of axonal length was using the protocol for AP-2 μ KO neurons, described above. For the Cathepsin D immunostaining, the neurons were fixed and immunostained with Cathepsin D antibody (see Table EV1). To determine the recycling of BACE1, the neurons were pulsed with HA antibody for 20 min at 37°C followed by acid-stripping, 20 min of chase and surface staining of HA (= recycled fraction) under non-permeabilizing condition using the protocol, described above for AP-2 μ KO neurons.

Imaging of BACE1-mKeima-Red in cultured neurons

To determine the functionality of mKeima fluorescence probe, BACE1-mKeima-Red-overexpressing neurons were incubated with 75 nM of LysoTracker Blue-White (Molecular Probes, Cat #L12490) for 15 min. Visualization of BACE1-mKeima in LysoTracker-positive organelles was performed in live neurons using confocal microscopy, and the extent of BACE1-mKeima localization to lysosomes was quantified by ImageJ. To analyze the delivery of BACE1 to lysosomes in AP-2 μ KO condition, WT and KO neurons were co-transfected with BACE1-mKeima and eBFP2-N1 plasmids at DIV 7–8. Neurons were imaged at DIV 11–12 using Leica SP8 confocal microscope (Leica Microsystems), equipped with a 63×/1.32 oil DIC objective and a pulsed excitation white light laser (WLL; < 80-ps pulse width, 80 MHz repetition rate; NKT Photonics). The temperature of live-cell imaging chamber was always maintained at 37°C. mKeima was sequentially excited at 438 and 550 nm with the pulsed WLL, and the emission at 620 nm was detected with a hybrid detector. The BFP was excited at 383 nm using an UV lamp and detected at 445 nm. For the quantification, the entire area of the neuron was manually selected using the ImageJ ROI manager, and the mean gray values at 438 nm and 550 nm of excitation were measured in the ROI after the background subtraction. The data were represented as the 550/438 ratio in WT and KO condition.

Quantitative RT-PCR

RNA isolation from DIV 11–12 cultured neurons was performed using TRIzol (Thermo Fisher Scientific) [32]. Twenty nanogram of total RNA was used for reverse transcription using the High Capacity cDNA Reverse Transcription Kit (Applied Biosystems). The qPCR was performed with qPCR BIO SyGreen Mix Kit (Applied Biosystems) in a 7500 Fast System. mRNA levels of *Bace1* were quantified by normalizing to *Gapdh* [87].

ELISA

A β _{1–40} and A β _{1–42} peptides in the media of cultured neurons were analyzed at DIV 11–12 using WAKO kit (# 294-64701 and # 292-64501, respectively) following the manufacturer's instructions.

Immunohistochemistry

Mice were sacrificed by transcardial perfusion either on postnatal day (p) 18–21 or at 13 weeks as previously described [32]. Brains were carefully taken out of the skull, postfixed overnight in the same fixative, and placed in a mixture of 20% glycerol and 2%

dimethyl sulfoxide in 0.1 M PBS for 24 h for cryoprotection. Frozen horizontal or coronal 40 μ m sections were collected in five series and stored at -80°C . Immunohistochemistry was performed according to a previously described protocol [32]. Images were acquired with Leica SP8 confocal microscopy equipped with 63 \times /1.32 oil DIC objective and pulse excitation white laser (WLL; 80-ps pulse width, 80 MHz repetition rate; NKT Photonics). Quantification of mean gray value was performed using ImageJ software. Co-localization between endogenous BACE1 and RAB7 was determined using Pearson's correlation coefficient. The levels of CTFs were determined by quantifying the integrated density of the immunofluorescence. Co-localization between PSD95 and Bassoon was determined by Mander's overlap coefficient. For Nissl staining, sections were mounted in 0.2% gelatine solution in 250 mM Tris-HCl and processed as previously described [32]. For analysis of cell number, three 40- μ m-thick consecutive sections containing the entorhinal cortex were selected for each genotype and scaled using Aperio ImageScope v12.3.2.8013. Neurons were counted in a fixed sized rectangle using ImageJ v.1.52a, and the cell density was determined by the normalization of the number of cells to the rectangle area.

Western blot

Analysis of lysates from cultured neurons

The lysates of cultured neurons were prepared by harvesting the neurons at DIV 11–12 using radioimmunoprecipitation assay buffer (RIPA) containing 50 mM Tris (pH = 8.0), 150 mM NaCl, 1.0% IGEPAL, 0.5% sodium deoxycholate, 0.1% SDS, and 1 \times protease inhibitor cocktail (Roche). Supernatants were collected after centrifugation at 14,000 g for 10 min, and protein concentration was measured by the Bradford assay. Samples were analyzed by SDS-PAGE on 10% Tris-Glycine gels followed by blotting on the nitrocellulose membrane. The membranes were blocked for 1 h at RT in 5% skim milk in TBS buffer (20 mM Tris pH = 7.6, 150 mM NaCl) containing 0.1% Tween (TBS-T) and incubated with primary antibodies (Table EV1) overnight at 4 $^{\circ}\text{C}$. Next, the membranes were washed two times (10 min each) with TBS-T and one time with TBS buffer and incubated with secondary antibody for 1.5 h at RT with 5% skim milk in TBS-T buffer. Afterward, the membranes were washed three times as above and subsequently developed using ECL-based autoradiography film system. Analysis was performed using ImageJ.

Analysis of lysates from the cortical tissues

Cortices from WT and *Ap2m1*^{lox/lox} \times *Tubulin1 α* -Cre KO mice were dissected at p20–21 and homogenized using RIPA buffer, and protein concentration was measured by the Bradford assay. The samples were then processed with 2 \times Tris-Tricine sample buffer (8% SDS, 24% Glycerol, 100 mM Tris, 100 mM Tricine, 0.2 M DTT, 0.02% Coomassie brilliant blue G250, pH = 8.25) and separated on 9–16% Tris-Tricine Gel (3 M Tris, 0.3% SDS, pH = 8.45) using cathode (0.1 M Tris, 0.1 M Tricine, 0.1% SDS, pH = 8.25) and anode (0.2 M Tris, pH = 8.9) buffers, where cathode buffer was used in the inner chamber and anode buffer was used in the outer chamber for separation of samples. Following separation, proteins were blotted using semi-dry transfer on the nitrocellulose membrane. The membranes were then processed as above and probed with corresponding antibodies (Table EV1).

Co-immunoprecipitation

Cortices from 8-week-old WT mice were dissected and homogenized in RIPA buffer. Proteins were extracted for 45 min on ice, followed by the centrifugation of lysates at 17,000 g for 20 min at 4 $^{\circ}\text{C}$. Equivalent amount of rabbit BACE1 antibody or non-specific rabbit IgG was coupled to Protein G Dynabeads (Invitrogen). Antibody-coupled Dynabeads were incubated with the supernatant for 1 h at 4 $^{\circ}\text{C}$ on the shaker. Following the incubation, Dynabeads were washed three times with RIPA buffer, and proteins were eluted using SDS-PAGE sample buffer and analyzed by Western blotting. For immunoprecipitation of AP-2 μ the cortices were homogenized in Co-IP buffer containing 50 mM Tris-HCl pH = 7.4, 100 mM NaCl, 1% NP-40, 2 mM MgCl₂, and 1 \times protease inhibitor. Proteins were extracted as above and incubated with mouse AP-2 μ or equivalent amount of mouse non-specific IgG-coupled Protein G Dynabeads. Following incubation, proteins were eluted and analyzed by Western blotting using antibodies described in Table EV1.

Surface biotinylation assay

Surface biotinylation assay was performed on WT- and AP-2 μ KO-cultured neurons at DIV 11–12. Neurons were first incubated with NHS-Sulfo-linked biotin (1 mg/ml in PBS; EZ-linkedTM-Sulfo-NHS-Biotin, Thermo Fisher Scientific) for 15 min on ice under gentle shaking. Next, the neurons were washed twice with quenching solution (10 mM Glycine in PBS) to remove the excess biotin and one time with ice-cold PBS. Following the washing steps, the neurons were harvested in RIPA buffer and protein extraction was performed as above. After the centrifugation (15,000 g for 20 min at 4 $^{\circ}\text{C}$), supernatants were collected and protein concentrations were measured. A portion of the supernatant was collected and used as input. To precipitate the biotinylated proteins, 60–80 μ g of the supernatant was incubated with Neutravidin agarose beads (Thermo Fisher Scientific) for 1 h at room temperature. Following the incubation, the beads were washed in RIPA buffer and proteins were eluted from the streptavidin beads by boiling in reducing sample buffer and then resolved by SDS-PAGE and immunoblotted using corresponding antibodies (BACE1, GAPDH, and AP-2 α , Table EV1).

HEK cells

HEK293T cells were maintained in DMEM (GIBCO), containing 10% FCS, penicillin (255 Units/ml), and streptomycin (255 μ g/ml). Twenty-four hours after seeding, the cells were transfected with mouse FLAG-BACE1 plasmid and co-transfected with either BACE1 shRNA or scrambled shRNA using the Lipofectamine 3000 (Invitrogen) (Tables EV2 and EV3). Ninety hours post-transfection, the cells were harvested and lysed in RIPA buffer. Extracted proteins were loaded onto a 10% SDS-PAGE gel, transferred onto the PVDF membranes, and subsequently probed with corresponding primary and HRP-conjugated secondary antibodies (Table EV1). Blots were developed using the ECL-based autoradiography film system and analyzed using ImageJ (NIH).

Transferrin uptake assay

HEK293T cells were transfected either with AP-2 μ [88] or scrambled siRNA [89] (see Table EV3) using Lipofectamine RNAiMax Reagent

(Invitrogen) on day 1 and co-transfected with mCherry or AP-2 μ -mCherry on day 2, followed by transfection with siRNA on day 3. Transferrin uptake was performed at day 5. Briefly, cells were incubated with starvation medium (DMEM containing 20 mM HEPES and 5 mg/ml BSA) for 30 min at 37°C. After the starvation, the cells were incubated with 50 μ g/ml Transferrin-Alexa-488 (Invitrogen) for 10 min in the same media at 37°C in CO₂ incubator. Cells were then washed three times with ice-cold PBS, and fixed and stained with mCherry antibody (Table EV1).

iPSC-derived neurons

iPSC lines

We used previously published iPSC lines derived from AD patients, as well as control individuals without dementia for the current study [90–93] (Table EV4). The iPSCs were maintained on Matrigel-coated (Corning) plates in StemMACS culture medium (Miltenyi Biotec). Medium was changed every day and cells passaged every 5–6 days using PBS lacking calcium and magnesium (Life Technologies).

Neural differentiation of the iPSC lines

For the neuronal differentiation, the embryoid body-based protocol was employed [94]. Briefly, on day 0, cells were harvested and re-cultivated in suspension in neural induction medium (NIM) (DMEM/F-12 (Thermo Scientific), 1% NEAA (Lonza), 1% N2 supplement (Thermo Scientific), 2 μ g/ml of Heparin (Sigma-Aldrich), and 1% P/S) supplemented with 1 μ M purmorphamine (Tocris Bioscience). At day 5, formed aggregates were harvested and re-plated as adherent cells in the same medium with purmorphamine. From days 10 to 18, primitive neuro-epithelia structures formed. Neural rosettes were selected with STEMdiff Neural Rosette Selection Reagent (Stem Cell Technologies) and re-cultured using NIM supplemented with B27 lacking retinoic acid (Thermo Scientific). After 10 days, the cells maintained as aggregates (neurospheres) were dissociated into single cells using accutase (Invitrogen), which were re-plated using neural differentiation medium (NDM) (Neurobasal 1% NEAA, 1% N2 supplement, 1% P/S supplemented with 1 μ M of cAMP (Sigma-Aldrich), and 10 ng/mL of BDNF, GDNF, and IGF-1 (all Immuno Tools)) on Matrigel (Corning). The iPSCs-derived neurons were then cultivated for approximately 2 months and harvested in RIPA buffer, and protein extraction was performed as described above. Ten microgram of supernatants was loaded on to 10% gel and analyzed by immunoblotting using antibodies against AP-2 α . The levels of AP-2 α were normalized against GAPDH (Table EV1).

Novel object recognition test (NOR)

The novel object recognition was performed on 19- to 20-day-old WT and AP-2 μ KO animals in a white painted square box (50 × 50 × 40 cm) illuminated with > 20lux. Objects used were a blue-colored cool pack, a diverse colored cube, and a flask filled with sand and stones. Objects differed in height, width, color, and shape and previous experiments demonstrated no spontaneous preference for none of the objects. Mice were monitored by a digital camera placed above the arena and connected to a video tracking system (EthoVision[®]XT, Noldus). Animals were first handled for 4 min on three successive days prior to the habituation phase. Habituation to the environment was performed on the fourth day, exposing the mice to the

open field for 10 min. On the fifth day, the training session was performed exposing the mice for 12 min to two copies of the same object (blue-colored cool pack), placed in the back left and right corners of the box. Animals were placed individually at the mid-point of the wall opposite to the sample objects with the nose pointing away from the objects. The positioning of the animals and objects was similar during the training and test sessions. One hour and a half after the training session, the first test session was performed. Mice were exposed for 10 min to one of the objects used in the training session and to a novel object (diverse colored cube). Twenty-four hours after the training session, the second test was performed by exposing the mice for 10 min to one of the objects used in the training session and a second novel object (flask). The animals were taken into the behavioral room 1 h before the habituation, training, and test sessions to avoid the stress. Before and after the testing, the box was always cleaned with water and soap first, then with water only and finally with 70% ethanol, followed by waiting period of at least 10 min. Males were always tested first.

Statistical analysis

Statistically significant estimates were obtained from total number of neurons or mice collected from minimum three independent experiments (N) (exceptions are control experiments Figs EV11 and EV3B and F). The statistical significance between two groups for all normally distributed values was evaluated with a two-tailed unpaired Student's *t*-test or one-sample *t*-test for normalized data. The statistical significance between more than two groups for all normally distributed values was evaluated using two-way ANOVA (Tukey's post hoc test was used to determine the statistical significance between the groups). Significant differences were accepted at *P* < 0.05. All data shown represent the mean \pm SEM from cells or axonal fragments acquired from N independent experiments. Power analysis was used to calculate the sample size (alpha 0.05). Non-normally distributed data (as in Fig EV4N and O) were transformed using square root transformation and analyzed using paired two-tailed *t*-test.

Expanded View for this article is available online.

Acknowledgements

The work of N.L.K. is supported by grants from the Deutsche Forschungsgemeinschaft (DFG, German Research Foundation) under Germany's Excellence Strategy —CECAD (EXC 2030 – 390661388), DFG (KO5091/2-1), and Fritz Thyssen Foundation (Az. 10.18.1.036MN). J.A. acknowledges the support from the Medical Faculty, Heinrich Heine University, Düsseldorf. We thank Dr. M. Kreutz (LIN, Magdeburg, Germany) for providing pmCherry-N1 and ptagRFP-C plasmids; Dr. J. Bonifacino (Eunice Kennedy Shriver National Institute of Child Health and Human Development (NICHD), NIH, USA) for providing the HA-BACE1-eGFP and HA-BACE1-LL/AA-stop-eGFP plasmids; Dr. M. Calamai (University of Florence, Italy) for providing mCherry-APP-P1-GFP and mCherry-APP-GFP plasmids; Dr. S. Iden (CECAD, Cologne) for providing the eBFP2-N1 plasmid; and Dr. Hans Zempel for providing LysoTracker Blue-White (Inst. of Human Genetics, Cologne). We are very grateful to Prof. M. Bergami for providing the AAV-Cre-GFP and AAV-Cre-GFP CamKII α viruses and giving us the possibility to use the stereotactic frame. We are indebted to the CECAD Imaging Facilities for expert assistance and to Dr. T. Sesia (University Hospital of Cologne) for the help in using Noldus. We also thank Prof. E. Rugarli (Univ. of Cologne), Dr. F. Liebsch (Univ. of Cologne), Dr. R. Langston (Univ. of Dundee), and Dr. L. Pernas (MPI for aging) for providing valuable comments on the manuscript.

Author contributions

SB and NLK contributed to the conception of the study and experimental design. SB, SC-P, ECB, AN-H, JR, EB, CW, NE, SM, and NLK performed the experiments, data analysis, and participated in the acquisition of data. JA provided reagents. SB and NLK prepared the manuscript. All the authors critically revised the manuscript and provided help with the interpretation of data. The final manuscript was read and approved by all authors.

Conflict of interest

The authors declare that they have no conflict of interest.

References

- Hardy J, Selkoe DJ (2002) The amyloid hypothesis of Alzheimer's disease: progress and problems on the road to therapeutics. *Science* 297: 353–356
- Jonsson T, Atwal JK, Steinberg S, Snaedal J, Jonsson PV, Bjornsson S, Stefansson H, Sulem P, Gudbjartsson D, Maloney J et al (2012) A mutation in APP protects against Alzheimer's disease and age-related cognitive decline. *Nature* 488: 96
- Haass C, Selkoe DJ (2007) Soluble protein oligomers in neurodegeneration: lessons from the Alzheimer's amyloid [beta]-peptide. *Nat Rev Mol Cell Biol* 8: 101–112
- Palop JJ, Mucke L (2010) Amyloid-[beta]-induced neuronal dysfunction in Alzheimer's disease: from synapses toward neural networks. *Nat Neurosci* 13: 812–818
- Gandy S, Heppner Frank L (2013) Microglia as dynamic and essential components of the amyloid hypothesis. *Neuron* 78: 575–577
- Zempel H, Mandelkow E (2014) Lost after translation: missorting of Tau protein and consequences for Alzheimer disease. *Trends Neurosci* 37: 721–732
- Wilquet V, Strooper BD (2004) Amyloid-beta precursor protein processing in neurodegeneration. *Curr Opin Neurobiol* 14: 582–588
- Postina R, Schroeder A, Dewachter I, Bohl J, Schmitt U, Kojro E, Prinzen C, Endres K, Hiemke C, Blessing M et al (2004) A disintegrin-metalloproteinase prevents amyloid plaque formation and hippocampal defects in an Alzheimer disease mouse model. *J Clin Invest* 113: 1456–1464
- Willem M, Tahirovic S, Busche MA, Ovsepian SV, Chafai M, Kootar S, Hornburg D, Evans LDB, Moore S, Daria A et al (2015) η -Secretase processing of APP inhibits neuronal activity in the hippocampus. *Nature* 526: 443
- Yan R, Vassar R (2014) Targeting the β secretase BACE1 for Alzheimer's disease therapy. *Lancet Neurol* 13: 319–329
- Luo Y, Bolon B, Damore MA, Fitzpatrick D, Liu H, Zhang J, Yan Q, Vassar R, Citron M (2003) BACE1 (β -secretase) knockout mice do not acquire compensatory gene expression changes or develop neural lesions over time. *Neurobiol Dis* 14: 81–88
- Willem M, Dewachter I, Smyth N, Van Dooren T, Borghgraef P, Haass C, Van Leuven F (2004) β -Site amyloid precursor protein cleaving enzyme 1 increases amyloid deposition in brain parenchyma but reduces cerebrovascular amyloid angiopathy in aging BACE \times APP[V717I] double-transgenic mice. *Am J Pathol* 165: 1621–1631
- Yang L-B, Lindholm K, Yan R, Citron M, Xia W, Yang X-L, Beach T, Sue L, Wong P, Price D et al (2003) Elevated β -secretase expression and enzymatic activity detected in sporadic Alzheimer disease. *Nat Med* 9: 3
- Li R, Lindholm K, Yang L-B, Yue X, Citron M, Yan R, Beach T, Sue L, Sabbagh M, Cai H et al (2004) Amyloid β peptide load is correlated with increased β -secretase activity in sporadic Alzheimer's disease patients. *Proc Natl Acad Sci USA* 101: 3632–3637
- Kuhn PH, Koroniak K, Hög S, Colombo A, Zeitschel U, Willem M, Volbracht C, Schepers U, Imhof A, Hoffmeister A et al (2012) Secretome protein enrichment identifies physiological BACE1 protease substrates in neurons. *EMBO J* 31: 3157
- Willem M, Garratt AN, Novak B, Citron M, Kaufmann S, Rittger A, De Strooper B, Saftig P, Birchmeier C, Haass C (2006) Control of peripheral nerve myelination by the β -secretase BACE1. *Science* 314: 664–666
- Dominguez D, Tournoy J, Hartmann D, Huth T, Cryns K, Deforce S, Serneels L, Camacho IE, Marjaux E, Craessaerts K et al (2005) Phenotypic and biochemical analyses of BACE1- and BACE2-deficient mice. *J Biol Chem* 280: 30797–30806
- Egan MF, Kost J, Tariot PN, Aisen PS, Cummings JL, Vellas B, Sur C, Mukai Y, Voss T, Furtek C et al (2018) Randomized trial of verubecestat for mild-to-moderate Alzheimer's disease. *N Engl J Med* 378: 1691–1703
- Sinha S, Anderson JP, Barbour R, Basi GS, Caccavello R, Davis D, Doan M, Dovey HF, Frigon N, Hong J et al (1999) Purification and cloning of amyloid precursor protein β -secretase from human brain. *Nature* 402: 537
- Vassar R, Bennett BD, Babu-Khan S, Kahn S, Mendiaz EA, Denis P (1999) Beta-secretase cleavage of Alzheimer's amyloid precursor protein by the transmembrane aspartic protease BACE. *Science* 286: 735–741
- Das U, Scott David A, Ganguly A, Koo Edward H, Tang Y, Roy S (2013) Activity-induced convergence of APP and BACE-1 in acidic microdomains via an endocytosis-dependent pathway. *Neuron* 79: 447–460
- Huse JT, Pijak DS, Leslie GJ, Lee VM-Y, Doms RW (2000) Maturation and endosomal targeting of β -site amyloid precursor protein-cleaving enzyme: the Alzheimer's disease β -secretase. *J Biol Chem* 275: 33729–33737
- Prabhu Y, Burgos PV, Schindler C, Farías GG, Magadán JG, Bonifacino JS (2012) Adaptor protein 2-mediated endocytosis of the β -secretase BACE1 is dispensable for amyloid precursor protein processing. *Mol Biol Cell* 23: 2339–2351
- Chia PZC, Toh WH, Sharples R, Gasnereau I, Hill AF, Gleeson PA (2013) Intracellular itinerary of internalised β -secretase, BACE1, and its potential impact on β -amyloid peptide biogenesis. *Traffic* 14: 997–1013
- Sannerud R, Declerck I, Peric A, Raemaekers T, Menendez G, Zhou L, Veerle B, Coen K, Munck S, De Strooper B et al (2011) ADP ribosylation factor 6 (ARF6) controls amyloid precursor protein (APP) processing by mediating the endosomal sorting of BACE1. *Proc Natl Acad Sci USA* 108: E559–E568
- Dittman J, Ryan TA (2009) Molecular circuitry of endocytosis at nerve terminals. *Annu Rev Cell Dev Biol* 25: 133–160
- Mitsunari T, Nakatsu F, Shioda N, Love PE, Grinberg A, Bonifacino JS, Ohno H (2005) Clathrin adaptor AP-2 is essential for early embryonic development. *Mol Cell Biol* 25: 9318–9323
- McMahon HT, Boucrot E (2011) Molecular mechanism and physiological functions of clathrin-mediated endocytosis. *Nat Rev Mol Cell Biol* 12: 517–533
- Ball CL, Hunt SP, Robinson MS (1995) Expression and localization of alpha-adaptin isoforms. *J Cell Sci* 108: 2865
- Kononenko NL, Puchkov D, Classen GA, Walter AM, Pechstein A, Sawade L, Kaempf N, Trimbuch T, Lorenz D, Rosenmund C et al (2014) Clathrin/AP-2 mediate synaptic vesicle reformation from endosome-like vacuoles but are not essential for membrane retrieval at central synapses. *Neuron* 82: 981–988
- Soykan T, Kaempf N, Sakaba T, Vollweider D, Goerdeler F, Puchkov D, Kononenko NL, Haucke V (2017) Synaptic vesicle endocytosis occurs on multiple timescales and is mediated by formin-dependent actin assembly. *Neuron* 93: 854–866.e854
- Kononenko NL, Claßen GA, Kuijpers M, Puchkov D, Maritzen T, Tempes A, Malik AR, Skalecka A, Bera S, Jaworski J et al (2017) Retrograde transport of

- TrkB-containing autophagosomes via the adaptor AP-2 mediates neuronal complexity and prevents neurodegeneration. *Nat Commun* 8: 1–16
33. Ubelmann F, Burrenha T, Salavessa L, Gomes R, Ferreira C, Moreno N, Guimas Almeida C (2016) Bin1 and CD2AP polarise the endocytic generation of beta-amyloid. *EMBO Rep* 18: 102–122
 34. de Wit H, Lichtenstein Y, Kelly RB, Geuze HJ, Klumperman J, van der Sluijs P (2001) Rab4 regulates formation of synaptic-like microvesicles from early endosomes in PC12 cells. *Mol Biol Cell* 12: 3703–3715
 35. Ren M, Xu G, Zeng J, De Lemos-Chiarandini C, Adesnik M, Sabatini DD (1998) Hydrolysis of GTP on rab11 is required for the direct delivery of transferrin from the pericentriolar recycling compartment to the cell surface but not from sorting endosomes. *Proc Natl Acad Sci USA* 95: 6187–6192
 36. Smith KR, Muir J, Rao Y, Browarski M, Gruenig MC, Sheehan DF, Haucke V, Kittler JT (2012) Stabilization of GABAA receptors at endocytic zones is mediated by an AP2 binding motif within the GABAA receptor β 3 subunit. *J Neurosci* 32: 2485
 37. Koh YH, von Arnim CAF, Hyman BT, Tanzi RE, Tesco G (2005) BACE is degraded via the lysosomal pathway. *J Biol Chem* 280: 32499–32504
 38. Katayama H, Kogure T, Mizushima N, Yoshimori T, Miyawaki A (2011) A sensitive and quantitative technique for detecting autophagic events based on lysosomal delivery. *Chem Biol* 18: 1042–1052
 39. Taylor MJ, Perrais D, Merrifield CJ (2011) A high precision survey of the molecular dynamics of mammalian clathrin-mediated endocytosis. *PLoS Biol* 9: e1000604
 40. Buggia-Prévat V, Fernandez CG, Riordan S, Vetrivel KS, Roseman J, Waters J, Bindokas VP, Vassar R, Thinakaran G (2014) Axonal BACE1 dynamics and targeting in hippocampal neurons: a role for Rab11 GTPase. *Mol Neurodegener* 9: 1
 41. Feng T, Tamminen P, Agrawal C, Jeong YY, Cai Q (2017) Autophagy-mediated regulation of BACE1 protein trafficking and degradation. *J Biol Chem* 292: 1679–1690
 42. Hara T, Nakamura K, Matsui M, Yamamoto A, Nakahara Y, Suzuki-Migishima R, Yokoyama M, Mishima K, Saito I, Okano H et al (2006) Suppression of basal autophagy in neural cells causes neurodegenerative disease in mice. *Nature* 441: 885–889
 43. Kang EL, Biscaro B, Piazza F, Tesco G (2012) BACE1 protein endocytosis and trafficking are differentially regulated by ubiquitination at lysine 501 and the di-leucine motif in the carboxyl terminus. *J Biol Chem* 287: 42867–42880
 44. Sisodia SS (1992) Beta-amyloid precursor protein cleavage by a membrane-bound protease. *Proc Natl Acad Sci USA* 89: 6075–6079
 45. Parenti N, Del Grosso A, Antoni C, Cecchini M, Corradetti R, Pavone FS, Calamai M (2017) Direct imaging of APP proteolysis in living cells. *PeerJ* 5: e3086
 46. Zhou L, Barão S, Laga M, Bockstael K, Borgers M, Gijzen H, Annaert W, Moechars D, Mercken M, Gevaer K et al (2012) The neural cell adhesion molecules L1 and CHL1 are cleaved by BACE1 protease *in vivo*. *J Biol Chem* 287: 25927–25940
 47. Koo EH, Squazzo SL, Selkoe DJ, Koo CH (1996) Trafficking of cell-surface amyloid beta-protein precursor. I. Secretion, endocytosis and recycling as detected by labeled monoclonal antibody. *J Cell Sci* 109: 991–998
 48. Levites Y, Das P, Price RW, Rochette MJ, Kostura LA, McGowan EM, Murphy MP, Golde TE (2006) Anti-Abeta42- and anti-Abeta40-specific mAbs attenuate amyloid deposition in an Alzheimer disease mouse model. *J Clin Invest* 116: 193–201
 49. Parvathy S, Davies P, Haroutunian V, Purohit DP, Davis KL, Mohs RC, Park H, Moran TM, Chan JY, Buxbaum JD (2001) Correlation between A β x-40-, A β x-42-, and A β x-43-containing amyloid plaques and cognitive decline. *JAMA Neurol* 58: 2025–2031
 50. Ou-Yang M-H, Kurz JE, Nomura T, Popovic J, Rajapaksha TW, Dong H, Contractor A, Chetkovich DM, Tourtellotte WG, Vassar R (2018) Axonal organization defects in the hippocampus of adult conditional BACE1 knockout mice. *Sci Transl Med* 10: eaa05620
 51. Liebsch F, Kulic L, Teunissen C, Shobo A, Ulku I, Engelschalt V, Hancock MA, van der Flier WM, Kunach P, Rosa-Neto P et al (2019) A β 34 is a BACE1-derived degradation intermediate associated with amyloid clearance and Alzheimer's disease progression. *Nat Commun* 10: 2240
 52. Raj T, Li Yi, Wong G, Humphrey J, Wang M, Ramdhani S, Wang Y-C, Ng B, Gupta I, Haroutunian V et al (2018) Integrative transcriptome analyses of the aging brain implicate altered splicing in Alzheimer's disease susceptibility. *Nat Genet* 50: 1584–1592
 53. Chen G, Chen KS, Knox J, Inglis J, Bernard A, Martin SJ, Justice A, McConnell L, Games D, Freedman SB et al (2000) A learning deficit related to age and β -amyloid plaques in a mouse model of Alzheimer's disease. *Nature* 408: 975
 54. Schmidt C, Wolff M, Weitz M, Bartlau T, Korth C, Zerr I (2011) Rapidly progressive Alzheimer disease. *Arch Neurol* 68: 1124–1130
 55. Tagliatela G, Hogan D, Zhang W-R, Dineley KT (2009) Intermediate- and long-term recognition memory deficits in Tg2576 mice are reversed with acute calcineurin inhibition. *Behav Brain Res* 200: 95–99
 56. Sanchez PE, Zhu L, Verret L, Vossel KA, Orr AG, Cirrito JR, Devidze N, Ho K, Yu G-Q, Palop JJ et al (2012) Levetiracetam suppresses neuronal network dysfunction and reverses synaptic and cognitive deficits in an Alzheimer's disease model. *Proc Natl Acad Sci USA* 109: E2895–E2903
 57. Lerdkrail C, Asavapanumas N, Brawek B, Kovalchuk Y, Mojtahedi N, Olmedillas del Moral M, Garaschuk O (2018) Intracellular Ca²⁺ stores control *in vivo* neuronal hyperactivity in a mouse model of Alzheimer's disease. *Proc Natl Acad Sci USA* 115: E1279–E1288
 58. Yu WH, Cuervo AM, Kumar A, Peterhoff CM, Schmidt SD, Lee J-H, Mohan PS, Mercken M, Farmery MR, Tjernberg LO et al (2005) Macroautophagy—a novel β -amyloid peptide-generating pathway activated in Alzheimer's disease. *J Cell Biol* 171: 87–98
 59. Maday S, Wallace KE, Holzbaur ELF (2012) Autophagosomes initiate distally and mature during transport toward the cell soma in primary neurons. *J Cell Biol* 196: 407–417
 60. Azarnia Tehran D, Kuijpers M, Haucke V (2018) Presynaptic endocytic factors in autophagy and neurodegeneration. *Curr Opin Neurobiol* 48: 153–159
 61. Ravikumar B, Moreau K, Jahreiss L, Puri C, Rubinsztein DC (2010) Plasma membrane contributes to the formation of pre-autophagosomal structures. *Nat Cell Biol* 12: 747–757
 62. Nilsson P, Loganathan K, Sekiguchi M, Matsuba Y, Hui K, Tsubuki S, Tanaka M, Iwata N, Saito T, Saido Takaomi C (2013) A β secretion and plaque formation depend on autophagy. *Cell Rep* 5: 61–69
 63. Nixon RA, Yang D-S (2011) Autophagy failure in Alzheimer's disease—locating the primary defect. *Neurobiol Dis* 43: 38–45
 64. Cataldo AM, Peterhoff CM, Troncoso JC, Gomez-Isla T, Hyman BT, Nixon RA (2000) Endocytic pathway abnormalities precede amyloid β deposition in sporadic Alzheimer's disease and Down syndrome: differential effects of APOE genotype and presenilin mutations. *Am J Pathol* 157: 277–286
 65. Israel MA, Yuan SH, Bardy C, Reyna SM, Mu Y, Herrera C, Hefferan MP, Van Gorp S, Napor KL, Boscolo FS et al (2012) Probing sporadic and familial Alzheimer's disease using induced pluripotent stem cells. *Nature* 482: 216–220

66. Karch CM, Goate AM (2015) Alzheimer's disease risk genes and mechanisms of disease pathogenesis. *Biol Psychiat* 77: 43–51
67. Zhao Z, Sagare AP, Ma Q, Halliday MR, Kong P, Kisler K, Winkler EA, Ramnathan A, Kanekiyo T, Bu G et al (2015) Central role for PICALM in amyloid- β blood-brain barrier transcytosis and clearance. *Nat Neurosci* 18: 978
68. Caglayan S, Takagi-Niidome S, Liao F, Carlo A-S, Schmidt V, Burgert T, Kitago Y, Füchtbauer E-M, Füchtbauer A, Holtzman DM et al (2014) Lysosomal sorting of amyloid- β by the sorla receptor is impaired by a familial Alzheimer's disease mutation. *Sci Transl Med* 6: 223ra220
69. Korvatska O, Leverenz JB, Jayadev S, McMillan P, Kurtz I, Guo X, Rumbaugh M, Matsushita M, Girirajan S, Dorschner MO et al (2015) R47H variant of TREM2 associated with Alzheimer disease in a large late-onset family: clinical, genetic, and neuropathological study. *JAMA Neurol* 72: 920–927
70. Korvatska O, Kiianitsa K, Ratushny A, Matsushita M, Chien W-M, Dorschner MO, Keene CD, Bammler TK, Bird TD, Raskind WH (2018) TREM2 R47H exacerbates immune response in Alzheimer's disease brain. *bioRxiv* <https://doi.org/10.1101/499319> [PREPRINT]
71. Seyfried NT, Dammer EB, Swarup V, Nandakumar D, Duong DM, Yin L, Deng Q, Nguyen T, Hales CM, Wingo T et al (2017) A multi-network approach identifies protein-specific co-expression in asymptomatic and symptomatic Alzheimer's disease. *Cell Syst* 4: 60–72.e64
72. Kanatsu K, Morohashi Y, Suzuki M, Kuroda H, Watanabe T, Tomita T, Iwatsubo T (2014) Decreased CALM expression reduces A β 42 to total A β ratio through clathrin-mediated endocytosis of γ -secretase. *Nat Commun* 5: 3386
73. Xiao Q, Gil S-C, Yan P, Wang Y, Han S, Gonzales E, Perez R, Cirrito JR, Lee J-M (2012) Role of phosphatidylinositol clathrin assembly lymphoid-myeloid leukemia (PICALM) in intracellular amyloid precursor protein (APP) processing and amyloid plaque pathogenesis. *J Biol Chem* 287: 21279–21289
74. Murdoch John D, Rostovsky Christine M, Gowrisankaran S, Arora Aman-deep S, Soukup S-F, Vidal R, Capece V, Freytag S, Fischer A, Verstreken P et al (2016) Endophilin-A deficiency induces the Foxo3a-Fbxo32 network in the brain and causes dysregulation of autophagy and the ubiquitin-proteasome system. *Cell Rep* 17: 1071–1086
75. Soukup S-F, Kuenen S, Vanhauwaert R, Manetsberger J, Hernández-Díaz S, Swerts J, Schoovaerts N, Vilain S, Gounko Natalia V, Vints K et al (2016) A LRRK2-dependent endophilina phosphoswitch is critical for macroautophagy at presynaptic terminals. *Neuron* 92: 829–844
76. De Strooper B, Karran E (2016) The cellular phase of Alzheimer's disease. *Cell* 164: 603–615
77. Garafalo SD, Luth ES, Moss BJ, Monteiro MI, Malkin E, Juo P (2015) The AP2 clathrin adaptor protein complex regulates the abundance of GLR-1 glutamate receptors in the ventral nerve cord of *Caenorhabditis elegans*. *Mol Biol Cell* 26: 1887–1900
78. Bonifacino JS, Traub LM (2003) Signals for sorting of transmembrane proteins to endosomes and lysosomes. *Annu Rev Biochem* 72: 395–447
79. Traub LM, Bannykh SI, Rodel JE, Aridor M, Balch WE, Kornfeld S (1996) AP-2-containing clathrin coats assemble on mature lysosomes. *J Cell Biol* 135: 1801–1814
80. Lundgren JL, Ahmed S, Schedin-Weiss S, Gouras GK, Winblad B, Tjernberg LO, Frykman S (2015) ADAM10 and BACE1 are localized to synaptic vesicles. *J Neurochem* 135: 606–615
81. Wang X, Zhang X-G, Zhou T-T, Li N, Jang C-Y, Xiao Z-C, Ma Q-H, Li S (2016) Elevated neuronal excitability due to modulation of the voltage-gated sodium channel Nav1.6 by A β 1–42. *Front Neurosci* 10: 94
82. Tian Y, Chang JC, Fan EY, Flajolet M, Greengard P (2013) Adaptor complex AP2/PICALM, through interaction with LC3, targets Alzheimer's APP-CTF for terminal degradation via autophagy. *Proc Natl Acad Sci USA* 110: 17071–17076
83. Heckmann BL, Teubner BJW, Tummers B, Boada-Romero E, Harris L, Yang M, Guy CS, Zakharenko SS, Green DR (2019) LC3-associated endocytosis facilitates β -amyloid clearance and mitigates neurodegeneration in murine Alzheimer's disease. *Cell* 178: 536–551.e514
84. Kononenko NL, Diril MK, Puchkov D, Kintscher M, Koo SJ, Pfuhl G, Winter Y, Wienisch M, Klingauf J, Breustedt J et al (2013) Compromised fidelity of endocytic synaptic vesicle protein sorting in the absence of stonin 2. *Proc Natl Acad Sci USA* 110: E526–E535
85. Singer O, Marr RA, Rockenstein E, Crews L, Coufal NG, Gage FH, Verma IM, Masliah E (2005) Targeting BACE1 with siRNAs ameliorates Alzheimer disease neuropathology in a transgenic model. *Nat Neurosci* 8: 1343
86. Chiba K, Yuki S, Masataka K, Toshiharu S, Seich U (2014) Simple and direct assembly of kymographs from movies using kymomaker. *Traffic* 15: 1–11
87. Kye MJ, Neveu P, Lee Y-S, Zhou M, Steen JA, Sahin M, Kosik KS, Silva AJ (2011) NMDA mediated contextual conditioning changes miRNA expression. *PLoS ONE* 6: e24682
88. Janvier K, Bonifacino JS (2005) Role of the endocytic machinery in the sorting of lysosome-associated membrane proteins. *Mol Biol Cell* 16: 4231–4242
89. Diril MK, Schmidt S, Krauss M, Gawlik V, Joost H-G, Schürmann A, Haucke V, Augustin R (2009) Lysosomal localization of GLUT8 in the testis—the ELL motif of GLUT8 is sufficient for its intracellular sorting via AP1- and AP2-mediated interaction. *FEBS J* 276: 3729–3743
90. Martins S, Bohndorf M, Schröter F, Assar F, Wruck W, Slegers K, Van Broeckhoven C, Adjaye J (2018) Lymphoblast-derived integration-free ISRM-CON9 iPSC cell line from a 75 year old female. *Stem Cell Res* 26: 76–79
91. Schröter F, Slegers K, Bohndorf M, Wruck W, Van Broeckhoven C, Adjaye J (2016) Lymphoblast-derived integration-free iPSC cell line from a 69-year-old male. *Stem Cell Res* 16: 29–31
92. Schröter F, Slegers K, Cuyvers E, Bohndorf M, Wruck W, Van Broeckhoven C, Adjaye J (2016) Lymphoblast-derived integration-free iPSC cell line from a 65-year-old Alzheimer's disease patient expressing the TREM2 p. R47H variant. *Stem Cell Res* 16: 113–115
93. Schröter F, Slegers K, Cuyvers E, Bohndorf M, Wruck W, Van Broeckhoven C, Adjaye J (2016) Lymphoblast-derived integration-free iPSC cell line from a female 67-year-old Alzheimer's disease patient with TREM2 (R47H) missense mutation. *Stem Cell Res* 17: 553–555
94. Liu Y, Liu H, Sauvey C, Yao L, Zarnowska ED, Zhang S-C (2013) Directed differentiation of forebrain GABA interneurons from human pluripotent stem cells. *Nat Protoc* 8: 1670



License: This is an open access article under the terms of the Creative Commons Attribution 4.0 License, which permits use, distribution and reproduction in any medium, provided the original work is properly cited.

Expanded View Figures

Figure EV1. AP-2 regulates the recycling of BACE1 in the brain.

- A BACE1 is co-immunoprecipitated (Co-IP) by the AP-2 μ -specific antibody (IP) from the mouse brain cortex (high exposure was used to show the input).
- B AP-2 α is co-immunoprecipitated (Co-IP) by the BACE1-specific antibody (IP) from the mouse brain cortex (high exposure was used to show the input).
- C Representative fluorescence images of neurons expressing the HA-BACE1-eGFP and immunostained for endogenous BACE1. Scale bars: 20 μ m (left panel), 5 μ m (zoomed images).
- D Representative fluorescence images of neurons expressing the HA-BACE1-eGFP or non-transfected neurons immunostained for endogenous BACE1. Scale bars: 20 μ m.
- E Schematic illustration of the assay used in Fig 1A.
- F Acid-stripping control for the removal of the membrane-bound HA antibody in AP-2 μ KO neurons, overexpressing the HA-BACE1-eGFP. Scale bar: 10 μ m.
- G Overview images of HA-BACE1-eGFP-expressing neurons shown in Fig 1C. Scale bar: 15 μ m.
- H Overview images of HA-BACE1-eGFP-expressing neurons shown in Fig 1E. Scale bar: 15 μ m.
- I Recycled-to-total BACE1 ratio in WT neurons overexpressing either eGFP or eGFP-RAB4. Twenty-eight eGFP-expressing neurons and 22 eGFP-RAB4-expressing neurons, $N = 2$ biological replicates.
- J, K Overview images of HA-BACE1-mCherry-expressing neurons, additionally co-expressing either GFP-RAB4 or GFP-RAB4S22N, shown in Fig 1G. Magnified axonal fragments are shown in (K). Scale bars: 10 μ m.
- L Recycled levels of BACE1 after 20 min of HA antibody chase in HA-BACE1-mCherry-transfected WT and KO neurons, co-expressing either eGFP or eGFP-RAB11-S25N, calculated as the HA(recycled)/mCherry(total) signal intensity ratio (WT^{GFP}: 0.12 ± 0.02 , KO^{GFP}: 0.23 ± 0.04 , WT^{GFP-RAB11-S25N}: 0.08 ± 0.02 , KO^{GFP-RAB11-S25N}: 0.13 ± 0.02 , pWT^{GFP} versus pKO^{GFP} = 0.024, pWT^{GFP} versus pWT^{GFP-RAB11-S25N} = 0.840, pKO^{GFP} versus pKO^{GFP-RAB11-S25N} = 0.047, pWT^{GFP-RAB11-S25N} versus pKO^{GFP-RAB11-S25N} = 0.587, 20–24 neurons per condition, $N = 3$ biological replicates).
- M, N Overview images of HA-BACE1-mCherry-expressing neurons, additionally co-expressing either GFP-RAB4 or GFP-RAB4S22N, shown in Fig 1J. Magnified axonal fragments are shown in (N). Scale bars: 10 μ m.
- O Levels of internalized BACE1 are increased in AP-2 μ KO neurons overexpressing the RAB11-S25N mutant (WT^{GFP}: 0.46 ± 0.05 , KO^{GFP}: 0.26 ± 0.02 , WT^{GFP-RAB11-S25N}: 0.49 ± 0.03 , KO^{GFP-RAB11-S25N}: 0.38 ± 0.03 , pWT^{GFP} versus pKO^{GFP} = 0.000, pWT^{GFP} versus pWT^{GFP-RAB11-S25N} = 0.919; pKO^{GFP} versus pKO^{GFP-RAB11-S25N} = 0.044, pWT^{GFP-RAB11-S25N} versus pKO^{GFP-RAB11-S25N} = 0.105, 40–42 neurons for each condition, $N = 5$ biological replicates).
- P Levels of BACE1 are significantly increased in AP-2 μ KO-cultured neuronal lysates compared to the WT set to 100% (KO: 165.42 ± 25.3 , $P = 0.040$, also see Fig 1L). $N = 4$ biological replicates.
- Q, R Loss of AP-2 μ does not impair the trafficking of BACE1 toward early endosomes, marked by overexpression of RAB5-Q79L in WT and AP-2 μ KO neurons. Line plot analysis in (R) indicates BACE1 distribution in early endosomes marked by dotted lines in (Q). Scale bar: 5 μ m.
- S Overview images of neurons shown in Fig 1O. Scale bar, 50 μ m.
- T, U Overview images of WT and AP-2 μ KO neurons immunostained for surface and total GABAR β 3. Ratio of surface to total GABAR β 3 is increased in KO neurons compared to WT (WT: 0.24 ± 0.03 , KO: 0.34 ± 0.03 , $P = 0.024$, 32 WT and 38 KO neurons, $N = 3$ biological replicates). Scale bar: 20 μ m.
- Data information: Rectangles in Appendix Fig S1G, H, J and M indicate regions magnified in Fig 1. All graphs show mean \pm SEM; statistical analysis was performed by unpaired two-tailed Student's *t*-test in (I, U), two-way ANOVA in (L, O), and one-sample Student's *t*-test in (P). n.s.—non-significant. * indicates $P \leq 0.05$; ** indicates $P \leq 0.01$; *** indicates $P \leq 0.001$.

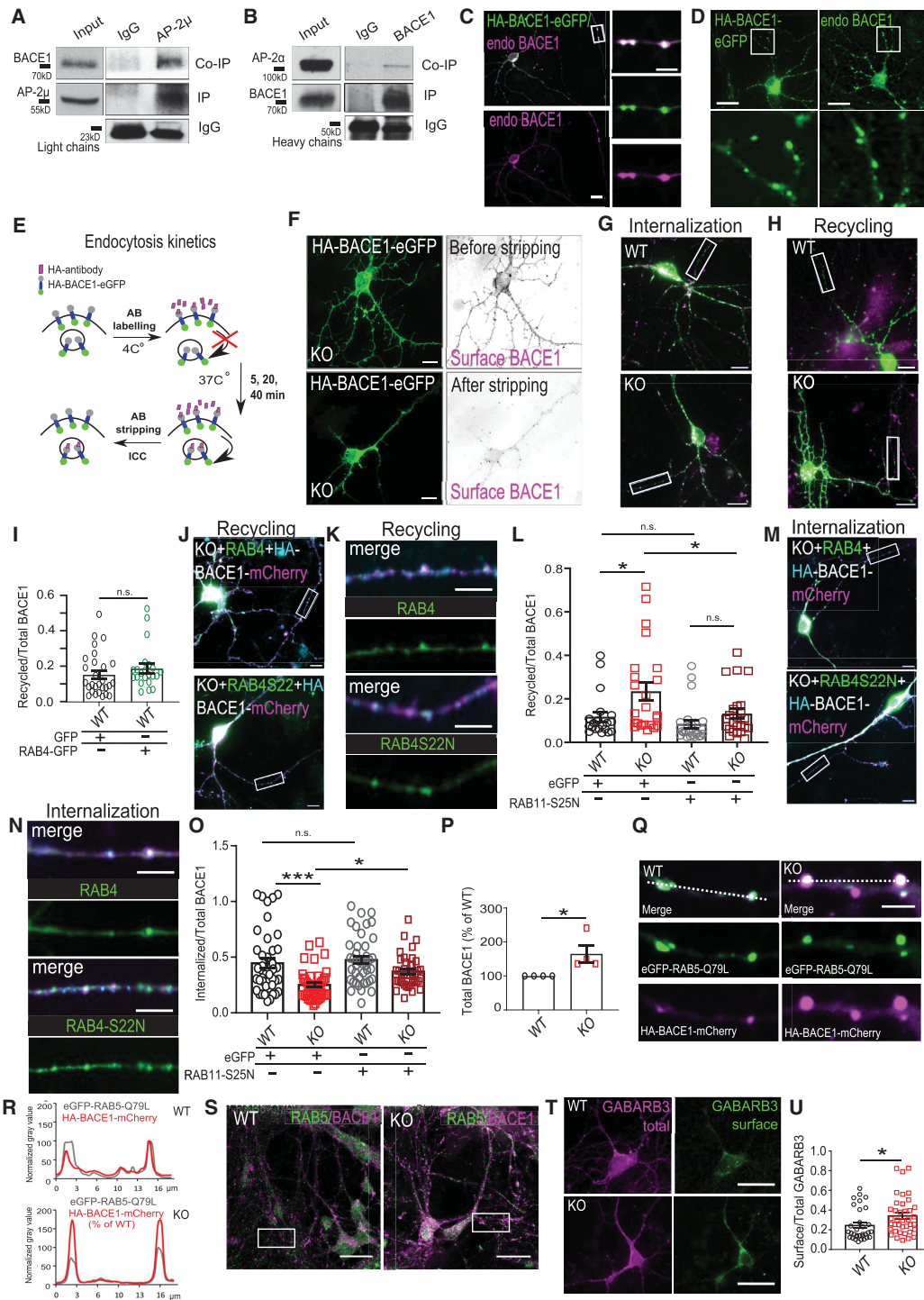


Figure EV1.

Figure EV2. AP-2 μ regulates lysosomal BACE1 levels.

- A Significantly reduced AP-2 α levels in the cortex of AP-2 μ KO mice. Protein levels in the KO were normalized to the WT set to 100% (KO: 31.49 ± 5.54 , $P < 0.000$, $N = 7$ biological replicates).
- B, C Significantly reduced AP-2 μ levels in the cortex of AP-2 μ KO mice. Protein levels in the KO were normalized to the WT set to 100% (KO: $20.05 \pm 5.39\%$, $P = 0.000$, $N = 4$ biological replicates).
- D, E Significantly reduced levels of AP-2 μ in AP-2 μ KO-cultured neurons. Protein levels in the KO were normalized to the WT set to 100% (KO: $8.87 \pm 3.17\%$, $P = 0.000$, $N = 3$ biological replicates).
- F, G Significantly increased BACE1 levels in AP-2 μ KO-cultured neurons. Protein levels in the KO were normalized to the WT set to 100% (KO: $180.51 \pm 25.99\%$, $P = 0.037$, $N = 4$ biological replicates).
- H *Bace1* mRNA levels measured by qPCR are not significantly altered in AP-2 μ KO neurons (KO/WT^{*Bace1*}: 1.00 ± 0.03 , KO/WT^{*Gapdh*}: 0.99 ± 0.02 , $P = 0.921$, $N = 3$ biological replicates). mRNA levels in the KO were normalized to the WT set to 1.
- I Overview images of neurites represented in Fig 2G. Scale bar, 20 μ m.
- J Overview images of neurites represented in Fig 2I. Scale bar, 20 μ m.
- K, L Horizontal sections from WT and AP-2 μ KO entorhinal cortex immunostained with either LAMP2a (K) or MAP2 (L) antibodies. Scale bars: 20 μ m
- M BACE1 levels are unaltered in lysates from cultured WT and AP-2 μ KO neurons, either treated with 5 μ M cycloheximide alone or co-treated with 80 nM bafilomycin A for 12 h.
- N Representative confocal images of BACE1-mKeima-Red-expressing neurons incubated with LysoTracker Blue-White for 15 min to label the lysosomes. Scale bar: 10 μ m, 1 μ m for zoomed images.
- O Percentage of BACE1-mKeima-Red puncta localized to lysosomes (94.61 ± 4.12), 17 cells from $N = 2$ biological replicates.
- P Representative confocal images of BACE1-mKeima-Red-expressing WT and AP-2 μ KO neurons. In the KO, the majority of BACE1-mKeima organelles at neutral pH was confined to axons located distally from the soma (arrows). Scale bars: 20 μ m.
- Data information: All graphs show mean \pm SEM; statistical analysis was performed by unpaired one-sample Student's *t*-test in (A, C, E, G, H). n.s.—non-significant. * indicates $P \leq 0.05$; ** indicates $P \leq 0.01$; *** indicates $P \leq 0.001$.

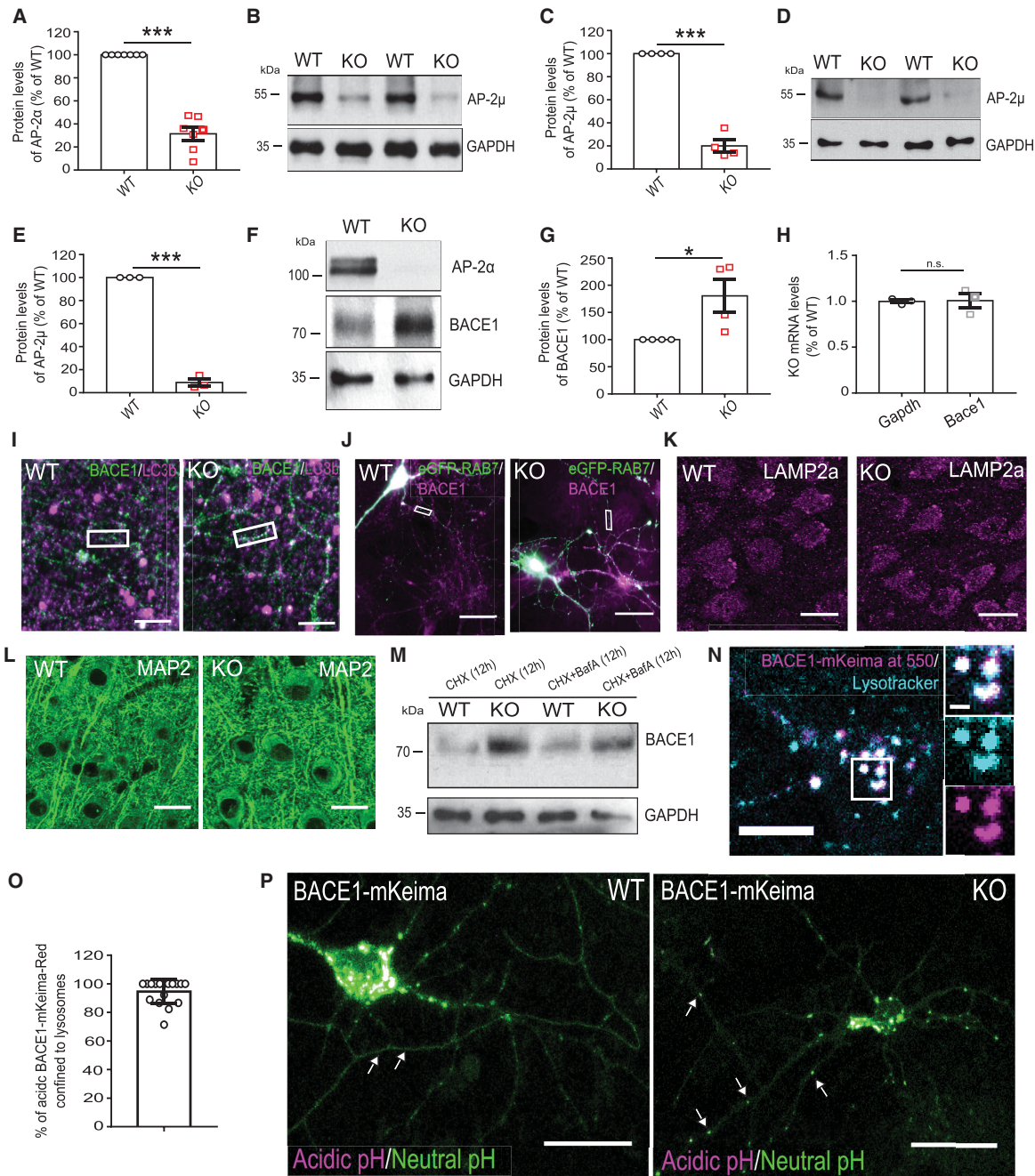


Figure EV2.

Figure EV3. Functionality of AP-2 μ -mCherry and HA-BACE1-eGFP constructs.

- A, B Overexpressed AP-2 μ -mCherry restores clathrin-mediated endocytosis of transferrin in HEK cells depleted of endogenous AP-2 μ (mCherry^{scr}: 0.19 ± 0.02 , mCherry^{AP-2 μ -siRNA}: 0.09 ± 0.01 , AP-2 μ -mCherry^{scr}: 0.23 ± 0.01 , AP-2 μ -mCherry^{AP-2 μ -siRNA}: 0.25 ± 0.01 , p^{mCherry-scr} versus p^{mCherry-AP-2 μ -siRNA} < 0.000; p^{mCherry-scr} versus p^{AP-2 μ -mCherry-scr} = 0.289, p^{mCherry-AP-2 μ -siRNA} versus p^{AP-2 μ -mCherry-AP-2 μ -siRNA} < 0.000, p^{AP-2 μ -mCherry-scr} versus p^{AP-2 μ -mCherry-AP-2 μ -siRNA} = 0.690, 26 cells for each condition, N = 1 biological replicates). Scale bars: 10 μ m.
- C, D Large portion ($81.8 \pm 3.37\%$) of overexpressed AP-2 μ -mCherry associates with endogenous AP-2 α , 20 axons from 10 neurons. Scale bar: 2 μ m.
- E, F A β_{1-42} levels are upregulated in neurons overexpressing the HA-BACE1-eGFP, comparing to cells expressing the eGFP only (GFP: 0.24 ± 0.8 , BACE1: 0.79 ± 0.16 , P = 0.006). Eleven eGFP- and 12 HA-BACE1-eGFP-expressing neurons, N = 1 biological replicates. Scale bars: 20 μ m.
- G Histogram representation of BACE1 retrograde velocity in control neurons overexpressing either the HA-BACE1-eGFP or the BACE1-eGFP (axonal fragments from 28 to 31 neurons, N = 3 biological replicates).
- H Percentage of BACE1 puncta colocalizing with AP-2 μ in control neurons ($74.22 \pm 2.09\%$), 48 neurons, N = 4 biological replicates.
- I Percentage of AP-2 μ puncta colocalizing with BACE1 in control neurons ($83.35 \pm 2.56\%$), 46 neurons, N = 4.
- J, K Co-localization of endogenous BACE1 and AP-2 μ , measured using Pearson's co-localization coefficient (0.88 ± 0.01 , 36 neurons, N = 3 biological replicates). Scale bars, 20 μ m (left panel), 5 μ m (zoomed images).
- L Percentage of mobile BACE1 carriers positive for AP-2 μ in control neurons, normalized to total double-labeled puncta set to 100% ($20.12 \pm 1.95\%$, 48 neurons, N = 4 biological replicates).
- M Representative fluorescence images and corresponding kymographs from time-lapse videos of WT and AP-2 μ KO neurons transfected with BACE1-eGFP. Scale bars: 2 μ m top panels, x = 2 μ m, y = 5s bottom panels.
- N Retrograde velocity of BACE1-eGFP carriers is significantly reduced in AP-2 μ KO neurons (WT^{retro}: 0.37 ± 0.03 , KO^{retro} = 0.25 ± 0.03 , P = 0.002, 29 WT and 30 KO neurons, N = 3 biological replicates). In these experiments, live-cell imaging was performed 24 h post-transfection to exclude the overexpression artifact.
- O Retrograde mobility of autophagic BACE1 in WT and AP-2 μ KO neurons (WT: $18.74 \pm 2.92\%$, KO: $6.60 \pm 1.6\%$, P = 0.000), 36 WT and 36 KO neurons, N = 4 biological replicates).
- P, Q Significantly decreased retrograde mobility of BACE1 in HA-BACE1-eGFP-expressing ATG5 KO neurons comparing to the WT (WT: $48.63 \pm 3.94\%$, KO^{ATG5}: $34.96 \pm 3.22\%$, P = 0.008, 30 WT and 35 KO neurons, N = 3 biological replicates). Scale bars: 2 μ m top panels, x = 2 μ m, y = 5 s bottom panels.
- R, S Increased recycling of BACE1-LL/AA when compared to WT BACE1 (WT: 0.05 ± 0.00 , LL/AA: 0.09 ± 0.01 , P = 0.003, 25–26 neurons per condition, N = 4 biological replicates). Scale bar, 5 μ m.
- T Representative images of neurons expressing either HA-BACE1-GFP or HA-BACE1-LL/AA-GFP and immunostained for Cathepsin D (CTSD). Scale bar 5 μ m.
- U Significantly decreased percentage of HA-BACE1-LL/AA puncta found in lysosomes compared to WT BACE1 (WT: $34.99 \pm 5.22\%$, KO: $19.98 \pm 3.49\%$, P = 0.019, 22–24 neurons per group, N = 3 biological replicates).

Data information: All graphs show mean \pm SEM; statistical analysis was performed by unpaired two-tailed Student's t-test in (F, N, O, Q, S, U) and two-way ANOVA in (B). n.s.—non-significant.* indicates P \leq 0.05; ** indicates P \leq 0.01; *** indicates P \leq 0.001.

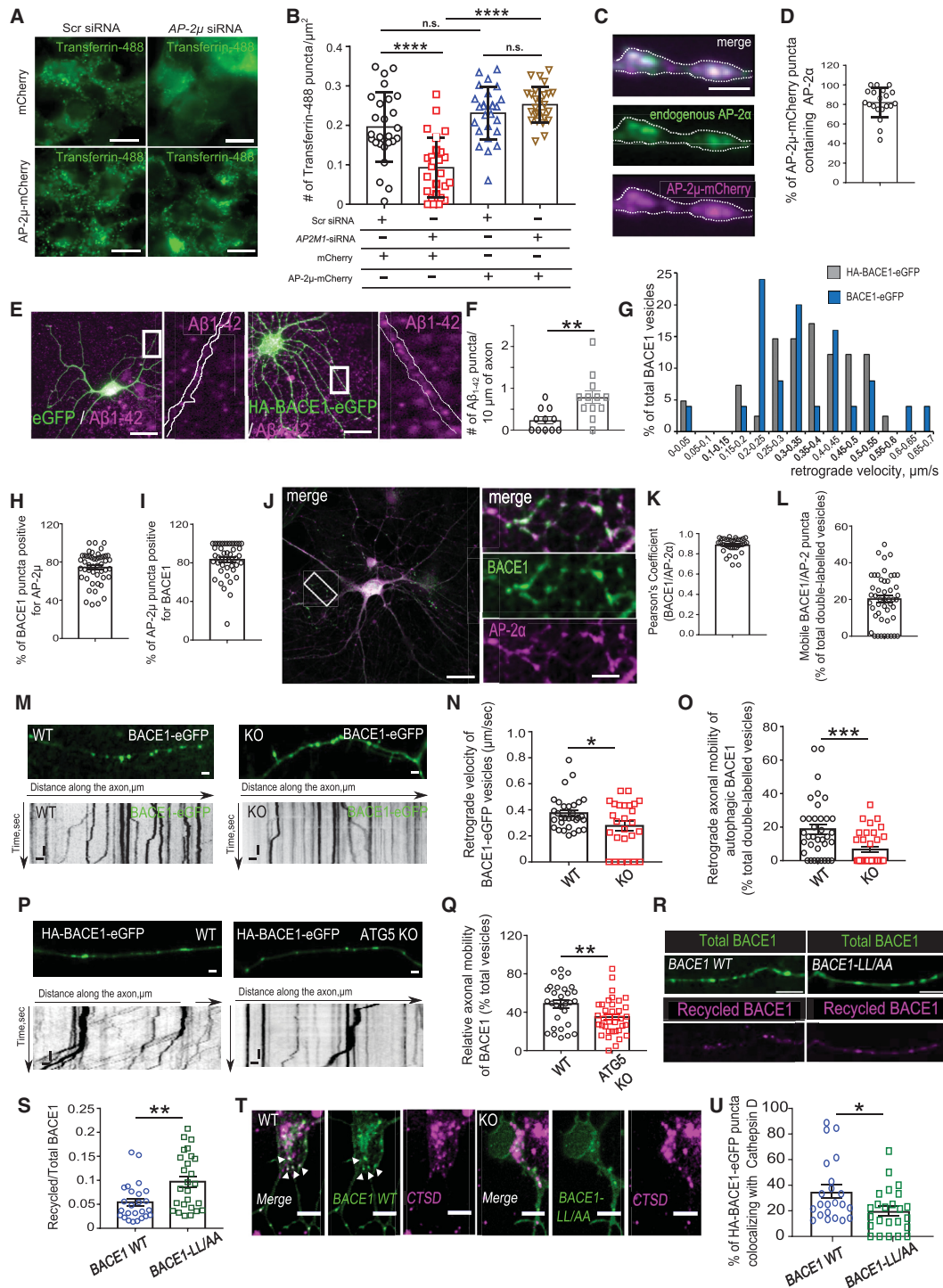


Figure EV3.

Figure EV4. Regulation of APP processing by the AP-2 μ in neurons.

- A Schematic illustration of BACE1 activity monitored using the APP Lys612Val mutant (mCherry-APP-P1-eGFP).
- B Representative fluorescence images of mCherry-APP-P1-eGFP-expressing WT and AP-2 μ KO neurons, immunostained for mCherry and GFP. Scale bar, 10 μ m.
- C Representative fluorescence images of HA-BACE1-eGFP-expressing WT and AP-2 μ KO neurons, immunostained for APP. Scale bars: 5 μ m (upper panels), 2 μ m (lower panels).
- D Percentage of BACE1 puncta colocalizing with APP in WT and AP-2 μ KO neurons (WT: 17.27 \pm 1.66%, KO: 29.19 \pm 3.57%, P = 0.003, 40 WT and 40 KO neurons, N = 4 biological replicates).
- E Percentage of APP puncta colocalizing with BACE1 in WT and AP-2 μ KO neurons (WT: 22.78 \pm 2.52%, KO: 31.78 \pm 3.18%, P = 0.030, 36 WT and 30 KO neurons, N = 4 biological replicates).
- F WT and AP-2 μ KO entorhinal cortex of mice at p21 immunostained for Reelin. Scale bars: 50 μ m.
- G, H Levels of L1-CTF β are significantly increased in AP-2 μ KO cortex compared to the WT set to 100% (KO^{C99}: 359.87 \pm 95.77%, P = 0.015, N = 4 biological replicates).
- I, J The mCherry (surface APP)/eGFP (total APP) signal intensity ratio is significantly increased in AP-2 μ KO condition compared to the WT (WT: 1.52 \pm 0.19, KO: 2.43 \pm 0.36, P = 0.028, 30 WT and 29 KO neurons, N = 3 biological replicates). Scale bars: 10 μ m.
- K Unaltered levels of Nicastrin in cortical lysates from AP-2 μ KO mice. Protein levels in KO condition were normalized to the WT set to 100% (KO: 105.03 \pm 9.02%, P = 0.300, N = 6 biological replicates).
- L Representative fluorescence images of axons from RFP-LC3B-expressing WT and AP-2 μ KO neurons immunostained for A β ₁₋₄₂. Scale bar: 4 μ m. Arrowheads indicate localization of A β ₁₋₄₂ puncta to LC3B-positive autophagosomes.
- M Autophagosomal levels of A β ₁₋₄₂ are increased in AP-2 μ KO neurons (WT: 1299.58 \pm 166.36, KO: 2002.6 \pm 185.72, P = 0.006, 41 WT and 41 KO neurons, N = 3 biological replicates). Scale bar: 5 μ m.
- N, O Levels of secreted A β ₁₋₄₀ (N) and A β ₁₋₄₂ (O) are significantly decreased in the media of AP-2 μ KO neurons compared to the WT (WT^{A β 1-40}: 7.85 \pm 1.33, KO^{A β 1-40}: 5.35 \pm 0.80, P = 0.011, N = 6 biological replicates; WT^{A β 1-42}: 8.69 \pm 0.45, KO^{A β 1-42}: 7.26 \pm 0.29, P = 0.037, N = 6 biological replicates). Values represent pmol/l raw data, which were square-root-transformed due to the lack of normality.
- P-R Levels of BACE1 are increased in control neurons overexpressing the HA-AP2Mut compared to HA-AP2x WT-expressing cells (WT: 0.22 \pm 0.03, Mut: 0.44 \pm 0.04, P < 0.000, 25 WT and 28 Mut neurons, N = 3 biological replicates). Rectangles in (P) indicate the area magnified in (Q). Scale bars, 10 μ m in (P), 2.5 μ m in (Q).
- S, T Analysis of BACE1 KD efficiency in HEK cells, expressing the mouse FLAG-BACE1. *Bace1* shRNA significantly reduces BACE1 levels compared to scr controls set to 100% (*Bace1*^{shRNA}: 7.86 \pm 1.78%, P < 0.000, N = 4 biological replicates).
- U, V Number of A β ₁₋₄₂ puncta is reduced in AP-2 μ KO neurons overexpressing the AP-2 μ -mRFP, when compared to KO neurons expressing the mCherry (WT^{mCherry}: 0.49 \pm 0.07, KO^{mCherry}: 0.79 \pm 0.10, WT^{AP-2 μ -mRFP}: 0.54 \pm 0.07, KO^{AP-2 μ -mRFP}: 0.46 \pm 0.06, pWT^{mCherry} versus pKO^{mCherry} = 0.026, pWT^{mCherry} versus pWT^{AP-2 μ -mRFP} = 0.963, pKO^{mCherry} versus pKO^{AP-2 μ -mRFP} = 0.008, pWT^{AP-2 μ -mRFP} versus pKO^{AP-2 μ -mRFP} = 0.840, 38-40 neurons per condition, N = 4 biological replicates). Scale bar: 2 μ m.

Data information: All graphs show mean \pm SEM; statistical analysis was performed by unpaired two-tailed Student's t -test in (D, E, J, M, R), two-way ANOVA in (V), and one-sample Student's t -test in (H, K, T). Non-normally distributed data (N,O) were transformed using square root transformation and analyzed using paired two-tailed Student's t -test. n.s.—non-significant. * indicates P \leq 0.05; ** indicates P \leq 0.01; *** indicates P \leq 0.001.

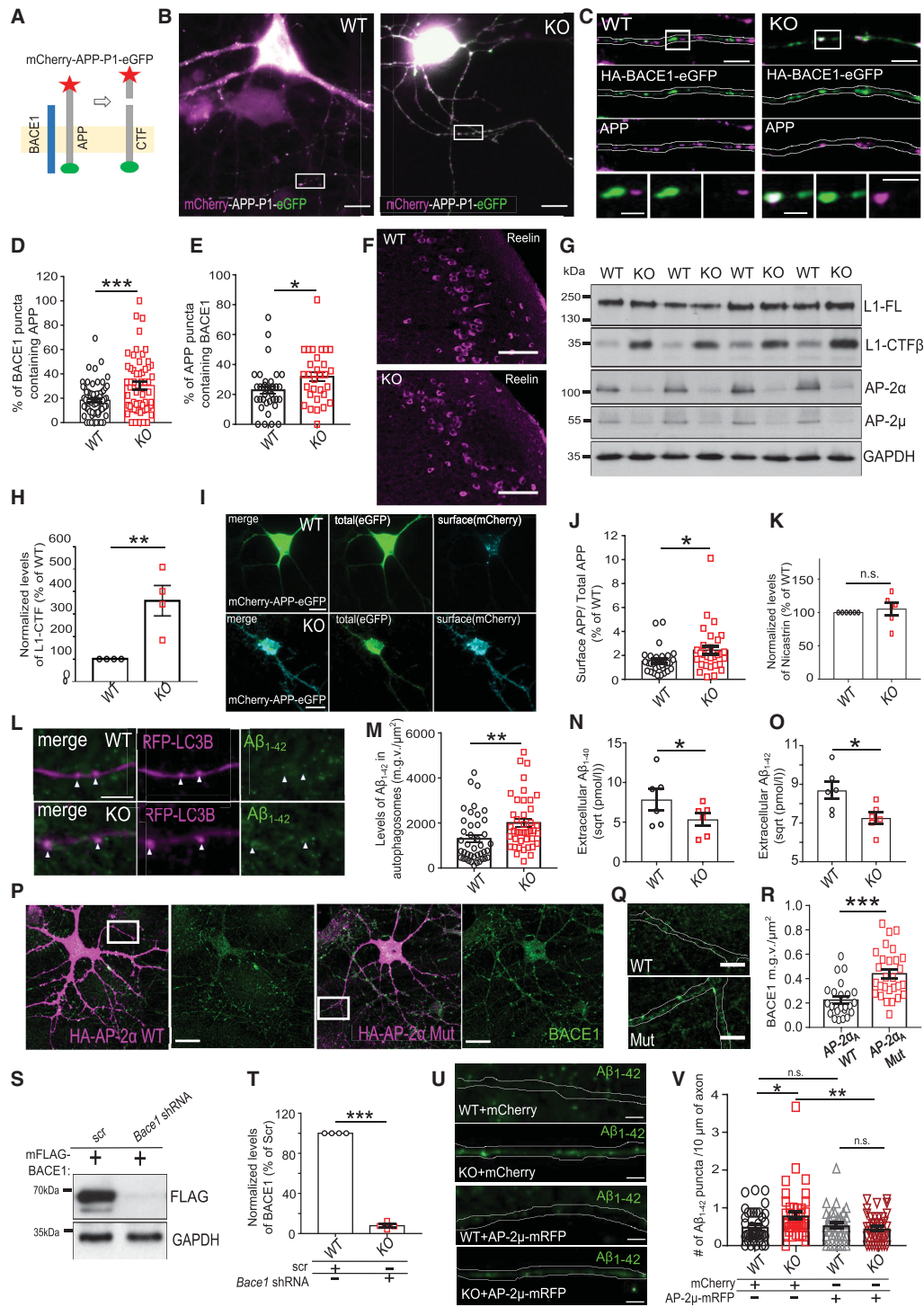


Figure EV4.

Figure EV5. AP-2-dependent BACE1 trafficking is required to prevent the neurodegeneration in the brain.

- A AP-1 γ 1 levels in lysates of iPSC-derived neurons from late-onset AD patients carrying the *TREM2 p.R47H* (AD-*TREM2-2* and AD-*TREM2-4*) variant compared to healthy controls (CON8 and CON9).
- B Confocal images of AAV-GFP^{CamKII α} -labeled WT and AP-2 μ KO dentate gyrus (DG) granule cells. Scale bars: 20 and 5 μ m.
- C, D Dendritic spine number is significantly reduced in eGFP-expressing AP-2 μ KO-cultured neurons when compared to the WT (WT: 4.08 ± 0.30 , KO: 2.36 ± 0.38 , $P = 0.000$), 26 WT and 24 KO neurons, $N = 3$ biological replicates. Scale bar: 2 μ m.
- E Overview images of WT and AP-2 μ KO entorhinal cortex shown in Fig 5E. Scale bar: 5 μ m.
- F Representative images of dendritic fragments of WT and AP-2 μ KO neurons either expressing mCherry or AP-2 μ -mRFP and immunostained for PSD95 and Bassoon. Scale bar, 5 μ m.
- G Overlap coefficient between Bassoon and PSD95 is increased in AP-2 μ KO neurons expressing the AP-2 μ -mRFP, compared to KO neurons expressing the mCherry (WT^{mCherry}: 0.63 ± 0.02 , KO^{mCherry}: 0.52 ± 0.02 , WT^{AP-2 μ -mRFP}: 0.63 ± 0.02 , KO^{AP-2 μ -mRFP}: 0.60 ± 0.02 , pWT^{mCherry} versus pKO^{mCherry} = 0.0003, pWT^{mCherry} versus pWT^{AP-2 μ -mRFP} > 0.999, pKO^{mCherry} versus pKO^{AP-2 μ -mRFP} = 0.015, pWT^{AP-2 μ -mRFP} versus pKO^{AP-2 μ -mRFP} = 0.609, 26–27 neurons per condition, $N = 4$ biological replicates).
- H Representative heatmaps, showing the position of the WT and AP-2 μ KO mouse in the experimental arena in the NOR training session.
- I No significant difference in the exploration time toward neither object 1 (Obj 1) nor Obj 2 was observed for WT and AP-2 μ KO mice during the training period (WT^{obj1}: 50.71 ± 7.34 , WT^{obj2}: 49.29 ± 7.85 , pWT^{obj1} versus WT^{obj2} = 0.901; KO^{obj1}: 38.48 ± 8.12 , KO^{obj2}: 61.52 ± 8.68 , pKO^{obj1} versus KO^{obj2} = 0.065; 7 WT and 8 KO mice).
- J Total exploration time in NOR test is not altered in AP-2 μ KO mice (WT: $45.55 \pm 7.24\%$, KO: $39.63 \pm 14.48\%$, $P = 0.733$, 7 WT and 8 KO mice).
- K Nissl-stained brain sections of WT and AP-2 μ KO mice shown in Fig 5M and N. Scale bars: 500 μ m. White boxes indicate the area magnified in Fig 5M and N.
- L Representative confocal images of WT and AP-2 μ KO brains haploinsufficient for BACE1 immunostained for activated caspase-3 and NeuN. Scale bar: 200 μ m.
- M The number of apoptotic cells is reduced in the hilus of AP-2 μ KO mice haploinsufficient for BACE1 (AP-2^{WT}/BACE^{WT}: 1.00 ± 0.58 , AP-2^{KO}/BACE^{WT}: 17.67 ± 3.28 , AP-2^{WT}/BACE^{HET}: 2.00 ± 0 , AP-2^{KO}/BACE^{HET}: 8.00 ± 1.54 ; p^{AP-2WT/BACE1WT} versus p^{AP-2KO/BACE1WT} = 0.000, p^{AP-2KO/BACE1WT} versus p^{AP-2KO/BACE1HET} = 0.020; p^{AP-2WT/BACE1HET} versus p^{AP-2KO/BACE1HET} = 0.153). Three sections from $N = 3$ mice for each genotype.

Data information: All graphs show mean \pm SEM; statistical analysis was performed by unpaired two-tailed Student's *t*-test in (D, J, I) and two-way ANOVA in (G, M). n.s.—non-significant. * indicates $P \leq 0.05$; ** indicates $P \leq 0.01$; *** indicates $P \leq 0.001$.

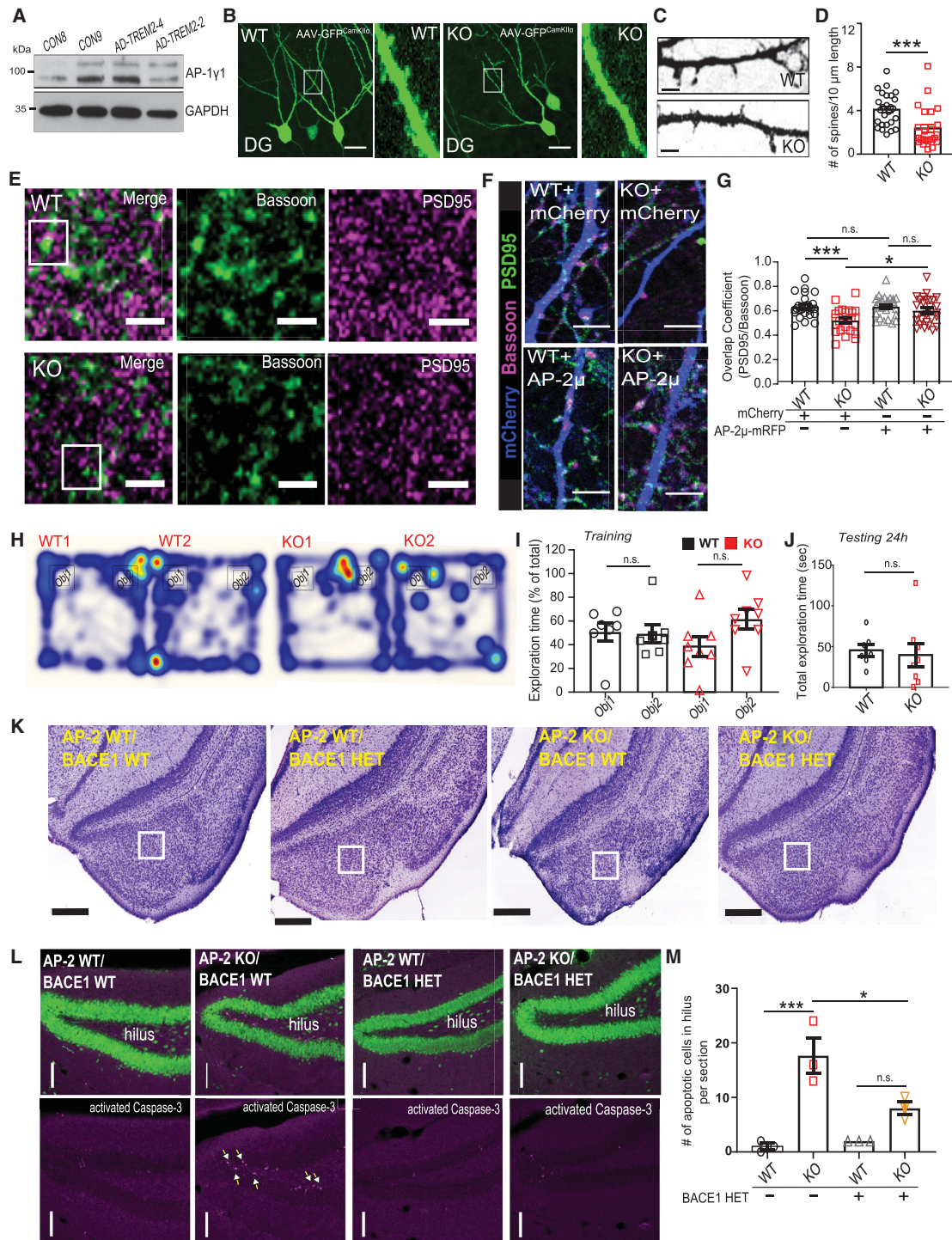


Figure EV5.

3 | Results II:

Modelling NBS using patient-derived 3D cerebral organoids

3.1 Fibroblast-derived integration-free iPSC line ISRM-NBS1 from an 18-year old Nijmegen Breakage Syndrome patient carrying the homozygous *NBN* c.657_661del5 mutation

Soraia Martins, Martina Bohndorf, Nina Graffmann, Wasco Wruck, Krystyna H.

Chrzanowska and James Adjaye

Stem Cell Research 34, (2019) 101372

Abstract

Human fibroblasts cells from a female diagnosed with Nijmegen Breakage Syndrome (NBS) carrying the homozygous *NBN* c.657_661del5 mutation were used to generate integration-free induced pluripotent stem cells (iPSCs) by over-expressing episomal-based plasmids harbouring OCT4, SOX2, NANOG, KLF4, c-MYC and LIN28. The derived iPSC line – ISRM-NBS1 was defined as pluripotent based on (i) expression of pluripotency-associated markers (ii) embryoid body-based differentiation into cell types representative of the three germ layers and (iii) the similarity between the transcriptome of the iPSC line and the human embryonic stem cell line H1 with a Pearson correlation of 0.955.

Author's contribution: 75 %

Conceptualization: SM and JA. Methodology: SM, MB and NG; Data curation: WW, Resources: KHC. Manuscript writing: SM and JA. All authors have read and agreed to the published version of the manuscript.

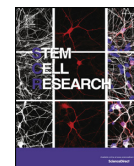
Status: Published in *Stem Cell Research* (doi.org/10.1016/j.scr.2018.101372)

This is an open access article under the terms of the Creative Commons Attribution 4.0 License.



Contents lists available at ScienceDirect

Stem Cell Research

journal homepage: www.elsevier.com/locate/scr

Lab resource: Stem Cell Line

Fibroblast-derived integration-free iPSC line ISRM-NBS1 from an 18-year-old Nijmegen Breakage Syndrome patient carrying the homozygous *NBN* c.657_661del5 mutation



Soraia Martins^a, Martina Bohndorf^a, Nina Graffmann^a, Wasco Wruck^a,
Krystyna H. Chrzanowska^b, James Adjaye^{a,*}

^a Institute for Stem Cell Research and Regenerative Medicine, Medical Faculty, Heinrich-Heine-University Düsseldorf, Moorenstr. 5, 40225 Düsseldorf, Germany

^b Department of Medical Genetics, Children's Memorial Health Institute, Warsaw, Poland

ABSTRACT

Human fibroblasts cells from a female diagnosed with Nijmegen Breakage Syndrome (NBS) carrying the homozygous *NBN* c.657_661del5 mutation were used to generate integration-free induced pluripotent stem cells (iPSCs) by over-expressing episomal-based plasmids harbouring OCT4, SOX2, NANOG, KLF4, c-MYC and LIN28. The derived iPSC line – ISRM-NBS1 was defined as pluripotent based on (i) expression of pluripotency-associated markers (ii) embryoid body-based differentiation into cell types representative of the three germ layers and (iii) the similarity between the transcriptome of the iPSC line and the human embryonic stem cell line H1 with a Pearson correlation of 0.955.

Resource table

Unique stem cell line identifier	HHUUKDi006-A.
Alternative name(s) of stem cell line	ISRM-NBS1
Institution	Institute for Stem Cell Research and Regenerative Medicine, Medical Faculty, Heinrich-Heine-University, Düsseldorf, Germany Department of Medical Genetics - Children's Memorial Health Institute, Warsaw, Poland
Contact information of distributor	James Adjaye, james.adjaye@med.uni-duesseldorf.de
Type of cell line	iPSC
Origin	Human
Additional origin info	Applicable for human ESC or iPSC Age:18 Sex: Female
Cell Source	Human dermal fibroblasts cells
Clonality	Clonal
Method of reprogramming	Episomal-based plasmid expressing OCT4, SOX2, NANOG, KLF4, c-MYC and LIN28
Genetic modification	No
Type of modification	n/a
Associated disease	Nijmegen Breakage Syndrome
Gene/locus	<i>NBN</i> c.657_661del5 homozygous
Method of modification	n/a
Name of transgene or resistance	None
	n/a

Inducible/constitutive system

Date archived/stock date 11-04-2018
Cell line repository/bank n/a
Ethical approval

Approved by the Ethics Committee of the Children's Memorial Health Center, Warsaw, Poland (approved on 5-04-1993 for a grant from the State Committee for Scientific Research of the Republic of Poland (PB 219/S4/93/05) to K. Chrzanowska)

Resource utility

The use of ISRM-NBS1 iPSC line provides an excellent platform for disease modelling to dissect the etiology of NBS and reveal potential therapeutic targets.

Resource details

Nijmegen Breakage Syndrome (NBS) is a rare autosomal recessive genetic disorder clinically characterized by congenital microcephaly, early growth retardation, chromosomal instability, immunodeficiency, impaired puberty, infertility in females and high predisposition to malignancy. NBS is caused by mutations in the *NBN* gene, being the most prevalent one the homozygous *NBN* c.657_661del5, which leads to the truncation of the wild-type protein Nibrin (p95-NBS1). The two

* Corresponding author.

E-mail address: james.adjaye@med.uni-duesseldorf.de (J. Adjaye).

<https://doi.org/10.1016/j.scr.2018.101372>

Received 13 November 2018; Accepted 17 December 2018

Available online 27 December 2018

1873-5061/ © 2019 The Authors. Published by Elsevier B.V. This is an open access article under the CC BY-NC-ND license (<http://creativecommons.org/licenses/by-nc-nd/4.0/>).

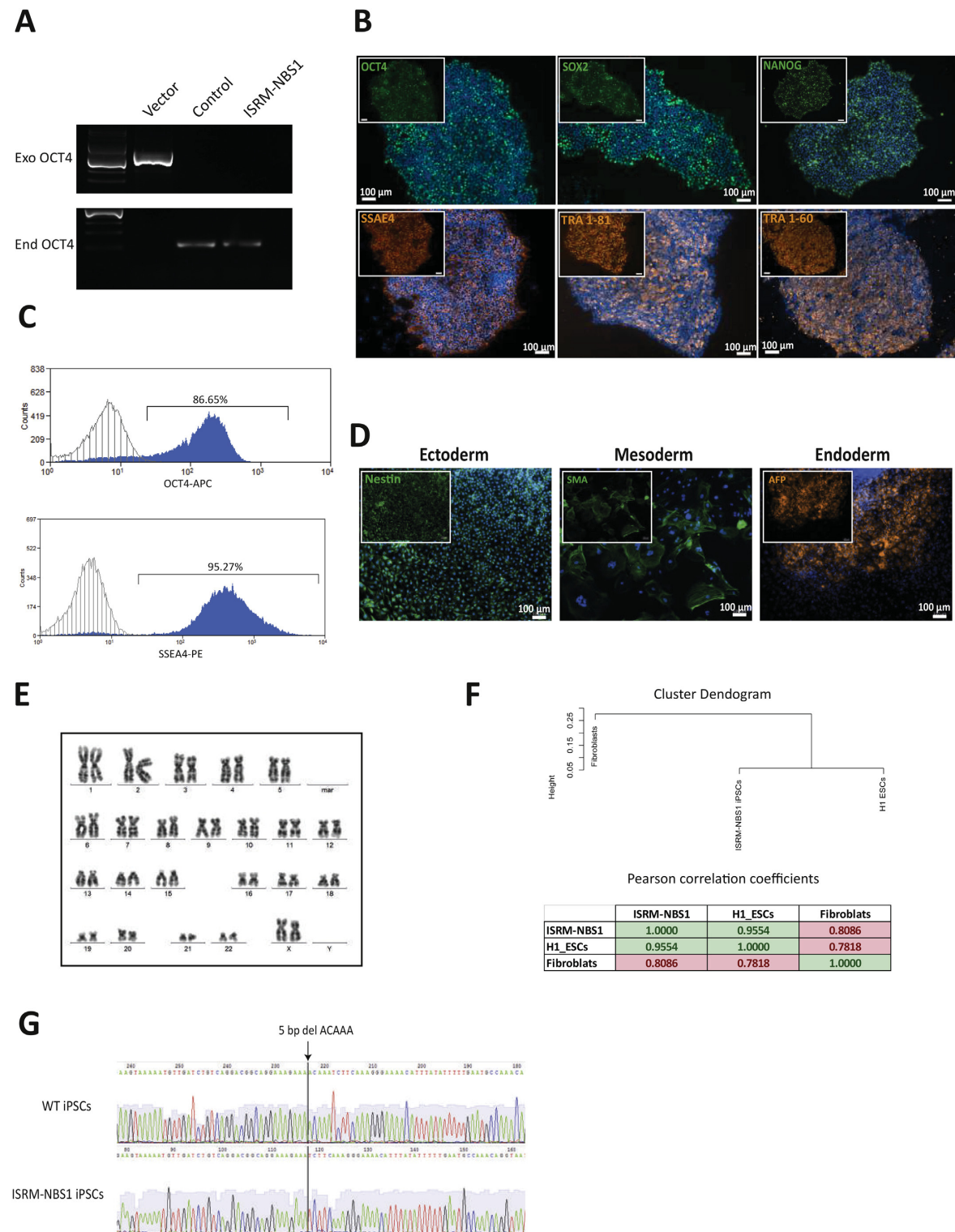


Fig. 1. Characterization of ISRM-NBS1 iPSC line.

Table 1
Characterisation and validation.

Classification	Test	Result	Data
Morphology Phenotype	Photography	Normal	Fig. 1 panel B
	Immunocytochemistry	Expression of pluripotency associated markers: OCT4, SOX2, NANOG, SSEA4, TRA-1-60, and TRA-1-81	Fig. 1 panel B
Genotype Identity	Flow cytometry	86.65% OCT4 positive cells and 95.27% SSEA4 positive cells.	Fig. 1 panel C
	Karyotype (G-banding) and resolution	46, XX, Resolution 150–300	Fig. 1 panel E
	Microsatellite PCR (mPCR) STR analysis	Not done DNA Fingerprinting PCR: three sites tested, matched	N/A Submitted in archive with journal
Mutation analysis (IF APPLICABLE) Microbiology and virology Differentiation potential	Sequencing	NBN c.657,661del5 homozygous mutation	Fig. 1 panel G
	Southern Blot OR WGS	Not applicable	N/A
	Mycoplasma	Mycoplasma testing by PCR Negative	Supplementary file 1
	Embryoid body formation OR Teratoma formation OR Scorecard	Expression of germ layer specific proteins Ectoderm: NESTIN, Endoderm: AFP Mesoderm: SMA	Fig. 1 panel D
Donor screening (OPTIONAL)	HIV 1 + 2 Hepatitis B, Hepatitis C	Not tested	N/A
Genotype additional info (OPTIONAL)	Blood group genotyping	Not tested	N/A
	HLA tissue typing	Not tested	N/A

Table 2
Reagents details.

Antibodies used for immunocytochemistry/flow-cytometry			
	Antibody	Dilution	Company Cat # and RRID
Flow-cytometry	Anti-OCT3/4-APC	1:11	Miltenyi Biotec Cat# 130-109-764, RRID: AB_2653082
Flow-cytometry	Anti-SSEA4-PE	1:11	Miltenyi Biotec Cat# 130-098-369, RRID: AB_2653519
Pluripotency Markers	Rabbit anti-OCT4	1:400	Cell Signaling Technologies; #2840S, RRID: AB_2167691
Pluripotency Markers	Rabbit anti-SOX2	1:400	Cell Signaling Technologies; #3579S, RRID: AB_2195767
Pluripotency Markers	Rabbit anti-NANOG	1:800	Cell Signaling Technologies; #4903S, RRID: AB_10559205
Pluripotency Markers	Mouse anti-SSEA4	1:1000	Cell Signaling Technology Cat# 4755S, RRID: AB_1264259
Pluripotency Markers	Mouse anti-Tra-1-60	1:1000	Cell Signaling Technologies; #4746S, RRID: AB_2119059
Pluripotency Markers	Mouse anti-Tra-1-81	1:1000	Cell Signaling Technologies; #4745S, RRID: AB_2119060
Differentiation Markers	Rabbit anti-Nestin	1:250	Sigma Aldrich; N5413, RRID: AB_1841032
Differentiation Markers	anti- α SMA	1:1000	Dako; # M0851, RRID: AB_2223500
Differentiation Markers	Rabbit anti-AFP	1:200	Cell Signaling Technology Cat# 2137S, RRID: AB_2209744
Secondary antibodies	anti-mouse-Alexa555	1:2000	Thermo Fisher Scientific Cat# A10521, RRID: AB_2534030
Secondary antibodies	anti-rabbit-Alexa488	1:2000	Thermo Fisher Scientific Cat# A27034, RRID: AB_2536097
Nuclear Co-Staining	Hoechst	1:5000	Thermo Fisher Scientific Cat# H3569, RRID: AB_2651133
Primers			
	Target	Forward/Reverse primer (5'-3')	
Fingerprinting	D21S2055	AACAGAACCAATAGGCTATCTATC/TACAGTAAATCACTTGGTAGGAGA	
Fingerprinting	D17S1290	TTTTGGTATTGGCCATCCTA/GAAAGGAACAGAGACAGGG	
Fingerprinting	D7S796	TTTTGGTATTGGCCATCCTA/GAAAGGAACAGAGACAGGG	
Episomal Plasmid (Exo)	OCT4	AGTGAGAGGCAACCTGGAGA/AGGAACTGCTTCCTCAGCA	
Endogenous OCT4	OCT4	GTGGAGGAAGCTGACAACAA/ATTCTCAGGTGCTCTCA	
NBN sequencing	NBN Exon6	CAGATAGTCACTCCGTTTACAA/ATGAATAGGCCAGTTATCACAG	
Mycoplasma	16S rRNA gene from Mycoplasma	GGGAGCAAACAGGATTAGATACCT/TGCACCATCTGTCACCTGTAACTCC	

resulting protein fragments (p26 and p70) retain sufficient functionality to ensure survival, however function of Nibrin in the coordination of the damage response to protect genome integrity is impaired (Chrzanowska et al., 2012; Digweed and Sperling, 2004; Mlody et al., 2017).

Here we report the generation of an iPSC line (ISRM-NBS1) from an NBS patient carrying the 657del5 within *NBN*. Dermal fibroblasts (S 267) derived from an 18-year-old female NBS patient was used to generate this iPSC line.

In brief, the fibroblasts were reprogrammed employing oriP/EBNA-1-based episomal plasmids expressing OCT4, SOX2, NANOG, KLF4, c-MYC and LIN28. Confirmation of the vector dilution of ISRM-NBS1 was carried out by analyzing expression of exogenous *OCT4* (vector) (top panel). Endogenous *OCT4* analysis (lower panel) was performed as an internal PCR control (Fig. 1A). Pluripotency was confirmed by (i) expression of OCT4, SOX2, NANOG, SSEA4, TRA-1-60 and TRA-1-81

(Fig. 1B), (ii) embryoid body (EB)-based spontaneous differentiation into cell types representative of the three germ layers, namely ectoderm (NESTIN), mesoderm (SMA – smooth muscle actin) and endoderm (AFP – Alpha fetoprotein) (Fig. 1D) and (iii) OCT4 and SSEA4 flow cytometry analysis (Fig. 1C). The DNA fingerprinting of ISRM-NBS1 iPSC line was identical to the parental fibroblast line S 267. Chromosomal content analysis revealed a normal 46, XX karyotype (Fig. 1E). As depicted in the Dendrogram (Fig. 1F), the transcriptome of the fibroblast line is distinct from ISRM-NBS1 and the embryonic stem cell line H1, which cluster together with a Pearson correlation of 0.9554. The reprogramming process did not alter the *NBN* 657del5 mutation - a homozygous 5 base pairs deletion within the exon 6 of *NBN*, as indicated by the black arrow (Fig. 1G). A PCR-based Mycoplasma contamination test was negative (Supplementary file 1).

Materials and methods

Cell culture

The fibroblasts were maintained in Fibroblast Growth Medium (FGM) composed of high glucose DMEM supplemented with 10% fetal bovine serum, 1% Glutamax, 1% NEAA and 1% Penicillin/Streptomycin at 37 °C and 5% CO₂.

Derivation of ISRM-NBS1

Fibroblasts were reprogrammed using a combination of two episomal based plasmids pEP4EO2SCK2MEN2L and pEP4EO2SET2K (7F1) (Yu et al., 2011) coding for OCT4, SOX2, NANOG, LIN28, c-MYC and KLF-4. 24 h after transfection the medium was replaced daily with fresh FGM containing 100 ng/ml of FGF2 and 0.5 μM of A83-01, 0.5 μM PD0325901 and 3 μM CHIR99021 in order to inhibit TGFβ- and MEK-signaling and activate WNT-signaling pathway. From day 7 onwards, the medium was replaced with mTESR (Stem Cells Technology), maintaining the three pathway inhibition for 7 additional days. Colonies emerged 4 weeks post-nucleofection. Well-defined distinct iPSCs colonies were manually picked and passaged for expansion on mouse embryonic fibroblasts (MEF) on Matrigel®-coated plates in mTESR medium. After stabilization of the colonies, iPSCs were re-seeded under feeder-free conditions in mTESR medium Table 1.

PCR

Genomic DNA was isolated from the parental fibroblasts, ISRM-NBS1 iPSCs and the human embryonic stem cell line (H1) employing the DNeasy Blood and Tissue Kit (Qiagen). Vector dilution and STR analysis were confirmed by PCR amplification. The absence of mycoplasma contamination was confirmed by testing cell culture supernatant from a dense culture. PCR was performed using GoTaq® DNA Polymerase (Promega). Primer sequences are shown in Table 2.

Embryoid body (EB) formation

To confirm pluripotency EB-based differentiation was performed. Sub-confluent iPSCs were transferred into a T25 flask for a week in high glucose DMEM, containing 1% NEAA. Afterwards, EBs were replated onto gelatin coated 12-well plate for 3–4 days.

Flow cytometry and Immunofluorescence-based detection of pluripotency associated proteins

iPSCs and differentiated EB cells were fixed with 4% paraformaldehyde for 15 min at room temperature. After blocking with 5% normal goat serum in 0.5% Triton-X100 PBS solution, cells were incubated with the primary antibody (Table 2) overnight at 4 °C. Alexa488 or Alexa555-conjugated secondary antibodies and Hoechst were used to visualize the signal. Fluorescent images were obtained by

an inverse fluorescence microscope LSM700 (Carl Zeiss). Flow-cytometric analysis using an anti-Oct3/4 antibody APC-conjugated and anti-SSEA4 PE-conjugated (Miltenyl Biotec) was carried out using the CyAn ADP Flow Cytometer (Dako). APC-conjugated (OCT4) or unstained (SSEA4) cells were used as negative control.

Karyotype analysis

The karyotype analysis was evaluated and performed at the Institute of Human Genetics and Anthropology, Heinrich-Heine-University, Düsseldorf.

Mutation sequencing

The mutation was confirmed by direct DNA sequencing after PCR amplification of the exon 6. The DNA sequencing was performed at the Genomics/Transcriptomic Laboratory of the BMFZ, HHU, Düsseldorf. Primers used for PCR amplification and direct sequencing of the exon 6 of *NBN* are listed in Table 2.

RNA-based microarray analysis

PrimeView Affymetrix microarrays were used to determine global gene expression. 1 μg of total RNA was used and all preparations were performed by the Genomics/Transcriptomic Laboratory of the BMFZ, HHU, Düsseldorf. The dendrogram was generated using the package affy of the R/Bioconductor software (Gentleman et al., 2004).

Acknowledgements

JA acknowledges support from the Medical Faculty, Heinrich-Heine-University, Düsseldorf.

Appendix A. Supplementary data

Supplementary data to this article can be found online at <https://doi.org/10.1016/j.scr.2018.101372>.

References

- Chrzanowska, K.H., Gregorek, H., Dembowska-Bagińska, B., Kalina, M.A., Digweed, M., 2012. Nijmegen Breakage Syndrome (NBS). *Orphanet J. Rare Dis.* 7 (1), 13.
- Digweed, M., Sperling, K., 2004. Nijmegen Breakage Syndrome: clinical manifestation of defective response to DNA double-strand breaks. *DNA Repair* 3 (8–9), 1207–1217.
- Gentleman, R.C., Carey, V.J., Bates, D.M., Zhang, J., 2004. Bioconductor: open software development for computational biology and bioinformatics. *Genome Biol.* 5 (10), R80.
- Mlody, B., Wruck, W., Martins, S., Sperling, K., Adjaye, J., 2017. Nijmegen Breakage Syndrome fibroblasts and iPSCs: cellular models for uncovering disease-associated signaling pathways and establishing a screening platform for anti-oxidants. *Sci. Rep.* 7 (1). <https://doi.org/10.1038/s41598-017-07905-2>.
- Yu, J., Chau, K.F., Vodyanik, M.A., Jiang, J., Jiang, Y., 2011. Efficient feeder-free episomal reprogramming with small molecules. *PLoS ONE* 6 (3), e17557.

3.2 Impaired p53-mediated DNA damage response contributes to microcephaly in Nijmegen Breakage Syndrome patient-derived cerebral organoids

Soraia Martins, Lars Erichsen, Angeliki Datsi, Wasco Wruck, Wolfgang Goering,
Krystyna Chrzanowska and James Adjaye

bioRxiv (2020)

Abstract

Nijmegen Breakage Syndrome (NBS) is a rare autosomal recessive genetic disorder caused by mutations within *NBN*, a DNA-damage repair protein. Hallmarks of NBS include several clinical manifestations such growth retardation, chromosomal instability, immunodeficiency and progressive microcephaly. However, the etiology of microcephaly in NBS patients remains elusive. Here, we employed induced pluripotent stem cell-derived brain organoids from two NBS patients to analyze the underlying mechanisms of microcephaly. We show that NBS-organoids carrying the homozygous 647del5 *NBN* mutation are significantly smaller in size with disrupted cyto-architecture. Patient-derived organoids exhibit premature differentiation together with neuronatin (NNAT) overexpression and key pathways related to DNA damage response and cell cycle are differentially regulated compared to controls. Moreover, we show that after exposure to bleomycin, NBS organoids undergo a delayed p53-mediated DNA damage response and aberrant trans-synaptic signalling, which ultimately leads to neuronal apoptosis. Our data provide insights into how mutations within *NBN* alters neurogenesis in NBS patients, thus providing a proof of concept that cerebral organoids are a valuable tool for studying DNA damage-related disorders.

Author's contribution: 75%

Conceptualization: **S.M.** and J.A.; Methodology: **S.M.**, L.E., W.G., A.D.; Formal analysis: **S.M.**, W.W., J.A.; Data curation: W.W.; Investigation: **S.M.**; Resources: K.C.; Writing—original draft preparation: **S.M.**; Writing—review and editing: J.A.; Supervision: J.A.

Status: Available in the open access preprint repository bioRxiv.
(doi.org/10.1101/2020.09.29.318527)

Impaired p53-mediated DNA damage response contributes to microcephaly in Nijmegen Breakage Syndrome patient-derived cerebral organoids

Soraia Martins¹, Lars Erichsen¹, Angeliki Datsi², Wasco Wruck¹, Wolfgang Goering³, Krystyna Chrzanowska⁴, and James Adjaye¹✉

¹Institute for Stem Cell Research and Regenerative Medicine, Medical Faculty, Heinrich-Heine University, 40225 Düsseldorf, Germany

²Institute for Transplantation Diagnostics and Cell Therapeutics, Heinrich-Heine University, 40225 Düsseldorf, Germany

³Institute for Pathology, University Hospital and Medical Faculty of the Heinrich-Heine University Düsseldorf, 40225 Düsseldorf, Germany

⁴Department of Medical Genetics, Children's Memorial Health Institute, Warsaw, Poland

Nijmegen Breakage Syndrome (NBS) is a rare autosomal recessive genetic disorder caused by mutations within *NBN*, a DNA-damage repair protein. Hallmarks of NBS include several clinical manifestations such as growth retardation, chromosomal instability, immunodeficiency and progressive microcephaly. However, the etiology of microcephaly in NBS patients remains elusive. Here, we employed induced pluripotent stem cell-derived brain organoids from two NBS patients to analyze the underlying mechanisms of microcephaly. We show that NBS-organoids carrying the homozygous 647del5 *NBN* mutation are significantly smaller in size with disrupted cyto-architecture. Patient-derived organoids exhibit premature differentiation together with neuronatin (NNAT) overexpression and key pathways related to DNA damage response and cell cycle are differentially regulated compared to controls. Moreover, we show that after exposure to bleomycin, NBS organoids undergo a delayed p53-mediated DNA damage response and aberrant trans-synaptic signalling, which ultimately leads to neuronal apoptosis. Our data provide insights into how mutations within *NBN* alters neurogenesis in NBS patients, thus providing a proof of concept that cerebral organoids are a valuable tool for studying DNA damage-related disorders.

NBS | iPSCs | cerebral organoids | disease modelling

Correspondence: james.adjaye@med.uni-duesseldorf.de

Introduction

Development of the nervous system is a strictly regulated process whereby neural progenitor cells (NPCs) rapidly proliferate and potentially generate high-levels of oxidative stress. Neurons albeit being post-mitotic cells display high rates of metabolism and mitochondria activity also contributing to a stressful environment which increases the susceptibility to DNA damage. Deficiency in the DNA damage response (DDR) causes many syndromes with pronounced neuropathology [1,2]. Hypomorphic mutations within *nibrin* (*NBN*), coding a DDR protein, leads to Nijmegen Breakage Syndrome (NBS), a rare autosomal recessive genetic disorder belonging to the chromosomal instability syndromes [3]. NBS was first described in 1979 at the University of

Nijmegen and it has been considered as a multisystemic disorder [4]. Clinically, NBS is characterized by severe and progressive microcephaly, growth retardation, typical facial appearance, premature ovarian failure, deterioration of the cognitive functions, immunodeficiency, chromosomal instability and elevated sensitivity to ionizing radiation. Apart from microcephaly, other developmental abnormalities of the brain have been reported in a few patients, including neuronal migration disorder, agenesis of the corpus callosum and arachnoid cysts [5–7]. By the age of 20 years, more than 40% of NBS patients develop malignancy diseases, predominantly of hematological origin which, in addition to the recurrent infections are the major cause of death in these patients [8].

The worldwide prevalence is estimated at 1:100000 live births, however NBS is particularly common in Eastern Europe with carrier frequencies as high as 1:155 in some populations of Czech Republic, Poland and Ukraine. [9]. More than 90% of the NBS patients are homozygous for a founder mutation, a five base pair deletion in exon 6 (657del5) within *NBN*. Due to alternative translation from a cryptic start site upstream of the deletion, this mutation leads to the truncation of the wild-type protein into two different fragments: a 26 kDa amino-terminal protein (p26) and a 70 kDa carboxy-terminal (p70), which retain some residual functions [10]. *NBN* together with *MRE11* and *RAD50* form the MNR complex which plays a central role in DNA damage signaling and repair, telomere maintenance, proper centromere duplication, cell cycle checkpoint activation and processing of stalled replication forks [11].

With *NBN* playing a multifunctional central role, it is not surprising that lymphoblasts and fibroblasts from NBS patients exhibit chromosomal instability with impaired cell cycle and regulation of apoptosis [12–14]. However, the functional consequences of *NBN* 657del5 during neurodevelopment remained largely unexplored. To this end several studies based on *Nbn* conditional knockdowns have been performed [15–20]. While these studies provided helpful information, some of the mouse models do not reproduce the

brain-related phenotype seen in patients and in the ones that the microcephaly phenotype was present, divergent results were found. Frappart *et al.* (2005) showed inactivation of *Nbn* in the mouse neuronal tissue resulted in decreased proliferation of the NPCs and increase apoptosis of postmitotic neurons in the cerebellum, by activation of p53 [20]. However, Zhou *et al.* (2012) showed that deletion of *Nbn* in the mouse central nervous system affects proliferation and apoptosis mainly in the cortex ventricular zone proliferating area (VZ), affecting only NPCs [19].

To bridge the gap between the mouse models and the human phenotype of NBS, induced pluripotent stem cells (iPSCs) technology provides the best platform to derive a reliable human disease model to study the effects of *NBN* mutations in neurons derived from NBS patients. In fact we previously reported that fibroblasts from NBS patients can be reprogrammed into iPSCs and thus by-passing premature senescence [21]. Global transcriptome analysis of NBS fibroblasts and NBS-iPSCs unveiled de-regulated cancer related pathways such as p53, cell cycle and glycolysis [22]. Differentiation of the NBS-iPSCs into NPCs showed these cells have de-regulated expression of neural developmental genes in-part due to NBS-NPCs inability to maintain normal levels of p53 [23]. Recent advances in *in vitro* culture of 3D cerebral organoids derived from iPSCs have illuminated the early mechanisms of mammalian neurodevelopment. Cerebral organoids provide a unique opportunity to model human organogenesis through the presence of an organizational feature unique to 3D brains, such as cortical layers [24–26]. Indeed, studies have shown the utility of cerebral organoids from patient-derived iPSCs to unveil the mechanisms of microcephaly and other neurodevelopmental disorders [27]. Here, we took advantage of the cerebral organoids system to analyze the underlying mechanisms of microcephaly and other brain abnormalities present in NBS patients. NBS-organoids carrying the homozygous 647del5 *NBN* mutation are significantly small with disrupted cyto-architecture. Both patient-derived organoids exhibit premature differentiation and key pathways related to DNA damage response and cell cycle are differentially regulated compared to controls. After exposure to DNA damage, NBS organoids present a delay in the activation of cell cycle arrest due to inability to stabilize p53. Our data provide insights into how hypomorphic mutations within *NBN* alters neurogenesis in the NBS patients, thus providing a proof of concept that cerebral organoids are a valuable tool enabling research into DNA damage-related disorders.

Results

iPSCs-derived from NBS patients exhibit chromosome instability.

In order to create an *in vitro* model system to study NBS, we previously generated iPSC lines from two NBS patients, referred here as NBS1 and NBS8-iPSCs [21,28]. NBS1-iPSCs carry the homozygous 657del5 mutation and NBS8-iPSCs the heterozygous 657del5 mutation. As NBS is characterized by chromosomal instability, genome integrity evaluation

was performed at the beginning of the current study. While NBS1-iPSCs presents a normal karyotype (**Table S1, Figure S1B**), copy number variations (CNV) analysis using array comparative genome hybridization (array-GCH) showed that, although no larger chromosomal aberrations was reported, there is a loss of heterozygosity (LOH) in chromosome 8q, region where *NBN* is located (**Supplementary figure 1A**). Of note, the detected LOH was pre-existing in the parental fibroblast line. Karyotype analysis of NBS8-iPSCs revealed a higher number of acquired CNVs and cytogenetic rearrangements, namely a duplication of most of the long arm of chromosome 5 and a duplication of the telomeric end of chromosome 3p (**Figure S1B-C**). These aberrations were acquired during the reprogramming process, as NBS8-iPSC line was generated by retroviral-based reprogramming.

Table S1 presents the detailed information about the iPSC lines used in this study. As controls, HFF-derived iPSCs [29], here referred as CTR1-iPSCs and urine cell-derived iPSCs [30], here referred as CTR2-iPSCs, were used.

NBS-iPSCs efficiently differentiate into cerebral organoids and recapitulate the microcephaly phenotype.

To address how human early neurodevelopment is affected in NBS and to dissect the mechanisms underlying microcephaly in NBS patients, we implemented a publish suspension protocol to generate forebrain organoids. An equal number of dissociated iPSCs were aggregated in a minimally pattern conditions and in the absence of extracellular scaffolding [31]. To facilitate neuralization, iPSCs were cultured in the presence of two inhibitors of the SMAD pathway, followed by a proliferation and corticogenesis progression phase due to the addition of EGF and FGF. The final maturation phase was achieved by exposing the cerebral organoids to BDNF. In order to increase oxygen and nutrient diffusion, cerebral organoids were kept under orbital shaking conditions (**Figure 1A**).

By day 20, immunohistochemical analysis revealed that control- and NBS-organoids showed an internal cyto-architecture composed mostly of the NPCs expressing SOX2 aligned in a VZ-like structure surrounded by the DCX+ neuroblasts that will gradually generate the neurons from the cortical plate (**Figure 1B**).

To evaluate the efficiency of the differentiation, mRNA levels of progenitor markers, pan-neuronal makers, early born neurons, late-born neurons and the astrocytes marker *GFAP* were assessed. While there is some heterogeneity between the expression of the neuronal markers between NBS1 and NBS8 organoids, neuronal progenitor markers such as *PAX6* were significantly down-regulated in NBS organoids. On the other hand, NBS organoids showed an up-regulation of the neuronal markers *DCX* and *TUBB3* (**Figure 1C**).

To test the regional specificity of the cerebral organoids, we performed a RT-qPCR for forebrain, midbrain and hindbrain markers. Despite the use of a protocol that was developed to yield region specific forebrain organoids, both 20 days control and NBS cerebral organoids expressed not only the fore-

brain markers *FOXG1* and *OTX1*, but also the midbrain markers *PAX5* and *FOXA2* and the hindbrain markers *HOXB4* and *HOXB6*, albeit at lower expression levels (**Figure 1D**).

To analyse the developmental stage of the cerebral organoids with respect to human fetal brain, we compared the transcriptome profile of CTR1, CTR2, NBS1 and NBS8-organoids at day 20 to the transcriptomic data from the Allen Human Brain Atlas (<https://www.brainspan.org>) [32]. Our cerebral organoids at day 20 were closely related to 8-9 post-conception week (pcw) (**Figure S2C**). To test if NBS-organoids could recapitulate the microcephaly phenotype we evaluated the size of the organoids over a period of 20 days. Although the size of NBS8-organoids was similar to that of controls at day 6, during prolonged culture the organoids became significantly larger. On the other hand, NBS1-organoids were significantly smaller in comparison to controls and the size was not compensated during the time in culture (**Figure 1E**). In addition to the smaller size, NBS1-organoids were relatively spherical and visually lacked the neuroepithelial structures observed in the controls and NBS8-organoids (**Figure 1F**).

Together these results imply that control- and NBS-iPSCs efficiently differentiate into cerebral organoids, which recapitulate aspects of early human brain development with defined molecular markers. Furthermore, NBS1-organoids, carrying the homozygous *NBN* mutation, recapitulate the microcephaly phenotype.

NBS organoids present a disrupted cyto-architecture with normal proliferation of the NPCs.

NPCs display incredible plastic features and an enhanced capacity to sense the environment. NPCs can divide both symmetrically and asymmetrically, stay quiescent for long periods, can undergo active proliferation or differentiate upon instruction. Environmental cues can trigger the proliferation of NPCs or the acquisition of a terminally differentiated phenotype [33]. We analysed the expression of the NPCs marker *SOX2* together with the proliferation marker *KI67* in our cerebral organoids (**Figure 2A**). At day 20 both control- and NBS-organoids were mainly composed of *SOX2*⁺ NPCs, with no significant differences in the total number of *SOX2*⁺ cells (**Figure 2B**) as well as in the *SOX2* mRNA expression (**Figure 2C**) between control- and NBS-organoids. Furthermore, a similar proliferation of the NPCs was observed based on *KI67* expression (**Figure 2D-F**).

Next, we examined if the reduction in size observed in NBS1-organoids was due to enhanced cell apoptosis in the cerebral organoids. We found a comparable number of cleaved Caspase-3⁺ cells between control and NBS organoids, mostly located outside the VZ and co-localized with the *DCX*⁺ cells. Lastly, we explored the internal cyto-architecture of the cerebral organoids by determined the number and the thickness of the VZ, as well as the length of the apical membrane. While control organoids displayed typical VZ containing *SOX2*⁺ NPCs proliferating at the apical surface of the ventricular zone (**Figure 2H**), NBS1-organoids exhibited a markedly reduction of these well-defined VZs (**Figure 2I**). Likewise, the

VZs present were significantly smaller (**Figure 2J**) with smaller apical membrane (**Figure 2K**). Notably, at day 20 there were no clear differences in the VZs from the NBS8-organoids compared to control.

Our results suggest that although the population of the NPCs is not affected in an early developmental stage, NBS1-organoids can show a disrupted cyto-architecture that can affect normal brain development.

NBS1 and NBS8 organoids show a distinct transcriptomic profile.

To gain further insights into the pathophysiology of NBS, we performed transcriptome analysis of both control and NBS organoids at day 20 of differentiation. We then applied bioinformatic analysis to our transcriptome data to perform a cluster analysis and to identify the differentially expressed genes (DEGs). Hierarchical clustering revealed one cluster containing the NBS8-organoids and the second cluster containing CTR1-, CTR2- and NBS1-organoids, thus indicating that NBS8-organoids have a distinct transcriptome profile (**Figure S2A-B**).

To further identify the DEGs, we compared the transcriptome of the NBS1- and NBS8-organoids to both CTR-organoids. Among the commonly expressed genes between NBS1 and controls, we found 198 up-regulated and 210 down-regulated DEGs (**Figure 3A, Table S2**). Enrichment analysis of the up-regulated DEGs showed *subpallium development, regulation of focal adhesion assembly, phospholipid dephosphorylation* and *centromere complex assembly* as the most enriched GOs (**Figure 3B**). Regarding the canonical pathways, up-regulated DEGs were significantly enriched in *RTMs methylate histone arginines, Signalling by GPCR, DNA damage/Telomere stress induce senescence* and *Cellular senescence* (**Figure 3C**). Down-regulated genes were enriched for GOs as *chemotaxis, negative regulation of proteolysis* and *cellular response to hormonal stimuli* (**Figure 3D**).

The same analysis was performed using the NBS8-organoids. 1289 genes were identified as up-regulated compared to both control-organoids. (**Figure 3E, Table S2**). Among the enriched GOs, we could identify clusters connected with synaptic signalling and regulation of neuron differentiation, as well as regulation of ion transport and regulation of cell adhesion (**Figure 3F**). On the other hand, the cluster analysis of the 1211 down-regulated genes identified *ribonucleoprotein complex biogenesis, protein-DNA complex assembly, microtubule-bases process* and *telomere organization* as the most enriched GOs (**Figure 3G**). The analysis of the canonical pathways identified genes involved in *Metabolism of RNA, RNA polymerase II transcription, Cell cycle, Cell cycle mitotic* and *Cell cycle checkpoints* pathways to be significantly reduced (**Figure 3H**). Inherently, NBS1- and NBS8-organoids show variable modulation of genes associated with regulation of gene expression such *chromatin assembly, DNA replication-dependent nucleosome assembly, negative regulation of gene expression/epigenetic* and *DNA packing* which were found up-regulated in NBS1 and down-regulated in NBS8 (**Table S2**). Notwithstanding, both NBS1 and NBS8

organoids downregulated genes associated with behaviour and cognition (Table S2). Our results indicate that although both NBS1- and NBS8-organoids carry the hypomorphic 657del5 mutation, heterozygous and homozygous carriers result in slightly different phenotypes.

NBS organoids show accumulation of DNA damage.

Defective DDR is a well-established cellular feature observed in NBS patients [34]. However, the precise mechanism how NBS cells respond to DSBs and how it affects brain development is poorly understood. In view of this, we took an extensive look into the DNA-damage response at day 20 of our cerebral organoids. At this time-point, we found down-regulation in the expression of genes involved in the DDR pathway (Figure 4A). Down-regulation of *ATM* was observed, which was confirmed by qRT-PCR (Figure 4B). Interestingly expression of *TP53* was not significantly regulated (Figure 4C). However, when the protein level was analysed, NBS-organoids clearly showed a reduction in p53 levels compared to control-organoids (Figure 4D).

To examine if the decrease in p53 expression was due to the presence of mutations, *TP53* target sequencing was carried out in order to identify disease-causing variants. No mutations were found in control- or NBS-organoids (data not shown). As *MDM2* is a key regulator of p53, *MDM2* mRNA expression was analysed and no significant differences between control- and NBS-organoids were found (Figure 4D). Surprisingly, NBS8-organoids expressed significantly higher levels of *CDKN1A* (Figure 4F), the major p53 target which controls cell cycle arrest after DNA damage [35]. Outstandingly, high levels of DSBs were observed in the NBS-organoids, judged by the increase of γ -H2AX nuclear foci formation co-localized with the *SOX2*⁺ NPCs (Figure 4G). We next asked whether the observed phenotype could be rescued by stabilization of p53. Thus, cerebral organoids were incubated with Nutlin-3a, an *MDM2* inhibitor (Figure S3A). After 72h of incubation (day 25) both CTR1- and NBS8-organoids started to have a dark appearance, indicating cell death (Figure S3B). The inhibition of p53 degradation led to the decrease in the level of *TP53* mRNA in CTR1-organoids, however no differences were observed in NBS8-organoids, where *TP53* levels remained very low (Figure S3C). A similar pattern was observed for *MDM2* expression. Remarkably, *CDKN1A* expression was dramatically up-regulated after Nutlin-3a in both CTR1- and NBS8-organoids (Figure S3D). Overall, Nutlin-3a led to a remarkable decrease in cell proliferation, also confirmed by the down-regulation of *KI67* mRNA expression in both CTR1- and NBS-8 organoids (Figure S3D).

Together, our results indicate that NBS-organoids display an impaired DDR pathway, with the accumulation of DNA damage and consequently genomic instability most probably due to the lower levels of p53. Moreover, stabilization of p53-induced by Nutlin-3a led to cell cycle arrest. This approach suggests that p53 plays a central role in orchestrating the fate of NPCs in NBS-organoids.

NBS organoids exhibit premature differentiation accompanied by NNAT overexpression.

To gain deeper insights into the molecular portraits of NBS-regulated gene expression, we analysed the exclusively expressed genes between NBS1- and NBS8-organoids compared to control. We identified 124 genes expressed exclusively in the NBS- and not in the control-organoids (Figure 5A). Functional enrichment analysis revealed that most of these genes are involved in *synaptic signalling*, *presynapse assembly* and *organ induction* (Figure 5B). Besides the genes directly linked with neuronal development, we found genes involved in the *regulation of interleukin-6* production and *matrisome-associated*, including regulators of the ECM and secreted factors. As already described, NBS-organoids showed up-regulation of a number of neuronal differentiation markers (Figure 1C).

To evaluate the differentiation propensity of NPCs, we analysed the expression of the neuronal marker DCX. Although mRNA expression was only upregulated in the NBS1-organoids (Figure 5C), both NBS1- and NBS8-organoids showed a significantly higher number of DCX⁺ cells (Figure 5D), thus suggesting premature neuronal differentiation. Likewise, NBS-organoids showed an increase in the number of β III-Tubulin⁺ cells, but more pronounced in the NBS8-organoids (Figure 5E,F).

Interestingly, we identified *neuronatin (NNAT)* as the most up-regulating gene in day 20 NBS-organoids. *NNAT* mRNA expression was barely detectable in the control organoids and highly upregulated in NBS organoids (Figure 5G). Consistent with the mRNA expression, *NNAT* protein was only present in NBS-organoids (Figure 5H). Regulation of *NNAT* expression depends on the degree of *NNAT* methylation [36]. Thus, we analysed the methylation status within a CpG island within the promoter region. We found high levels of methylation in this region in the control-organoids (CTR1=99,24% and CTR2=100%) and NBS1-organoids (97,5%). However, a markedly decrease in the methylation at this CpG island was observed in NBS8 organoids (51,2%) (Figure 5I).

Collectively, our results suggest that NBS-organoids undergo premature neurogenesis governed by *NNAT* and this abnormal over-expression is controlled by the loss of methylation in a regulatory region within the *NNAT* promoter.

NBS organoids at day 40 acquire an abnormal regulation of cell cycle.

To further investigate the consequences of NBS in postmitotic neurons, we differentiated the cerebral organoids for 40 days and performed single organoid transcriptome analysis (SOT-analysis). To ensure the maturity of the organoids, dissociation into single cells for further FACS analysis and re-plating in 2D was performed (Figure 6A). As before, we examined the expression of *SOX2*, β III-Tubulin, *DCX* and *KI67*. Compared with control-organoids, NBS-organoids were composed of fewer *SOX2*⁺ cells (NBS=45.97%; control=59.48%). On the other hand, the population of β III-Tubulin⁺ cells was slightly higher (NBS=35.15%; control=28.6%) (Figure S3A-C), suggesting a more differen-

tiated population in NBS organoids. Around 95% of the NBS-organoids are composed of DCX+ cells, were 20% of these cells are proliferating indicated by the presence of DCX+/KI67+ cells (Figure S3A-C). These results are in line with previous observations of an increase in DCX expression at day 20.

After re-plating in 2D, we could still observe the presence of SOX2+ NPCs and a neuronal network formed by the β III-Tubulin+ neurons (Figure S3D), showing the integrity of our cerebral organoids after 40 days of differentiation.

SOT-analysis identified 516 upregulated and 592 down-regulated genes in NBS1-organoids compared to control-organoids (CTR1 and CTR2) (Figure 6B, Table S3). Analysis of the enriched GOs showed a persistent upregulation of *chemical synaptic transmission* and *regulation of AMPA receptor activity* in the NBS1-organoids (Figure 6C). Interestingly upregulation of *FAIM2*, *PAK3*, *NR4A3*, *NEFL*, *HYOU1*, *EGLN3*, *EPHB1*, *KCNB1*, *JAK2*, *FGF8*, *JUN*, *BDNF*, *SNCA*, *NTRK1* and *CD200* involved in the regulation of neuron apoptotic process was observed (Figure 6D).

We therefore evaluated the presence of apoptosis by immunostaining for cleaved CASP-3 together with the neuronal marker β III-Tubulin in the cerebral organoids. At day 40, we detected some apoptotic cells in control organoids in the areas where β III-Tubulin+ neurons reside. However, NBS-organoids besides the unorganized cyto-architecture observed with the lack of the VZ, the number of cleaved CASP-3+ cells was high. Interestingly, these apoptotic cells were distributed throughout the entire organoid, affecting not only the β III-Tubulin+ neurons but also the NPCs (Figure 6E).

Interestingly, among the downregulated DEGs, transcripts related to *cell division*, *cell cycle*, *DNA G2/M DNA damage checkpoint* were identified (Figure 6F). The transcripts with reduced expression included *CHEK1*, *NBN*, *MRE11*, *CCNA2*, *CDK1*, *CDC42*, *CCNB1*, *CDKN2C* and *RAD9B*. Furthermore, DNA repair, regulation of TP53 activity were also observed as down-regulated GOs (Table S3).

Taken together, our results imply that NBS-organoids undergo premature neurodifferentiation along with increased apoptosis. Furthermore, SOT-analysis points to a down-regulation of cell cycle as the pivotal mechanism underlying perturbed neurodevelopment in the NBS organoids.

Bleomycin-induced cytotoxicity highlights the aberrant NBS phenotype.

To understand the effects of how increased accumulation of DNA damage affects brain development in NBS patients, we subjected the cerebral organoids to bleomycin treatment over a period of 72h and subsequent SOT-analysis. (Figure 7A). Evaluation of DEGs in control organoids after bleomycin treatment revealed an up-regulation of 139 genes (Figure 7B). The subsequent functional enrichment analysis showed that these genes are part of the *P53 downstream pathway* and *TP53 regulates transcription of cell death receptors and ligands* (Figure 7C), thus highlighting bleomycin-induced DNA damage as having a significant effect on the p53 sig-

nalling pathway in control organoids.

Focusing on NBS organoids, 198 up-regulated genes were identified when comparing bleomycin treatment to control conditions (Figure 7D). Interestingly, these genes were also enriched for *P53 downstream pathway-TP53 regulates transcription of cell death genes*. Furthermore, bleomycin treatment re-enforces axon guidance, regulation of synaptic organization and forebrain development, already exacerbated in basal conditions in the NBS-organoids (Figure 7E).

We next evaluated the levels of mRNA expression of the genes up-regulated within the *TP53 downstream pathway* between control and NBS organoids after bleomycin treatment. While both CTR2- and NBS1-organoids activate the p53 signalling pathway to mediate DDR, NBS organoids showed an impairment in the activation of these genes compared to CTR2-organoids, as observed by the significantly lower expression of these genes which include *CDKN1A*, *FAS* and *GADD45A* (Figure 7F).

Additionally, the analysis of the DEGs upon bleomycin treatment showed 287 down-regulated genes in control organoids (Figure S5A). These genes were highly significantly enriched for cell cycle and cell cycle checkpoints (Figure S5B). NBS1-organoids followed the same pattern, with 187 down-regulated genes (Figure S5C) being enriched for *cell cycle*, *cell division*, *Mitotic G1 phase and G1/M transition* and *DNA Double-strand break repair* (Figure S5D). Next, we evaluated the expression of the common set of genes between CTR2 and NBS1-organoids which belong to the *cell cycle pathway*. While CTR2-organoids significantly down-regulated cell cycle-related genes, NBS1 organoids were not able to induce such dramatic changes in gene expression after bleomycin treatment (Figure S5E).

The consequences of these impairments are correlated with the expression of *MKI67*, where CTR2-organoids drastically reduced *MKI67* levels in contrast with a slight reduction observed in NBS1-organoids (Figure S5F). To have a better understanding of the specific effects of bleomycin treatment in NBS organoids, we performed enrichment analysis of the 94 exclusively expressed genes (Figure S5G). Bleomycin treatment specifically induced the expression of genes associated with *trans-synaptic signalling*, *glycosphingolipid biosynthesis*, *leukocyte apoptotic process* and *neurotransmitter transport* in the NBS-organoids (Figure S5H).

Taken together, our results have shown that after exposure to a genotoxic agent, NBS organoids undergo an impairment in P53-regulated pathways and consequently cell cycle regulation due to the low levels of p53.

Discussion

While microcephaly is the hallmark of NBS, the mechanisms that lead to reduced brain size in these patients are largely unknown mostly due to the hurdles and limitations associated with studying NBS. By generating for the first-time patient iPSC-derived cerebral organoids we were able to investigate cellular and molecular effects of the *NBN* mutation during early neurogenesis.

In this work, two distinct NBS patient-derived iPSC lines

Results II: Modelling NBS using patient-derived cerebral organoids

bioRxiv preprint doi: <https://doi.org/10.1101/2020.09.29.318527>; this version posted September 30, 2020. The copyright holder for this preprint (which was not certified by peer review) is the author/funder. All rights reserved. No reuse allowed without permission.

carrying the hypomorphic *NBN* 657del5 mutation were analysed- NBS1 and NBS8. NBS is an autosomal recessive disorder however NBS8-iPSCs are heterozygous for the *NBN* 657del5 mutation, indicating that other missense mutations within *NBN* could be present [37]. NBS8-iPSCs present a much higher chromosomal instability, with aberrations acquired during the reprogramming process, as such duplications of chromosome 5q, which can confer growth advantages during the reprogramming process [38]. These differences in the genotype of both iPSC lines can result in distinct phenotypes. Indeed, a variable phenotype as a result of neurodevelopmental abnormalities has been observed in a number of NBS patients [7].

NBS-organoids has allowed not only to identify distinct phenotypes but also to identify common mechanisms underlying the etiology of brain abnormalities in NBS patients. As NPCs and post-mitotic neurons respond differently to endogenous DNA damage [1], we analysed the cerebral organoids at two time-points: 20 days and 40 days of differentiation. Day 20 cerebral organoids correspond to 8-9 pcw in human brain development and are composed mainly by cells with a forebrain identity. However, a sub-population of cells with midbrain and hindbrain identity were also present as observed by others [24]. Microcephaly-associated abnormalities are a hallmark of NBS which frequently occur during the early neurodevelopmental stages, although in some patients only develop postnatally [7,39]. While both NBS1- and NBS8-organoids showed a similar expression profile for the analysed differentiation markers, morphology-based analysis revealed distinct phenotypes. Although an increase in size at day 20 was observed, NBS8-organoids (heterozygous) presented NPCs aligned in the apical membrane of the VZs and neurons in the cortical region similar to control-organoids. On the other hand, NBS1-organoids (homozygous) were significantly smaller in size and presented a disrupted architecture with a disorganized distribution of cells, resulting in less and small VZs, thus recapitulating the microcephaly phenotype. As already mentioned, the different morphologies between the NBS-organoids can be attributed to the distinct genetic composition and highlights the potential of using cerebral organoids to model NBS.

So far, the use of brain organoids to model microcephaly has only been performed with iPSC-derived from patients carrying centrosome-related mutations. Apart from the smaller size of those organoids, a depletion of NPCs was observed [24,40–42]. Interestingly, neither the number nor the proliferation of NPCs was affected in NBS-organoids in comparison to the controls. These results hint at a different mechanism underlying microcephaly in NBS patients.

Transcriptome-based analysis after 20 days of differentiation reinforced that NBS1- and NBS8-organoids respond in distinct manner to the endogenous levels of oxidative stress due to the proliferation of the NPCs. NBS1-organoids showed up-regulation of genes involved in epigenetic regulation of gene expression, centromere complex assembly and senescence, implying these cells attempt to maintain genomic and epigenomic integrity, since DNA methylation and chromatin

remodelling are linked to DNA damage and repair [43]. However, a number of genes that regulate gene expression were found down-regulated in the NBS8-organoids, together with genes associated with cell cycle and cell cycle checkpoints.

Following DSBs, ATM is activated by auto-phosphorylation and undergoes spatial relocation to the DSB site, followed by the phosphorylation of H2AX. In turn, H2AX recruits the MNR complex to the DSB, a process which requires NBN. The DNA damage response is then reinforced by further deposition of ATM at the DSB site, promoted by the MNR complex. Besides sensing DSBs, NBN phosphorylates ATM to control cell cycle checkpoints [44,45]. Among the several genes within the DDR pathway de-regulated in the NBS-organoids, *ATM* was found significantly down-regulated, in accord with previous studies demonstrating that NBS cells dramatically reduce ATM activation [46]. The ATM-dependent signaling events lead to rapid p53 stabilization and transcriptional induction of *CDKN1A*, which encodes p21- a cyclin-dependent kinase inhibitor which triggers G1 cell cycle arrest or a permanent state of senescence or apoptosis [44,45]. NBS-organoids showed a dramatic reduction in p53 protein levels, with no differences in *TP53* mRNA expression. Our results are in line with our previous study where we showed that NPCs derived from NBS-iPSCs express low levels of p53 [23]. In an early neurodifferentiation phase, p53 is still able to activate the transcription of *CDKN1A* (p21) in the NBS-organoids, thus demonstrating that p53 function is not completely abrogated. However, the DDR pathway is compromised, as shown by an increase in γ -H2AX nuclear foci formation in the NPCs of the NBS-organoids, thus higher levels of DNA damage.

As an attempt to increase the stabilization of p53, we treated the cerebral organoids with nutlin-3a, which functions as to inhibit the interaction between MDM2 and p53 [47]. NBS-organoids underwent significant up-regulation of *CDKN1A*, leading to a down-regulation of *MKI67* and subsequent cell death. Our results indicate that inhibition of MDM2-p53 interaction by nutlin-3a allows p53 stabilization and the enhanced response to nutlin-3a further demonstrates that the levels of DNA damage are higher in NBS-organoids. Our data supports previous findings showing that the presence of the truncated p70-nibrin, as a result of the 647del5 *NBN* mutation, is able to retain residual activity to ensure survival [10]. However, an impaired DDR pathway was observed in the NBS-organoids, probably due to the attenuation of the ATM-p53 pathway activation after endogenous DNA damage, in line with previous studies [48,49]. Our data suggests this impairment has an impact on the fate of the NPCs, leading to premature differentiation.

NBS-organoids exclusively expressed genes associated with synaptic signalling and neuronal differentiation as indicated by the increased number of DCX and β III-tubulin⁺ cells. Our results are in contrast with the previous findings in NBS using NPCs derived from NBS-iPSCs showing delayed neurogenesis [23]. This discrepancy could be due to the different approaches used, such as different differentiation

protocols and the iPSC were differentiated only to the NPC stage in Halevy *et al.* (2016).

Premature differentiation of the NPCs leading to its depletion is the common mechanism underlying microcephaly described in patient-derived organoids [24,40–42]. The accumulation of DNA-damage can promote accelerated neurogenesis by increasing the expression of genes that regulate cellular, circuitry and cognitive functions which includes neurite outgrowth and synapsis development, as our data shows [50]. During neurodevelopment, DNA methylation is a key process that regulates the expression of these genes and therefore the maintenance and fate specifications of NPCs [51]. Our results suggest that the premature differentiation observed could be explained by the over-expression of NNAT as a result of the loss of methylation within a CpG island in the *NNAT* promoter observed in the NBS8-organoids. Despite the methylation profile of NBS1-organoids was similar to both control organoids, we cannot entirely exclude the presence of hypomethylation in another regulatory region of the *NNAT* promoter. Hence, further detailed methylation analysis in the NBS-organoids should be performed. NNAT is a small transmembrane proteolipid that has been reported to promote neuronal differentiation and a key molecule that maintains cellular homeostasis [52,53]. Interestingly, NNAT expression has been associated with the regulation of stress levels in cells. However, in addition to its protective role, over-expression of NNAT is frequently found in patients with glioblastoma and contributes to the neuronal pathogenesis of in Lafora disease due its strong propensity to misfold and aggregate leading to subsequent apoptosis and neuronal loss [53,54]. Day 40 transcriptomic data revealed an increase in neuron apoptosis, in contrast no differences in apoptosis was observed in day 20 NPCs. Along with increased apoptosis, NBS-organoids down-regulated genes involved in cell division, cell cycle, chromosome segregation and the G2/M damage checkpoint. The defects in this core pathways observed at day 40 led to the increase in the numerical and structural alterations, both common features of NBS, hence suggestive of a progressive phenotype. With the increase of DNA-damage, mimicked here by bleomycin, NBS-organoids showed delayed activation of p53 downstream targets and as a result not being able to activate DNA damage checkpoints and stop cell division at the same magnitude seen in control organoids.

Together, our data suggests the *NBN* 657del5 mutation induces a progressive phenotype. In an early developmental stage, cells try to maintain homeostasis and genomic integrity. However, due to the inability to efficiently repair damaged DNA, NPCs undergo premature differentiation with disrupted structural organization. We hypothesize that this process is in part triggered by the over-expression of NNAT. The observed increase in genomic instability is a consequence of delayed p53-mediated DNA damage response. Ultimately, the increase in DNA damage together with an aberrant trans-synaptic signalling leads to neuronal apoptosis. We suggest that the premature differentiation

of the NPCs and an increase in apoptosis in the NPCs and post-mitotic neurons as the mechanism underlying progressive microcephaly-the hallmark of NBS.

Materials and Methods

iPSC derivation and culture methods.

The iPSC lines derived from NBS patients (NBS1 and NBS8) as well as the control individuals CTR1 and CTR2 used in this study have been described [21,28,29,55]. iPSC lines were cultured in mTESR medium (Stem Cell Technologies) supplemented with Penicillin/ Streptomycin (P/S) on Matrigel-coated plates (Corning). The medium was changed every day and cells were passaged every 5-6 days using PBS without Calcium and Magnesium (Life Technologies).

Generation of cerebral organoids.

For the generation of cerebral organoids, iPSCs were differentiated as described [56], but with further optimization. On day 0, iPSCs were dissociated using TrypLE Express (Gibco) and plated into a 96-well ultra-low-attachment (10000 cells/well, Nucleon™ Sphera™, Thermo Scientific) in mTEST supplemented with 10 μM ROCK inhibitor Y-27632 (Tocris Bioscience). Neural induction was initiated on day 1 by adding Neural induction medium (NiM) (DMEM/F12, 20% Knock-out serum replacement, 1%NEAA, 0.5% GlutaMAX and 0.1mM 2-Mercaptoethanol (all from Gibco) with 10 μM SB-431542 (Tocris Bioscience), 5 μM Dorsomorphine (Tocris Bioscience) and 10 μM ROCK inhibitor Y-27632 . Medium was changed daily. After 5 days the spheroids were transferred to Neural differentiation medium (NdM) (Neurobasal, 2% B27, 1% GlutaMAX, 1% P/S (all from Gibco) supplemented with 20 ng/mL of EGF and FGF2 (both PreproTech) in non-adhesive 100 mm dishes. Organoids were further cultured under continuous agitation (60 rpm) in a shaker incubator(New Brunswick S41i, Eppendorf) with daily medium change until day 16, and from day 16 onwards medium was changed every other day. At day 25 medium was replaced to NdM supplemented with 20 ng/mL of BDNF with medium change every 2-3 days. From day 40 onwards, organoids were kept in NdM with medium change every 4 days. To induce DNA damage, cerebral organoids at day 37 were incubated with 30 μg/mL of Bleomycin (Millipore) for 72h before harvesting for RNA extraction and for protein lysate preparation.

Single-cell dissociation and 2D neuronal culture.

40-day CTR1-, NBS1- and NBS8-organoids were dissociated to a single cell suspension for 30 minutes using the Papain dissociation kit (Worthington) according to the manufactures' instructions. 300000 cells were replated into poly-L-ornithine and laminin (Sigma) coated coverslips in neural differentiation medium [(Neurobasal, 1% NEAA, 1% N2, 1% P/S (all Thermo Fisher Scientific) supplemented with 1μM of cAMP (Thermo Fisher Scientific, Rockford, IL, USA) and 10 ng/mL of BDNF, GDNF and IGF-1 (all Immuno Tools)].

Organoid sectioning and immunostainings.

Cerebral organoids were fixed in 4% paraformaldehyde (PFA) for 30 min at room temperature, washed with PBS and dehydrated in 30% sucrose in PBS overnight at 4°C. Subsequently organoids were transferred into embedding medium (Tissue-Tek OCT Compound 4583, Sakura Finetek), snap-frozen on dry ice and stored at -80°C. Organoids were cut into 10 µm sections and captured in Superfrost Plus slides (Thermo Scientific) using a Cryostat Leica CM3050 S. Cryosections were permeabilized with 0.1% Triton X-100 for 10 min and blocked with 3% BSA in PBS for 1h. Samples were then incubated with the following primary antibodies overnight at 4°C: mouse anti-βIII-tubulin (1:200, CST TU-20), mouse anti-SOX2 (1:100, Invitrogen, Thermo Fisher Scientific 20G5), rabbit anti-SOX2 (1:200, CST 3579S), guinea pig anti-DCX (1:200, SySy 326004), mouse anti-KI67 (1:200, CST 9449), rabbit anti-cleaved CASP3 (1:200, CST 9664). After washing with PBS, cells were then incubated with the appropriate secondary antibody conjugated with Alexa-488, Alexa-555 or Alexa-647 (1:500, Invitrogen, Thermo Fisher Scientific) for 1h at RT. The nuclear stain Hoechst 33258 (2µg/mL, Sigma) was added at the time of the secondary antibody incubation. Slices were mounted with Fluoromount-G (SouthernBiotech) and fluorescent and confocal images were obtained using a LSM 700 microscope (Carl Zeiss), and processed using ZEN software (Carl Zeiss).

Quantitative assessment of cerebral organoids and image analysis of histological sections.

The size of the organoids was measured employing a Digital Microscope Leica DMS100. Two perpendicular measurements of the organoids diameter (µm) was determined using ImageJ and the mean was calculated. For quantification of the number of ventricular zones-like structures per organoid, organoid slides were stained with SOX2, DCX and nuclei stained with Hoeschst. For quantification of the loop diameter (µm) for each ventricular zones-like structure, two measurements (0 and 45 degrees) were performed, from the apical membrane to the basal membrane, and the mean calculated. To determine the number was SOX2+, KI67+, DCX+, and βIII-Tubulin+ cells relative to the total number of cells, the total integrated intensity for each antibody was calculated and divided by the integrated intensity of the nuclei staining. At least 4 sections per organoid were analysed. Loop diameter, apical membrane length and integrity intensity were measured using ImageJ software.

Reverse transcriptase PCR (RT-PCR).

Total RNA was extracted from day 20 (3 pooled-organoids) or day 40 (single organoids) using TRIzol (Life technologies) and Direct-zol RNA Mini Prep (Zymo Research) according to the manufacturer's protocol. 500 ng of purified RNA was used for cDNA synthesis using TaqMan reverse transcription reagent (Applied Biosystems). cDNA was used for subsequent PCR analysis. To detect the presence of transcripts, RT-PCR reactions were performed using 20 ng of cDNA of WT2 and NBS8 organoids using GoTaq® DNA Polymerase

(Promega). Total RNA from commercially human fetal and adult brain (BioChain®) was used as positive control. Transcripts abundance was determined by reverse transcription quantitative PCR (qRT-PCR) using the SYBR® Green RT-PCR assay (Applied Biosystems). Amplification, detection of specific gene products and quantitative analysis were performed using a 'ViiA7' sequence detection system (Applied Biosystem). The expression levels were normalized relative to the expression of the housekeeping gene RPS16 using the comparative Ct-method 2-Ct. Experiments were carried out in biological triplicates except for 40d organoids (technical triplicates). RT-qPCR data are depicted as mean values with 95% confidence interval. Primers are listed in Table S5.

Microarray analysis.

100 ng of total RNA was subjected to hybridization on the Human Clarion S Array (Affymetrix, Thermo Fisher Scientific) at the BMFZ (Biomedizinisches Forschungszentrum) core facility of the Heinrich-Heine Universität, Düsseldorf. RNA integrity was evaluated using a Fragment Analyzer (Advanced Analytical Technologies, AATI). Data analysis of the Affymetrix raw data was performed in the R/Bioconductor [57] environment using the package affy [58]. The obtained data were background-corrected and normalized by employing the Robust Multi-array Average (RMA) method from the package affy. Hierarchical clustering dendrograms and heatmaps were generated using the heatmap.2 function from the gplots package with Pearson correlation as similarity measure and colour scaling per genes [59]. Expressed genes were compared in venn diagrams employing package VennDiagram [60]. Gene expression was assessed with a threshold of 0.05 for the detection-p-value which was calculated as described in Graffmann et al. [61]. Comprehensive functional analysis of the clustered GO biological processes and pathways (KEGG pathways, Reactome Gene Sets, Canonical pathways and CO-RUM) of the candidate genes was performed using Metascape tool (<http://metascape.org>) [62]. The default parameters were used: terms with $p < 0.01$, minimum overlap 3 and enrichment factor > 1.5 .

Western Blot.

Cells of 5 pooled organoids were washed with PBS and then lysed in RIPA buffer containing complete protease and phosphatase inhibitor cocktail (Roche). Lysates were cleared by centrifugation at 20.000g for 10min and quantified with the Pierce™ BCA Protein Assay kit (Thermo Scientific). 25 µg of the lysates were then separated on NuPAGE 4-12% Bis-Tris gels (Invitrogen) and blotted to a 0.45 µm nitrocellulose membrane for 3h at 300mA. The blots were blocked in PBS/ 0,05%Tween20 containing 5% skim milk and then probed with the following primary antibodies over night at 4°C: mouse anti-P53 (1:100, Merck), rabbit anti-H2AX (1:1000, Cell Signaling), mouse anti β-actin (1:4000, Cell Signaling). After washing the blots three times with PBS/ 0,05%Tween20 they were incubated with the appropriate secondary antibody: goat anti-mouse IRDye 680RD and 800CW

as well as goat anti-rabbit IRDye 680RD and 800CW (all from LI-COR Biosciences). Following three times washing with TBS/0.05% Tween20 the fluorescent signals were quantified by applying the Odyssey infrared imaging system (LI-COR Biosciences).

Flow cytometry.

The cell marker expression of the 40-day organoids was analyzed by Flow cytometry analysis. To conduct this analysis, 100000 single-cells derived from CTR1-, NBS1- and NBS8-organoids were used. Cell pellet was fixed for 20 minutes in the dark in fixation buffer (Biolegend) followed by permeabilization with permeabilization buffer (Biolegend). Pelleted cells by centrifugation for 5 min at 300g were stained for 20 min in the dark with the following antibodies: mouse anti-SOX2 (1:200, CST 3579S) mouse anti- β -tubulin (1:200, CST TU-20), mouse anti-KI67 (1:200, CST 9449) and guinea pig anti-DCX (1:200, SySy 326004). The cell pellet was washed with permeabilization buffer and incubated with the appropriate secondary antibody Alexa488 and Alexa647 (1:500, Thermo Fisher Scientific). Alexa488 and Alexa647-coupled IgG were used as negative control. Cell pellet was resuspended in PBS/2mM EDTA/0.5%BSA and cell fluorescence was measured using CytoFLEX S (Beckman Coulter). Flow cytometry data were analyzed using FlowJo X v10.6.1 software (FlowJo LLC, Ashland, OR).

Karyotyping and array comparative genomic hybridization (array-CGH).

The karyotype analysis of NBS-iPSCs was carried out by the Institute of Human Genetics and Anthropology, Heinrich-Heine-University, Düsseldorf, Germany. Genomic DNA from NBS- and NBS8-iPSC lines was extracted using the DNeasy Blood Tissue Kit (Qiagen) and array-CGH was performed using the Illumina HumanOmni2.5Exome-8 BeadChip v1.3chip at LifeBrain GmbH, Bonn. Genotype and copy number variation (CNV) analysis was performed using Illumina GenomeStudio V2.0.2 (Illumina).

Analysis of mutational status of TP53: Library preparation and massive parallel sequencing.

DNA was quantified by a custom-made qPCR assay (Primer for: 5' AAACGCCAATCCTGAGTGTC-3'; Primer rev: 5' CATAGCTCCTCCGATTCCAT-3'). Library preparation was carried out using Ion AmpliSeq™ Library Kit 2.0 and Ion AmpliSeq™ Colon and Lung Cancer ResearchPanel v2 with 10 ng of amplifiable DNA following manufacturer's recommendations. Ion Xpress™ Barcode Adapters Kits were utilized for barcoding the libraries. Afterwards, libraries were quantified by qPCR using Ion Library TaqMan™ Quantitation Kit on a StepOnePlus™ Real-Time PCR System and were compiled equimolarly for subsequent sequencing reaction. Massive parallel sequencing was conducted on an Ion S5 System using the Ion 520™ Ion 530™ Kit-OT2 with an Ion 530™ Chip. Primary data analyses were performed by Ion Torrent Suite Software. For variant annotation generated Binary Alignment Map (BAM), files were uploaded to and

analyzed by Ion Reporter™ Software using recommended analysis parameter for the Ion AmpliSeq™ Colon and Lung Cancer ResearchPanel v2. Detected variants were examined using the Integrative Genomics Viewer (IGV) [63,64]. All reagents and software were from ThermoFisher (Darmstadt, Germany). Selected parts of Exon 2, Exon 4 - 8 and Exon 10 from the TP53 gene (NM_000546.5) are covered by the Ion AmpliSeq™ Colon and Lung Cancer ResearchPanel v2 including following amino acids: Ex 2: Met1 - Ser20; Ex 4: Glu68 - Gly112; Ex 5: Tyr126 - Ala138 Ser149 - Gly187; Ex 6: Gly187 - Pro223; Ex 7: Val225 - Glu258; Ex 8: Asn263 - Ala 307; Ex 10: Ile332-Ser367.

Bisulfite genomic sequencing.

Bisulfite conversion of 500ng of DNA of CTR1, CTR2, NBS1 and NBS8-organoids at day 20 was conducted using the EpiTect Kit (Qiagen, Hilden, Germany) as described [65]. PCR primers for specific amplification of NNAT (NG_009263.1) promoter are listed in Table S5. The amplification conditions were denaturation at 95°C for 13min, followed by 35 cycles of 95°C for 60s, 51°C for 50s, and 72°C for 25s. PCR reactions were performed using 25ng bisulfite converted DNA using GoTaq® DNA Polymerase (Promega). The TA Cloning Kit (Invitrogen) was used for cloning of the amplification product (281bp) according to the manufacturer's instructions. Sanger sequencing was performed at the BMFZ (Biomedizinisches Forschungszentrum) core facility of the Heinrich-Heine Universität, Düsseldorf. 12 clones were sequenced to obtain the methylation profile per sample. Analysis of methylated CpGs and methylation graphs were obtained by using QUMA(<http://quma.cdb.riken.jp/>) [66] software.

Statistical analysis.

Statistical analysis was performed with GraphPad Prism Software version 8.02 (GraphPad software, San Diego, CA, USA). Ordinary one-way ANOVA was used for statistical significance analysis for comparisons of the mean among groups, followed by a post hoc test with the use of Dunnett's multiple comparison test. Statistical significance was assumed at $p < 0.05$, $**p < 0.01$ and $***p < 0.001$ and $****p < 0.0001$. All data are expressed as mean \pm 95% confidence interval (qRT-PCR data) or mean \pm standard deviation (SD). N and p-values are reported in each figure legend.

AUTHOR CONTRIBUTIONS

Conceptualization: S.M. and J.A.; Methodology: S.M., L.E., W.G., A.D.; Formal analysis: S.M., W.W., J.A.; Data curation: W.W.; Investigation: S.M.; Resources: K.C.; Writing—original draft preparation: S.M.; Writing—review and editing: J.A.; Supervision: J.A.

ACKNOWLEDGEMENTS

The authors thank Prof. Gerhard Fritz and Dr. Nina Graffmann for inspiring discussions and comments on the work and the manuscript presented here. Thanks to Martina Bohndorf for technical support. JA acknowledges support from the Medical Faculty, Heinrich-Heine-University, Düsseldorf. This preprint is formatted using a LATEX class by Ricardo Henriques.

Bibliography

1. Barzilai, A., Biton, S. Shiloh, Y. The role of the DNA damage response in neuronal development, organization and maintenance. *DNA repair* 7, 1010–27 (2008).
2. Halliwell, B. Oxidative stress and neurodegeneration: where are we now? *Journal of Neurochemistry* 97, 1634–1658 (2006).
3. Chrzanowska, K. H., Gregorek, H., Dembowska-Bagińska, B., Kalina, M. A. Digweed, M. Nijmegen breakage syndrome (NBS). *Orphanet journal of rare diseases* 7, 13 (2012).
4. Weemaes, C. M. et al. A new chromosomal instability disorder: the Nijmegen breakage syndrome. *Acta paediatrica Scandinavica* 70, 557–64 (1981).
5. Varon, R., Demuth, I. Chrzanowska, K. H. Nijmegen Breakage Syndrome. *GeneReviews®* (University of Washington, Seattle, 1993).
6. Digweed, M. Sperling, K. Nijmegen breakage syndrome: clinical manifestation of defective response to DNA double-strand breaks. *DNA Repair* 3, 1207–1217 (2004).
7. Chrzanowska, K. H. et al. Atypical clinical picture of the Nijmegen breakage syndrome associated with developmental abnormalities of the brain. *Journal of medical genetics* 38, E3 (2001).
8. Seemanova, E. et al. Cancer Risk of Heterozygotes With the NBN Founder Mutation. *JNCI Journal of the National Cancer Institute* 99, 1875–1880 (2007).
9. Varon, R. et al. Clinical ascertainment of Nijmegen breakage syndrome (NBS) and prevalence of the major mutation, 657del5, in three Slav populations. *European Journal of Human Genetics* 8, 900–902 (2000).
10. Maser, R. S., Zinkel, R. Petrini, J. H. J. An alternative mode of translation permits production of a variant NBS1 protein from the common Nijmegen breakage syndrome allele. *Nature Genetics* 27, 417–421 (2001).
11. Stracker, T. H. Petrini, J. H. J. The MRE11 complex: starting from the ends. *Nature reviews. Molecular cell biology* 12, 90–103 (2011).
12. Jongmans, W. et al. Nijmegen breakage syndrome cells fail to induce the p53-mediated DNA damage response following exposure to ionizing radiation. *Molecular and cellular biology* 17, 5016–22 (1997).
13. Buscemi, G. et al. Chk2 activation dependence on Nbs1 after DNA damage. *Molecular and cellular biology* 21, 5214–22 (2001).
14. Sullivan, K. E., Veksler, E., Lederman, H. Lees-Miller, S. P. Cell Cycle Checkpoints and DNA Repair in Nijmegen Breakage Syndrome. *Clinical Immunology and Immunopathology* 82, 43–48 (1997).
15. Williams, B. R. et al. A murine model of Nijmegen breakage syndrome. *Current biology: CB* 12, 648–53 (2002).
16. Kang, J., Bronson, R. T. Xu, Y. Targeted disruption of NBS1 reveals its roles in mouse development and DNA repair. *The EMBO Journal* 21, 1447–1455 (2002).
17. Shull, E. R. P. et al. Differential DNA damage signaling accounts for distinct neural apoptotic responses in ATLD and NBS. *Genes development* 23, 171–80 (2009).
18. Demuth, I. et al. An inducible null mutant murine model of Nijmegen breakage syndrome proves the essential function of NBS1 in chromosomal stability and cell viability. *Human Molecular Genetics* 13, 2385–2397 (2004).
19. Zhou, Z., Bruhn, C. Wang, Z.-Q. Differential function of NBS1 and ATR in neurogenesis. *DNA Repair* 11, 210–221 (2012).
20. Frappart, P.-O. et al. An essential function for NBS1 in the prevention of ataxia and cerebellar defects. *Nature Medicine* 11, 538–544 (2005).
21. Mlody, B. Adjaye, J. Generation of iPSC lines from a Nijmegen Breakage Syndrome patient. *Stem Cell Research* 15, 629–632 (2015).
22. Mlody, B., Wruck, W., Martins, S., Sperling, K. Adjaye, J. Nijmegen Breakage Syndrome fibroblasts and iPSCs: Cellular models for uncovering disease-associated signaling pathways and establishing a screening platform for anti-oxidants. *Scientific Reports* (2017).
23. Halevy, T. et al. Chromosomal Instability and Molecular Defects in Induced Pluripotent Stem Cells from Nijmegen Breakage Syndrome Patients. *Cell reports* 16, 2499–511 (2016).
24. Lancaster, M. A. et al. Cerebral organoids model human brain development and microcephaly. *Nature* 501, 373–9 (2013).
25. Paşca, A. M. et al. Functional cortical neurons and astrocytes from human pluripotent stem cells in 3D culture. *Nature Methods* 12, 671–678 (2015).
26. Mariani, J. et al. Modeling human cortical development in vitro using induced pluripotent stem cells. *Proceedings of the National Academy of Sciences of the United States of America* 109, 12770–5 (2012).
27. Gabriel, E., Ramani, A., Altinisik, N. Gopalakrishnan, J. Human Brain Organoids to Decode Mechanisms of Microcephaly. *Frontiers in Cellular Neuroscience* 14, 115 (2020).
28. Martins, S. et al. Fibroblast-derived integration-free iPSC line ISRM-NBS1 from an 18-year-old Nijmegen Breakage Syndrome patient carrying the homozygous NBN c.657_661del5 mutation. *Stem Cell Research* 34, 101372 (2019).
29. Wang, Y. Adjaye, J. A Cyclic AMP Analog, 8-Br-cAMP, Enhances the Induction of Pluripotency in Human Fibroblast Cells. *Stem Cell Reviews and Reports* 7, 331–341 (2011).
30. Bohndorf, M. et al. Derivation and characterization of integration-free iPSC line ISRM-UM51 derived from SIX2-positive renal cells isolated from urine of an African male expressing the CYP2D6 *4/*17 variant which confers intermediate drug metabolizing activity. *Stem Cell Research* 25, 18–21 (2017).
31. Sloan, S. A., Andersen, J., Paşca, A. M., Birey, F. Paşca, S. P. Generation and Assembly of Human Brain Region-Specific Three-Dimensional Cultures. *Nature protocols* 13, 2062 (2018).
32. Miller, J. A. et al. Transcriptional landscape of the prenatal human brain. *Nature* 508, 199–206 (2014).
33. Ottoboni, L., von Wunster, B. Martino, G. Therapeutic

- Plasticity of Neural Stem Cells. *Frontiers in Neurology* 11, 148 (2020).
34. Komatsu, K. NBS1 and multiple regulations of DNA damage response. *Journal of Radiation Research* 57, i11 (2016).
35. el-Deiry, W. S. et al. WAF1, a potential mediator of p53 tumor suppression. *Cell* 75, 817–25 (1993).
36. Pitale, P. M., Howse, W., Gorbatyuk, M. Neuronatin Protein in Health and Disease. *Journal of Cellular Physiology* 232, 477–481 (2017).
37. Seemanová, E. et al. Nijmegen breakage syndrome (NBS) with neurological abnormalities and without chromosomal instability. *Journal of medical genetics* 43, 218–24 (2006).
38. M, S. et al. Methods of Reprogramming to Induced Pluripotent Stem Cell Associated With Chromosomal Integrity and Delineation of a Chromosome 5q Candidate Region for Growth Advantage. *Stem cells and development* 24, (2015).
39. Seeman, P., Gebertová, K., Paďěrová, K., Sperling, K., Seemanová, E. Nijmegen breakage syndrome in 13% of age-matched Czech children with primary microcephaly. *Pediatric Neurology* 30, 195–200 (2004).
40. Li, R. et al. Recapitulating cortical development with organoid culture in vitro and modeling abnormal spindle-like (ASPM related primary) microcephaly disease. *Protein cell* 8, 823–833 (2017).
41. Gabriel, E. et al. CPAP promotes timely cilium disassembly to maintain neural progenitor pool. *The EMBO Journal* 35, 803–819 (2016).
42. Zhang, W. et al. Modeling microcephaly with cerebral organoids reveals a WDR62-CEP170-KIF2A pathway promoting cilium disassembly in neural progenitors. *Nature communications* 10, 2612 (2019).
43. Dabin, J., Fortuny, A., Polo, S. E. Epigenome Maintenance in Response to DNA Damage. *Molecular Cell* 62, 712–727 (2016).
44. Georgakilas, A. G., Martin, O. A., Bonner, W. M. p21: A Two-Faced Genome Guardian. *Trends in Molecular Medicine* 23, 310–319 (2017).
45. Jackson, S. P., Bartek, J. The DNA-damage response in human biology and disease. *Nature* 461, 1071–1078 (2009).
46. Cerosaletti, K., Wright, J., Concannon, P. Active Role for Nibrin in the Kinetics of Atm Activation. *Molecular and Cellular Biology* 26, 1691–1699 (2006).
47. Kojima, K. et al. Mdm2 inhibitor Nutlin-3a induces p53-mediated apoptosis by transcription-dependent and transcription-independent mechanisms and may overcome Atm-mediated resistance to fludarabine in chronic lymphocytic leukemia. *Blood* 108, 993–1000 (2006).
48. Fiévet, A. et al. DNA repair functional analyses of NBN hypomorphic variants associated with NBN-related infertility. *Human Mutation* 41, 608–618 (2020).
49. Uziel, T. et al. Requirement of the MRN complex for ATM activation by DNA damage. *EMBO Journal* (2003).
50. Su, Y., Ming, G. L., Song, H. DNA damage and repair regulate neuronal gene expression. *Cell Research* 25, 993–994 (2015).
51. Niklison-Chirou, M. V., Agostini, M., Amelio, I., Melino, G. Regulation of Adult Neurogenesis in Mammalian Brain. *International Journal of Molecular Sciences* 21, 4869 (2020).
52. Lin, H.-H. et al. Neuronatin promotes neural lineage in ESCs via Ca(2+) signaling. *Stem cells (Dayton, Ohio)* 28, 1950–60 (2010).
53. Shinde, V., Pitale, P. M., Howse, W., Gorbatyuk, O., Gorbatyuk, M. Neuronatin is a stress-responsive protein of rod photoreceptors. *Neuroscience* 328, 1–8 (2016).
54. Joseph, R. M. Neuronatin gene: Imprinted and misfolded. Studies in Lafora disease, diabetes and cancer may implicate NNAT-aggregates as a common downstream participant in neuronal loss. *Genomics* 103, 183–188 (2014).
55. M, B. et al. Derivation and characterization of integration-free iPSC line ISRM-UM51 derived from SIX2-positive renal cells isolated from urine of an African male expressing the CYP2D6 *4/*17 variant which confers intermediate drug metabolizing activity. *Stem cell research* 25, (2017).
56. Sloan, S. A., Andersen, J., Paşca, A. M., Birey, F., Paşca, S. P. Generation and assembly of human brain region-specific three-dimensional cultures. *Nature Protocols* 13, 2062–2085 (2018).
57. Gentleman, R. C. et al. Bioconductor: open software development for computational biology and bioinformatics. *Genome Biology* 5, R80 (2004).
58. Gautier, L., Cope, L., Bolstad, B. M., Irizarry, R. A. affy-analysis of Affymetrix GeneChip data at the probe level. *Bioinformatics (Oxford, England)* 20, 307–315 (2004).
59. Warnes, G. R. et al. gplots: Various R Programming Tools for Plotting Data. (2015).
60. Chen, H., Boutros, P. C. VennDiagram: a package for the generation of highly-customizable Venn and Euler diagrams in R. *BMC Bioinformatics* 12, 35 (2011).
61. Graffmann, N. et al. Modeling Nonalcoholic Fatty Liver Disease with Human Pluripotent Stem Cell-Derived Immature Hepatocyte-Like Cells Reveals Activation of PLIN2 and Confirms Regulatory Functions of Peroxisome Proliferator-Activated Receptor Alpha. *Stem Cells and Development* 25, 1119–1133 (2016).
62. Zhou, Y. et al. Metascape provides a biologist-oriented resource for the analysis of systems-level datasets. *Nature Communications* (2019). doi:10.1038/s41467-019-09234-6
63. Robinson, J. T. et al. Integrative genomics viewer. *Nature biotechnology* 29, 24–6 (2011).
64. Thorvaldsdóttir, H., Robinson, J. T., Mesirov, J. P. Integrative Genomics Viewer (IGV): high-performance genomics data visualization and exploration. *Briefings in bioinformatics* 14, 178–92 (2013).
65. Erichsen, L. et al. Basic Hallmarks of Urothelial Cancer Unleashed in Primary Uroepithelium by Interference with the Epigenetic Master Regulator ODC1. *Scientific reports* 10, 3808 (2020).
66. Kumaki, Y., Oda, M., Okano, M. QUMA: quantification tool for methylation analysis. *Nucleic acids research* 36, W170-5 (2008).

Figure Legends

Figure 1. Generation and characterization of NBS cerebral organoids. (A) Schematic outline of the main stages of the differentiation protocol to generate the iPSC-derived cerebral organoids. (B) Representative immunocytochemistry images of the distribution of cells expressing SOX2, KI67 and DCX in cerebral organoids at day 20. Scale bars, 100µm. (C) Relative mRNA expression analysis of progenitor markers (*PAX6*, *NES* and *TBR2*), pan-neuronal makers (*TUBB3*, *MAP2*, *DCX*), early-born neurons (*TRB1*, *CTIP2*), late-born neurons (*BRN2* and *STAB2*) and the astrocytes marker *GFAP* in NBS-organoids (NBS1 and NBS8) compared to control-organoids (CTR1 and CTR2). (D) RT-PCR analysis for brain-region specificity at day 20 in control- and NBS-organoids (forebrain: *FOXP1* and *OTX1*; midbrain: *PAX5* and *FOXA2* and hindbrain: *HOXB4* and *HOXB6*). FB, fetal brain control. (E) Comparison of the diameter of control- (n=76 day 6, n=61 day 10 and n=55 day 20 for both CTR1 and CTR2), NBS1- (n=15 day 6, n=22 day 10 and n=18 day 20) and NBS8-organoids (n=36 day 6, n=35 day 10 and n=33 day 20) cerebral organoids at day 6, 10 and 20. The diameter was significantly smaller in NBS1-organoids. Significance in comparison to control (CTR1 and CTR2) was calculated with one-way ANOVA followed by Dunnett's multiple comparison test; *p<0.05, **p<0.01, ***p<0.001. (F) Representative bright-field images of control and NBS-cerebral organoids at day 20. NBS1 organoids visually lack neuroepithelial structures. Scale bars, 100µm.

Figure 2. Analysis of proliferation of the NPCs and VZs cyto-architecture at day 20. (A) Representative confocal pictures of immunostainings for SOX2 and KI67 in CTR2-, NBS1- and NBS8-organoids. Scale bars, 50µm. (B) qRT-PCR analysis of *SOX2* mRNA expression in NBS1 and NBS8-organoids relative to control organoids (CTR1 and CTR2). Results are mean ± 95% confidence interval derived from 3 independent differentiations. (C) Quantification of the SOX2-positive cells in CTR2 and NBS1- and NBS8-organoids. Results are mean ± SD derived from 3 organoids from independent differentiations. (D) qRT-PCR analysis of *MKI67* mRNA expression in NBS1 and NBS8-organoids relative to control organoids (CTR1 and CTR2). Results are mean ± 95% confidence interval derived from 3 independent differentiations. (E) Quantification of the KI67-positive cells in CTR2 and NBS1- and NBS8-organoids. Results are mean ± SD derived from 3 organoids from independent differentiations. (F) Quantification of the KI67-positive cells within the SOX2-positive cells in CTR2-, NBS1- and NBS8-organoids. Results are mean ± SD derived from 3 organoids from independent differentiations. (G) Representative confocal pictures of immunostainings for SOX2, cleaved-CASP3 and DCX in CTR2-, NBS1- and NBS8-organoids. Cleaved-CASP3 colocalized with the DCX positive cells. Scale bars, 50µm. (H) Schematic illustration of a ventricular zone (VZ) and how the thickness of the VZ and the length of the apical membrane were calculated in order to evaluate the cyto-architecture of the cerebral organoids. (I) Quantification of the number of the VZs per organoid in control (CTR1 and CTR2) and NBS1 and NBS8-organoids. Results are mean ± SD derived from 3 organoids from independent differentiations. Significance in comparison to control was calculated with one-way ANOVA followed by Dunnett's multiple comparison test. *p<0.05. (J) Quantification of the thickness of the VZs in µm in control (CTR1 and CTR2) and NBS1 and NBS8-organoids. Results are mean ± SD derived from 3 organoids from independent differentiations. Significance in comparison to control was calculated with one-way ANOVA followed by Dunnett's multiple comparison test. *p<0.05 (K) Quantification of the length of the apical membrane per VZ in control-, NBS1- and NBS8-organoids; 3 organoids from independent differentiations were analysed.

Figure 3. Global transcriptome functional analysis of control and NBS organoids at day 20. (A) Venn diagram showing genes expressed only in NBS1 organoids (300), in control organoids (392) and common to both organoids (12828; detection p value < 0.05) (B) Bar chart of the enriched clustered GOs (Top 10 ranked) of the significantly up-regulated 198 genes in NBS1-organoids compared to control-organoids. (C) Canonical pathways enrichment analysis of the up-regulated 198 genes in NBS1-organoids compared to control-organoids (Top 10 ranked). (D) Bar chart of the enriched clustered GOs (Top 10 ranked) of the significantly down-regulated 210 genes in NBS1-organoids compared to control-organoids. (E) Venn diagram showing genes expressed only in NBS8-organoids (361), in control-organoids (619) and common to both organoids (14401; detection p value < 0.05) (F) Bar chart of the enriched clustered GOs (Top 10 ranked) of the significantly up-regulated 1289 genes in NBS8-organoids compared to control organoids. (G) Bar chart of the enriched clustered GOs (Top 10 ranked) of the significantly down-regulated 1211 genes in NBS8-organoids compared to control-organoids. (H) Canonical pathways enrichment analysis of the down-regulated 1211 genes in NBS1-organoids compared to control-organoids (Top 10 ranked).

Figure 4. DNA damage response analysis in NBS organoids. (A) Heatmap showing differential gene expression analysis of selected DNA damage repair-related genes expressed in control- and NBS-organoids at day 20. (B-C) qRT-PCR analysis of *ATM* (C) and *TP53* (D) mRNA expression in NBS1 and NBS8-organoids relative to control organoids (CTR1 and CTR2). Results are mean ± 95% confidence interval derived from 3 independent differentiations. Significance in comparison to control was calculated with one-way ANOVA followed by Dunnett's multiple comparison test. *p<0.05 (D) Immunoblotting for total p53 and phosphorylated histone H2A.X in CTR1, CTR2 and NBS1 iPSCs and 20 days cerebral organoids. (E-F) qRT-

PCR analysis of *MDM2* (E) and *CDKN1A* (F) mRNA expression in NBS1 and NBS8-organoids relative to control organoids (CTR1 and CTR2). Results are mean \pm 95% confidence interval derived from 3 independent differentiations. Significance in comparison to control was calculated with one-way ANOVA followed by Dunnett's multiple comparison test. ** $p < 0.01$. (G) Representative confocal pictures of immunostainings for SOX2, γ H2A.X and DCX in CTR2-, NBS1- and NBS8-organoids. NBS-organoids display and increase in γ H2A.X nuclear foci formation. Scale bars, 50 μ m.

Figure 5. Neurodifferentiation propensity of NBS organoids (A) Venn diagram showing the exclusively expressed genes in NBS1- and NBS8-organoids (124) compared with in control-organoids (detection p value < 0.05). (B) Bar chart of the enriched clustered GOs (Top 10 ranked) of the exclusively expressed genes (124) NBS1- and NBS8-organoids compared to control organoids. (C) qRT-PCR analysis of *DCX* mRNA expression in NBS1 and NBS8-organoids relative to control organoids (CTR1 and CTR2). Results are mean \pm 95% confidence interval from 3 independent differentiations. (D-E) Quantification of the DCX- (D) and β III-Tubulin (E) positive cells in 20 days CTR2-, NBS1- and NBS8-organoids. Results are mean \pm SD from 3 organoids from independent differentiations. (F) Representative pictures of immunostainings of SOX2 and β III-Tubulin in CTR1- CTR2-, NBS1- and NBS8-organoids showing an increase in β III-Tubulin+ cells. (G) qRT-PCR analysis of *NNAT* mRNA expression in NBS1 and NBS8-organoids relative to control organoids (CTR1 and CTR2). Results are mean \pm 95% confidence interval from 3 independent differentiations. Significance in comparison to control was calculated with one-way ANOVA followed by Dunnett's multiple comparison test. **** $p < 0.0001$. (H) Immunoblotting for NNAT in CTR1- and NBS8-organoids at day 20 and CTR2- and NBS1-organoids at day 40. (I) Bisulfite sequencing of a CpG island within the promoter region of *NNAT*. The % of methylated CpG dinucleotides in CTR1-, CTR2-, NBS1- and NBS8- organoids at day 20 is shown. Filled circles denote methylated CpG dinucleotides. White circles denote unmethylated CpGs.

Figure 6. NBS-organoids profile at day 40. (A) Schematic depicting the analysis of the NBS and control organoids at day 40. SOT-analysis was performed. Also, cerebral organoids were dissociated into single cells for FACS analysis and re-plating in 2D. SOT: single organoid transcriptome. (B) Venn diagram showing genes expressed only in NBS1-organoids (441), in control-organoids (437) and common to both at day 40 (14409; detection p value < 0.05). (C) Bar chart of the enriched clustered GOs and Pathways (Top 10 ranked) of the up-regulated genes (1516) in NBS1- organoids compared to control organoids at day 40. (D) mRNA expression of *FAIM2*, *PAK3*, *NR4A3*, *NEFL*, *HYOU1*, *EGLN3*, *EPHB1*, *KCNB1*, *JAK2*, *FGF8*, *JUN*, *BDNF*, *SNCA*, *NTRK1* and *CD200* genes part of the GO: Regulation of neuron apoptotic process in NBS1- compared to CTR2-organoids at day 40. Gene expression extracted from the SOT-analysis. (E) Representative pictures of immunostainings of cleaved-CASP3 and β III-Tubulin in CTR1- and NBS1-organoids showing an increase apoptosis in NBS1-organoids. (F) Bar chart of the enriched clustered GOs (Top 10 ranked) of the down-regulated genes (592) in NBS1- organoids compared to control-organoids at day 40.

Figure 7. Effects of bleomycin in NBS-organoids at day 40. (A) Schematic depicting the strategy to induce DNA damage with Bleomycin treatment during 72h from day 37 to day 40 of CTR2- and NBS1-organoids. (B) Venn diagram showing genes expressed only in CTR2_Bleomycin organoids (330), in CTR2_control organoids (700) and common to both (144146; detection p value < 0.05). (C) Bar chart of the enriched clustered GOs and Pathways (Top 10 ranked) of the up-regulated genes (139) in CTR2_Bleomycin-organoids compared to CTR2_control-organoids. (D) Venn diagram showing genes expressed only in NBS1_Bleomycin-organoids (284), in NBS1_control-organoids (474) and common to both (414346; detection p value < 0.05). (E) Bar chart of the enriched clustered GOs and Pathways (Top 10 ranked) of the up-regulated genes (198) in NBS1_Bleomycin-organoids compared to NBS1_control-organoids. (F) mRNA expression of the genes part of the up-regulated *TP53 downstream pathway* in CTR2_Bleomycin-organoids and NBS1_Bleomycin-organoids compared to CTR2_control-organoids and NBS1_control-organoids, respectively. All genes were significantly up-regulated in CTR2 after bleomycin treatment. (G) mRNA expression of *TP53* in CTR2_Bleomycin-organoids and NBS1_Bleomycin-organoids compared to CTR2_control-organoids and NBS1_control-organoids. (H) Western blot analyses of total p53 in CTR2- and NBS1-organoids after bleomycin treatment.

Results II: Modelling NBS using patient-derived cerebral organoids

bioRxiv preprint doi: <https://doi.org/10.1101/2020.09.29.318527>; this version posted September 30, 2020. The copyright holder for this preprint (which was not certified by peer review) is the author/funder. All rights reserved. No reuse allowed without permission.

Figure 1

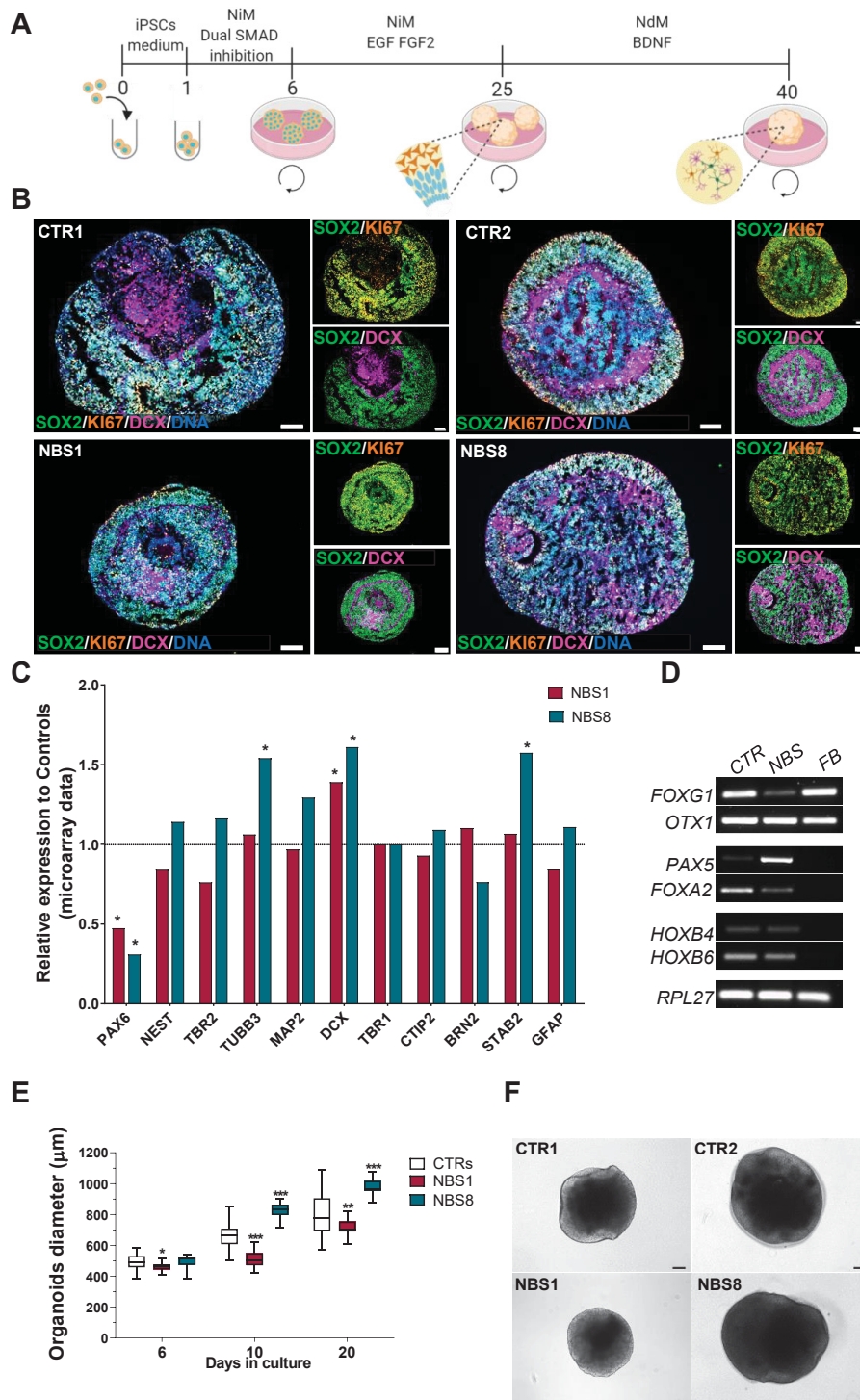
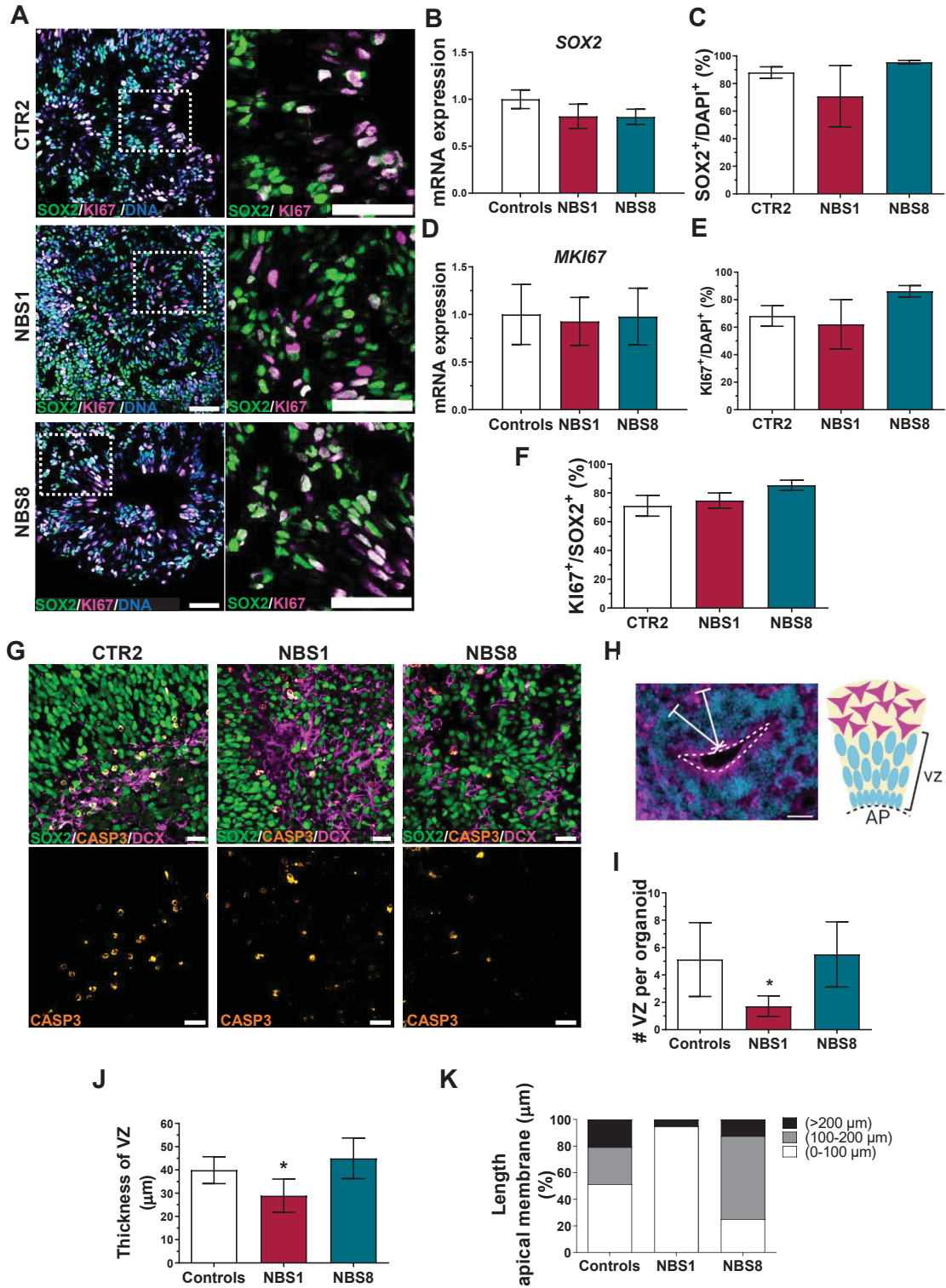


Figure 2



Results II: Modelling NBS using patient-derived cerebral organoids

bioRxiv preprint doi: <https://doi.org/10.1101/2020.09.29.318527>; this version posted September 30, 2020. The copyright holder for this preprint (which was not certified by peer review) is the author/funder. All rights reserved. No reuse allowed without permission.

Figure 3

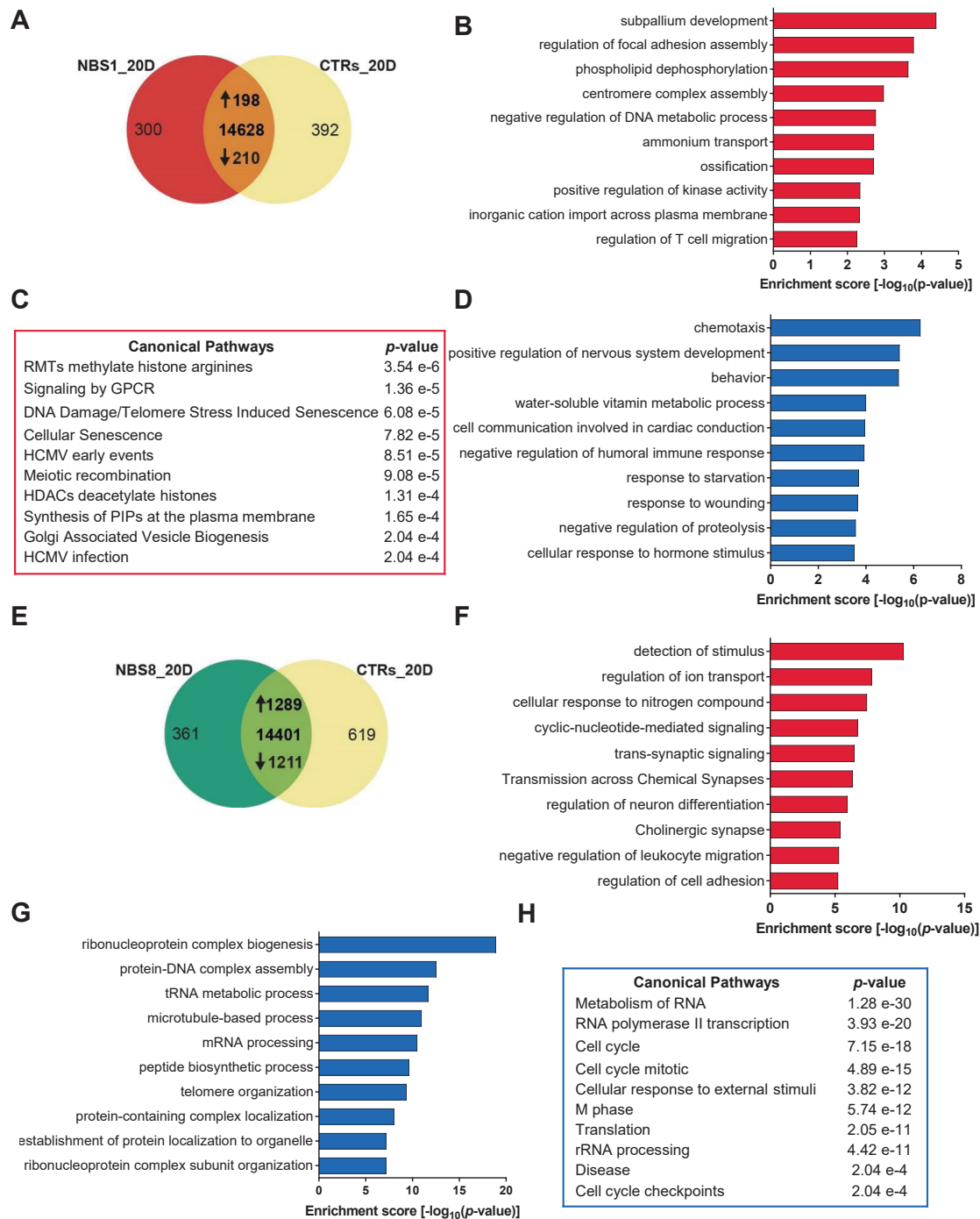
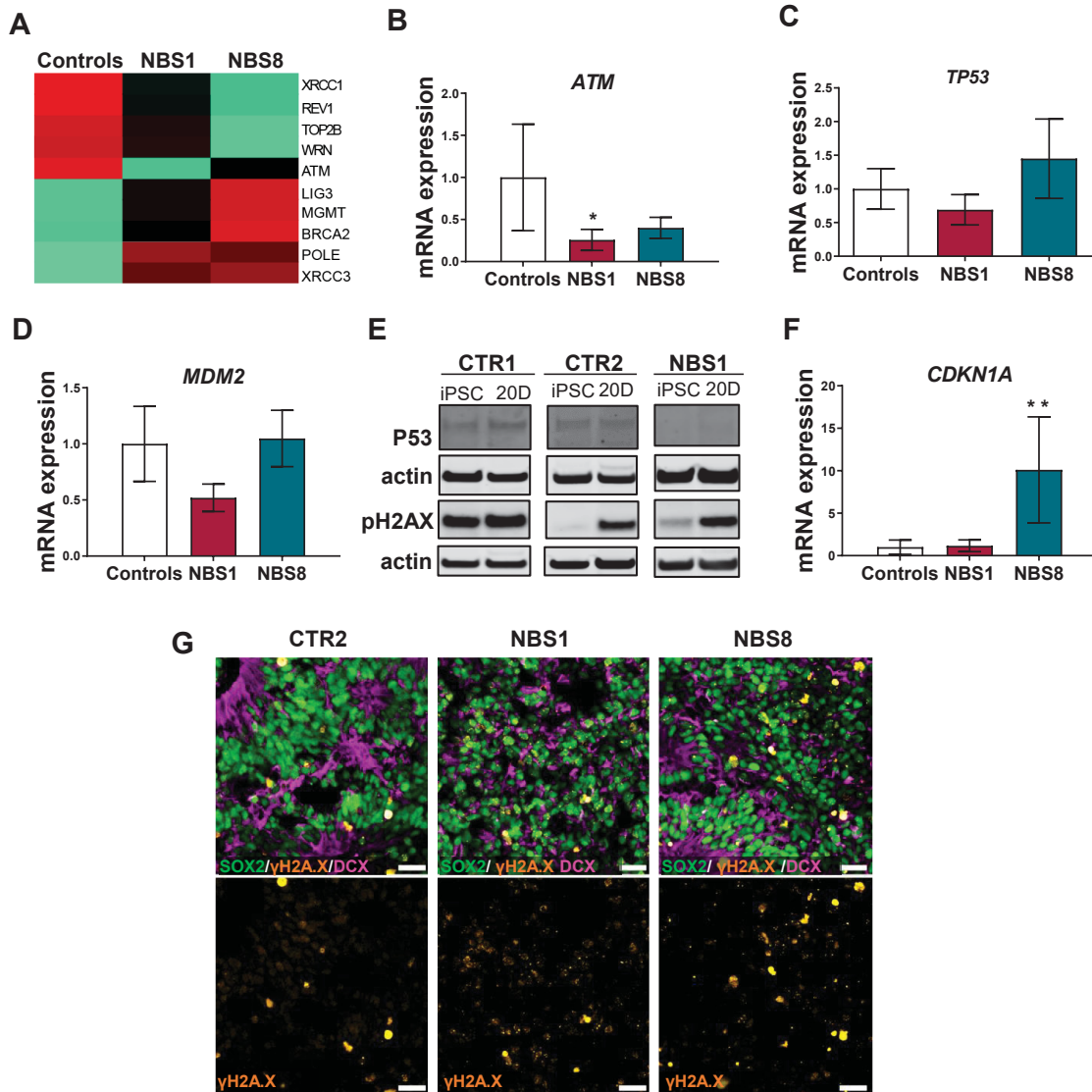


Figure 4



Results II: Modelling NBS using patient-derived cerebral organoids

bioRxiv preprint doi: <https://doi.org/10.1101/2020.09.29.318527>; this version posted September 30, 2020. The copyright holder for this preprint (which was not certified by peer review) is the author/funder. All rights reserved. No reuse allowed without permission.

Figure 5

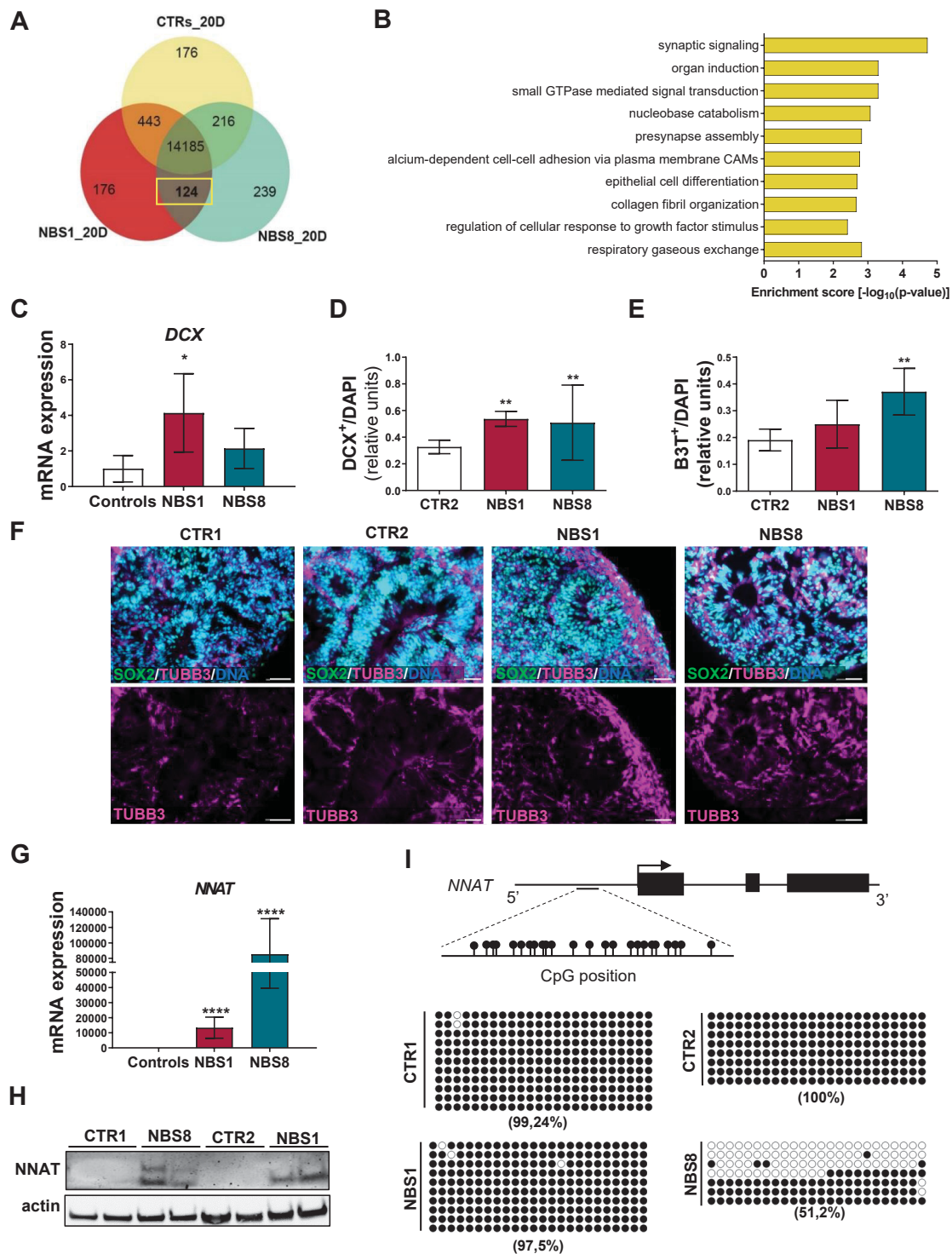
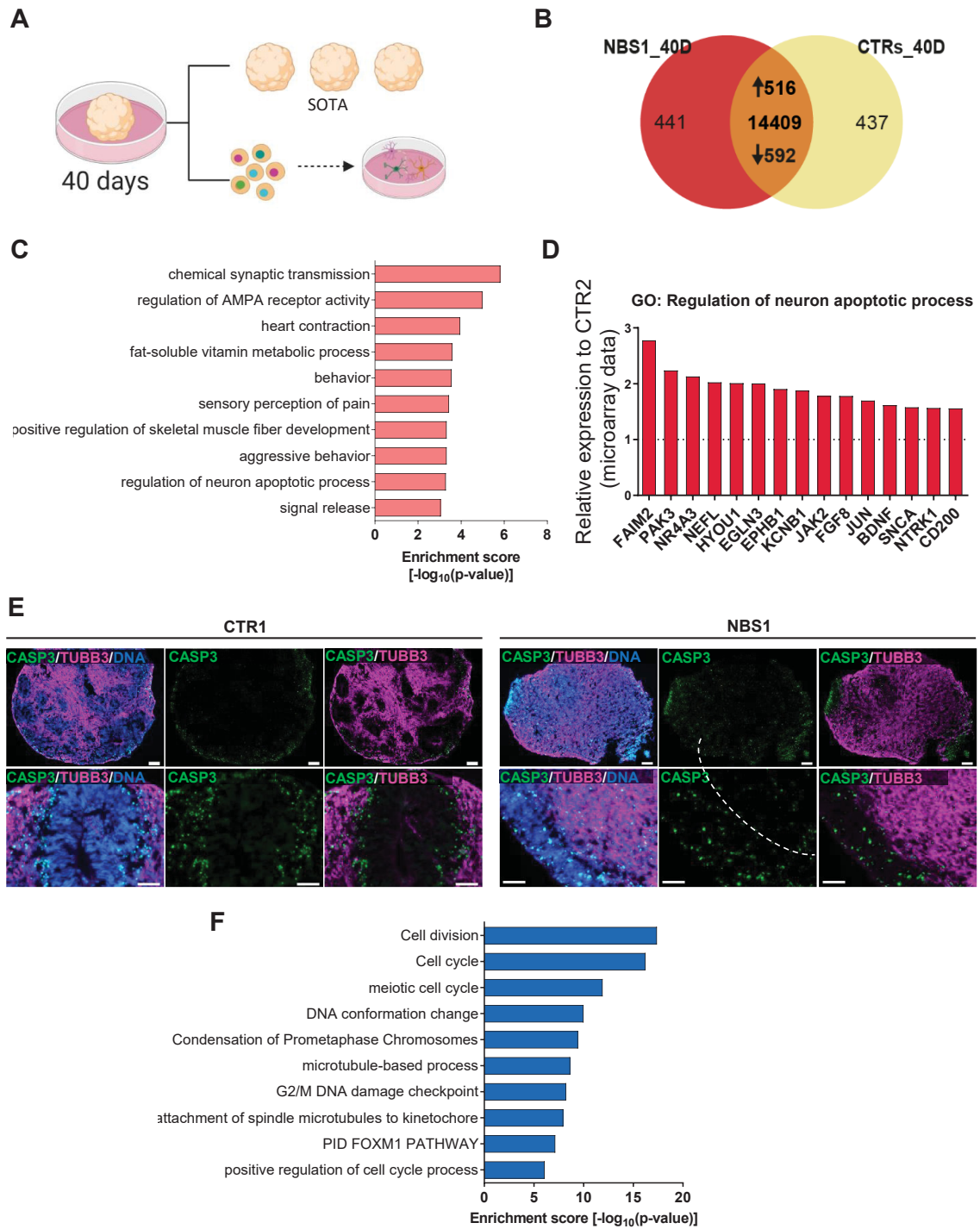


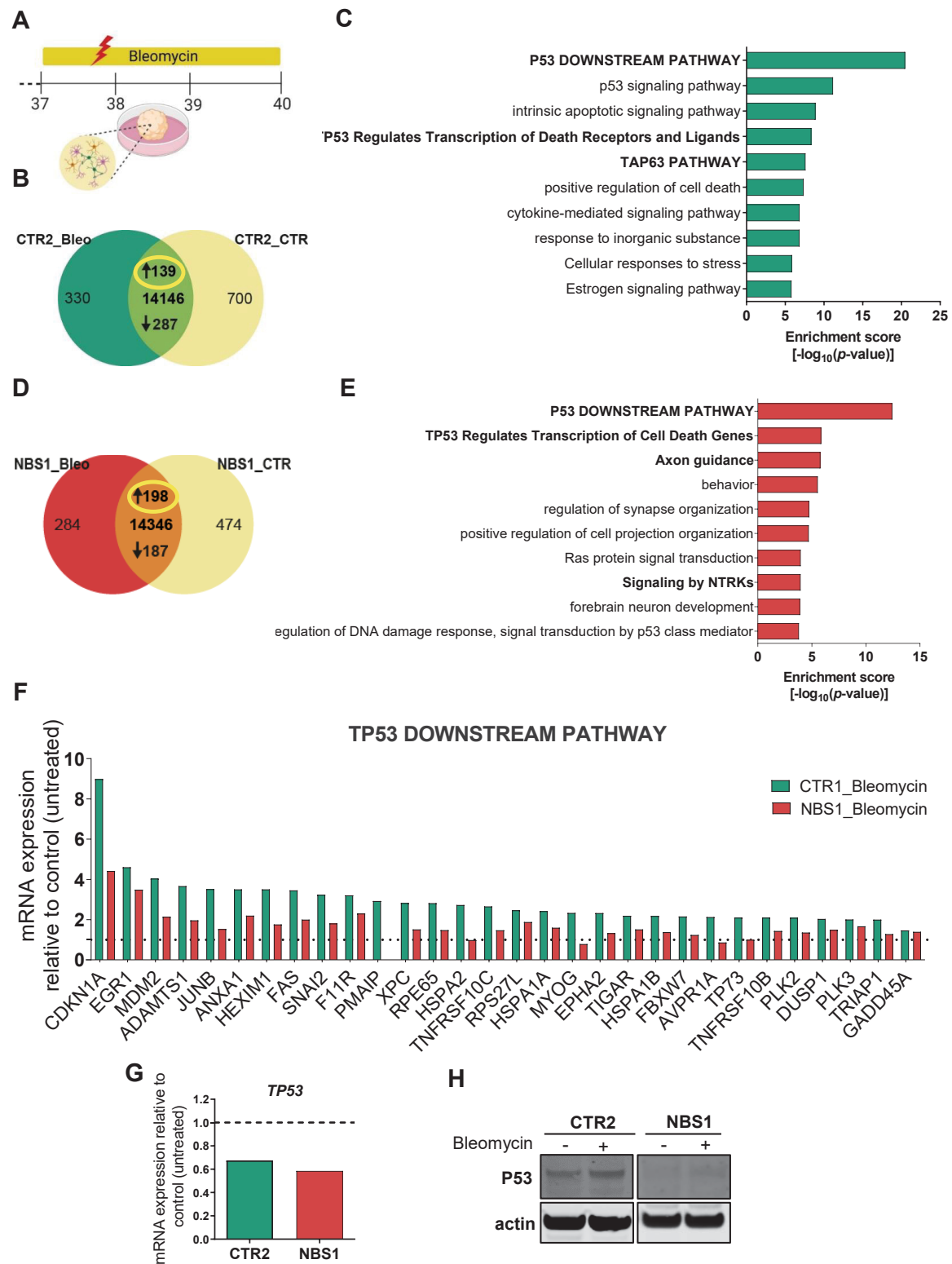
Figure 6



Results II: Modelling NBS using patient-derived cerebral organoids

bioRxiv preprint doi: <https://doi.org/10.1101/2020.09.29.318527>; this version posted September 30, 2020. The copyright holder for this preprint (which was not certified by peer review) is the author/funder. All rights reserved. No reuse allowed without permission.

Figure 7



bioRxiv preprint doi: <https://doi.org/10.1101/2020.09.29.318527>; this version posted September 30, 2020. The copyright holder for this preprint (which was not certified by peer review) is the author/funder. All rights reserved. No reuse allowed without permission.

Supplementary material

Deciphering the etiology of microcephaly using Nijmegen Breakage Syndrome patient-derived induced pluripotent stem cells.

Soraia Martins, Lars Erichsen, Angeliki Datsi, Wasco Wruck, Wolfgang Goering, Krystyna Chrzanowska and James Adjaye

PREPRINT

Results II: Modelling NBS using patient-derived cerebral organoids

bioRxiv preprint doi: <https://doi.org/10.1101/2020.09.29.318527>; this version posted September 30, 2020. The copyright holder for this preprint (which was not certified by peer review) is the author/funder. All rights reserved. No reuse allowed without permission.

Supplementary Tables

Table S1. Overview of the iPSC lines used in this study.

iPSC line	Gender	Genotype	Age of the donor	Derived from	Reprogramming method	Karyotype
NBS1	f	homozygous <i>NBN</i> 657del5	18	human dermal fibroblasts	episomal reprogramming	46,XX
NBS8	m	heterozygous <i>NBN</i> 657del5	7	human dermal fibroblasts	retroviral transduction	46,XY,add(5)(q22),der(11)t(5;11)(q14;q?23)[14]/46,idem,add(4)(q31)[10]
CTR1	m	-	newborn	human foreskin fibroblasts	retroviral transduction	-
CTR2	m	-	51	urine cells	episomal reprogramming	46,XY

Table S2. Complete GOs and canonical pathways enrichment analysis of NBS-organoids at day 20 as shown in Figure 3 and 5.

Table S3. Complete GOs and canonical pathways enrichment analysis of CTR2- and NBS1-organoids at day 40 as shown in Figure 6.

Table S4. Complete GOs and canonical pathways enrichment analysis of the bleomycin treatment in CTR- and NBS-organoids at day 40 as shown in Figure 6.

Table S5. Primer sequences used in this study.

Gene	Forward	Reverse
<i>OTX2</i>	TGCAGGGGTTCTTCTGTGAT	AGGGTCAGAGCAATTGACCA
<i>ATM</i>	AGCTCGGATGCTTTCTCAA	CTCCATCGAGAAGGTCCACG
<i>CDKN1A</i>	GGAGACCATGTGGACCTGT	GGCGTTTGGAGTGGTAGAAA
<i>DCX</i>	AAGACTTCAGCCAAGAGCCC	GCGTAGAGATGGGAGACTGC
<i>EMX1</i>	AGACGCAGGTGAAGGTGTGG	CAGGCAGGCAGGCTCTCC
<i>FOXA2</i>	CCACCACCAACCCACAAAATG	TGCAACACCGTCTCCCCAAAGT
<i>FOXF1</i>	CCCTCCCATTTCTGTACGTTT	CTGGCGGCTCTTAGAGAT
<i>HOXA2</i>	TCAGCAAAATGCCCTCTCT	TAGGCCAGCTCCACAGTTCT
<i>HOXB2</i>	TTTAGCCGTTTCGCTTAGAGG	CGGATAGCTGGAGACAGGAG
<i>HOXB4</i>	ACACCCGCTAACAAATGAGG	GCACGAAAGATGAGGGAGAG
<i>HOXB6</i>	GAAGTGGAGGAGCGGACTCAC	CTGGGATCAGGGAGTCTTCA
<i>MDM2</i>	AAACTGGGGAGTCTTGAGGG	TGCACATTTGCCTGCTCCTC
<i>MKI67</i>	TCGTCCCAGTGAAGAGTTG	CGACCCCGCTCCTTTTGAT
<i>NNAT</i>	CGGCTGGTACATCTCCGC	TGTCCCTGGAGGATTCGAAA
<i>NNAT</i> (bissulfite-specific)	GGGTTAGGTAGTTTGTGGAA	CCCCCAAACCTAATAAAT
<i>PAX5</i>	AGGATGCCGCTGATGGAGTAC	TGGAGGAGTGAATCAGCTTGG
<i>SOX2</i>	GAGCTTTGCAGGAAGTTTGC	GCAAGAAGCCTCTCCTTGAA
<i>TP53</i>	CAGGGCAGCTACGTTTCC	CAGTTGGCAAACATCTTGTTGAG

Supplementary Figures

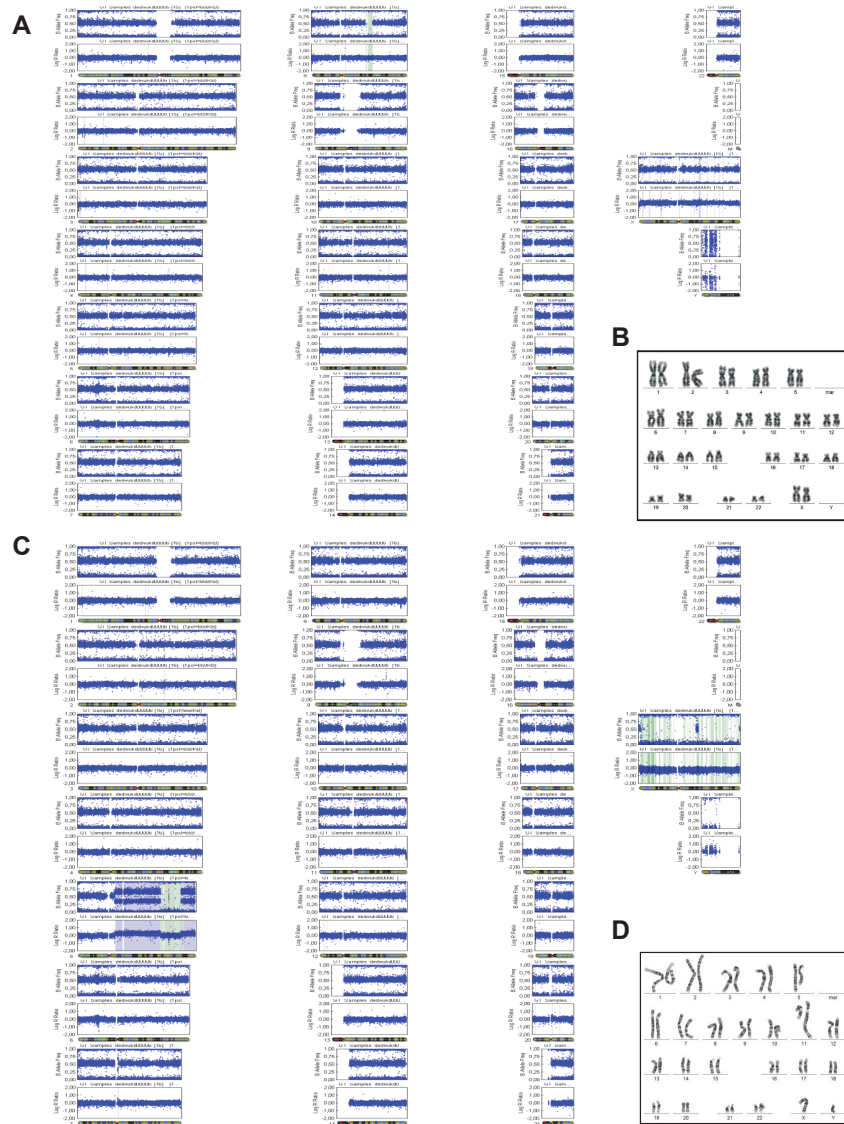


Figure S1. Identification of chromosomal aberrations in NBS-iPSCs. Relative to Table S1. (A) Illustration of whole genome profile of CNV analysis after Array-CGH of NBS1-iPSCs showing a LOH in chromosome 8q. CNV, copy number variations; LOH, loss of heterozygosity. (B) G-banding karyotype of NBS1-iPSC: 46,XX (C) Illustration of whole genome profile of CNV analysis after Array-CGH of NBS8-iPSCs. CNV, copy number variations (D) G-banding karyotype of NBS8-iPSCs: 46,XY,add(5)(q22),der(11)t(5;11)(q14;q23)[14]/46,idem,add(4)(q31)[10].

Results II: Modelling NBS using patient-derived cerebral organoids

bioRxiv preprint doi: <https://doi.org/10.1101/2020.09.29.318527>; this version posted September 30, 2020. The copyright holder for this preprint (which was not certified by peer review) is the author/funder. All rights reserved. No reuse allowed without permission.

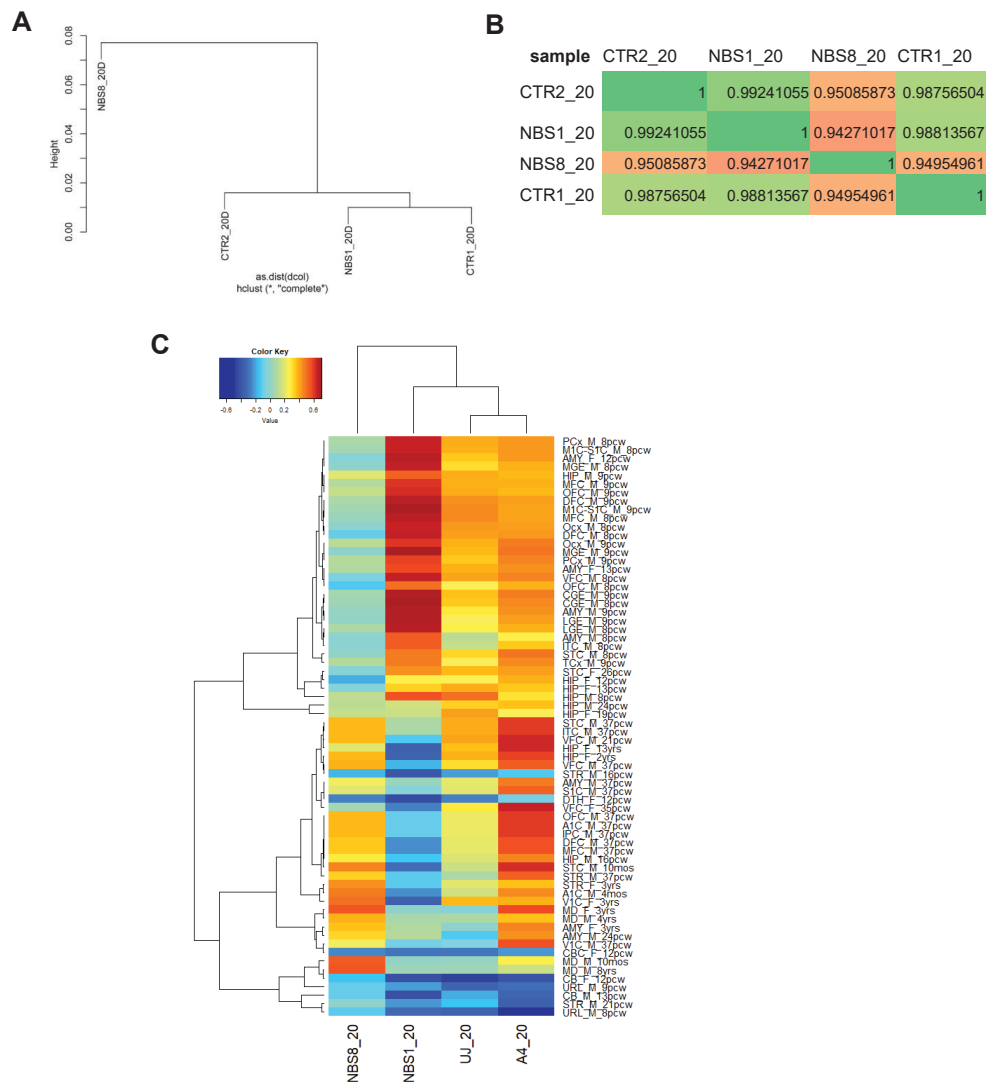


Figure S2. Gene expression profiles of control and NBS organoids. Relative to Figure 3 and Figure 5. (A) Dendrogram obtained by hierarchical cluster analysis of microarray-based gene expression data for CTR1, CTR2, NBS1 and NBS8 cerebral organoids. (B) Pearson's correlation coefficient matrix of the transcriptomic data showing NBS8 has a distinct transcriptome profile. (C) Heat map of enrichment scores of transcriptomic data from control and NBS organoids in comparison with the Allen Brain Atlas (ABA) human developmental Brain NGS data (<https://www.brainspan.org/>).

bioRxiv preprint doi: <https://doi.org/10.1101/2020.09.29.318527>; this version posted September 30, 2020. The copyright holder for this preprint (which was not certified by peer review) is the author/funder. All rights reserved. No reuse allowed without permission.

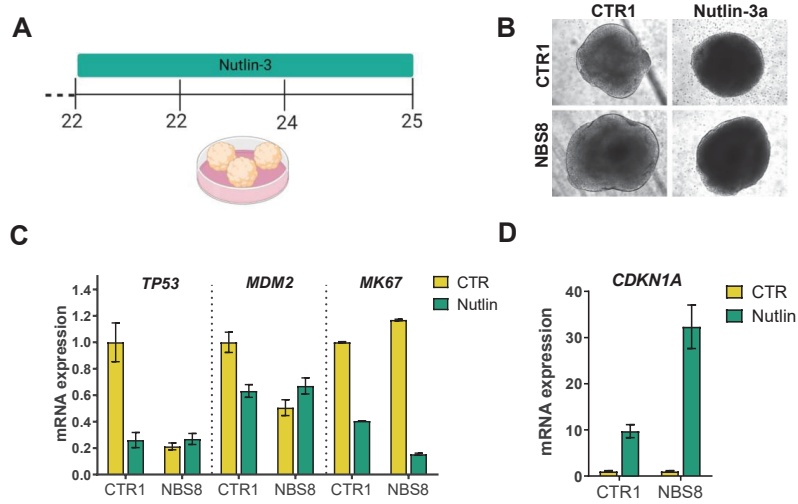


Figure S3. Stabilization of p53-induced by Nutlin 3a. Relative to Figure 4 (A) Schematic depicting the strategy to stabilize p53 via incubation with Nutlin-3a during 72h from day 22 to day 25 of CTR1- and NBS8-organoids. (C-D) qRT-PCR analysis of TP53, MDM2, MKI67 (C) and CDKN1A (D) mRNA expression in CTR1- and NBS8-organoids after Nutlin-3a treatment relative to control (untreated) CTR1: n=3 and NBS8: n=3 technical replicates. Results are mean +/- 95% confidence interval.

Results II: Modelling NBS using patient-derived cerebral organoids

bioRxiv preprint doi: <https://doi.org/10.1101/2020.09.29.318527>; this version posted September 30, 2020. The copyright holder for this preprint (which was not certified by peer review) is the author/funder. All rights reserved. No reuse allowed without permission.

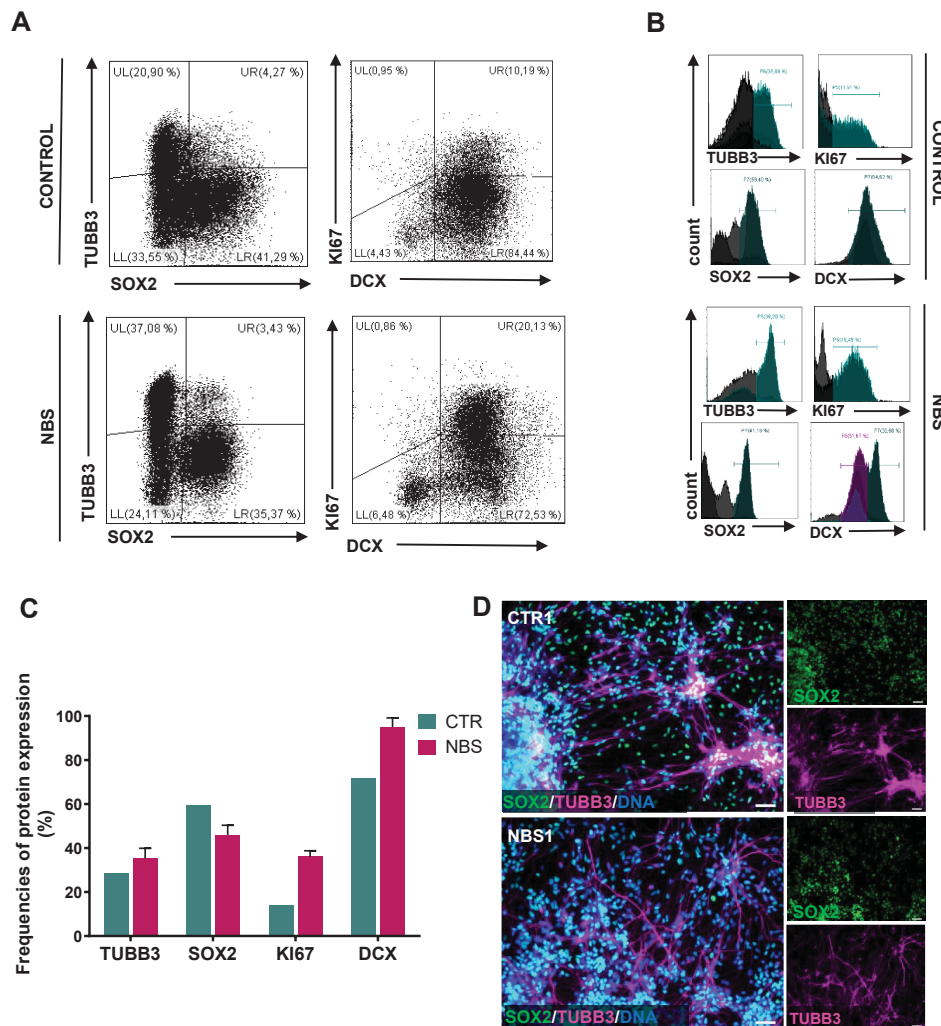


Figure S4. Increase abundance of BIII-Tubulin and DCX-positive neurons in NBS-organoids. Relative to Figure 6 (A) Expression of BIII-Tubulin (TUBB3), SOX2, KI67 and DCX was assessed in single cell suspension of brain organoids by multicolor flow cytometry. Gates and quadrants were set according to negative controls and frequencies of single- and double-expressors are indicated in these representative dot plots. (B) Representative histograms of single-expression of TUBB3, SOX2, KI67 and DCX in single cell suspension of brain organoids. Gates were set according to negative controls. (C) Quantitative assessment of the protein expression in frequencies (%) Data are representative of n 3 independent experiments and presented as mean \pm SD. (D) Representative pictures of immunostainings of SOX2 and β III-Tubulin in CTR1- and NBS1-organoids after 1 week of single cell dissociation and re-plating in 2D.

Results II: Modelling NBS using patient-derived cerebral organoids

bioRxiv preprint doi: <https://doi.org/10.1101/2020.09.29.318527>; this version posted September 30, 2020. The copyright holder for this preprint (which was not certified by peer review) is the author/funder. All rights reserved. No reuse allowed without permission.

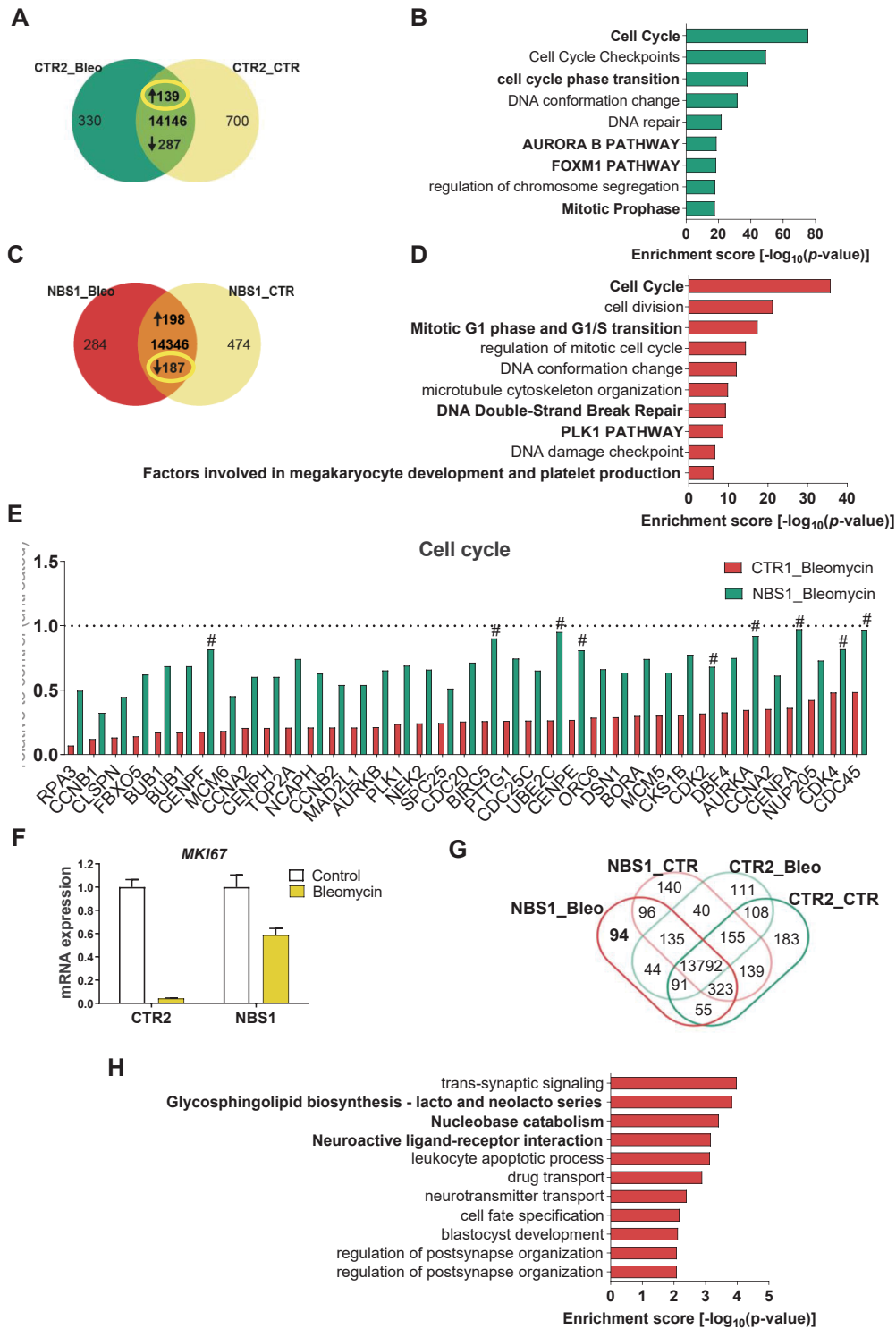


Figure S5. Analysis of the effect of bleomycin in the down-regulated and exclusively expressed genes in CTR2- and NBS1-organoids. Relative to Figure 7. (A-B) Venn diagram showing the 287 down-regulated genes (A) in CTR2_Bleomycin-organoids compared to CTR2_control-organoids and the respective bar chart (B) of the enriched clustered GOs and pathways (Top 10 ranked). (C-D) Venn diagram showing the 187 down-regulated genes (A) in NBS1_Bleomycin-organoids compared to NBS1_control-organoids and the respective bar chart (B) of the enriched clustered GOs and pathways (Top 10 ranked). (E) mRNA expression of genes associated with the down-regulated cell cycle pathway in CTR2_Bleomycin-organoids and NBS1_Bleomycin-organoids compared to CTR_control-organoids and NBS1_control-organoids, respectively. All genes were significantly down-regulated in NBS1 and CTR2 after bleomycin treatment, except genes assigned with in CTR2_Bleomycin-organoids. (F) qRT-PCR analysis of MKI67 of mRNA expression in CTR1- and NBS1-organoids after bleomycin treatment relative to control (untreated) organoids. CTR2: n=3 and NBS1: n=3 technical replicates. Results are mean \pm 95% confidence interval. (G) Venn diagram dissecting 94 exclusively expressed genes expressed in NBS1_Bleomycin-organoids. (H) Bar chart of the enriched clustered GOs and Pathways (Top 10 ranked) 94 exclusively expressed genes in NBS1_Bleomycin-organoids.

PREPRINT

4 | General Discussion

4.1 Discussion

Neurodegenerative and neurodevelopmental diseases affect millions of people worldwide and represent a complex social and economic burden, which is expected to dramatically rise with the increase in life expectancy [77,78]. Development of effective treatment to delay or halt disease progression has become the ultimate goal of neurosciences research. To that end, it is necessary to understand the molecular mechanisms that underlie the pathology. However, many of these remain largely unknown due to the unavailability of human models that accurately recapitulate the disease phenotype. Recent advances in iPSCs technology opened a new avenue to study neurological disorders in an unprecedented way, not only providing new tools to identify new therapeutic targets, but also giving insights into the molecular mechanism underlying the disease. The work described herein aimed to employ patient-derived iPSCs to model a neurodegenerative disease- Alzheimer's disease; and a rare neurodevelopmental disease – Nijmegen Breakage Syndrome. The focus was on the generation of patient-derived iPSCs, namely iPSC derived from late-onset Alzheimers disease patients carrying the *TREM2* R47H variant, and iPSCs derived from Nijmegen Breakage syndrome patients carrying the *NBN* 647del5 mutation. While certain molecular phenotypes may be observed in iPSC-derived neurons at early developmental stages, downstream phenotypes associated with AD may only be observed in mature neurons. To this end, different neuronal differentiation models which recapitulate the disease phenotype were established, an iPSCs-derived 2D neuronal cultures to model AD, and iPSC-derived 3D cerebral organoids to model NBS. The generated models were used to unravel molecular mechanism underlying disease pathogenesis and provide a valuable tool for further

applications in drug screening and disease modelling. Figure 7 summarises the overview of the work developed in this thesis, with a focus on the aims and achievements (chapter 2 and 3).

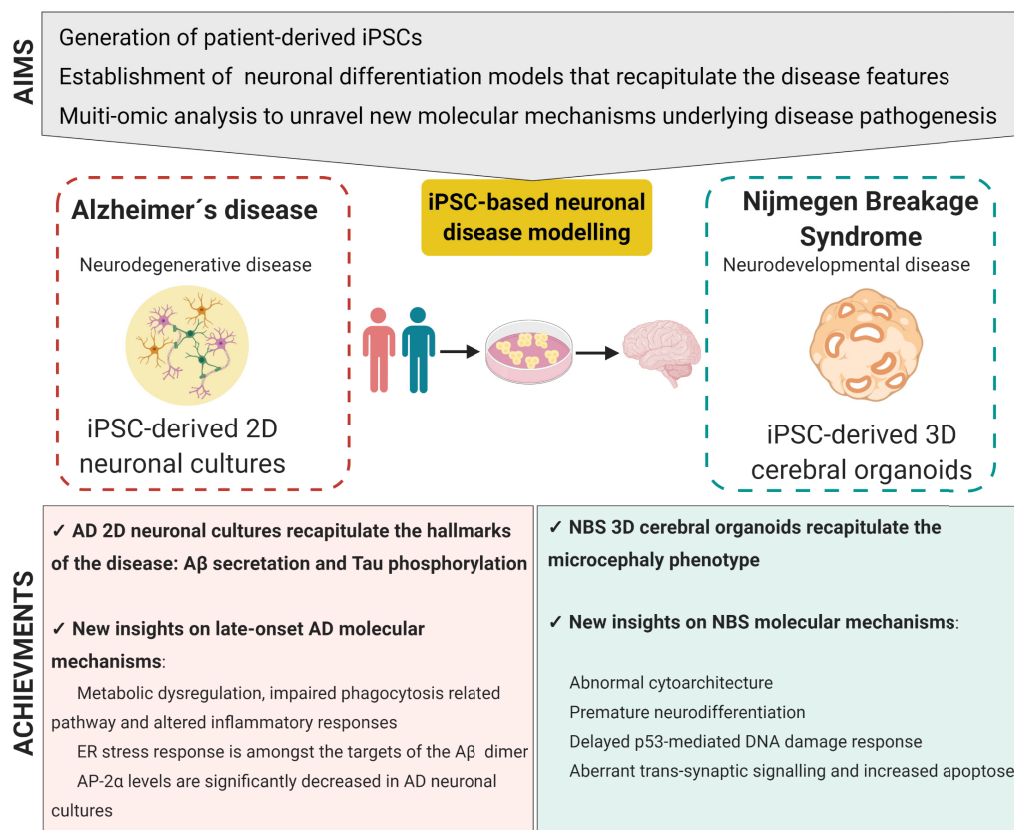


Figure 7 – Schematic representation of the major aims and achievements of the thesis.

4.1.1 Modelling Alzheimers disease using patient-derived iPSCs

AD has been a focus of study over several decades, however the etiology and pathogenesis underlying it remain largely unknown. One of the reasons is the lack of meaningful *in vitro* models which can recapitulate the hallmarks of the disease: the amyloid plaques and the neurofibrillary tangles [90]. Recently AD patient-derived iPSCs have provided valuable information regarding new mechanisms associated with the etiology of AD. The majority of these studies were focused on familiar AD patient-derived iPSCs, however more than 95% of the total AD cases are late-onset. While no LOAD-causative mutations have been found, genome wide association studies demonstrated a considerable number of genetic risk fac-

tors that increase the risk for developing LOAD. Recently, expression of the rare variant *TREM2* R47H has been shown to increase the risk for developing AD 2-3 fold [94,95,97]. However, the effect of this genetic risk variant on human brain function is still poorly understood. The main focus of chapter 2 were: (1) generation and characterization of iPSC lines from AD patients carrying the *TREM2* R47H mutation; (2) establishment of functional 2D neuronal cultures that recapitulate the disease phenotype; (3) multi-omic analysis to unravel the early molecular mechanism underlying late-onset AD; and (4) proof-of-concept of AD 2D neuronal cultures applicability to identify new mechanisms of APP processing and A β production and therefore identifying novel therapeutic targets of AD.

To establish and validate an AD iPSC-based platform to enable studying the effect of the *TREM2* R47H variant on disease progression, lymphoblasts from AD patients carrying that variant were reprogrammed (chapter 2.1 and 2.2). To ensure a valid disease model platform, aged-matched non-demented control iPSC line was also generated (chapter 2.3). Control and AD lymphoblasts were reprogrammed using an episomal-based plasmid carrying the Yamanaka factors. The generated iPSC lines were fully characterized by accessing the expression of the pluripotency markers, the ability to form EBs, and comparing the global transcriptome analysis with ESCs. Importantly, the donors genetic background was maintained in the generated iPSC, giving these cells a unique advantage in the study of LOAD [143–145].

GABAergic neurotransmission plays a very important role in AD pathogenesis, such as A β toxicity and hyperphosphorylation of Tau [146]. To that end, two AD iPSC lines and two aged-match control iPSC lines were differentiated to generate neuronal cultures enriched in GABAergic interneurons. While certain molecular phenotypes may be observed in iPSC-derived neurons at early developmental stages, downstream phenotypes associated with AD may only be observed in mature neurons [147]. In the attempt to obtain functional and mature iPSC-derived neuronal cultures, iPSCs were differentiated in a course of 80 days.

As described in chapter 2.4, the generated iPSC-derived neuronal cultures expressed the neural synaptic marker Synapsin-I and the neurofilaments SMI-32, suggesting maturation. These neuronal cultures exhibited alterations in key signalling pathways related to metabolism and immune response, suggesting that the *TREM2* R47H variant contributes

to an inadequate immune response and ultimately to neurotoxicity. *TREM2* is predominantly expressed in microglia [148], however we found *TREM2* mRNA expression in our neuronal cultures. Though we have not analysed our neuronal cultures for the presence of microglia, these might have been harboured in the mixed neuronal culture. To validate the AD iPSC-based platform, the presence of the AD hallmarks was assessed. Control and AD neuronal cultures secreted high levels of A β and expressed phosphorylated Tau. However, no significant differences were found between the AD and control neuronal networks, in line with previous studies which have shown that A β secretion is not altered in LOAD-derived neurons [107,149]. While mutations in *APP* and *PSEN1* directly affect APP processing, it is crucial to understand how the presence of the genetic risk factors, in this case the *TREM2* mutation, affects the amyloid cascade hypothesis. Based on that, one crucial question is: What are the early events which trigger neurodegeneration before the presence of amyloid plaques? In this work, iPSC-derived neuronal cultures were stimulated with an A β -S8C dimer. With the capacity to induce neurotoxicity and abnormal synaptic signalling in the absence of plaque pathology, A β -S8C dimer is a valuable tool in identifying early events of LOAD [150]. By employing global transcriptome analysis, we were able to identify metabolic dysregulation, impaired phagocytosis-related pathways, altered inflammatory response and endoplasmic reticulum (ER)-stress as the early events underlying LOAD carrying the *TREM2* R47H variant. The effect of *TREM2* mutations on phagocytosis is an active area of study, with variable results. Recent studies showed iPSC-derived microglia harboring the *TREM2* R47H mutation exhibit a substantial deficit in the ability to phagocytose A β [151]. According to the amyloid cascade hypothesis, the formation of the A β plaques are due to an imbalance between A β production and clearance. A β peptide is generated from the sequential proteolytic cleavage of APP by β - and γ -secretases [90]. APP processing is intimately linked to its intracellular trafficking and seems to take place mostly in the endolysosomal system, where BACE1 is mostly located [152]. Indeed, recent evidence points to A β accumulation as a mechanism dependent of BACE1 activity. Deficient endolysosomal pathway, including aberrant endosome trafficking, endocytosis and progressive lysosomal dysfunction are hypothesised to underlie the earlier pathology of AD [153]. Interestingly, we found lysosome-associated membrane protein 2 (*LAMP2*)

mRNA down-regulated after A β -S8C dimer stimulation. Supporting our findings, endocytosis was found as one of the down-regulated gene sets in the hippocampus of AD *TREM2* R47H patients [152]. However, and after intensive focus of study, there is still a critical open question: What is the precise mechanism by which BACE1 intracellular trafficking is regulated in neurons that leads to A β accumulation? Here we showed that APP processing and A β production are controlled by the protein complex-2 (AP-2), an endocytic adaptor required for APP endocytosis. AP-2 regulates the intracellular trafficking of BACE1, and thus acting as a critical regulator of amyloidogenesis (chapter 2.5). Our data shows that loss of AP-2 causes defective transport of BACE1-containing autophagosomes and late endosomes en route to lysosomes, which results in increased amyloidogenic processing of APP. Astonishingly, we showed AP-2 is decreased in iPSCs-derived neuronal networks carrying the *TREM2* R47H. These findings are highly interesting as they suggest cells expressing *TREM2* R47H variant might transcriptionally regulate AP-2 levels in brains of AD patients [155].

Overall, an AD iPSC-based platform to enable studying the effect of the *TREM2* R47H variant was successfully generated. Furthermore, this is the first report where LOAD iPSC-derived neuronal cultures were stimulated with the A β -S8C dimer. This approach provided valuable biological pathways that mirror some of the pathways that have been identified in LOAD brain biopsies. Our AD-iPSC based model contributed massively to the identification of a novel mechanisms by which APP processing and A β production are controlled. These new insights from the mechanism underlying the earlier pathology of AD provide new opportunities for screening of potential therapeutic targets. Further studies are required to better characterize the population of cells in the AD iPSC-based neuronal cultures and to clarify expression of *TREM2*. Most of the identified LOAD risk factors are expressed primarily in non-neuronal cells, making it clear that multiple different brain cell types can contribute to AD progression [148]. The greatest weakness of the AD iPSC-based neuronal cultures is the reduced number of non-neuronal cells present. Increasing the population of iPSC-derived microglia, astrocytes and oligodendrocytes to the culture could better recapitulate the disease phenotype contributing to a better understanding of the *TREM2* R47H variant effects. 3D cerebral organoids opened a new avenue for AD research, which have

already proven to better recapitulate the AD hallmarks [111,113]. 3D co-culture models provide a unique opportunity to examine the potential interactions that may occur between different cell-types due to the different AD-linked mutations. However, it still remains very much work in progress in the 3D cerebral organoids technology. As these techniques continue to be refined, the ability to model AD using iPSCs will improve and may bring us closer to an effective treatment.

4.1.2 Modelling Nijmegen Breakage Syndrome using patient-derived cerebral organoids

Although NBS is considered a rare disease, the frequency of heterozygous genotypes in some populations of the Czech Republic, Poland and Ukraine is extremely high 1:555. More than 90% of the NBS are homozygous for the founder mutation 657del5 within *NBN*. Whereas the clinical manifestations of the disorder are described, the mechanistic events that lead to the progressive microcephaly and other deleterious neuronal effects are still unknown. When NBS patient-derived iPSCs were differentiated into NPCs, a de-regulated expression of neural developmental genes due to the inability to maintain normal levels of p53 was suggested [132]. However, the 2D experiments did not further allow to dissect the molecular mechanism that cause microcephaly in NBS patients. Thus the main focus on chapter 3 was on (1) generation and characterization of iPSC line from NBS patient carrying the homozygous *NBN* 657del5 mutation; (2) establishment of functional 3D cerebral organoid culture systems that recapitulates the disease phenotype, and (3) multi-omic analysis to unravel the molecular mechanism underlying microcephaly in NBS patients.

Understanding and investigating the NBS mechanism is challenging because of the genetic instability inherent to these cells. We previously reported the generation of NBS-iPSCs carrying the heterozygous *NBN* 657del5 mutation presenting genomic instability, which was exacerbated by retroviral-based reprogramming (NBS8-iPSCs) [127]. To create a precise disease modelling system, it is essential to ensure the quality of the iPSCs used. As a starting point, a second NBS-iPSC line was generated, as described in chapter 3.1. In an effort to minimize genome instability, NBS1-iPSC line was generated by reprogramming NBS patient

fibroblasts using episomal-based delivery system [156]. To our knowledge, this is the first NBS-iPSC line generated with a non-integrative method. Genome integrity of both NBS-iPSCs was assessed by a combination of G-banded karyotype and copy number variation (CNV) analysis. NBS1-iPSCs present a normal karyotype with no differences between the donor cells and the iPSC regarding the CNV count, contrasting with NBS8-iPSCs. Apart from differences in the genetic stability, NBS1 and NBS8-iPSC present different genotypes, as NBS1 is homozygous while NBS8 is heterozygous for the *NBN* 657del5 mutation. The arising question is: are NBS-cerebral organoids capable of resembling the progressive microcephaly observed in both NBS patients? Following that, chapter 3.2 describes the use of 3D cerebral organoids to decipher the molecular mechanism underlying microcephaly using NBS-iPSCs.

Differentiation of NBS-iPSCs into cerebral organoids was successfully implemented. The generated organoids recapitulate aspects of the early human brain development with defined molecular markers. When compared to the control-organoids, NBS1-organoids presented smaller size, recapitulating the microcephaly phenotype. A disrupted cytoarchitecture was also observed in NBS1-organoids characterized by an almost complete lack of VZs. Albeit no differences in the number and proliferative capacity of the NPCs was observed at 20 days of differentiation, we proposed that the disrupted cytoarchitecture affects the normal interkinetic nuclear migration and the proper development of a contiguous cortical formation. No differences in size and cytoarchitecture was observed in NBS8-organoids, probably due to the distinct genetic composition. This heterogeneity was also highlighted when the global transcriptome was analysed, where a different modulation of genes between NBS1 and NBS8-organoids was observed. We suggested that NBS1 and NBS8-organoids respond in distinct manner to the endogenous levels of oxidative stress due to the proliferation of NPCs, probably due to the presence of additional mutations in NBS8-iPSCs which can confer growth advantages [157]. However, our data suggests both NBS-organoids display a compromised DDR, supported by *ATM* mRNA downregulation, dramatic reduction in p53 protein expression and increase in γ -H2AX nuclear foci formation. Our findings are in line with the previous reports suggesting an impairment in the ATM-p53 pathway activation after endogenous DNA damage in NBS cells [158,159]. As consequence, our data suggests

NBS-NPCs undergo premature differentiation, supported by the increased number of DCX and β III-tubulin⁺ cells. Ample evidence has been accumulated on premature differentiation of the NPCs leading to its depletion as the common mechanism underlying microcephaly described in patient-derived organoids. This premature differentiation has been linked to an increase in asymmetric division [56,135,137,139]. We were not able to access the cell division cleavage plan and therefore our data could not argue for an increase in asymmetric division. Rather, we propose that the premature differentiation observed could be explained by the massive over-expression of NNAT, corroborated by the loss of methylation within its promoter. NNAT has been reported to promote neuronal differentiation and to maintain cellular homeostasis. Despite that protective role, increased expression of NNAT has been associated with apoptosis and neuronal loss. Accordingly, an increase in apoptosis was observed at 40 days of differentiation, along with down-regulation of genes involved in cell division and cell cycle. With increase accumulation of DNA-damage, mimicked here by bleomycin, NBS-organoids showed delayed activation of p53 downstream targets. As a result, cells were not able to activate DNA damage checkpoints and stop cell division at the same magnitude seen in control organoids.

Together, we propose that *NBN* 657del5 mutation induces a progressive phenotype. In an early developmental stage, cells try to maintain homeostasis and genomic integrity. However, due to the inability to efficiently repair damaged DNA, NPCs undergo premature differentiation with disrupted structural organization. We hypothesize that this process is in part triggered by the over-expression of NNAT. The observed increase in genomic instability is a consequence of delayed p53-mediated DNA damage response. Ultimately, the increase in DNA damage together with an aberrant trans-synaptic signalling lead to neuronal apoptosis. We propose the premature differentiation of the NPCs and an increase in apoptosis in the NPCs and post-mitotic neurons as the mechanism underlying progressive microcephaly-the hallmark of NBS.

Albeit the highly challenging task proposed in this thesis, here we report for the first time a 3D platform to model NBS using cerebral organoids. The data generated here serves as a valuable and powerful contribution to understanding the underlying mechanism of microcephaly as a consequence of the *NBN* 657del5 mutation. Nevertheless, in this work

many angles were left open and several questions were raised. Albeit more than 90% of the patients are homozygous for the *NBN* 657del5 mutation, some patients are carrying heterozygous mutations. Further studies focused on the *NBN* gene screening to identify the presence of point mutations and how these mutations contribute to the disease phenotype should be performed. One limitation of our study is the small sample size that generates some degree of heterogeneity. NBS is a rare disease and thus the availability of patient primary fibroblasts is limited. Furthermore, there are numerous hurdles associated with reprogramming these cells, as we previously reported [127]. The generation of NBS-iPSCs carrying the *NBN* 657del5 mutation using the CRISPR-Cas9 gene editing technique is a promising approach to overcome the challenges inherent with modelling NBS. This would also allow the generation of isogenic control iPSC line, which could facilitate the identification of the *NBN* 657del5 mutation target effects. Nonetheless, with this work we show the usability and feasibility of NBS-organoids as a model system, as well as some limitations that can be taken into account in order to improve further studies.

4.2 Conclusion and future perspectives

The work developed in this thesis describes the development and application of 2D and 3D human neural cell models for disease modelling of AD and NBS. Despite many challenges objected in this thesis, lessons from the chapter 2 and 3 brought this thesis to its purpose, achieving the overall aims initially proposed. Together the work in this thesis shows that iPSC models offer a tremendous opportunity to address neuronal pathologies that animal models lack. Specifically, iPSC-derived from AD and NBS patients have proven to be a powerful platform for evaluation of disease-related phenotypes, opening new avenues for the disease modelling and drug discovery fields. However, we need to take into consideration the limitations of these *in vitro* systems. iPSC-based 3D cerebral organoids provide a more realistic platform to investigate neurodevelopment and neurodegenerative diseases. However, there are some factors that may limit their utility, and further optimization of the existing models is required. New robust and standardize protocols of differentiation and maturation of cerebral organoids, with increased complexity while maintaining repro-

ducibility are needed. Incorporation of astrocytes, oligodendrocytes, and microglia into the cerebral organoids system are crucial to allow the functional interaction between these cells mimicking the brain microenvironment. Also, the incorporation of a vascular network and ultimately the blood-brain-barrier will overcome the lack of oxygen and nutrient flow to the inner cells. Combination of refined cerebral organoids systems with technological advances in the “-omics” methodologies and genome editing tools will improve our ability to model neurological diseases using iPSCs.

5 | References

1. Kolios, G.; Moodley, Y. Introduction to Stem Cells and Regenerative Medicine. *Respiration* 2013, *85*, 3–10, doi:10.1159/000345615.
2. Adjaye, J.; Huntriss, J.; Herwig, R.; BenKahla, A.; Brink, T.C.; Wierling, C.; Hultschig, C.; Groth, D.; Yaspo, M.-L.; Picton, H.M.; et al. Primary Differentiation in the Human Blastocyst: Comparative Molecular Portraits of Inner Cell Mass and Trophectoderm Cells. *Stem Cells* 2005, *23*, 1514–1525, doi:10.1634/stemcells.2005-0113.
3. De Los Angeles, A.; Ferrari, F.; Xi, R.; Fujiwara, Y.; Benvenisty, N.; Deng, H.; Hochedlinger, K.; Jaenisch, R.; Lee, S.; Leitch, H.G.; et al. Hallmarks of pluripotency. *Nature* 2015, *525*, 469–478.
4. Singh, V.K.; Kalsan, M.; Kumar, N.; Saini, A.; Chandra, R. Induced pluripotent stem cells: Applications in regenerative medicine, disease modeling, and drug discovery. *Frontiers in Cell and Developmental Biology* 2015, *3*.
5. Thomson, J.A. Embryonic stem cell lines derived from human blastocysts. *Science* 1998, *282*, 1145–1147, doi:10.1126/science.282.5391.1145.
6. Takahashi, K.; Tanabe, K.; Ohnuki, M.; Narita, M.; Ichisaka, T.; Tomoda, K.; Yamanaka, S. Induction of Pluripotent Stem Cells from Adult Human Fibroblasts by Defined Factors. *Cell* 2007, *131*, 861–872, doi:10.1016/j.cell.2007.11.019.
7. Liu, G.; David, B.T.; Trawczynski, M.; Fessler, R.G. Advances in Pluripotent Stem Cells: History, Mechanisms, Technologies, and Applications. *Stem Cell Reviews and Reports* 2020, *16*, 3–32.
8. Romito, A.; Cobellis, G. Pluripotent stem cells: Current understanding and future directions. *Stem Cells International* 2016, *2016*.
9. Rony, I.K.; Baten, A.; Bloomfield, J.A.; Islam, M.E.; Billah, M.M.; Islam, K.D. Inducing pluripotency in vitro: Recent advances and highlights in induced pluripotent stem cells generation and pluripotency reprogramming. *Cell Proliferation* 2015, *48*, 140–156.
10. Yu, J.; Vodyanik, M.A.; Smuga-Otto, K.; Antosiewicz-Bourget, J.; Frane, J.L.; Tian, S.; Nie, J.; Jonsdottir, G.A.; Ruotti, V.; Stewart, R.; et al. Induced pluripotent stem cell lines derived from human somatic cells. *Science* 2007, *318*, 1917–1920, doi:10.1126/science.1151526.
11. Takahashi, K.; Yamanaka, S. A decade of transcription factor-mediated reprogramming to pluripotency. *Nature Reviews Molecular Cell Biology* 2016, *17*, 183–193.
12. Kawamura, T.; Suzuki, J.; Wang, Y. V.; Menendez, S.; Morera, L.B.; Raya, A.; Wahl, G.M.; Belmonte, J.C.I. Linking the p53 tumour suppressor pathway to somatic cell reprogramming. *Nature* 2009, *460*, 1140–1144, doi:10.1038/nature08311.
13. Zhao, Y.; Yin, X.; Qin, H.; Zhu, F.; Liu, H.; Yang, W.; Zhang, Q.; Xiang, C.; Hou, P.; Song, Z.; et al.

- Two Supporting Factors Greatly Improve the Efficiency of Human iPSC Generation. *Cell Stem Cell* 2008, 3, 475–479.
14. Zhang, R.; Zhang, L.-H.; Xie, X. iPSCs and small molecules: a reciprocal effort towards better approaches for drug discovery. *Acta Pharmacologica Sinica* 2013, 34, 765–776, doi:10.1038/aps.2013.21.
 15. Prigione, A.; Fauler, B.; Lurz, R.; Lehrach, H.; Adjaye, J. The senescence-related mitochondrial/oxidative stress pathway is repressed in human induced pluripotent stem cells. *Stem Cells* 2010, 28, 721–733, doi:10.1002/stem.404.
 16. Zhu, S.; Li, W.; Zhou, H.; Wei, W.; Ambasudhan, R.; Lin, T.; Kim, J.; Zhang, K.; Ding, S. Reprogramming of human primary somatic cells by OCT4 and chemical compounds. *Cell Stem Cell* 2010, 7, 651–655.
 17. Polo, J.M.; Hochedlinger, K. When fibroblasts MET iPSCs. *Cell Stem Cell* 2010, 7, 5–6.
 18. Raab, S.; Klingenstein, M.; Liebau, S.; Linta, L. A Comparative View on Human Somatic Cell Sources for iPSC Generation. *Stem Cells International* 2014, 2014.
 19. Loh, Y.H.; Agarwal, S.; Park, I.H.; Urbach, A.; Huo, H.; Heffner, G.C.; Kim, K.; Miller, J.D.; Ng, K.; Daley, G.Q. Generation of induced pluripotent stem cells from human blood. *Blood* 2009, 113, 5476–5479, doi:10.1182/blood-2009-02-204800.
 20. Streckfuss-Bömeke, K.; Wolf, F.; Azizian, A.; Stauske, M.; Tiburcy, M.; Wagner, S.; Hübscher, D.; Dressel, R.; Chen, S.; Jende, J.; et al. Comparative study of human-induced pluripotent stem cells derived from bone marrow cells, hair keratinocytes, and skin fibroblasts. *European Heart Journal* 2013, 34, 2618–2629, doi:10.1093/eurheartj/ehs203.
 21. Zhou, T.; Benda, C.; Duzinger, S.; Huang, Y.; Li, X.; Li, Y.; Guo, X.; Cao, G.; Chen, S.; Hao, L.; et al. Generation of induced pluripotent stem cells from urine. *Journal of the American Society of Nephrology* 2011, 22, 1221–1228, doi:10.1681/ASN.2011010106.
 22. Bohndorf, M.; Ncube, A.; Spitzhorn, L.S.; Enczmann, J.; Wruck, W.; Adjaye, J. Derivation and characterization of integration-free iPSC line ISRM-UM51 derived from SIX2-positive renal cells isolated from urine of an African male expressing the CYP2D6 *4/*17 variant which confers intermediate drug metabolizing activity. *Stem Cell Research* 2017, 25, 18–21, doi:10.1016/j.scr.2017.10.004.
 23. Martí, M.; Mulero, L.; Pardo, C.; Morera, C.; Carrió, M.; Laricchia-Robbio, L.; Esteban, C.R.; Belmonte, J.C.I. Characterization of pluripotent stem cells. *Nature Protocols* 2013, 8, 223–253, doi:10.1038/nprot.2012.154.
 24. Maherali, N.; Hochedlinger, K. Guidelines and Techniques for the Generation of Induced Pluripotent

- Stem Cells. *Cell Stem Cell* 2008, 3, 595–605.
25. Yoshihara, M.; Hayashizaki, Y.; Murakawa, Y. Genomic Instability of iPSCs: Challenges Towards Their Clinical Applications. *Stem Cell Reviews and Reports* 2017, 13, 7–16.
 26. Karagiannis, P.; Takahashi, K.; Saito, M.; Yoshida, Y.; Okita, K.; Watanabe, A.; Inoue, H.; Yamashita, J.K.; Todani, M.; Nakagawa, M.; et al. Induced pluripotent stem cells and their use in human models of disease and development. *Physiological Reviews* 2019, 99, 79–114.
 27. Zhu, Z.; Huangfu, D. Human pluripotent stem cells: An emerging model in developmental biology. *Development (Cambridge)* 2013, 140, 705–717.
 28. Graffmann, N.; Spitzhorn, L.-S.; Martins, S.; Rahman, M.S.; Nguyen, L.; Adjaye, J. Stem Cell Therapy. In *Drug Discovery and Evaluation: Methods in Clinical Pharmacology*; Springer International Publishing: Cham, 2020; pp. 637–667.
 29. Vadodaria, K.C.; Jones, J.R.; Linker, S.; Gage, F.H. Modeling brain disorders using induced pluripotent stem cells. *Cold Spring Harbor Perspectives in Biology* 2020, 12, 1–15, doi:10.1101/cshperspect.a035659.
 30. Shi, Y.; Inoue, H.; Wu, J.C.; Yamanaka, S. Induced pluripotent stem cell technology: A decade of progress. *Nature Reviews Drug Discovery* 2017, 16, 115–130.
 31. Stiles, J.; Jernigan, T.L. The basics of brain development. *Neuropsychology Review* 2010.
 32. Ming, G. li; Song, H. Adult Neurogenesis in the Mammalian Brain: Significant Answers and Significant Questions. *Neuron* 2011.
 33. Molyneaux, B.J.; Arlotta, P.; Menezes, J.R.L.; Macklis, J.D. Neuronal subtype specification in the cerebral cortex. *Nature Reviews Neuroscience* 2007.
 34. Domingues, H.S.; Portugal, C.C.; Socodato, R.; Relvas, J.B. Oligodendrocyte, astrocyte, and microglia crosstalk in myelin development, damage, and repair. *Frontiers in Cell and Developmental Biology* 2016, 4, 71.
 35. Tao, Y.; Zhang, S.C. Neural Subtype Specification from Human Pluripotent Stem Cells. *Cell Stem Cell* 2016, 19, 573–586.
 36. Paridaen, J.T.; Huttner, W.B. Neurogenesis during development of the vertebrate central nervous system. *EMBO Reports* 2014.
 37. Taverna, E.; Götz, M.; Huttner, W.B. The cell biology of neurogenesis: toward an understanding of the development and evolution of the neocortex. *Annual review of cell and developmental biology* 2014.
 38. Götz, M.; Barde, Y.A. Radial glial cells: Defined and major intermediates between embryonic stem cells and CNS neurons. *Neuron* 2005, 46, 369–372.

39. Florio, M.; Huttner, W.B. Neural progenitors, neurogenesis and the evolution of the neocortex. *Development (Cambridge)* 2014, *141*, 2182–2194.
40. Jiang, X.; Nardelli, J. Cellular and molecular introduction to brain development. *Neurobiology of Disease* 2016.
41. Jiang, X.; Zhang, J.; Huang, Y. Tetraspanins in Cell Migration. *Cell Adhesion & Migration* 2015, 1–10, doi:10.1080/19336918.2015.1005465.
42. Dwyer, N.D.; Chen, B.; Chou, S.J.; Hippenmeyer, S.; Nguyen, L.; Ghashghaei, H.T. Neural stem cells to cerebral cortex: Emerging mechanisms regulating progenitor behavior and productivity. In Proceedings of the Journal of Neuroscience; Society for Neuroscience, 2016; Vol. 36, pp. 11394–11401.
43. Hébert, J.M.; Fishell, G. The genetics of early telencephalon patterning: Some assembly required. *Nature Reviews Neuroscience* 2008, *9*, 678–685.
44. Masserdotti, G.; Gascón, S.; Götz, M. Direct neuronal reprogramming: Learning from and for development. *Development (Cambridge)* 2016, *143*, 2494–2510.
45. Martynoga, B.; Drechsel, D.; Guillemot, F. Molecular control of neurogenesis: A view from the mammalian cerebral cortex. *Cold Spring Harbor Perspectives in Biology* 2012, *4*, doi:10.1101/cshperspect.a008359.
46. Fernández, V.; Llinares-Benadero, C.; Borrell, V. Cerebral cortex expansion and folding: what have we learned? *The EMBO Journal* 2016, *35*, 1021–1044, doi:10.15252/embj.201593701.
47. Barkovich, A.J.; Guerrini, R.; Kuzniecky, R.I.; Jackson, G.D.; Dobyns, W.B. A developmental and genetic classification for malformations of cortical development: Update 2012. *Brain* 2012, *135*, 1348–1369.
48. Suzuki, I.K.; Vanderhaeghen, P. Is this a brain which i see before me? Modeling human neural development with pluripotent stem cells. *Development (Cambridge)* 2015, *142*, 3138–3150.
49. McComish, S.F.; Caldwell, M.A. Generation of defined neural populations from pluripotent stem cells. *Philosophical Transactions of the Royal Society B: Biological Sciences* 2018, *373*, 20170214, doi:10.1098/rstb.2017.0214.
50. Chambers, S.M.; Fasano, C.A.; Papapetrou, E.P.; Tomishima, M.; Sadelain, M.; Studer, L. Highly efficient neural conversion of human ES and iPS cells by dual inhibition of SMAD signaling. *Nature Biotechnology* 2009, *27*, 275–280, doi:10.1038/nbt.1529.
51. Kirkeby, A.; Grealish, S.; Wolf, D.A.; Nelander, J.; Wood, J.; Lundblad, M.; Lindvall, O.; Parmar, M. Generation of Regionally Specified Neural Progenitors and Functional Neurons from Human

- Embryonic Stem Cells under Defined Conditions. *Cell Reports* 2012, 1, 703–714, doi:10.1016/j.celrep.2012.04.009.
52. Liu, Y.; Liu, H.; Sauvey, C.; Yao, L.; Zarnowska, E.D.; Zhang, S.C. Directed differentiation of forebrain GABA interneurons from human pluripotent stem cells. *Nature Protocols* 2013, 8, 1670–1679, doi:10.1038/nprot.2013.106.
53. Shi, Y.; Kirwan, P.; Livesey, F.J. Directed differentiation of human pluripotent stem cells to cerebral cortex neurons and neural networks. *Nature Protocols* 2012, doi:10.1038/nprot.2012.116.
54. Jorfi, M.; D’Avanzo, C.; Kim, D.Y.; Irimia, D. Three-Dimensional Models of the Human Brain Development and Diseases. *Advanced Healthcare Materials* 2018, 7, doi:10.1002/adhm.201700723.
55. Eiraku, M.; Watanabe, K.; Matsuo-Takasaki, M.; Kawada, M.; Yonemura, S.; Matsumura, M.; Wataya, T.; Nishiyama, A.; Muguruma, K.; Sasai, Y. Self-Organized Formation of Polarized Cortical Tissues from ESCs and Its Active Manipulation by Extrinsic Signals. *Cell Stem Cell* 2008, 3, 519–532, doi:10.1016/j.stem.2008.09.002.
56. Lancaster, M.A.; Renner, M.; Martin, C.-A.; Wenzel, D.; Bicknell, L.S.; Hurles, M.E.; Homfray, T.; Penninger, J.M.; Jackson, A.P.; Knoblich, J.A. Cerebral organoids model human brain development and microcephaly. *Nature* 2013, 501, 373–9, doi:10.1038/nature12517.
57. Qian, X.; Song, H.; Ming, G.L. Brain organoids: Advances, applications and challenges. *Development (Cambridge)* 2019, 146.
58. Camp, J.G.; Badsha, F.; Florio, M.; Kanton, S.; Gerber, T.; Wilsch-Bräuninger, M.; Lewitus, E.; Sykes, A.; Hevers, W.; Lancaster, M.; et al. Human cerebral organoids recapitulate gene expression programs of fetal neocortex development. *Proceedings of the National Academy of Sciences of the United States of America* 2015, 112, 15672–15677, doi:10.1073/pnas.1520760112.
59. Velasco, S.; Kedaigle, A.J.; Simmons, S.K.; Nash, A.; Rocha, M.; Quadrato, G.; Paulsen, B.; Nguyen, L.; Adiconis, X.; Regev, A.; et al. Individual brain organoids reproducibly form cell diversity of the human cerebral cortex. *Nature* 2019, 570, 523–527, doi:10.1038/s41586-019-1289-x.
60. Quadrato, G.; Nguyen, T.; Macosko, E.Z.; Sherwood, J.L.; Yang, S.M.; Berger, D.R.; Maria, N.; Scholvin, J.; Goldman, M.; Kinney, J.P.; et al. Cell diversity and network dynamics in photosensitive human brain organoids. *Nature* 2017, 545, 48–53, doi:10.1038/nature22047.
61. Sidhaye, J.; Knoblich, J.A. Brain organoids: an ensemble of bioassays to investigate human neurodevelopment and disease. *Cell Death and Differentiation* 2020.
62. Sakaguchi, H.; Kadoshima, T.; Soen, M.; Narii, N.; Ishida, Y.; Ohgushi, M.; Takahashi, J.; Eiraku, M.; Sasai, Y. Generation of functional hippocampal neurons from self-organizing human embryonic stem cell-derived dorsomedial telencephalic tissue. *Nature Communications* 2015, 6,

doi:10.1038/ncomms9896.

63. Birey, F.; Andersen, J.; Makinson, C.D.; Islam, S.; Wei, W.; Huber, N.; Fan, H.C.; Metzler, K.R.C.; Panagiotakos, G.; Thom, N.; et al. Assembly of functionally integrated human forebrain spheroids. *Nature* 2017, *545*, 54–59, doi:10.1038/nature22330.
64. Kadoshima, T.; Sakaguchi, H.; Nakano, T.; Soen, M.; Ando, S.; Eiraku, M.; Sasai, Y. Self-organization of axial polarity, inside-out layer pattern, and species-specific progenitor dynamics in human ES cell-derived neocortex. *Proceedings of the National Academy of Sciences of the United States of America* 2013, *110*, 20284–20289, doi:10.1073/pnas.1315710110.
65. Xiang, Y.; Tanaka, Y.; Cakir, B.; Patterson, B.; Kim, K.Y.; Sun, P.; Kang, Y.J.; Zhong, M.; Liu, X.; Patra, P.; et al. hESC-Derived Thalamic Organoids Form Reciprocal Projections When Fused with Cortical Organoids. *Cell Stem Cell* 2019, doi:10.1016/j.stem.2018.12.015.
66. Qian, X.; Nguyen, H.N.; Song, M.M.; Hadiono, C.; Ogden, S.C.; Hammack, C.; Yao, B.; Hamersky, G.R.; Jacob, F.; Zhong, C.; et al. Brain-Region-Specific Organoids Using Mini-bioreactors for Modeling ZIKV Exposure. *Cell* 2016, doi:10.1016/j.cell.2016.04.032.
67. Jo, J.; Xiao, Y.; Sun, A.X.; Cukuroglu, E.; Tran, H.D.; Göke, J.; Tan, Z.Y.; Saw, T.Y.; Tan, C.P.; Lokman, H.; et al. Midbrain-like Organoids from Human Pluripotent Stem Cells Contain Functional Dopaminergic and Neuromelanin-Producing Neurons. *Cell Stem Cell* 2016, doi:10.1016/j.stem.2016.07.005.
68. Muguruma, K.; Nishiyama, A.; Kawakami, H.; Hashimoto, K.; Sasai, Y. Self-organization of polarized cerebellar tissue in 3D culture of human pluripotent stem cells. *Cell Reports* 2015, *10*, 537–550, doi:10.1016/j.celrep.2014.12.051.
69. Sloan, S.A.; Andersen, J.; Paşca, A.M.; Birey, F.; Paşca, S.P. Generation and assembly of human brain region-specific three-dimensional cultures. *Nature Protocols* 2018, *13*, 2062–2085, doi:10.1038/s41596-018-0032-7.
70. Bagley, J.A.; Reumann, D.; Bian, S.; Lévi-Strauss, J.; Knoblich, J.A. Fused cerebral organoids model interactions between brain regions. *Nature Methods* 2017, *14*, 743–751, doi:10.1038/nmeth.4304.
71. Paşca, A.M.; Sloan, S.A.; Clarke, L.E.; Tian, Y.; Makinson, C.D.; Huber, N.; Kim, C.H.; Park, J.-Y.; O’Rourke, N.A.; Nguyen, K.D.; et al. Functional cortical neurons and astrocytes from human pluripotent stem cells in 3D culture. *Nature Methods* 2015, *12*, 671–678, doi:10.1038/nmeth.3415.
72. Bhaduri, A.; Andrews, M.G.; Mancía Leon, W.; Jung, D.; Shin, D.; Allen, D.; Jung, D.; Schmunk, G.; Haeussler, M.; Salma, J.; et al. Cell stress in cortical organoids impairs molecular subtype specification. *Nature* 2020, *578*, 142–148, doi:10.1038/s41586-020-1962-0.
73. Gopalakrishnan, J. The Emergence of Stem Cell-Based Brain Organoids: Trends and Challenges.

- BioEssays* 2019, *41*, 1900011, doi:10.1002/bies.201900011.
74. Sloan, S.A.; Andersen, J.; Paşca, A.M.; Birey, F.; Paşca, S.P. Generation and Assembly of Human Brain Region-Specific Three-Dimensional Cultures. *Nature protocols* 2018, *13*, 2062, doi:10.1038/S41596-018-0032-7.
75. Luo, C.; Lancaster, M.A.; Castanon, R.; Nery, J.R.; Knoblich, J.A.; Ecker, J.R. Cerebral Organoids Recapitulate Epigenomic Signatures of the Human Fetal Brain. *Cell Reports* 2016, *17*, 3369–3384, doi:10.1016/j.celrep.2016.12.001.
76. Di Lullo, E.; Kriegstein, A.R. The use of brain organoids to investigate neural development and disease. *Nature Reviews Neuroscience* 2017, *18*, 573–584.
77. World Health Organization 2006 Challenges., Neurological disorders : public health. *WHO Library Cataloguing-in-Publication Data* 2019, doi:10.1007/978-3-319-43504-6.
78. GBD 2016 Traumatic Brain Injury and Spinal Cord Injury Collaborators, S.L.; Theadom, A.; Ellenbogen, R.G.; Bannick, M.S.; Montjoy-Venning, W.; Lucchesi, L.R.; Abbasi, N.; Abdulkader, R.; Abraha, H.N.; Adsuar, J.C.; et al. Global, regional, and national burden of traumatic brain injury and spinal cord injury, 1990–2016: a systematic analysis for the Global Burden of Disease Study 2016. *The Lancet. Neurology* 2019, *18*, 56–87, doi:10.1016/S1474-4422(18)30415-0.
79. Logan, S.; Arzua, T.; Canfield, S.G.; Seminary, E.R.; Sison, S.L.; Ebert, A.D.; Bai, X. Studying Human Neurological Disorders Using Induced Pluripotent Stem Cells: From 2D Monolayer to 3D Organoid and Blood Brain Barrier Models. In *Comprehensive Physiology*; Wiley, 2019; Vol. 9, pp. 565–611.
80. Dolmetsch, R.; Geschwind, D.H. The human brain in a dish: The promise of iPSC-derived neurons. *Cell* 2011, *145*, 831–834.
81. Silva, M.C.; Haggarty, S.J. Human pluripotent stem cell–derived models and drug screening in CNS precision medicine. *Annals of the New York Academy of Sciences* 2019, *1471*, 18–56.
82. Hall, V.J. Modelling Neurodegenerative Diseases Using Human Pluripotent Stem Cells. In *Pluripotent Stem Cells - From the Bench to the Clinic*; InTech, 2016.
83. Haenseler, W.; Rajendran, L. Concise Review: Modeling Neurodegenerative Diseases with Human Pluripotent Stem Cell-Derived Microglia. *STEM CELLS* 2019, *37*, 724–730, doi:10.1002/stem.2995.
84. Brennand, K.J.; Simone, A.; Jou, J.; Gelboin-Burkhart, C.; Tran, N.; Sangar, S.; Li, Y.; Mu, Y.; Chen, G.; Yu, D.; et al. Modelling schizophrenia using human induced pluripotent stem cells. *Nature* 2011, *473*, 221–225, doi:10.1038/nature09915.
85. Das, D.; Feuer, K.; Wahbeh, M.; Avramopoulos, D. Modeling Psychiatric Disorder Biology with Stem Cells. *Current Psychiatry Reports* 2020, *22*, 1–23.

86. Logan, S.; Arzua, T.; Canfield, S.G.; Seminary, E.R.; Sison, S.L.; Ebert, A.D.; Bai, X.; Author, C. Studying Human Neurological Disorders Using Induced Pluripotent Stem Cells: from 2D Monolayer to 3D Organoid and Blood Brain Barrier Models HHS Public Access. *Compr Physiol* 2019, *9*, 565–611, doi:10.1002/cphy.c180025.
87. Gabriel, E.; Ramani, A.; Altinisik, N.; Gopalakrishnan, J. Human Brain Organoids to Decode Mechanisms of Microcephaly. *Frontiers in Cellular Neuroscience* 2020, *14*, 115.
88. Krefft, O.; Koch, P.; Ladewig, J. Cerebral organoids to unravel the mechanisms underlying malformations of human cortical development. *Seminars in Cell and Developmental Biology* 2020.
89. Patterson, C. World Alzheimer Report 2018 The state of the art of dementia research: New frontiers. *Alzheimer's Disease International (ADI)* 2018.
90. Hardy, J.A.; Higgins, G.A. Alzheimer's disease: The amyloid cascade hypothesis. *Science* 1992, *256*, 184–185.
91. Polanco, J.C.; Li, C.; Bodea, L.G.; Martinez-Marmol, R.; Meunier, F.A.; Götz, J. Amyloid- β and tau complexity - Towards improved biomarkers and targeted therapies. *Nature Reviews Neurology* 2018, *14*, 22–40.
92. Hardy, J.; Selkoe, D.J. The amyloid hypothesis of Alzheimer's disease: Progress and problems on the road to therapeutics. *Science* 2002, *297*, 353–356.
93. Cacace, R.; Sleegers, K.; Van Broeckhoven, C. Molecular genetics of early-onset Alzheimer's disease revisited. *Alzheimer's & Dementia* 2016, *12*, 733–748, doi:10.1016/J.JALZ.2016.01.012.
94. Carmona, S.; Hardy, J.; Guerreiro, R. The genetic landscape of Alzheimer disease. In *Handbook of Clinical Neurology*; 2018; Vol. 148, pp. 395–408 ISBN 9780444640765.
95. Bettens, K.; Sleegers, K.; Van Broeckhoven, C. Genetic insights in Alzheimer's disease. *The Lancet Neurology* 2013, *12*, 92–104, doi:10.1016/S1474-4422(12)70259-4.
96. Farrer, L.A.; Cupples, L.A.; Haines, J.L.; Hyman, B.; Kukull, W.A.; Mayeux, R.; Myers, R.H.; Pericak-Vance, M.A.; Risch, N.; Duijn, C.M. van Effects of Age, Sex, and Ethnicity on the Association Between Apolipoprotein E Genotype and Alzheimer Disease. *JAMA* 1997, *278*, 1349, doi:10.1001/jama.1997.03550160069041.
97. Verheijen, J.; Sleegers, K. Understanding Alzheimer Disease at the Interface between Genetics and Transcriptomics. *Trends in Genetics* 2018, *34*, 434–447, doi:10.1016/j.tig.2018.02.007.
98. Hollingworth, P.; Harold, D.; Sims, R.; et al Common variants at ABCA7, MS4A6A/MS4A4E, EPHA1, CD33 and CD2AP are associated with Alzheimer's disease. *Nature genetics* 2011, *43*, 429–35, doi:10.1038/ng.803.

99. Harold, D.; Abraham, R.; Hollingworth, P.; Sims, R. *Genome-wide association study identifies variants at CLU and PICALM associated with Alzheimer's disease*; 2009;
100. Lambert, J.C.; Heath, S.; Even, G.; Campion, D.; Sleegers, K.; Hiltunen, M.; Combarros, O.; Zelenika, D.; Bullido, M.J.; Tavernier, B.; et al. Genome-wide association study identifies variants at CLU and CR1 associated with Alzheimer's disease. *Nat Genet* 2009, *41*, 1094–1099, doi:10.1038/ng.439.
101. Guerreiro, R.; Wojtas, A.; Bras, J.; Carrasquillo, M.; Rogaeve, E.; Majounie, E.; Cruchaga, C.; Sassi, C.; Kauwe, J.S.K.; Younkin, S.; et al. TREM2 variants in Alzheimer's disease. *The New England journal of medicine* 2013, *368*, 117–27, doi:10.1056/NEJMoa1211851.
102. Wray, S. Modelling neurodegenerative disease using brain organoids. *Seminars in Cell and Developmental Biology* 2020.
103. Arber, C.; Lovejoy, C.; Wray, S. Stem cell models of Alzheimer's disease: Progress and challenges. *Alzheimer's Research and Therapy* 2017, *9*.
104. Rowland, H.A.; Hooper, N.M.; Kellett, K.A.B. Modelling Sporadic Alzheimer's Disease Using Induced Pluripotent Stem Cells. *Neurochemical Research* 2018, *43*, 2179–2198.
105. Israel, M.A.; Yuan, S.H.; Bardy, C.; Reyna, S.M.; Mu, Y.; Herrera, C.; Hefferan, M.P.; Van Gorp, S.; Nazor, K.L.; Boscolo, F.S.; et al. Probing sporadic and familial Alzheimer's disease using induced pluripotent stem cells. *Nature* 2012, *482*, 216–220, doi:10.1038/nature10821.
106. Hossini, A.M.; Megges, M.; Prigione, A.; Lichtner, B.; Toliat, M.R.; Wruck, W.; Schröter, F.; Nuernberg, P.; Kroll, H.; Makrantonaki, E.; et al. Induced pluripotent stem cell-derived neuronal cells from a sporadic Alzheimer's disease donor as a model for investigating AD-associated gene regulatory networks. *BMC Genomics* 2015, *16*, 84, doi:10.1186/s12864-015-1262-5.
107. Ochalek, A.; Mihalik, B.; Avci, H.X.; Chandrasekaran, A.; Téglási, A.; Bock, I.; Giudice, M. Lo; Tancos, Z.; Molnár, K.; László, L.; et al. Neurons derived from sporadic Alzheimer's disease iPSCs reveal elevated TAU hyperphosphorylation, increased amyloid levels, and GSK3B activation. *Alzheimer's Research & Therapy* 2017, *9*, 90, doi:10.1186/s13195-017-0317-z.
108. Young, J.E.; Boulanger-Weill, J.; Williams, D.A.; Woodruff, G.; Buen, F.; Revilla, A.C.; Herrera, C.; Israel, M.A.; Yuan, S.H.; Edland, S.D.; et al. Elucidating molecular phenotypes caused by the SORL1 Alzheimer's disease genetic risk factor using human induced pluripotent stem cells. *Cell Stem Cell* 2015, *16*, 373–385, doi:10.1016/j.stem.2015.02.004.
109. Kondo, T.; Asai, M.; Tsukita, K.; Kutoku, Y.; Ohsawa, Y.; Sunada, Y.; Imamura, K.; Egawa, N.; Yahata, N.; Okita, K.; et al. Cell Stem Cell Modeling Alzheimer's Disease with iPSCs Reveals Stress Phenotypes Associated with Intracellular Ab and Differential Drug Responsiveness. 2013, doi:10.1016/j.stem.2013.01.009.

110. Flamier, A.; El Hajjar, J.; Adjaye, J.; Fernandes, K.J.; Abdouh, M.; Bernier, G. Modeling Late-Onset Sporadic Alzheimer's Disease through BMI1 Deficiency. *Cell Reports* 2018, doi:10.1016/j.celrep.2018.04.097.
111. Lee, H.K.; Velazquez Sanchez, C.; Chen, M.; Morin, P.J.; Wells, J.M.; Hanlon, E.B.; Xia, W. Three dimensional human neuro-spheroid model of Alzheimer's disease based on differentiated induced pluripotent stem cells. *PLoS ONE* 2016, *11*, doi:10.1371/journal.pone.0163072.
112. Balez, R.; Steiner, N.; Engel, M.; Muñoz, S.S.; Lum, J.S.; Wu, Y.; Wang, D.; Vallotton, P.; Sachdev, P.; O'Connor, M.; et al. Neuroprotective effects of apigenin against inflammation, neuronal excitability and apoptosis in an induced pluripotent stem cell model of Alzheimer's disease. *Scientific Reports* 2016, *6*, 1–16, doi:10.1038/srep31450.
113. Chen, M.; Lee, H.K.; Moo, L.; Hanlon, E.; Stein, T.; Xia, W. Common proteomic profiles of induced pluripotent stem cell-derived three-dimensional neurons and brain tissue from Alzheimer patients. *Journal of Proteomics* 2018, *182*, 21–33, doi:10.1016/j.jpro.2018.04.032.
114. Duan, L.; Bhattacharyya, B.J.; Belmadani, A.; Pan, L.; Miller, R.J.; Kessler, J.A. Stem cell derived basal forebrain cholinergic neurons from Alzheimer's disease patients are more susceptible to cell death. *Molecular Neurodegeneration* 2014, *9*, 3, doi:10.1186/1750-1326-9-3.
115. Chrzanowska, K.H.; Gregorek, H.; Dembowska-Bagińska, B.; Kalina, M.A.; Digweed, M. Nijmegen breakage syndrome (NBS). *Orphanet journal of rare diseases* 2012, *7*, 13, doi:10.1186/1750-1172-7-13.
116. Weemaes, C.M.; Hustinx, T.W.; Scheres, J.M.; van Munster, P.J.; Bakkeren, J.A.; Taalman, R.D. A new chromosomal instability disorder: the Nijmegen breakage syndrome. *Acta paediatrica Scandinavica* 1981, *70*, 557–64, doi:10.1111/j.1651-2227.1981.tb05740.x.
117. Varon, R.; Demuth, I.; Chrzanowska, K.H. *Nijmegen Breakage Syndrome*; University of Washington, Seattle, 1993;
118. Digweed, M.; Sperling, K. Nijmegen breakage syndrome: clinical manifestation of defective response to DNA double-strand breaks. *DNA Repair* 2004, *3*, 1207–1217, doi:10.1016/J.DNAREP.2004.03.004.
119. Chrzanowska, K.H.; Stumm, M.; Bekiesiska-Figatowska, M.; Varon, R.; Bialecka, M.; Gregorek, H.; Michakiewicz, J.; Krajewska-Walasek, M.; Jówiak, S.; Reis, A. Atypical clinical picture of the Nijmegen breakage syndrome associated with developmental abnormalities of the brain. *Journal of medical genetics* 2001, *38*, E3, doi:10.1136/jmg.38.1.e3.
120. Seemanova, E.; Jarolim, P.; Seeman, P.; Varon, R.; Digweed, M.; Swift, M.; Sperling, K. Cancer Risk of Heterozygotes With the NBN Founder Mutation. *JNCI Journal of the National Cancer Institute* 2007, *99*, 1875–1880, doi:10.1093/jnci/djm251.

121. Varon, R.; Seemanova, E.; Chrzanowska, K.; Hnateyko, O.; Piekutowska-Abramczuk, D.; Krajewska-Walasek, M.; Sykut-Cegielska, J.; Sperling, K.; Reis, A. Clinical ascertainment of Nijmegen breakage syndrome (NBS) and prevalence of the major mutation, 657del5, in three Slav populations. *European Journal of Human Genetics* 2000, 8, 900–902, doi:10.1038/sj.ejhg.5200554.
122. Maser, R.S.; Zinkel, R.; Petrini, J.H.J. An alternative mode of translation permits production of a variant NBS1 protein from the common Nijmegen breakage syndrome allele. *Nature Genetics* 2001, 27, 417–421, doi:10.1038/86920.
123. Stracker, T.H.; Petrini, J.H.J. The MRE11 complex: starting from the ends. *Nature reviews. Molecular cell biology* 2011, 12, 90–103, doi:10.1038/nrm3047.
124. Jongmans, W.; Vuillaume, M.; Chrzanowska, K.; Smeets, D.; Sperling, K.; Hall, J. Nijmegen breakage syndrome cells fail to induce the p53-mediated DNA damage response following exposure to ionizing radiation. *Molecular and cellular biology* 1997, 17, 5016–22, doi:10.1128/mcb.17.9.5016.
125. Buscemi, G.; Savio, C.; Zannini, L.; Miccichè, F.; Masnada, D.; Nakanishi, M.; Tauchi, H.; Komatsu, K.; Mizutani, S.; Khanna, K.; et al. Chk2 activation dependence on Nbs1 after DNA damage. *Molecular and cellular biology* 2001, 21, 5214–22, doi:10.1128/MCB.21.15.5214-5222.2001.
126. Sullivan, K.E.; Veksler, E.; Lederman, H.; Lees-Miller, S.P. Cell Cycle Checkpoints and DNA Repair in Nijmegen Breakage Syndrome. *Clinical Immunology and Immunopathology* 1997, 82, 43–48, doi:10.1006/CLIN.1996.4275.
127. Mlody, B.; Wruck, W.; Martins, S.; Sperling, K.; Adjaye, J. Nijmegen Breakage Syndrome fibroblasts and iPSCs: Cellular models for uncovering disease-associated signaling pathways and establishing a screening platform for anti-oxidants. *Scientific Reports* 2017, doi:10.1038/s41598-017-07905-2.
128. Barzilai, A.; Biton, S.; Shiloh, Y. The role of the DNA damage response in neuronal development, organization and maintenance. *DNA repair* 2008, 7, 1010–27, doi:10.1016/j.dnarep.2008.03.005.
129. Halliwell, B. Oxidative stress and neurodegeneration: where are we now? *Journal of Neurochemistry* 2006, 97, 1634–1658, doi:10.1111/j.1471-4159.2006.03907.x.
130. Frappart, P.-O.; Tong, W.-M.; Demuth, I.; Radovanovic, I.; Herceg, Z.; Aguzzi, A.; Digweed, M.; Wang, Z.-Q. An essential function for NBS1 in the prevention of ataxia and cerebellar defects. *Nature Medicine* 2005, 11, 538–544, doi:10.1038/nm1228.
131. Zhou, Z.; Bruhn, C.; Wang, Z.-Q. Differential function of NBS1 and ATR in neurogenesis. *DNA Repair* 2012, 11, 210–221, doi:10.1016/J.DNAREP.2011.10.021.
132. Halevy, T.; Akov, S.; Bohndorf, M.; Mlody, B.; Adjaye, J.; Benvenisty, N.; Goldberg, M. Chromosomal Instability and Molecular Defects in Induced Pluripotent Stem Cells from Nijmegen Breakage Syndrome Patients. *Cell reports* 2016, 16, 2499–511, doi:10.1016/j.celrep.2016.07.071.

133. Bowen, M.E.; Attardi, L.D. The role of p53 in developmental syndromes. *Journal of Molecular Cell Biology* 2019, *11*, 200–211.
134. Marin Navarro, A.; Pronk, R.J.; van der Geest, A.T.; Oliynyk, G.; Nordgren, A.; Arsenian-Henriksson, M.; Falk, A.; Wilhelm, M. p53 controls genomic stability and temporal differentiation of human neural stem cells and affects neural organization in human brain organoids. *Cell Death and Disease* 2020, *11*, 1–16, doi:10.1038/s41419-019-2208-7.
135. Gabriel, E.; Wason, A.; Ramani, A.; Gooi, L.M.; Keller, P.; Pozniakovskiy, A.; Poser, I.; Noack, F.; Telugu, N.S.; Calegari, F.; et al. CPAP promotes timely cilium disassembly to maintain neural progenitor pool. *The EMBO Journal* 2016, *35*, 803–819, doi:10.15252/embj.201593679.
136. Li, R.; Sun, L.; Fang, A.; Li, P.; Wu, Q.; Wang, X. Recapitulating cortical development with organoid culture in vitro and modeling abnormal spindle-like (ASPM related primary) microcephaly disease. *Protein & cell* 2017, *8*, 823–833, doi:10.1007/s13238-017-0479-2.
137. Zhang, W.; Yang, S.-L.; Yang, M.; Herrlinger, S.; Shao, Q.; Collar, J.L.; Fierro, E.; Shi, Y.; Liu, A.; Lu, H.; et al. Modeling microcephaly with cerebral organoids reveals a WDR62-CEP170-KIF2A pathway promoting cilium disassembly in neural progenitors. *Nature communications* 2019, *10*, 2612, doi:10.1038/s41467-019-10497-2.
138. Gabriel, E.; Ramani, A.; Altinisik, N.; Gopalakrishnan, J. Human Brain Organoids to Decode Mechanisms of Microcephaly. *Frontiers in Cellular Neuroscience* 2020, *14*, 115, doi:10.3389/fncel.2020.00115.
139. Li, Y.; Muffat, J.; Omer, A.; Bosch, I.; Lancaster, M.A.; Sur, M.; Gehrke, L.; Knoblich, J.A.; Jaenisch, R. Induction of Expansion and Folding in Human Cerebral Organoids. *Cell Stem Cell* 2017, *20*, 385–396.e3, doi:10.1016/j.stem.2016.11.017.
140. Iefremova, V.; Manikakis, G.; Krefft, O.; Jabali, A.; Weynans, K.; Wilkens, R.; Marsoner, F.; Brändl, B.; Müller, F.J.; Koch, P.; et al. An Organoid-Based Model of Cortical Development Identifies Non-Cell-Autonomous Defects in Wnt Signaling Contributing to Miller-Dieker Syndrome. *Cell Reports* 2017, *19*, 50–59, doi:10.1016/j.celrep.2017.03.047.
141. Bershteyn, M.; Nowakowski, T.J.; Pollen, A.A.; Lullo, E. Di; Nene, A.; Wynshaw-Boris, A.; Kriegstein Correspondence, A.R. Human iPSC-Derived Cerebral Organoids Model Cellular Features of Lissencephaly and Reveal Prolonged Mitosis of Outer Radial Glia. 2017, doi:10.1016/j.stem.2016.12.007.
142. Klaus, J.; Kanton, S.; Kyrousi, C.; Ayo-Martin, A.C.; Di Giaimo, R.; Riesenberger, S.; O'Neill, A.C.; Camp, J.G.; Tocco, C.; Santel, M.; et al. Altered neuronal migratory trajectories in human cerebral organoids derived from individuals with neuronal heterotopia. *Nature Medicine* 2019, *25*, 561–568, doi:10.1038/s41591-019-0371-0.

143. Martins, S.; Yigit, H.; Bohndorf, M.; Graffmann, N.; Fiszl, A.R.; Wruck, W.; Slegers, K.; Van Broeckhoven, C.; Adjaye, J. Lymphoblast-derived integration-free iPSC line AD-TREM2-1 from a 67 year-old Alzheimer's disease patient expressing the TREM2 p.R47H variant. *Stem Cell Research* 2018, *29*, 60–63, doi:10.1016/j.scr.2018.03.011.
144. Martins, S.; Yigit, H.; Bohndorf, M.; Graffmann, N.; Fiszl, A.R.; Wruck, W.; Slegers, K.; Van Broeckhoven, C.; Adjaye, J. Lymphoblast-derived integration-free iPSC line AD-TREM2-3 from a 74 year-old Alzheimer's disease patient expressing the TREM2 p.R47H variant. *Stem Cell Research* 2018, *30*, 141–144, doi:10.1016/j.scr.2018.05.018.
145. Martins, S.; Bohndorf, M.; Schröter, F.; Assar, F.; Wruck, W.; Slegers, K.; Van Broeckhoven, C.; Adjaye, J. Lymphoblast-derived integration-free ISRM-CON9 iPS cell line from a 75 year old female. *Stem Cell Research* 2018, *26*, doi:10.1016/j.scr.2017.12.007.
146. Levenga, J.; Krishnamurthy, P.; Rajamohamedsait, H.; Wong, H.; Franke, T.F.; Cain, P.; Sigurdsson, E.M.; Hoeffer, C.A. Tau pathology induces loss of GABAergic interneurons leading to altered synaptic plasticity and behavioral impairments. *Acta neuropathologica communications* 2013, *1*, 34, doi:10.1186/2051-5960-1-34.
147. Berry, B.J.; Smith, A.S.T.; Young, J.E.; Mack, D.L. Stem Cells / Review Article Advances and Current Challenges Associated with the Use of Human Induced Pluripotent Stem Cells in Modeling Neurodegenerative Disease. *Cells Tissues Organs* 2018, *205*, 331–349, doi:10.1159/000493018.
148. Penney, J.; Ralvenius, W.T.; Tsai, L.H. Modeling Alzheimer's disease with iPSC-derived brain cells. *Molecular Psychiatry* 2020, *25*, 148–167.
149. Kondo, T.; Asai, M.; Tsukita, K.; Kutoku, Y.; Ohsawa, Y.; Sunada, Y.; Imamura, K.; Egawa, N.; Yahata, N.; Okita, K.; et al. Modeling Alzheimer's disease with iPSCs reveals stress phenotypes associated with intracellular A β and differential drug responsiveness. *Cell Stem Cell* 2013, *12*, 487–496, doi:10.1016/j.stem.2013.01.009.
150. Müller-Schiffmann, A.; Herring, A.; Abdel-Hafiz, L.; Chepkova, A.N.; Schäble, S.; Wedel, D.; Horn, A.H.C.; Sticht, H.; de Souza Silva, M.A.; Gottmann, K.; et al. Amyloid- β dimers in the absence of plaque pathology impair learning and synaptic plasticity. *Brain : a journal of neurology* 2016, *139*, 509–25, doi:10.1093/brain/awv355.
151. Piers, T.M.; Cosker, K.; Mallach, A.; Johnson, G.T.; Guerreiro, R.; Hardy, J.; Pocock, J.M. A locked immunometabolic switch underlies TREM2 R47H loss of function in human iPSC-derived microglia. *The FASEB Journal* 2020, *34*, 2436–2450, doi:10.1096/fj.201902447R.
152. Vassar, R.; Kovacs, D.M.; Yan, R.; Wong, P.C. The β -secretase enzyme BACE in health and Alzheimer's disease: Regulation, cell biology, function, and therapeutic potential. In Proceedings of the Journal of Neuroscience; Society for Neuroscience, 2009; Vol. 29, pp. 12787–12794.

153. Nixon, R.A.; Yang, D.S. Autophagy failure in Alzheimer's disease-locating the primary defect. *Neurobiology of Disease* 2011, *43*, 38–45.
154. Korvatska, O.; Kiianitsa, K.; Ratushny, A.; Matsushita, M.; Beeman, N.; Chien, W.-M.; Satoh, J.-I.; Dorschner, M.O.; Keene, C.D.; Bammler, T.K.; et al. TREM2 R47H exacerbates immune response in Alzheimer's disease brain. *bioRxiv* 2020, 499319, doi:10.1101/499319.
155. Bera, S.; Cambor-Perujo, S.; Calleja Barca, E.; Negrete-Hurtado, A.; Racho, J.; De Bruyckere, E.; Wittich, C.; Ellrich, N.; Martins, S.; Adjaye, J.; et al. AP -2 reduces amyloidogenesis by promoting BACE 1 trafficking and degradation in neurons. *EMBO reports* 2020, *21*, doi:10.15252/embr.201947954.
156. Martins, S.; Bohndorf, M.; Graffmann, N.; Wruck, W.; Chrzanowska, K.H.; Adjaye, J. Fibroblast-derived integration-free iPSC line ISRM-NBS1 from an 18-year-old Nijmegen Breakage Syndrome patient carrying the homozygous NBN c.657_661del5 mutation. *Stem Cell Research* 2019, *34*, 101372, doi:10.1016/J.SCR.2018.101372.
157. M, S.; D, R.; L, C.; A, K.; J, S.; N, D. Methods of Reprogramming to Induced Pluripotent Stem Cell Associated With Chromosomal Integrity and Delineation of a Chromosome 5q Candidate Region for Growth Advantage. *Stem cells and development* 2015, *24*, doi:10.1089/SCD.2015.0061.
158. Fiévet, A.; Bellanger, D.; Zahed, L.; Burglen, L.; Derrien, A.; Dubois d'Enghien, C.; Lespinasse, J.; Parfait, B.; Pedespan, J.; Rieunier, G.; et al. DNA repair functional analyses of NBN hypomorphic variants associated with NBN-related infertility. *Human Mutation* 2020, *41*, 608–618, doi:10.1002/humu.23955.
159. Uziel, T.; Lerenthal, Y.; Moyal, L.; Andegeko, Y.; Mittelman, L.; Shiloh, Y. Requirement of the MRN complex for ATM activation by DNA damage. *EMBO Journal* 2003, doi:10.1093/emboj/cdg541.

6 | Appendix

6.1 Acknowledgements

I would like to express my sincere gratitude to everyone who supported me in the last years, for your contribution to this journey and making this dissertation possible.

First of all, I would like to deeply thank my supervisor Prof. Dr. James Adjaye for accepting me into his lab and supporting me throughout the development of this work. It was an absolute pleasure to work under his supervision and mentoring. I am grateful for his exceptional dedication, patience, trust and encouragement. Thank you for giving me the opportunity to try out my ideas, for always being so positive and a special thank you for keeping my passion for science alive. I would also like to thank Prof. Dr. Gerhald Fritz for kindly accepted to be my co-supervisor, and for the inspiring discussions and constructive comments.

In addition, I would like to show my appreciation to all collaborators and co-authors, without whom this thesis would have not been possible. Thank you to the graduate schools, iBrain, and iGRAD for giving me the opportunity to participate in inspiring scientific meetings and congresses.

To the entire ISRM lab team, thank you for the wonderful work atmosphere: Jan Greulich, Dr. Jörg Otte, Dr. Lucas Spitzhorn, Lisa Nguyen, Martina Bohndorf, Rita Ofterdinger, Silke Wehrmeyer, Shaifur Rahman and Dipl. Ing. Wasco Wruck. Thank you for your support, your help and for the good moments and laughs inside and outside the lab. From the first day, you always made me feel at home. I would like to especially thank Dr. Nina Graffmann for the unconditional help, for all the patience and the fruitful discussions in our cosy office; and Dr. Lars Erichsen for sharing with me his passion and knowledge about the epigenetic world. Additionally, a big thank you to Audrey Ncube and Robert Fiszl with whom I shared all my ups and downs, but most of all for always being there in good and not so good moments.

To my Dusseldorf buddy Edita; thanks for all the support and for the relaxing and good moments we spent together.

Obrigada Joana por todo o apoio incondicional, preocupação e por todos os conselhos. Obrigada pelas horas passadas ao telemóvel, por todas as discussões científicas (e não tão científicas) e sobretudo por estares sempre presente nos bons e maus momentos.

Gracias Marcos, por todo el cariño, soporte y por toda la paciencia. Gracias por creer siempre en mi y por ser mi pilar de apoyo durante esta etapa de mi vida.

Aos meus pais e irmã, porque tudo o que sou o devo a vocês. Obrigada por toda a força, ternura, coragem, confiança e apoio incondicional. Obrigada por terem estado sempre presentes na minha vida, apesar dos 2000 km que nos separam. Obrigada por sempre acreditarem em mim e por me estimularem a querer sempre ir mais longe e melhor.

6.2 Scientific publications

Peer-reviews journal articles:

1. **Martins S**, Müller-Schiffmann A, Erichsen L, Bohndorf M, Wruck W, Slegers K, Van Broeckhoven C, Korth C, Adjaye J. IPSC-Derived Neuronal Cultures Carrying the Alzheimer's Disease Associated TREM2 R47H Variant Enables the Construction of an A β -Induced Gene Regulatory Network. *Int. J. Mol. Sci.* 2020, 21, 4516.
2. Bera S, Cambor-Peruj, S, Calleja Barca E, Negrete-Hurtado A, Racho J, De Bruyckere E, Wittich C, Ellrich N, **Martins S**, Adjaye J, Kononenko, N. AP -2 reduces amyloidogenesis by promoting BACE 1 trafficking and degradation in neurons. *EMBO reports* 2020, 21,
3. Rahman M.S, Wruck W, Spitzhorn L., Nguyen L, Bohndorf M, **Martins S**, Asar F, Ncube A, Erichsen L, Graffmann N, Adjaye J. (2020) The FGF, TGF β and WNT axis Modulate Self-renewal of Human SIX2+ Urine Derived Renal Progenitor Cells. *Sci Rep* 10, 739
4. **Martins S**, Bohndorf M, Graffmann N, Wruck W, Chrzanowska K, Adjaye J. (2019) Fibroblast-derived integration-free iPSC line ISRM-NBS1 from an 18-year-old Nijmegen Breakage Syndrome patient carrying the homozygous NBN c.657_661del5 mutation. *Stem Cell Research*, 34: 101372
5. **Martins S**, Correia P, Dias R, da Cruz e Silva O, Vieira S. (2019) CD81 promotes a migratory phenotype in neuronal-like cells, *Microscopy and Microanalysis*, 1-7
6. **Martins S**, Yigit H, Bohndorf M, Graffmann N, Fiszl AR, Wruck W, Slegers K, Van Broeckhoven C and Adjaye J. (2018). Lymphoblast-derived integration-free iPSC line AD-TREM2-3 from a 74year-old Alzheimer's disease patient expressing the TREM2 p.R47H variant, *Stem Cell Research*, 30: 141-144
7. **Martins S**, Yigit H, Bohndorf M, Graffmann N, Fiszl AR, Wruck W, Slegers K, Van Broeckhoven C and Adjaye J. (2018) Lymphoblast-derived integration-free iPSC line

AD-TREM2-1 from a 67 year-old Alzheimer's disease patient expressing the TREM2 p.R47H variant, *Stem Cell Research*, 29: 60-63

8. **Martins S**, Bohndorf M, Schröter F, Assar F, Wruck W, Slegers K, Van Broeckhoven C. and Adjaye J. (2018). Lymphoblast-derived integration-free ISRM-CON9 iPSC cell line from a 75 year old female. *Stem Cell Res.* 26: 76-79
9. Mlody B, Wruck W, **Martins S**, Sperling K, Adjaye J. (2017) Nijmegen Breakage Syndrome fibroblasts and iPSCs: cellular models for uncovering disease-associated signaling pathways and establishing a screening platform for anti-oxidants. *Sci Rep.* 2017 Aug 8;7(1):7516
10. Tavares, RS , **Martins S**, Almeida-Santos T, Sousa AP, Ramalho-Santos J, da Cruz e Silva OA. (2017) Alzheimer's disease-related amyloid- β 1–42 peptide induces the loss of human sperm function. *Cell Tissue Res* 369: 647.

Book chapters and other publications:

1. **Soraia Martins**, Lars Erichsen, Angeliki Datsi, Wasco Wruck, Wolfgang Goering, Krystyna Chrzanowska, James Adjaye. Impaired p53-mediated DNA damage response contributes to microcephaly in Nijmegen Breakage Syndrome patient-derived cerebral organoids. *bioRxiv* 2020.09.29.318527; doi: <https://doi.org/10.1101/2020.09.29.318527>
2. Graffmann N, Spitzhorn LS, **Martins S**, Rahman M.S, Nguyen L., Adjaye J. (2020) Stem Cell Therapy. In: Hock F., Gralinski M. (eds) *Drug Discovery and Evaluation: Methods in Clinical Pharmacology*. Springer, Cham
3. **Soraia Martins** , Andreas Müller-Schiffmann , Martina Bohndorf, Wasco Wruck, Kristel Slegers, Christine Van Broeckhoven, Carsten Korth and James Adjaye. (2019) iPSC-derived neuronal cultures expressing the Alzheimer's disease associated rare TREM R47H variant enables the construction of an A β -induced gene regulatory network. *bioRxiv* 652446; doi: <https://doi.org/10.1101/652446>

Oral communications:

1. **Soraia Martins**, Martina Bohndorf, Wasco Wruck, Krystyna Chrzanowska and James Adjaye. Deciphering the etiology of microcephaly using cerebral organoids from Nijmegen Breakage Syndrome patient-derived induced pluripotent stem cells. Stem Cell Summit, Cologne, Germany, 25th October 2019 (**Invited speaker**)
2. **Soraia Martins** , Andreas Müller-Schiffmann , Martina Bohndorf, Wasco Wruck, Kristel Slegers, Christine Van Broeckhoven, Carsten Korth and James Adjaye. Establishing and validating an Alzheimer's disease iPSC-based platform to enable studying the effect of the TREM2 R47H rare variant on disease progression. Next-Gen Regenerative Medicine Tissue Engineering Conference, Frankfurt, Germany, 8-9th October 2018 (**Invited speaker**)
3. **Soraia Martins**, Martina Bohndorf, Wasco Wruck, Krystyna Chrzanowska and James Adjaye. Deciphering the etiology of microcephaly using Nijmegen Breakage Syndrome patient-derived induced pluripotent stem cells. Internal Meeting KNW, Bonn, Germany, 4-5th May 2018

Poster communications:

1. **Soraia Martins** , Andreas Müller-Schiffmann , Martina Bohndorf, Wasco Wruck, Kristel Slegers, Christine Van Broeckhoven, Carsten Korth and James Adjaye. "The TREM2 R47H rare variant and Alzheimer's disease: an iPSC-based platform for disease modeling". ISSCR annual meeting. Los Angeles, USA, 26-29th June 2019
2. **Soraia Martins**, Martina Bohndorf, Wasco Wruck, Krystyna Chrzanowska and James Adjaye. "Deciphering the etiology of microcephaly using cerebral organoids from Nijmegen Breakage Syndrome patient-derived iPSCs". ISSCR international symposia: Stem Cells Organoids in Development Disease, Amsterdam, The Netherlands, 20-22nd February 2019
3. **Soraia Martins**, Andreas Müller-Schiffmann , Martina Bohndorf, Wasco Wruck, Kristel Slegers, Christine Van Broeckhoven, Carsten Korth and James Adjaye. "Es-

establishing and validating an Alzheimer's disease iPSC-based platform to enable studying the effect of TREM2 and CR1 variants on disease progression". Düsseldorf-Jülich Symposium on Neurodegenerative Diseases: Formation, aggregation and propagation of amyloids, Düsseldorf, Germany, 27-28th November 2017

4. **Soraia Martins**, Wasco Wruck, Barbara Mlody, Karl Sperling and James Adjaye. Nijmegen Breakage "Syndrome patient derived iPSCs as a screening platform for anti-oxidants and a tool for understanding the underlying mechanisms of microcephaly". 9th International Meeting Stem Cell Network NRW, Münster, Germany, 16-17th May 2017

6.3 Declaration of Authorship

Ich, Soraia Alexandra Araújo Martins, versichere an Eides statt, dass die vorliegende Dissertation von mir selbstständig und ohne unzulässige fremde Hilfe unter Beachtung der „Grundsätze zur Sicherung guter wissenschaftlicher Praxis an der Heinrich-Heine-Universität Düsseldorf“ erstellt worden ist.

Düsseldorf, 20 October 2020

(Soraia Alexandra Araújo Martins)